# Block Copolymer-Derived Porous Polyimides and Carbon for High-Performance Energy Storage

Dong Guo

Dissertation submitted to the faculty of the Virginia Polytechnic Institute and State University in partial fulfillment of the requirements for the degree of

Doctor of Philosophy

In

Chemistry

Guoliang Liu, Chair

Louis A. Madsen

Timothy E. Long

Robert B. Moore

April 25th, 2022

Blacksburg, Virginia

**Keywords**: mesopore, polyimides, carbon fibers, lithium-metal batteries, fast charging, zinc-ion batteries

# Block Copolymer-Derived Porous Polyimides and Carbon for High-Performance Energy Storage

Dong Guo

**ABSTRACT**

Block copolymer-derived nanoporous materials are featured with microstructures defined by the microphase separation of constituent blocks, enabling various applications in energy storage. Dictated by the molecular weights and volume fractions of constituent blocks, the microphase separation forms nanoscale microstructures of 1-100 nm. Selective removal of a sacrificial phase produces nanopores with tailored pore width, continuity, and tortuosity. The remaining phase customizes the properties of resulting nanoporous materials, including specific surface area, electrical conductivity/insulation, and mechanical performance. Therefore, block copolymer-derived porous materials are felicitous for use in high-performance energy storage. This dissertation presents the utilization of block copolymers to derive nanoporous materials: i) high-modulus polyimide separators for lithium-metal batteries, and ii) high-surface-area carbon electrodes for fast-charging zinc-ion batteries.

In lithium-metal batteries, the dendritic growth of lithium leads to deteriorating performance and severe safety concerns. Suppressing lithium dendrites is imperative to guarantee both high performance and safe cycling. Mesoporous polyimide separators are promising for dendrite suppression: i) the mesopores are smaller than the width of lithium dendrites, preventing lithium dendrites from penetrating the separator. ii) The high-

modulus polyimide ceases the growth of lithium dendrites. Herein, this dissertation reports a mesoporous polyimide separator produced by thermalizing polylactide-*b*-polyimide-*b*-polylactide at 280 °C. The mesoporous polyimide separator exhibits a median pore width of 21 nm and a storage modulus of 1.8 GPa. When serving as a dendrite-suppressing separator in lithium-metal batteries, the mesoporous polyimide separator enables safe cycling for 500 hours at a current density of 4 $mA/cm^2$.

In zinc-ion batteries, developing cathodes compatible with fast charging remains a challenge. Conventional $MnO_2$ gravel cathodes suffer from low electrical conductivity and slow ion (de-)insertion, resulting in poor recharging performance. In this dissertation, porous carbon fiber (PCF) supported $MnO_2$ (PCF@$MnO_2$), comprising nanometer-thick $MnO_2$ deposited on block copolymer-derived PCF, serves as a fast-charging cathode. The high electrical conductivity of PCF and fast ion (de-)insertion in nanometer-thick $MnO_2$ both contribute to a high rate capability. The PCF@$MnO_2$ cathode, with a $MnO_2$ loading of 59.1 wt%, achieves a $MnO_2$-based specific capacity of 326 and 184 mAh/g at a current density of 0.1 and 1.0 A/g, respectively.

This dissertation investigates approaches to utilizing block copolymers-derived nanoporous materials for high-performance energy storage. Those approaches are envisaged to inspire the design of block copolymer-derived nanoporous materials, and advance the development of “beyond Li-ion” energy storage.

# Block Copolymer-Derived Porous Polyimides and Carbon for High-Performance Energy Storage

Dong Guo


## GENERAL AUDIENCE ABSTRACT

When we talk with friends on mobile phones, accomplish works on laptops, drive back home and see family's smiling faces under lamplights, we must have noticed that our daily life significantly relies on electrical energy. Although being predominantly employed in today's rechargeable energy storage, lithium-ion batteries using graphite anodes have approached their theoretical energy limits. We are expecting better-performance batteries for a more convenient life: to fully charge our phones faster, to use our laptops for a longer time, and to drive our electric cars for a further distance. Lithium-metal batteries and aqueous zinc-ion batteries stand out for "beyond lithium-ion" energy storage because they deliver more energy and charge faster. The commercialization of lithium-metal batteries and zinc-ion batteries may benefit from revolutionary porous materials derived from block copolymers.

On one hand, lithium-metal batteries employ metallic lithium anodes, storing about 10 times of energy compared to equal-weight graphite anodes and allowing faster charging rates. However, the lithium-metal anodes grow needle-shaped dendrites during cycling. Those lithium dendrites traverse the battery separator through its large pores, causing internal short circuits and even fire hazards. Suppressing lithium dendrites is imperative for safe lithium-metal batteries. Stiff separators with small pores can suppress lithium

dendrites. The small pores prevent lithium dendrites from traversing, and the stiff separators cease the dendritic growth. This dissertation introduces a dendrite-suppressing separator derived from block copolymers comprising stiff polyimide blocks and vulnerable blocks. When those block copolymers form films, the vulnerable blocks spontaneously disperse as a network embedded in the polyimide. Then, the vulnerable blocks are removed at elevated temperatures to create interconnected small pores. This porous polyimide separator suppresses lithium dendrites to allow safe cycling for 500 hours, surpassing today's separators which encounter short circuits within 60 hours.

On the other hand, zinc-ion batteries require fast-charging cathodes for high charging rates. A fast-charging cathode demands both good electrical conductivity and fast ion insertion. Herein, this dissertation reports a porous carbon fiber supported $MnO_2$ cathode. The block copolymers comprise a polyacrylonitrile block and a vulnerable block. The vulnerable blocks form a network dispersing in the polyacrylonitrile fibers. At elevated temperatures, polyacrylonitrile is converted to graphitic carbon fibers, and the vulnerable network decomposes to create interconnected pores. The porous carbon fibers afford a large surface area, allowing a high loading of $MnO_2$ to deposit as nanometer-thick sheaths. The resulting cathode combines good electrical conductivity of porous carbon fibers and the fast ion insertion in thin $MnO_2$ sheaths, therefore, exhibiting superior fast-charging performance.

This dissertation reports the methods of using block copolymers to produce porous materials for high-performance batteries. We envisage those methods to inspire the design of block copolymer-derived porous materials, and advance the development of high-performance energy storage for a more convenient life.

# Dedication

This dissertation is dedicated to my wife, Wenting Fan, the love of my life.

## Acknowledgments

First of all, I would like to thank my advisor, Dr. Guoliang Liu, for his meticulous supervision throughout my life at Virginia Tech. I still clearly remember the heart-warming scene of how I joined the Liu research group in my first year. I intercepted Dr. Liu at his office door, telling him "I want to work in your lab", with a lab coat and a pair of goggles in my hands. After a moment of waiting with anxiety, Dr. Liu replied "yes". Time elapses, I still feel grateful and fortunate for my choice. For both my research and life here, I benefit a lot from Dr. Liu's wisdom, especially his advice on how to *work smartly* always guides me through difficulties and confusions. Three suggestions reconstruct my philosophy as a graduate researcher. First, *have a big picture of the project*. When I worked on synthesizing a polylactide-*b*-polyetherimide-*b*-polylactide as the precursor for mesoporous polyetherimide thin films, I targeted the weight fraction of polylactide at 40%. However, due to the intractable conversion to polylactide using stannous catalyst at low temperatures, the actual weight fractions of polylactide in my products were fluctuating between 35% and 42%. I was bewildered by this detail and spent weeks to try narrowing the weight fractions of polylactide to be exactly 40%. Dr. Liu allowed me to try on this work initially, but when he found that I was stranded on this detailed work, he suggested considering what is the big picture of this project, what is the most important concept-proving step, and when is the best time to revisit this detail. Till that moment did I realize that I had over-focused on this less important detail. Thanks to this suggestion, I recognize the importance of a big picture in guiding a project, especially on how to determine the priority of elucidating details and proving concepts, as well as the significance of time management. Following his suggestion, I was able to accomplish this project efficiently. The second suggestion I

always benefit from is *reaching out for help rather than working behind a closed door*. In my initial years, my misunderstanding of independent research always overwhelmed me with mastering every step and detail in my projects. This misunderstanding limited my resource of knowledge and help, as well as slowed down my research progression. For instance, when I tested my porous polyimide separator in lithium-metal batteries, my immature battery tests only afforded deceptive results. Dr. Liu encouraged me to initiate collaborations with battery specialists on campus. Benefiting from this collaboration, I gained the expertise in battery testing to expedite my progress and learned how to improve my separators. The third suggestion is *a work not published is likely a work not done*. I used to be obsessed with fulfilling my curiosity and validating my hypothesis during my research, but underestimated the importance of publications. Dr. Liu reminded me of the importance of publications, on both fulfilling the graduation requirements and contributing to the chemical society. Therefore, I paid extra attention to writing the manuscripts while analyzing data, which was truly helpful for my publications. Those three suggestions not only educate me to be a productive graduate researcher, but also develop a skill set including time management, collaborations, problem-solving, and data presentation/publication, which will be an advantage in my entire career.

I also want to express my profound appreciation to my research committee at Virginia Tech, Professor Louis A. Madsen, Robert B. Moore, and Timothy E. Long, for their devotion in the guidance to me in my literature review, preliminary exam, graduate seminars/meetings, and job interviews. I still clearly remember the meticulous comments from my committee on the feedback of my literature review. Those detailed comments are always helpful when I compose a manuscript. For example, *A figure is worth a thousand*

*words*. An introductory concept figure to organize and summarize the projects facilitates the audience's comprehension. And I also want to thank Professor S. Richard Turner and Alan R. Esker for their availability when I am in urgent need of extra committee guidance. When I received different job offers and felt extremely hard to make a choice, my committee offered me suggestions and inspirations on how to plan for a long-term career goal, especially opportunities to grow, development of network, work-life balance surpassing a high salary. Their wisdom and generosity to offer help are precious assets for my career development.

It is my great fortune to work with all Liu Group members, especially Dr. Zhengping Zhou, Dr. Assad U. Khan, Dr. Tianyu Liu, Dr. Wenqi Zhao, Dr. Fuping Pan, Dr. Ke Chen, Joel M. Serrano, Zhen Xu, Zac L. Croft, and Jocelyn A. Riet. Their collective intelligence, critical comments, and collaborative supports constantly benefit me in progressing my projects.

I would truthfully thank Professor Feng Lin and Dr. Linqin Mu for their professional assistance and insightful suggestions for my battery tests. The inspiriting comments offered me precious help with both the design of experiments and the interpretation of results. The beneficial discussions with them always motivated me to improve my projects.

I sincerely thank Ms. Joli Huynh for her coordination through my graduate program. Her professional suggestions and efficient assistance always addressed my concerns and questions in the timeliest manner, especially during this challenging pandemic phase.

I also thank Stephen McCartney at Nanoscale Characterization and Fabrication Laboratory (NCFL), Rituraj Borgohain at Materials Characterization Lab (MCL), and Ken

Sharp-Knott in the Department of Chemistry for their supportive training and generous help with various facilities.

I sincerely thank Dr. Stephen Z.D. Cheng for his dedicating guidance during my time at the University of Akron. His generosity to share life philosophy, rigorous scholarship and humble personality set a good example showing what an honorable scientist is. Also, I appreciate the faithful friendships and hands-on training from Dr. Wenpeng Shan and Dr. Xueyan Feng. Those friendship and skillsets are my lifetime assets.

Finally, I am wholeheartedly grateful to my family. As a first-generation graduate student, I received tremendous support from my parents, Hongxin Guo and Chuanmei Zhang, as well as my sister, Liang Guo. I also thank my wife, Wenting Fan, for her accompanying, encouragement, and wisdom beyond me. My family is the driving force I overcome most difficulties, the catalyst I keep challenging myself, and the most precious product I am fortunate to possess.

# Attributions

Chapter 2, 3, and 5 of this dissertation were adopted from publications. Chapter 4 will be submitted for future publication.

**Prof. Guoliang Liu** is a professor in the Department of Chemistry, Macromolecules Innovation Institute, Division of Nanoscience, Academy of Integrated Science at Virginia Tech. He is the author's research advisor and principal investigator. Prof. Liu supervised all the projects and assisted in writing and editing those manuscripts.

**Dr. Assad U. Khan** was a graduate researcher in Prof. Guoliang Liu's research group. He is a collaborator for Chapter 2 and 3.

**Dr. Zhengping Zhou** was a postdoctoral scholar in Prof. Guoliang Liu's research group. He contributed to Chapter 2.

**Dr. Yichen Guo** was a postdoctoral scholar in Prof. Guoliang Liu's research group. He contributes to Chapter 3.

**Jocelyn A. Riet** was an undergraduate researcher in Prof. Guoliang Liu's research group, and he was a collaborator for Chapter 3.

**Dr. Tianyu Liu** was a postdoctoral scholar in Prof. Guoliang Liu's research group. He contributed to Chapter 2 and 3.

**Zhen Xu** is a graduate researcher in Prof. Guoliang Liu's research group. He is a collaborator for Chapter 3 and 4.

**Prof. Feng Lin** is a professor in the Department of Chemistry, Virginia Tech. He is a collaborator and provides scientific insights for Chapter 4.

**Dr. Linqin Mu** was a postdoctoral scholar in Prof. Feng Lin's research group. She is a collaborator and provides scientific insights for Chapter 4.

**Dr. Wenqi Zhao** was a postdoctoral scholar in Prof. Guoliang Liu's research group. She is a collaborator for Chapter 5.

**Dr. Fuping Pan** was a postdoctoral scholar in Prof. Guoliang Liu's research group. He is a collaborator for Chapter 5.

# Table of Content

# Chapter 1. Block copolymer-derived porous nanomaterials

## 1.1. Introduction

The progress of human society is powered by evolving energy.[1, 2] Today, our unprecedentedly high demand for energy requires high-performance energy storage providing higher energy densities and faster charging rates.[2] Nowadays, lithium-ion batteries, employing graphite anodes, dominate the energy storage markets. The energy density of lithium-ion batteries, however, has been approaching its theoretical limit.[3] To develop next-generation high-performance energy storage, scientists must keep their persistence in developing novel nanomaterials to enable higher energy densities and faster charging rates. Block copolymers provide a versatile and robust platform for producing various nanomaterials.

Lithium-metal batteries (LMBs) and zinc-ion batteries (ZIBs) are two of the most promising candidates of "beyond Li-ion" energy storage (Figure 1.1a). On one hand, LMBs employ metallic lithium as the anodes, providing a high anodic capacity of 3860 mAh/g and a low potential of -3.040 V vs. the standard hydrogen electrode.[4] However, the dendritic growth of lithium-metal anodes during cycling leads to deteriorative performance and severe safety concerns (Figure 1.1b). Suppressing the dendritic growth of lithium anode is imperative for the high performance and safe cycling of LMBs. On the other hand, ZIBs adopt an aqueous electrolyte and a zinc-metal anode, affording high (dis)charging rates and good safety. However, developing a cathode compatible with fast charging remains a challenge. Conventional cathodes consist of metal oxide gravels, carbon additives, and binders, suffering from insufficient electrical conductivity and sluggish ion (de-)insertion at high charging rates (Figure 1.1c). The optimized cathode must have

synergistically combined good electrical conductivity and prompt ion (de-)insertion to allow fast electrochemical reactions during (dis-)charging.

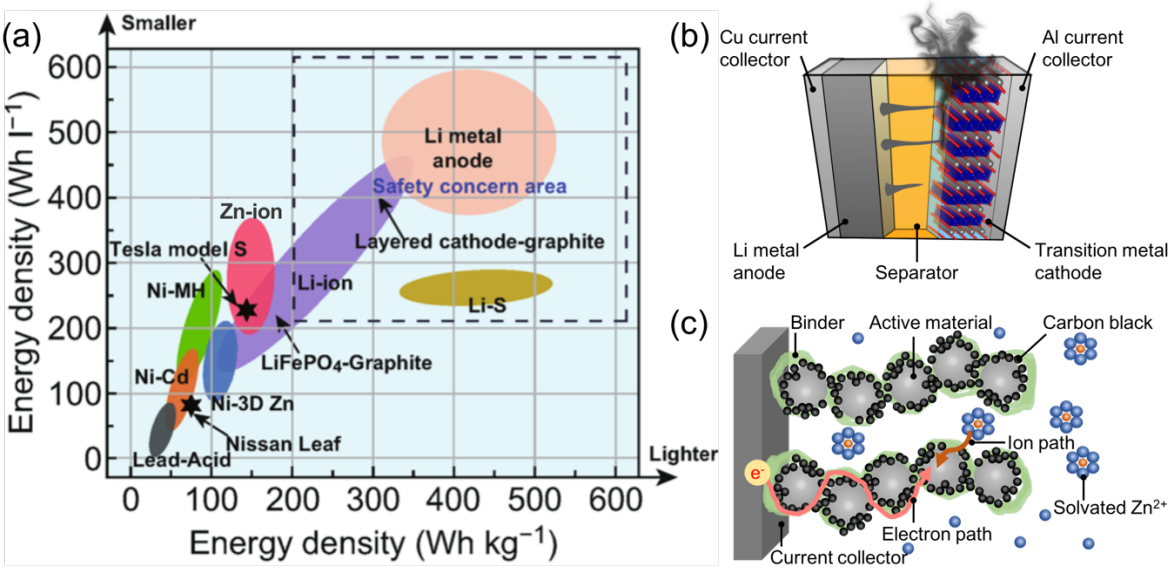


**Figure 1.1** (a) Gravimetric and volumetric energy densities of rechargeable batteries. Lithium-metal batteries and zinc-ion batteries show high energy densities, holding great promise for "beyond Li-ion" energy storage. Reprinted with permission from *Energy Environ. Sci.* **2018**, 11, 3168-3175.[5] Copyright 2018 Royal Society of Chemistry. (b) Lithium dendrites traverse a macroporous separator, resulting in short circuit and fire hazards. (c) Schematic illustration of electron and ion paths in conventional cathodes consisting of $MnO_2$ gravels, carbon black, and binders. The insufficient electrical conductivity and slow ion (de-)insertion limit the recharging performance. Reprinted with permission from *Adv. Energy Mater.* **2016**, 6, 1600655.[6] Copyright 2016 Wiley-VCH Verlag GmbH & Co. KGaA, Weinheim.

Herein, this dissertation reports the approaches of using block copolymer-derived porous nanomaterials to build high-performance energy storage. On one hand, a mesoporous polyimide thin film, serving as a dendrite-suppressing separator, enables the safe cycling of LMBs. This mesoporous polyimide thin film is produced from an ABA-type triblock copolymer consisting of

a polyimide middle block and sacrificial end blocks. The selective removal of the sacrificial blocks from the microphase-separated block copolymers creates mesoporous polyimide thin films. On the other hand, porous carbon fibers, supporting thin-layered $MnO_2$, produce fast-charging cathodes for aqueous ZIBs. Those porous carbon fibers are produced *via* the carbonization of polyacrylonitrile-based block copolymers, where the polyacrylonitrile phase is converted to graphitic carbon, whereas sacrificial blocks decompose to create pores. The good electrical conductivity of porous carbon fibers and fast ion (de-)insertion of thin-layered $MnO_2$ enable high rate capabilities and high energy/power densities for aqueous ZIBs.

## 1.2 Microphase separation of broad-dispersity ABA-type triblock copolymers

Block copolymers are able to undergo microphase separations due to the surface energy-driving incompatibility of constituent blocks.[7-9] The phase-separated microstructures have molecularly defined morphologies and domain sizes, enriching the toolbox to design and produce nanomaterials for innumerable applications.[7, 10] Polymers routinely consist of chains of different molecular weights. Dispersity (Đ) describes the distribution of molecular weights of polymer chains.[11] The "living" or controlled polymerizations produce polymers with narrow dispersity close to 1. Whereas the uncontrolled chain-growth polymerizations and step-growth polymerizations usually grow polymers with broad dispersity of about 2.[11] The microphase separations of AB-type diblock or ABA-type triblock copolymers consisting of narrow-dispersity blocks have been extensively studied. Dictated by the volume fraction($f$), interaction parameter ($\chi$), and the total degree of polymerization ($N$) of A and B blocks, the microphase separations of block copolymers form exquisite microstructures (Figure 1.2a and c).[10] The phase diagrams were not only investigated by theoretical prediction using self-consistent mean field theory (Figure

1.2a), but also explored by experiments employing narrow-dispersity polystyrene-*b*-polyisoprene copolymer (Figure 1.2b). Both theoretical and experimental conclusions show remarkable resemblance on the resulting phase diagram, except the experimental phase diagram shows an extra metastable phase, perforated layers (PL).[7-10, 12, 13] Importantly, both the theoretical and experimental phase diagrams are generally symmetric. At the $f_A$ of 0.5, the microphase separation affords a lamellar structure. Increasing or decreasing $f_A$ both show the morphological progression changing from lamellae to gyroids, cylinders, spheres, and disordered. But Increasing and decreasing $f_A$ result in opposite major phases.

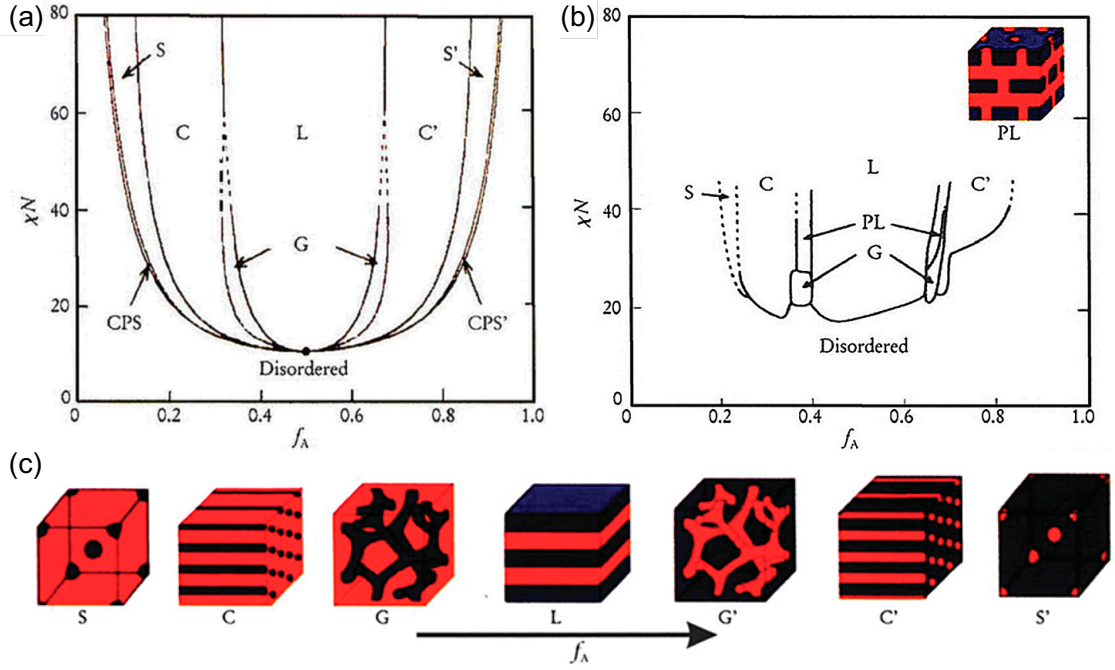


**Figure 1.2.** Phase diagram for AB-type diblock or ABA-type triblock copolymers. (a) Theoretical phase diagram using self-consistent mean field theory, where L represents lamellae, G represents gyroid, C and C' represent hexagonally packed cylinder, S and S' represent body-centered cubic sphere, CPS and CPS' represent closely packed sphere.[8] (b) Experimental phase diagram of polystyrene-*b*-polyisoprene. PL represents perforated layers.[13] (c) Equilibrium morphologies of

AB-type diblock copolymers. Reproduced from *Physics Today* **1999**, 52, 32-38,[10] with the permission of AIP Publishing.

Conversely, the AB-type diblock or ABA-type triblock block copolymers containing broad-dispersity B blocks show an asymmetric phase diagram (Figure 1.3).[14-16] A poly(styrene-*b*-1,4-butadiene-*b*-styrene) copolymer (SBS), consisting of narrow-dispersity polystyrene and broad-dispersity polybutadiene building blocks, show the lamellar structures at a volume fraction of polybutadiene, $f_B$, ranging from 56 to 80%, instead of around 50% as in narrow-dispersity block copolymers.[14] The shifted $f_B$ of SBS for lamellae arises from the broad dispersity of B blocks. The low-molecular-weight portion of B blocks is incommensurate to undergo the microphase separation due to a low $\chi N$, thus simply mixing in the A phase (Figure 1.4).[17] Importantly, besides the regular morphologies observed in narrow-dispersity block copolymers, the broad-dispersity

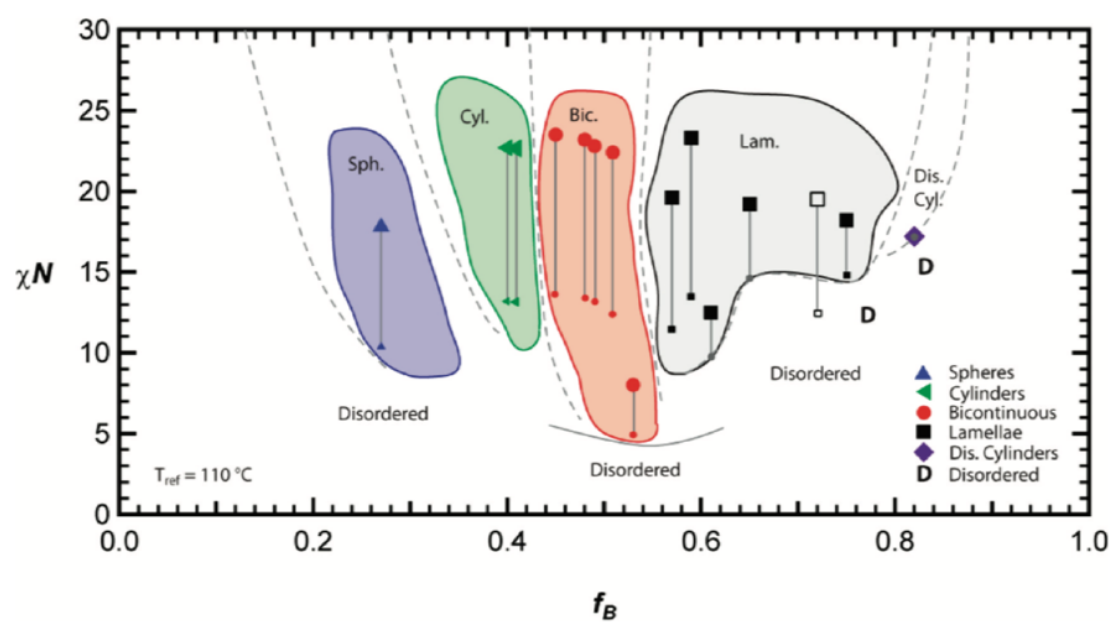


**Figure 1.3.** The phase diagram of SBS triblock copolymers with broad-dispersity B blocks shows a progression of morphologies at increasing $f_B$: disorder, spheres, cylinders, disordered bicontinuous microstructures, lamellae, disordered cylinders, and disorder. Reprint with

permission from *J. Am. Chem. Soc*. **2012**, 134, 3834-384.[14] Copyright 2012 American Chemical Society.

SBS triblock copolymers show a unique bicontinuous structure, even at an enormously low $\chi N$ of 5 and a molecular weight of 12 kDa.[14] Those characteristics of forming bicontinuous microstructures at low molecular weights are enticing for applications demanding small and continuous domains, such as nanoporous polymer films. Based on the bicontinuous microstructure, the selective removal of one phase creates continuous nanopores. Simultaneously, the remaining phase affords a nanoporous matrix.

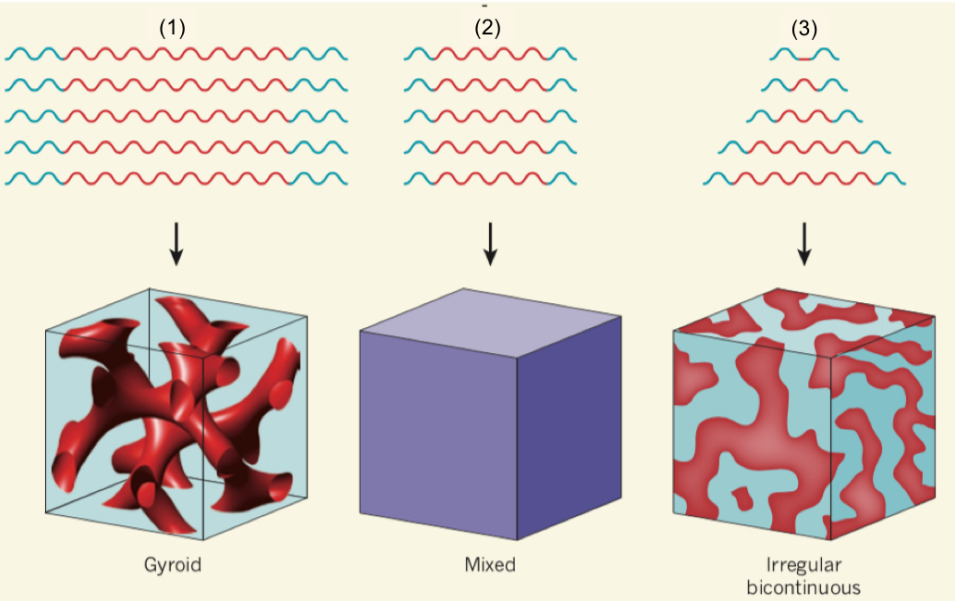


**Figure 1.4.** Morphologies of ABA-type triblock copolymers. Case (1): all A and B blocks are narrow-dispersed and long enough to phase-separate. Those block copolymers self-assemble into a bicontinuous gyroid microstructure at a certain volume fraction. Case (2): all A and B blocks are narrow-dispersed, but the lengths are incommensurate to phase-separate. Therefore, A and B blocks simply mix without forming domains. Case (3): ABA-type triblock copolymers form a robust bicontinuous microstructure, even though A blocks have the same lengths as in Case (2)

and broad-dispersity B blocks have a shorter average length than that in Case (2). Reprint with permission from *Nature* **2012**, 483, 167-168.[17] Copyright 2012 Springer Nature.

## 1.3 ABA-type triblock copolymer-derived Porous polyimides.

Porous polyimides have high mechanical performance, extraordinary thermal stability, and good chemical resistance. Therefore, porous polyimides are broadly applied in catalysis,[18] gas separation,[19-23] water purification,[24, 25] microelectronics,[26-31] etc. Conventional strategies of preparing porous polyimides employ polyimide-based ABA-type triblock copolymers.[32-42] Those triblock copolymers consist of a broad-dispersity polyimide middle block, flanked by two narrow-dispersity labile peripheral blocks.[32-42] The microphase separation of those ABA-type block copolymers form a microstructure where labile domains are embedded in a polyimide matrix. Subsequently, the labile domains were removed at high temperatures to create pores.[32-42] Various labile blocks have been investigated using the thermolysis method, including poly(ethylene oxide),[32] poly(propylene oxide),[33-37] poly(methyl methacrylate),[41, 42] polystyrene,[38] poly($\alpha$-methyl styrene),[39, 40] polycaprolactone,[27, 43-45] etc. Although the domain sizes of the labile phase are tens of nanometers, the resulting pore widths are hundreds of nanometers, even micrometers due to the "blowing effect" (Figure 1.5a).[46] During the thermolysis, the high temperatures decompose the labile phase into a large amount of gaseous species. Simultaneously, the polyimide matrix is softened at temperatures higher than the glass transition temperatures ($T_g$). Therefore, the decomposition gas produced by thermolysis of the labile phase expands in softened polyimide, resulting in macroporous polyimides.[46] Avoiding the "blowing effect" is imperative to produce mesoporous polyimides.

To avoid the decomposition gas plasticizing softened polyimide matrix, two strategies have been explored in this dissertation (Figure 1.5b). First, removing the labile phase at temperatures lower than the softening temperatures of polyimide matrixes. The combination of thermally labile end blocks and high-$T_g$ polyimide middle block allows a temperature window to remove the labile phase at relatively low temperatures without perturbing the polyimide matrix. Second, removing the labile phase *via* hydrolysis instead of thermolysis.[47, 48] The hydrolysis degrades the labile phase into products soluble in the aqueous solution, avoiding producing any gaseous species. Therefore, the hydrolysis prevents the "blowing effect" and produces mesopores, even for low-$T_g$ polyimides.

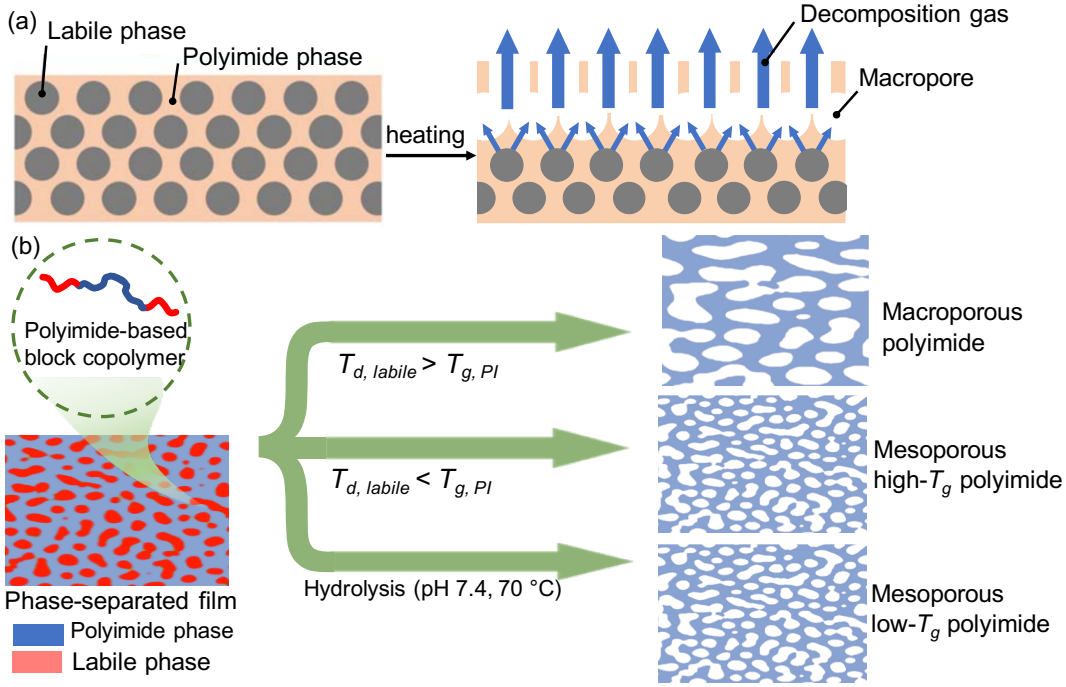


**Figure 1.5.** ABA-type triblock copolymer-derived porous polyimides. (a) Illustration of "blowing effect". At high temperatures, the decomposition gas of the labile phase plasticizes the softened polyimide matrix, resulting in macroporous polyimides. Reprint with permission from *Polym. Eng. Sci.* **2016**, 56, 1191-1200.[46] Copyright 2016 Wiley-VCH Verlag GmbH & Co. KGaA, Weinheim. (b) Macro or Mesopores of polyimides arise from different methods. Polyimide-based ABA-type triblock copolymers form phase-separated films. Decomposing the labile phase at temperatures

($T_{d,labile}$) higher than the $T_g$ of polyimide results in macroporous polyimides. Whereas removing the labile phase at temperatures lower than the $T_g$ of polyimide, or hydrolyzing the labile phase, both produce mesoporous polyimides.

Herein, this dissertation reports mesoporous polyimide thin films prepared by both of the aforementioned strategies. On one hand, mesoporous polyetherimide thin films are prepared *via* the hydrolysis of polylactide-*b*-polyetherimide-*b*-polylactide. The hydrolysis takes place in a phosphate buffer solution at a pH of 7.4 at 70 °C. Those mild hydrolytic conditions not only prevent the thermal softening of polyetherimide matrix, but also efficiently remove polylactide to create mesoporous polyetherimide thin films. The resulting mesoporous polyetherimide thin films show a median pore width of 24 nm and a high storage modulus of 1.22 GPa. On the other hand, the thermolysis of polylactide-*b*-polyimide-*b*-polylactide at a judiciously controlled temperature window produces mesoporous polyimide thin films. In this temperature window, polylactide was removed slowly to create mesopores without perturbing the polyimide matrix. The resulting mesoporous polyimide thin films show mesopores with a median pore width of 21 nm, as well as a high storage modulus of 1.80 GPa. The mesoporous polyimide thin films are applied as dendrite-suppressing separators in lithium-metal batteries in the following chapter.

## 1.4 Dendrite-suppressing strategies for lithium-metal batteries.

Lithium-metal batteries (LMBs) are credited as the holy grail of energy storage, because lithium-metal anodes provide a high theoretical capacity (3860 mAh/g) and the lowest electrochemical potential (-3.040 V vs. the standard hydrogen electrode).[2, 49, 50] The commercialization of LMBs, however, is plagued by serious safe concerns arising from lithium dendrites.[2] During the charging process, the nonuniform nucleation of lithium forms protrusions on the metallic surface.[51] The

self-amplified electrical field near the protrusions expedites the dendritic growth of lithium.[52] Governed by the charging current, the transport of $Li^+$ competes with the electroplating onto the lithium.[51] The scarcity of $Li^+$ near the metallic lithium surface further promotes the fast on-tip dendritic growth.[52] The growing dendrites expose reactive surface reacting with the electrolyte to form a solid-electrolyte interphase (SEI), supposedly slowing down further consumption of lithium and electrolyte.[50, 53, 54] However, the nonuniform striping/plating of lithium constantly causes cumulative stress and eventually brittle fractures in the SEI.[50, 53] Consequently, the freshly exposed lithium surface continues to consume the electrolyte to form thicker SEI. The growth of SEI and depletion of electrolytes increase the internal impedance, resulting in deteriorative performance of LMBs.[54] Even worse, the lithium dendrites penetrate the separator and contract the cathode, causing internal short circuits and subsequent catastrophic results.[51, 52]

The lithium dendrites exhibit three morphologies in liquid electrolytes depending on the charging currents: needle-like, moss-like and, fractal lithium dendrites (Figure 1.6).[51] The charging current regulates the rates of electroplating vs. $Li^+$ transport near the lithium electrode surface. The specific current density resulting in a $Li^+$ concentration approaching zero at the surface of lithium electrodes is defined as the limiting current density, $i_L$, expressed as Equation 1.1.[51]

$$i_L = \frac{2CDF}{(1-t_{Li})L} \qquad \text{(Equation 1.1)}$$

where $C$ is the salt concentration in the electrolyte in mol $L^{-1}$, $D$ is the salt diffusion coefficient in $cm^2\ S^{-1}$, $F = 96485$ C $mol^{-1}$ is the Faraday Constant, $t_{Li} = 0.38$ is the transference number of $Li^+$, $L$ is the distance between two electrodes in cm.[51, 52] Needle-like lithium dendrites grow in the shape of whiskers at an ultra-low current ranging from $10^{-7}$ and $10^{-3}$ of $i_L$. The low current allows whiskers to propagate simultaneously at the root, near the top, and at kinks along the stem without forming branches (Figure 1.6a and d).[55] When the propagating needle-like dendrites contact a high-

modulus obstacle, the longitudinal growth is gradually ceased due to the axial compressive stress. Further accumulating stress will result in bent and collapse of lithium whiskers.[49, 56] The moss-like dendrites are featured with a root-growing ramified structure with a high surface area, usually forming at a current density of $10^{-3}$ to $10^{-1}$ of $i_L$. The moss-like dendrites, comprising a bundle of unoriented whiskers, show an average width of several micrometers, thus those dendrites are usually blocked by separators. (Figure 1.6b and e).[52] The fractal dendrites, showing a tree-like morphology, form at current densities close to and above $i_L$. The low concentration of $Li^+$ at the root of fractal dendrites promotes a fast tip-growing manner, resulting in a branched topology with small widths (Figure 1.6c and f).[52] Today's polyolefin battery separators, showing pore widths ranging from 40 to 400 nm, have macropores larger than the width of fractal lithium dendrites.[57] Therefore, fractal dendrites can traverse those polyolefin separators and cause short circuits in LMBs. The practical applications of LMBs require high charging currents, necessitating two improvements to ensure safety: i) designing LMBs having a high $i_L$, and ii) applying dendrite-suppressing separators.

In recent decades, strategies to suppress lithium dendrites have been extensively investigated, including (1) applying concentrated electrolytes or pulse charging currents to mitigate the depletion of $Li^+$ near anode surface.[50, 58, 59] (2) Increasing the temperatures to facilitate the diffusion of $Li^+$ and modify the morphologies of lithium dendrite.[1, 60] (3) Employing a three-dimensional lithium electrode to enlarge the surface area and lower the local current density.[61-63] (4) Engineering the composition, density, elasticity, and conductivity of SEI to increase the interphase stability.[50, 63-65] Among those strategies, the high concentration of electrolyte and fast diffusion of $Li^+$ increase the $i_L$, whereas, the high surface area of three-dimensional lithium electrodes and good ionic conductivity of SEI decrease the local charging current density. Both increasing the $i_L$ and

decreasing the local current density reduce the formation of fractal lithium dendrites. However, the conventional SEI, having a thickness of <200 nm and limited mechanical strength, is vulnerable to the invasion of lithium dendrites.[54] Thus, dendrite-suppressing separators are necessary to secure the safe cycling of LMBs.

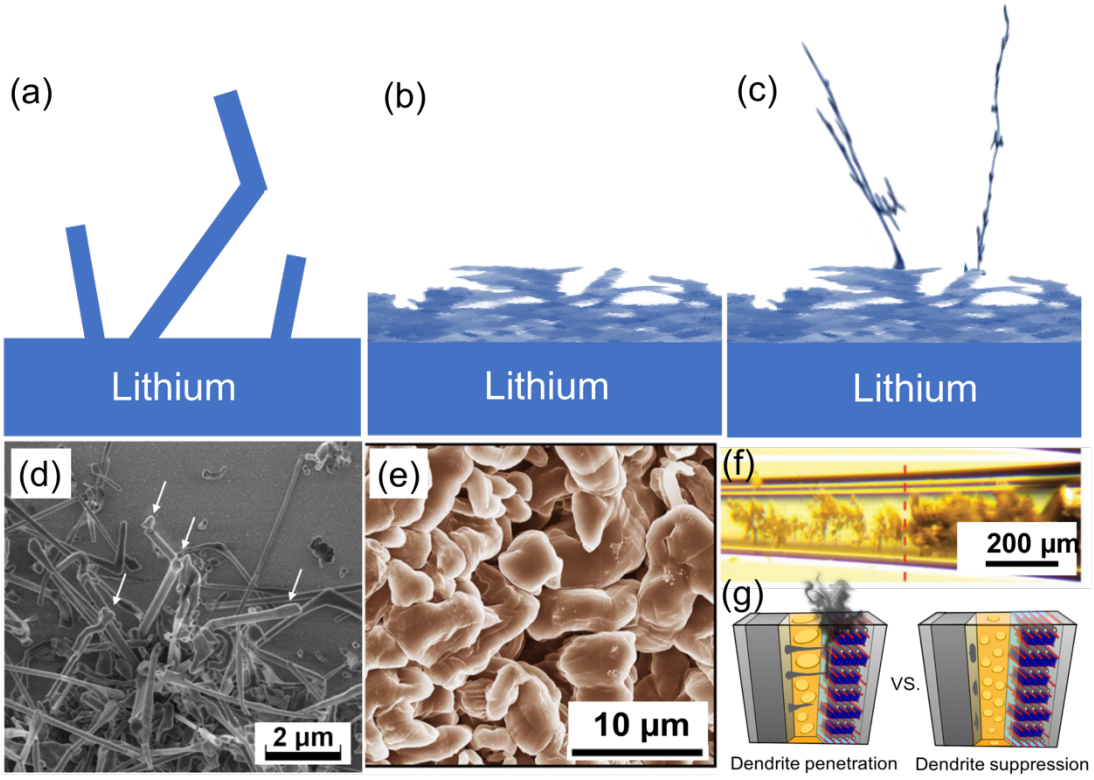


**Figure 1.6.** Morphologies of lithium dendrites. (a)(b)(c) Schematic illustrations and (d)(e)(f) experimental observations of (a)(d) needle-like, (b)(e) moss-like and (c)(f) fractal lithium dendrites. The red dashed line in (f) shows the boundary of moss-like (right) and fractal (left) dendrites. (g) Mesoporous polyimide separator suppresses the growth of lithium dendrite, therefore preventing the internal short circuit and fire hazard. (d) Reprint with permission from *J. Power Sources* **2014**, 261, 112-119.[55] Copyright 2014 Elsevier B.V. (e) Reprint with permission from *Nat. Commun.* **2015**, 6, 6362.[66] Copyright 2015 Springer Nature. (f) Reprint with permission from *Energy Environ. Sci.* **2016**, 9, 3221-3229.[52] Copyright 2016 The Royal Society of Chemistry.

Herein in this dissertation, a mesoporous polyimide thin film is applied as a dendrite-suppressing separator (Figure 1.6g). The dendrite-suppressing capability benefits from three traits of the separator. First, the separator has mesopores with a median pore width of 21 nm. Those mesopores are smaller than the width of lithium dendrites, therefore, efficiently preventing lithium dendrites from penetrating the separator. Second, those mesopores allow a uniform $Li^+$ flux onto the lithium-metal anode, facilitating the even electrodeposition of lithium.[67, 68] Third, the good mechanical performance prevents lithium dendrite from fracturing the separator. Instead, the high modulus ceases the growth of lithium dendrites toward the cathode.[49, 69-72] Therefore, this mesoporous polyimide separator enables the long-term safe cycling of LMBs.

## 1.5 Fast-Charging cathodes for zinc-ion batteries.

Zn-ion batteries (ZIBs) have attracted extensive attention in both wearable electronics and stationary energy storage, thanks to their high energy density, excellent safety, low cost, and environmental benignity.[5, 73-85] ZIBs usually employ a metallic zinc anode and an aqueous or hydrogel electrolyte. The aqueous or hydrogel electrolytes not only have a higher ionic conductivity than conventional organic electrolytes, but also eliminate the concerns of fire hazards at high charging rates. Simultaneously, the zinc-metal anodes profit the fast electrochemical stripping/plating during fast (dis)charging. Therefore, ZIBs hold a great promise to serve as fast-charging energy storage. However, developing the cathodes compatible with fast-charging ZIBs remains a challenge.[75, 76, 81, 82, 84, 86] Since the debut of Leclanché cell in 1866, $MnO_2$-based cathodes have been the first choice for ZIBs.[87] The $MnO_2$-based cathodes provide both a high voltage and a high specific capacity, therefore, the highest energy density in comparison to other Vanadium-based, polymer-based and Prussian Blue-based cathodes (Figure 1.7a).[79, 88-94]

Furthermore, altering the redox of $Mn^{4+}/Mn^{3+}$ to $Mn^{4+}/Mn^{2+}$ in $MnO_2$-based cathodes provides the opportunity to increase the energy density of Zn-$MnO_2$ batteries to above 1000 Wh/kg.[88] Today's $MnO_2$-based cathodes contain electrolytic $MnO_2$ (EMD) showing particle sizes ranging from micrometers to tens of micrometers (Figure 1.7b).[95] Although packed with carbon additives and binders, the micrometer-sized $MnO_2$ gravels suffer from both low electrical conductivity ($10^{-5}$ S/m) and sluggish ion (de-)insertion, therefore, showing poor recharging performance with a state of charging of < 10% (Figure 1.8a).[90, 95] Even worse, the volume contraction/expansion during charging/discharging results in crystal collapse of $MnO_2$ gravels, leading to severe capacity fading within tens of cycles.[96-101]

To overcome the limitations of low electrical conductivity and/or slow ion (de-)insertion, two strategies have been conceived: i) depositing $MnO_2$ on carbon cloth to increase the electrical conductivity,[76, 102-105] ii) reducing the dimension of $MnO_2$ to facilitate the ion (de-)insertion.[75, 91, 97, 100, 106-114] In the former strategy, the carbon cloth, as the support of $MnO_2$, offers a good electrical conductivity of $10^2$ S/m.[76, 102-105] However, due to the small surface area of carbon cloth, the thickness of $MnO_2$ shell is several micrometers, hindering the ion (de-)insertion at high (dis)charging rates (Figure 1.7c and 1.8b).[76, 102-105] Conversely, hydrothermal reactions produce nanostructured $MnO_2$, such as nanorods,[75, 93, 97, 100, 106] nanosheets,[91, 107-109] nanospheres (Figure 1.7d, e and f).[110-115] The dimensions of nanostructured $MnO_2$, ranging from nanometers to tens of nanometers, drastically reduce the diffusion distance during ion (de-)insertion.[76] However, those discrete $MnO_2$ nanoparticles rely on carbon additives, and binders to construct the continuous and conductive cathodes (Figure 1.8b). The low overall conductivity is insufficient for fast charging.[97, 107, 116] Therefore, the optimal fast-charging cathodes require synergistically combined good electrical conductivity of carbon support and fast ion (de-)insertion in nanostructured $MnO_2$.

Herein, this dissertation reports an approach of using porous carbon fiber-supported $MnO_2$ as the fast-charging cathodes in ZIBs. The graphitic carbon fibers provide good electrical conductivity. Simultaneously, the mesopores offer a high specific surface area, enabling a high loading of $MnO_2$ deposing as nanometer-thick layers (Figure 1.8c). The thin-layered $MnO_2$ affords not only fast ion (de-)insertion, but also good recovery from the volume change during cycling. Therefore, this porous carbon fiber-supported $MnO_2$ enables the good fast-charging performance and stable cycling of aqueous ZIBs.

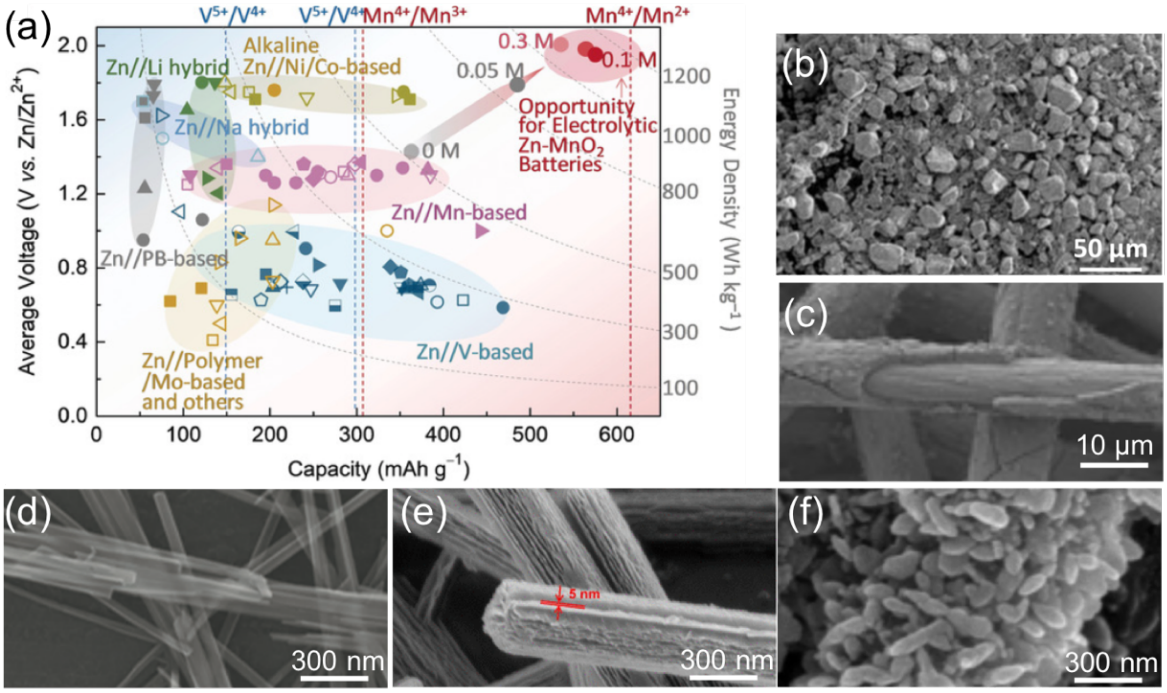


**Figure1.7.** $MnO_2$-based cathodes for ZIBs. (a) Mn-based cathodes provide both high voltages and high specific capacities, thus the leading energy densities surpassing other cathodes. Moreover, the $Mn^{4+}/Mn^{2+}$ redox mechanism offers an opportunity to further increase the energy density of Zn-$MnO_2$ batteries. (b) Electrolytic $MnO_2$ gravels in conventional cathodes show particle sizes ranging from micrometers to tens of micrometers. (c) $MnO_2$ depositing on carbon cloth shows a thickness of micrometers. Whereas, the nanostructured $MnO_2$, including (d) nanorods, (e)

nanosheets, and (f) nanospheres, shows low dimensions of nanometers to tens of nanometers. (a) Reprint with permission from *Angew. Chem. Int. Ed*. **2019**, 58, 7823-7828.[88] Copyright 2019 Wiley-VCH Verlag GmbH & Co. KGaA, Weinheim. (b) Reprint with permission from *ACS Appl. Mater. Interfaces* **2019**, 11, 37524-37530.[95] Copyright 2019 American Chemical Society. (c) Reprint with permission from *Energy Environ. Sci*. **2020**, 13, 135-143.[103] Copyright 2020 Royal Society of Chemistry (d) Reprint with permission from *Small* **2018**, 14, 1703850.[97] Copyright 2018 Wiley-VCH Verlag GmbH & Co. KGaA, Weinheim. (e) Reprint with permission from *ACS Nano* **2018**, 12, 1033-1042.[108] Copyright 2018 American Chemical Society. (f) Reprint with permission from *Electrochim. Acta* **2020**, 345, 136189.[110] Copyright 2020 Elsevier Ltd.

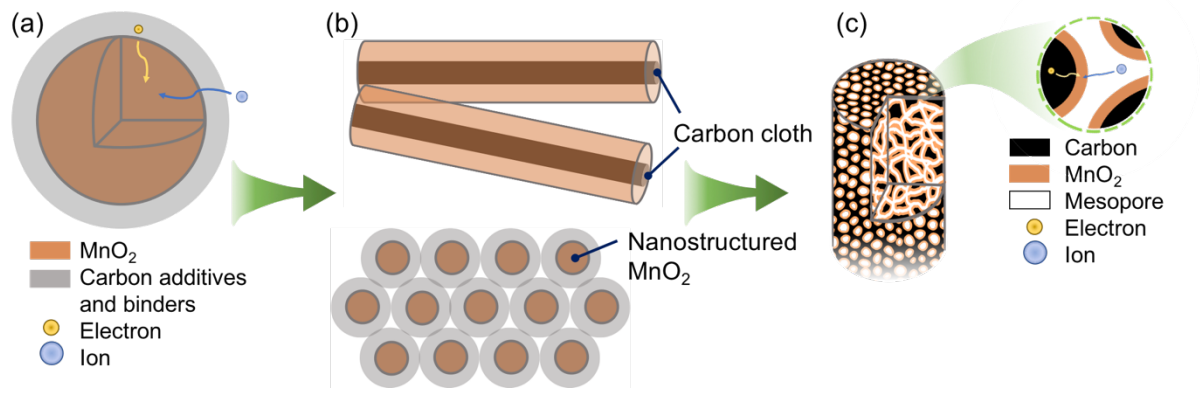


**Figure 1.8.** Schematic illustrations of $MnO_2$-based cathodes. (a) The large size of conventional $MnO_2$ gravels hinders ion insertion. Moreover, the overall electrical conductivity of carbon additives and binders is not sufficient for fast charging. (b) Upper: cathodes comprising $MnO_2$ on carbon cloth suffer from thick $MnO_2$ layers. Lower: The discrete nanostructured $MnO_2$ is disadvantaged by the insufficient electrical conductivity of carbon additives and binders. (c) Porous carbon fibers-supported $MnO_2$ enables fast charging. The high surface area of porous carbon fibers affords nanometer-thick $MnO_2$ to minimize the ion (de-)insertion length, and the

continuous graphitic fibers provide highly conductive pathways for electrons to ensure fast charging.

## 1.6 Dissertation overview

This dissertation reports the approaches to utilizing block copolymer-derived nanoporous materials for high-performance energy storage, including i) a mesoporous polyimide separator suppressing the growth of lithium dendrites in lithium-metal batteries, and ii) a porous carbon fiber-supported $MnO_2$ cathode enabling superior fast charging performance in aqueous zinc-ion batteries.

**Chapter 2** explores the microphase separation of polyimide-based ABA-type triblock copolymers. Those triblock copolymers consist of a broad-dispersity polyetherimide middle block and narrow-dispersity oligomeric polystyrene end blocks. Although the overall molecular weights are as low as 11, 13, and 15 kDa, those triblock copolymers can undergo microphase separation to form bicontinuous microstructures. The polystyrene domain sizes, as characterized using both scanning electron microscopy (SEM) and small-angle X-ray diffraction (SAXD), are smaller than 10 nm because of the ultra-low molecular weight of polystyrene blocks.

**Chapter 3** describes an approach of preparing mesoporous polyetherimide thin films *via* hydrolysis of polylactide-*b*-polyetherimide-*b*-polylactide copolymers. The polylactide-*b*-polyetherimide-*b*-polylactide copolymers, comprising 40 vol% of polylactide, undergo microphase separation to form a bicontinuous microstructure showing polylactide domains embedded in the polyetherimide matrix. Subsequently, the hydrolysis removed the polylactide phase to create interconnected mesopores with a median pore width of 24 nm. The resulting mesoporous polyetherimide thin films exhibit a high glass transition temperature of about 230 °C

and a high storage modulus of 1.22 GPa, as characterized using dynamic mechanical analysis (DMA).

**Chapter 4** reports mesoporous polyimide thin films serving as dendrite-suppressing separators to enable the safe cycling of lithium-metal batteries. The mesoporous polyimide thin film is derived from the thermolysis of polylactide-*b*-polyimide-*b*-polylactide. The thermolysis temperatures are judiciously controlled to decompose the polylactide phase slowly without perturbing the polyimide matrix. The resulting mesoporous polyimide thin film exhibits a median pore width of 24 nm and a high modulus of 1.80 GPa. The mesopores prevent lithium dendrites from penetrating the separator and short-circuiting the battery, therefore, enabling the safe cycling of lithium-metal batteries for 500 hours.

**Chapter 5** reports block copolymer-derived porous carbon fiber supported $MnO_2$ as fast-charging cathodes for aqueous zinc-ion batteries. The block copolymer, poly(methyl methacrylate)-*b*-polyacrylonitrile, is synthesized *via* reversible addition-fragmentation chain transfer (RAFT) polymerization. Subsequently, the block copolymer is processed into polymer fibers using the electrospinning technique. The polymer fibers are thermalized to produce porous carbon fibers, where the polyacrylonitrile phase produces graphitic carbon and poly(methyl methacrylate) decomposes to create mesopores. A thin layer of $MnO_2$, several nanometers in thickness, is deposited on the surface of porous carbon fibers to produce a cathode. The cathode combines the good electrical conductivity in graphitic carbon fibers and fast ion (de-)insertion in the thin-layered $MnO_2$. Therefore, this porous carbon fiber-supported $MnO_2$ cathode shows superior fast-charging performance in aqueous zinc-ion batteries.

**Chapter 6** summarizes the overall conclusions of investigations in applying block copolymer-derived mesoporous materials in high-performance energy storage. To further advance

the projects in this dissertation, future perspectives provide suggesting prospective works, including i) designing ABA-type block copolymers consisting of all broad-dispersity A and B blocks, and then investigating the effects of the end-block dispersity on microphase separations. ii) Improving the hydrolysis efficiency of polylactide-*b*-polyetherimide-*b*-polylactide by tuning the pH and temperatures, and exploring the effects of polylactide volume fraction on phase continuity, as well as the polylactide residue after hydrolysis. iii) Reducing the thickness of mesoporous polyimide separators to increase the ionic conductivity. The perspective also proposes a design of thin-film lithium-metal batteries employing ultra-thin mesoporous polyimide separators. iv) Improving the incubation conditions to enable more efficient and uniform $MnO_2$ deposition on porous carbon fibers. The future work also suggests a design of textile zinc-ion batteries utilizing the porous carbon fiber-supported $MnO_2$ cathodes.

## 1.7 References


1. Li, L.; Base, S.; Wang, Y.; Chen, Z.; Hundekar, P.; Wang, B.; Shi, J.; Shi, Y.; Narayanan, S.; Koratkar, N., Self-Heating-Induced Healing of Lihtium Dendrites. *Science* **2018**, *359*, 1513-1516.

2. Tarascon, J. M.; Armand, M., Issues and Challenges Facing Rechargeable Lithium Batteries. *Nature* **2001**, *414*, 359-367.

3. Grey, C. P.; Hall, D. S., Prospects for Lithium-Ion Batteries and Beyond-A 2030 Vision. *Nat. Commun.* **2020**, *11*, 6279.

4. Mukhopadhyay, A.; Jangid, M. K., Li Metal Battery, Heal Thyself. *Science* **2018**, *359*, 1463.

5. Wang, F.; Hu, E.; Sun, W.; Gao, T.; Ji, X.; Fan, X.; Han, F.; Yang, X.-Q.; Xu, K.; Wang, C., A Rechargeable Aqueous $Zn^{2+}$-Battery with High Power Density and a Long Cycle-Life. *Energy Environ. Sci.* **2018**, *11*, 3168-3175.

6. Kraytsberg, A.; Ein-Eli, Y., Conveying Advanced Li-Ion Battery Materials into Practice the Impact of Electrode Slurry Preparation Skills. *Adv. Energy Mater.* **2016**, *6*, 1600655.

7. Matsen, M. W.; Bates, F. S., Unifying Weak- and Strong-Segregation Block Copolymer Theories. *Macromolecules* **1996**, *29*, 1091-1098.

8. Matsen, M. W.; Schick, M., Stable and Unstable Phases of a Linear Multiblock Copolymer Melt. *Macromolecules* **1994**, *27*, 7157-7163.

9. Matsen, M. W.; Schick, M., Stable and Unstable Phases of a Diblock Copolymer Melt. *Phys. Rev. Lett.* **1994**, *72*, 2660-2663.

10. Bates, F. S.; Fredrickson, G. H., Block Copolymers-Designer Soft Materials. *Physics Today* **1999**, *52*, 32-38.

11. Odian, G., Principles of Polymerization In *Principles of Polymerizaiton*, 4th ed.; John Wiley & Sons, Inc.: Hoboken, New Jersey, 2004; pp 289-292.

12. Matsen, M. W.; Schick, M., Microphase Separation in Starblock Copolymer Melts. *Macromolecules* **1994**, *27*, 6761-6767.

13. Khandpur, A. K.; Stephan Forster; Bates, F.; Hamley, I. W.; Ryan, A. J.; Bras, W.; Almdal, K.; Mortensen, K., Polyisoprene-Polystyrene Diblock Copolymer Phase Diagram near the Order-Disorder Transition. *Macromolecules* **1995**, *28*, 8796-8806.

14. Widin, J. M.; Schmitt, A. K.; Schmitt, A. L.; Im, K.; Mahanthappa, M. K., Unexpected Consequences of Block Polydispersity on the Self-Assembly of ABA Triblock Copolymers. *J. Am. Chem. Soc.* **2012**, *134*, 3834-3844.

15. Xu, H.; Greve, E. M.; Mahanthappa, M. K., Morphological Impact of Segment Dispersity in Lithium Salt-Doped Poly(styrene)/Poly(ethylene oxide) Triblock Polymers. *Macromolecules* **2019**, *52*, 5722-5734.

16. Schmitt, A. K.; Mahanthappa, M. K., Characteristics of Lamellar Mesophases in Strongly Segregated Broad Dispersity ABA Triblock Copolymers. *Macromolecules* **2014**, *47*, 4346-4356.

17. Register, R. A., Continuity through Dispersity. *Nature* **2012**, *483*, 167-168.

18. Zhu, W.; Wang, X.; Li, T.; Shen, R.; Hao, S.-J.; Li, Y.; Wang, Q.; Li, Z.; Gu, Z.-G., Porphyrin-Based Porous Polyimide Polymer/Pd Nanoparticle Composites as Efficient Catalysts for Suzuki-Miyaura Coupling Reactions. *Polym. Chem.* **2018**, *9*, 1430-1438.

19. Li, G.; Wang, Z., Microporous Polyimides with Uniform Pores for Adsorption and Separation of $CO_2$ Gas and Organic Vapors. *Macromolecules* **2013**, *46*, 3058-3066.

20. Niwa, M.; Kawakami, H.; Kanamori, T.; Shinbo, T.; Kaito, A.; Nagaoka, S., Gas Separator of Asymmetric 6FDA Polyimide Membrane with Oriented Surface Skin Layer. *Macromolecules* **2001**, *34*, 9039-9044.

21. Iwase, M.; Sannomiya, A.; Nagaoka, S.; Suzuki, Y.; Iwaki, M.; Kawakami, H., Gas Permeation Properties of Asymmetric Polyimide Membranes with Partially Carbonized Skin Layer. *Macromolecules* **2004**, *37*, 6892-6897.

22. Swaidan, R.; Al-Saeedi, M.; Ghanem, B.; Litwiller, E.; Pinnau, I., Rational Design of Intrinsically Ultramicroporous Polyimides Containing Bridgehead-Substituted Triptycene for Highly Selective and Permeable Gas Separation Membranes. *Macromolecules* **2014**, *47*, 5104-5114.

23. Swaidan, R.; Ghanem, B.; Al-Saeedi, M.; Litwiller, E.; Pinnau, I., Role of Intrachain Rigidity in the Plasticization of Intrinsically Microporous Triptycene-Based Polyimide Membranes in Mixed-Gas $CO_2/CH_4$ Separations. *Macromolecules* **2014**, *47*, 7453-7462.

24. Pan, Z.; Zhang, X.; Wang, X., Adsorption of Acid Orange 10 on Cross-Linked Porous Polyimide. *SN Appl. Sci.* **2019**, *1*, 239-248.

25. Zhao, G.; Huang, X.; Tang, Z.; Huang, Q.; Niu, F.; Wang, X., Polymer-Based Nanocomposites for Heavy Metal Ions Removal from Aqueous Solution: A Review. *Polym. Chem.* **2018**, *9*, 3562-3582.

26. Jin, Y.; Tang, J.; Hu, J.; Han, X.; Shang, Y.; Liu, H., One-Step Fabrication of Ultralow Dielectric Polyimide Films Consisting of Size-Controlled Mesoporous Nanoparticles. *Colloids Surf. A* **2011**, *392*, 178-186.

27. Ju, J.; Wang, Q.; Wang, T.; Wang, C., Low Dielectric, Nanoporous Fluorinated Polyimide Films Prepared from PCL-PI-PCL Triblock Copolymer Using Retro-Diels-Alder Reaction. *J. Colloid Interface Sci.* **2013**, *404*, 36-41.

28. Meador, M. A. B.; Wright, S.; Sandberg, A.; Nguyen, B. N.; Van Keuls, F. W.; Mueller, C. H.; Rodríguez-Solís, R.; Miranda, F. A., Low Dielectric Polyimide Aerogels as Substrates for Lightweight Patch Antennas. *ACS Appl. Mater. Interfaces* **2012**, *4*, 6346-6353.

29. Meador, M. A.; Aleman, C. R.; Hanson, K.; Ramirez, N.; Vivod, S. L.; Wilmoth, N.; McCorkle, L., Polyimide Aerogels with Amide Cross-Links: A Low Cost Alternative for Mechanically Strong Polymer Aerogels. *ACS Appl. Mater. Interfaces* **2015**, *7*, 1240-1249.

30. Carter, K. R.; Cha, H. J.; Dipietro, R. A.; Hawker, C. J.; Hedrick, J. L.; Labadie, J. W.; McGrath, J. E.; Russell, T. P.; Sanchez, M. I.; Swanson, S. A.; Volksen, W.; Yoon, D. Y., Polyimide Nanofoams for Low Dielectric Applications. *MRS Proceedings* **2011**, *381*, 79-91.

31. Chen, D.; Liu, C.; Tang, J.; Luo, L.; Yu, G., Fluorescent Porous Organic Polymers. *Polym. Chem.* **2019**, *10*, 1168-1181.

32. Wang, L.; Lu, J.; liu, M.; Lin, L.; Li, J., Preparation of Porous Polyimide Microspheres by Thermal Degradation of Block Copolymers. *Particuology* **2014**, *14*, 63-70.

33. Hedrick, J. L.; Carter, K.; Sanchez, M.; Pietro, R. D.; Swanson, S., Crosslinked Polyimide Foams Derived from Poly(imide-propylene oxide) Copolymers. *Macromol. Chem. Phys.* **1997**, *198*, 549-559.

34. Hedrick, J. L.; Russell, T. P.; Labadie, J.; Lucas, M.; Swanson, S., High Temperature Nanofoams Derived from Rigid and Semi-Rigid Polyimides. *Polymer* **1995**, *36*, 2685-2697.

35. Chung, C.-M.; Lee, J.-H.; Cho, S.-Y.; Kim, J.-G.; Moon, S.-Y., Preparation of Porous Thin Films of a Partially Aliphatic Polyimide. *J. Appl. Polym. Sci.* **2006**, *101*, 532-538.

36. Charlier, Y.; Hedrick, J. L.; Russell, T. P.; Jonas, A.; Volksen, W., High Temperature Polymer Nanofoams Based on Amorphous, High $T_g$ Polyimides. *Polymer* **1995**, *36*, 987-1002.

37. Carter, K. R.; DiPietro, R. A.; Sanchez, M. I.; Swanson, S. A., Nanoporous Polyimides Derived from Highly Fluorinated Polyimide/Poly(propylene oxide) Copolymers. *Chem. Mater.* **2001**, *13*, 213-221.

38. Hedrick, J. L.; Hawker, C. J.; DiPietro, R.; Jérôme, R.; Charlier, Y., The Use of Styrenic Copolymers to Generate Polyimide Nanofoams. *Polymer* **1995**, *36*, 4855-4866.

39. Hedrick, J. L.; DiPietro, R.; Plummer, C. J. G.; Hilborn, J.; Jérôme, R., Polyimide Foams Derived from a High Tg Polyimide with Grafted Poly(α-Methylstyrene). *Polymer* **1996**, *37*, 5229-5236.

40. Charlier, Y.; Hedrick, J. L.; Russell, T. P.; Swanson, S.; Sanchez, M., Crosslined Polyimide Foams Derived from Pyromellitic Dianhydride and 1,1-Bis(4-aminophenyl)-1-phenyl-2,2,3-trifluoroethane with Poly(α-methylstyrene). *Polymer* **1995**, *36*, 1315-1320.

41. Miyata, S.; Yoshida, K.; Shirokura, H.; Kashio, M.; Nagai, K., Solid and Thermal Properties of Aba-Type Triblock Copolymers Designed Using Difunctional Fluorine-Containing Polyimide Macroinitiators with Methyl Methacrylate. *Polym. Int.* **2009**, *58*, 1148-1159.

42. Fu, G. D.; Zong, B. Y.; Kang, E. T.; Neoh, K. G., Nanoporous Low-Dielectric Constant Polyimdie Films via Poly(amic acid)s with RAFT-Graft Copolymerized Methyl Methacrylate Side Chains. *Ind. Eng. Chem. Res* **2004**, *43*, 6723-6730.

43. Hedrick, J. L.; Russell, T. P.; Sanchez, M.; DiPietro, R.; Swanson, S., Polyimide Nanofoams from Caprolactone-Based Copolymers. *Macromolecules* **1996**, *29*, 3642-3646.

44. Meleshko, T. K.; Kashina, A. V.; Saprykina, N. N.; Kostyuk, S. V.; Vasilenko, I. V.; Nikishev, P. A.; Yakimanskii, A. V., Synthesis and Morphology of Polycaprolactone-*block*-Polyimide-*block*-Polycaprolactone Triblock Copolymers for Film Separation Membranes. *Russ. J. Appl. Chem.* **2017**, *90*, 602-612.

45. Liu, C.; Liu, B.; Chan-Park, M. B., Synthesis of Polycaprolactone-Polyimide-Polycaprolactone Triblock Copolymers via a 2-Step Sequential Copolymerization and Their Application as Carbon Nanotube Dispersants. *Polym. Chem.* **2017**, *8*, 674-681.

46. Ando, S.; Yoshida, A.; Nagai, K., Preparation of Porous Membranes by Selective Decomposition of Adamantane Unit in ABA-Type Triblock Copolymer. *Polym. Eng. Sci.* **2016**, *56*, 1191-1200.

47. Guo, D.; Riet, J.; Khan, A.; Guo, Y.; Xu, Z.; Liu, T.; Liu, G., Mesoporous Polyetherimide Thin Films via Hydrolysis of Polylactide-*b*-Polyetherimide-*b*-Polylactide. *Polym. Chem.* **2021**, *12*, 3939-3946.

48. Li, S.; McCarthy, S., Further Investigations on the Hydrolytic Degradation of Poly($_{DL}$-lactide). *Biomaterials* **1999**, *20*, 35-44.

49. He, Y.; Ren, X.; Xu, Y.; Engelhard, M. H.; Li, X.; Xiao, J.; Liu, J.; Zhang, J. G.; Xu, W.; Wang, C., Origin of Lithium Whisker Formation and Growth under Stress. *Nat. Nanotechnol.* **2019**, *14*, 1042-1047.

50. Cao, X.; Ren, X.; Zou, L.; Engelhard, M. H.; Huang, W.; Wang, H.; Matthews, B. E.; Lee, H.; Niu, C.; Arey, B. W.; Cui, Y.; Wang, C.; Xiao, J.; Liu, J.; Xu, W.; Zhang, J.-G., Monolithic Solid-Electrolyte Interphases Formed in Fluorinated Orthoformate-Based Electrolytes Minimize Li Depletion and Pulverization. *Nat. Energy* **2019**, *4*, 796-805.

51. Frenck, L.; Sethi, G. K.; Maslyn, J. A.; Balsara, N. P., Factors That Control the Formation of Dendrites and Other Morphologies on Lithium Metal Anodes. *Front. Energy Res.* **2019**, *7*, 115.

52. Bai, P.; Li, J.; Brushett, F. R.; Bazant, M. Z., Transition of Lithium Growth Mechanisms in Liquid Electrolytes. *Energy Environ. Sci.* **2016**, *9*, 3221-3229.

53. Deng, Q.; Hu, R.; Xu, C.; Chen, B.; Zhou, J., Modeling Fracture of Solid Electrolyte Interphase in Lithium-Ion Batteries During Cycling. *J. Solid State Electrochem.* **2019**, *23*, 2999-3008.

54. Peled, E.; Menkin, S., Review-SEI: Past, Present and Future. *J. Electrochem. Soc.* **2017**, *164*, A1703-A1719.

55. Steiger, J.; Kramer, D.; Mönig, R., Mechanisms of Dendritic Growth Investigated by in situ Light Microscopy During Electrodeposition and Dissolution of Lithium. *J. Power Sources* **2014**, *261*, 112-119.

56. Zhang, L.; Yang, T.; Du, C.; Liu, Q.; Tang, Y.; Zhao, J.; Wang, B.; Chen, T.; Sun, Y.; Jia, P.; Li, H.; Geng, L.; Chen, J.; Ye, H.; Wang, Z.; Li, Y.; Sun, H.; Li, X.; Dai, Q.; Tang, Y.; Peng, Q.; Shen, T.; Zhang, S.; Zhu, T.; Huang, J., Lithium Whisker Growth and Stress Generation in an in situ Atomic Force Microscope-Environmental Transmission Electron Microscope Set-Up. *Nat. Nanotechnol.* **2020**, *15*, 94-98.

57. Peter, C.; Nikolowski, K.; Reuber, S.; Wolter, M.; Michaelis, A., Chronoamperometry as an Electrochemical in situ Approach to Investigate the Electrolyte Wetting Process of Lithium-Ion Cells. *J. Appl. Electrochem.* **2020**, *50*, 295-309.

58. Chen, S.; Zheng, J.; Mei, D.; Han, K. S.; Engelhard, M. H.; Zhao, W.; Xu, W.; Liu, J.; Zhang, J. G., High-Voltage Lithium-Metal Batteries Enabled by Localized High-Concentration Electrolytes. *Adv. Mater.* **2018**, *30*, 1706102.

59. Li, Q.; Tan, S.; Li, L.; Lu, Y.; He, Y., Understanding the Molecular Mechanism of Pulse Current Charging for Stable Lithium-Metal Batteries. *Sci. Adv.* **2017**, *3*, 1701246.

60. Wang, J.; Huang, W.; Pei, A.; Li, Y.; Shi, F.; Yu, X.; Cui, Y., Improving Cyclability of Li Metal Batteries at Elevated Temperatures and Its Origin Revealed by Cryo-Electron Microscopy. *Nat. Energy* **2019**, *4*, 664-670.

61. Niu, C.; Pan, H.; Xu, W.; Xiao, J.; Zhang, J. G.; Luo, L.; Wang, C.; Mei, D.; Meng, J.; Wang, X.; Liu, Z.; Mai, L.; Liu, J., Self-Smoothing Anode for Achieving High-Energy Lithium Metal Batteries under Realistic Conditions. *Nat. Nanotechnol.* **2019**, *14*, 594-601.

62. Cao, D.; Xing, Y.; Tantratian, K.; Wang, X.; Ma, Y.; Mukhopadhyay, A.; Cheng, Z.; Zhang, Q.; Jiao, Y.; Chen, L.; Zhu, H., 3D Printed High-Performance Lithium Metal Microbatteries Enabled by Nanocellulose. *Adv. Mater.* **2019**, *31*, 1807313.

63. Xie, J.; Wang, J.; Lee, H. R.; Yan, K.; Li, Y.; Shi, F.; Huang, W.; Pei, A.; Chen, G.; Subbaraman, R.; Christensen, J.; Cui, Y., Engineering Stable Interfaces for Three-Dimensional Lithium Metal Anodes. *Sci. Adv.* **2018**, *4*, eaat5168.

64. Zhao, C.-Z.; Chen, P.-Y.; Zhang, R.; Chen, X.; Li, B.-Q.; Zhang, X.-Q.; Cheng, X.-B.; Zhang, Q., An Ion Redistributor for Dendrite-Free Lithium Metal Anodes. *Sci. Adv.* **2018**, *4*, eaat3446.

65. Fang, C.; Lu, B.; Pawar, G.; Zhang, M.; Cheng, D.; Chen, S.; Ceja, M.; Doux, J.-M.; Musrock, H.; Cai, M.; Liaw, B.; Meng, Y. S., Pressure-Tailored Lithium Deposition and Dissolution in Lithium Metal Batteries. *Nat. Energy* **2021**, *6*, 987-994.

66. Qian, J.; Henderson, W. A.; Xu, W.; Bhattacharya, P.; Engelhard, M.; Borodin, O.; Zhang, J. G., High Rate and Stable Cycling of Lithium Metal Anode. *Nat. Commun.* **2015**, *6*, 6362.

67. Chen, X. R.; Yao, Y. X.; Yan, C.; Zhang, R.; Cheng, X. B.; Zhang, Q., A Diffusion-Reaction Competition Mechanism to Tailor Lithium Deposition for Lithium-Metal Batteries. *Angew. Chem. Int. Ed.* **2020**, *59*, 7743-7747.

68. Nagasaki, M.; Kanamura, K., High-Performance Lithium Metal Rechargeable Battery Using an Ultrafine Porous Polyimide Separator with Three-Dimensionally Ordered Macroporous Structure. *ACS Appl. Energy Mater.* **2019**, *2*, 3896-3903.

69. Ferrese, A.; Newman, J., Mechanical Deformation of a Lithium-Metal Anode Due to a Very Stiff Separator. *J. Electrochem. Soc.* **2014**, *161*, A1350-A1359.

70. Monroe, C.; Newman, J., The Impact of Elastic Deformation on Deposition Kinetics at Lithium/Polymer Interfaces. *J. Electrochem. Soc.* **2005**, *152*, A396-A404.

71. Na, W.; Lee, A. S.; Lee, J. H.; Hwang, S. S.; Kim, E.; Hong, S. M.; Koo, C. M., Lithium Dendrite Suppression with UV-Curable Polysilsesquioxane Separator Binders. *ACS Appl. Mater. Interfaces* **2016**, *8*, 12852-12858.

72. Wan, J.; Xie, J.; Kong, X.; Liu, Z.; Liu, K.; Shi, F.; Pei, A.; Chen, H.; Chen, W.; Chen, J.; Zhang, X.; Zong, L.; Wang, J.; Chen, L. Q.; Qin, J.; Cui, Y., Ultrathin, Flexible, Solid Polymer Composite Electrolyte Enabled with Aligned Nanoporous Host for Lithium Batteries. *Nat. Nanotechnol.* **2019**, *14*, 705-711.

73. Zhang, N.; Cheng, F.; Liu, J.; Wang, L.; Long, X.; Liu, X.; Li, F.; Chen, J., Rechargeable Aqueous Zinc-Manganese Dioxide Batteries with High Energy and Power Densities. *Nat. Commun.* **2017**, *8*, 405.

74. Sun, W.; Wang, F.; Zhang, B.; Zhang, M.; Küpers, V.; Ji, X.; Theile, C.; Bieker, P.; Xu, K.; Wang, C.; Wenter, M., A Rechargeable Zinc-Air Battery Based on Zinc Peroxide Chemistry. *Science* **2021**, *371*, 46-51.

75. Pan, H.; Shao, Y.; Yan, P.; Cheng, Y.; Han, K. S.; Nie, Z.; Wang, C.; Yang, J.; Li, X.; Bhattacharya, P.; Mueller, K. T.; Liu, J., Reversible Aqueous Zinc/Manganese Oxide Energy Storage from Conversion Reactions. *Nat. Energy* **2016**, *1*, 16039.

76. Sun, W.; Wang, F.; Hou, S.; Yang, C.; Fan, X.; Ma, Z.; Gao, T.; Han, F.; Hu, R.; Zhu, M.; Wang, C., $Zn/MnO_2$ Battery Chemistry with $H^+$ and $Zn^{2+}$ Coinsertion. *J. Am. Chem. Soc.* **2017**, *139*, 9775-9778.

77. Yuan, D.; Zhao, J.; Ren, H.; Chen, Y.; Chua, R.; Jie, E. T. J.; Cai, Y.; Edison, E.; Manalastas, W., Jr.; Wong, M. W.; Srinivasan, M., Anion Texturing Towards Dendrite-Free Zn Anode for Aqueous Rechargeable Batteries. *Angew. Chem. Int. Ed.* **2021**, *60*, 7213-7219.

78. Chao, D.; Zhu, C. R.; Song, M.; Liang, P.; Zhang, X.; Tiep, N. H.; Zhao, H.; Wang, J.; Wang, R.; Zhang, H.; Fan, H. J., A High-Rate and Stable Quasi-Solid-State Zinc-Ion Battery with Novel 2d Layered Zinc Orthovanadate Array. *Adv. Mater.* **2018**, *30*, 1803181.

79. Chen, M.; Chen, J.; Zhou, W.; Han, X.; Yao, Y.; Wong, C. P., Realizing an All-Round Hydrogel Electrolyte toward Environmentally Adaptive Dendrite-Free Aqueous $Zn-MnO_2$ Batteries. *Adv. Mater.* **2021**, *33*, 2007559.

80. Dunn, B.; Kamath, H.; Tarascon, J. M., Electrical Energy Storage for the Grid: A Battery of Choices. *Science* **2011**, *334*, 928-935.

81. Xia, C.; Guo, J.; Lei, Y.; Liang, H.; Zhao, C.; Alshareef, H. N., Rechargeable Aqueous Zinc-Ion Battery Based on Porous Framework Zinc Pyrovanadate Intercalation Cathode. *Adv. Mater.* **2018**, *30*, 1705580.

82. Li, S.; Liu, Y.; Zhao, X.; Shen, Q.; Zhao, W.; Tan, Q.; Zhang, N.; Li, P.; Jiao, L.; Qu, X., Sandwich-Like Heterostructures of $MoS_2$/Graphene with Enlarged Interlayer Spacing and Enhanced Hydrophilicity as High-Performance Cathodes for Aqueous Zinc-Ion Batteries. *Adv. Mater.* **2021**, *33*, 2007480.

83. Ding, J.; Du, Z.; Li, B.; Wang, L.; Wang, S.; Gong, Y.; Yang, S., Unlocking the Potential of Disordered Rocksalts for Aqueous Zinc-Ion Batteries. *Adv. Mater.* **2019**, *31*, 1904369.

84. Wang, W.; Kale, V. S.; Cao, Z.; Lei, Y.; Kandambeth, S.; Zou, G.; Zhu, Y.; Abouhamad, E.; Shekhah, O.; Cavallo, L.; Eddaoudi, M.; Alshareef, H. N., Molecular Engineering of Covalent Organic Framework Cathodes for Enhanced Zinc-Ion Batteries. *Adv. Mater.* **2021**, *33*, 2103617.

85. Tan, Q.; Li, X.; Zhang, B.; Chen, X.; Tian, Y.; Wan, H.; Zhang, L.; Miao, L.; Wang, C.; Gan, Y.; Jiang, J.; Wang, Y.; Wang, H., Valence Engineering via in situ Carbon Reduction on Octahedron Sites $Mn_3O_4$ for Ultra-Long Cycle Life Aqueous Zn-Ion Battery. *Adv. Energy Mater.* **2020**, *10*, 2001050.

86. Liu, S.; Zhu, H.; Zhang, B.; Li, G.; Zhu, H.; Ren, Y.; Geng, H.; Yang, Y.; Liu, Q.; Li, C. C., Tuning the Kinetics of Zinc-Ion Insertion/Extraction in $V_2O_5$ by in situ Polyaniline Intercalation Enables Improved Aqueous Zinc-Ion Storage Performance. *Adv. Mater.* **2020**, *32*, 2001113.

87. George Blomgren, J. H., Batteries, Primary Cells. In *Kirk-Othmer Encyclopedia of Chemical Technology.*, John Wiley & Sons, Inc.: 2000; Vol. 3, pp 434-477.

88. Chao, D.; Zhou, W.; Ye, C.; Zhang, Q.; Chen, Y.; Gu, L.; Davey, K.; Qiao, S. Z., An Electrolytic Zn-$MnO_2$ Battery for High-Voltage and Scalable Energy Storage. *Angew. Chem. Int. Ed.* **2019**, *58*, 7823-7828.

89. Li, Y.; Fu, J.; Zhong, C.; Wu, T.; Chen, Z.; Hu, W.; Amine, K.; Lu, J., Recent Advances in Flexible Zinc-Based Rechargeable Batteries. *Adv. Energy Mater.* **2018**, *9*, 1802605.

90. Shin, J.; Seo, J. K.; Yaylian, R.; Huang, A.; Meng, Y. S., A Review on Mechanistic Understanding of $MnO_2$ in Aqueous Electrolyte for Electrical Energy Storage Systems. *Int. Mater. Rev.* **2019**, *65*, 356-387.

91. Liu, L.; Wu, Y. C.; Huang, L.; Liu, K.; Duployer, B.; Rozier, P.; Taberna, P. L.; Simon, P., Alkali Ions Pre-Intercalated Layered $MnO_2$ Nanosheet for Zinc-Ions Storage. *Adv. Energy Mater.* **2021**, *11*, 2101287.

92. Chao, D.; Ye, C.; Xie, F.; Zhou, W.; Zhang, Q.; Gu, Q.; Davey, K.; Gu, L.; Qiao, S. Z., Atomic Engineering Catalyzed $MnO_2$ Electrolysis Kinetics for a Hybrid Aqueous Battery with High Power and Energy Density. *Adv. Mater.* **2020**, *32*, 2001894.

93. Cheng, F. Y.; Chen, J.; Gou, X. L.; Shen, P. W., High-Power Alkaline Zn-$MnO_2$ Batteries Using $\gamma$-$MnO_2$ Nanowires/Nanotubes and Electrolytic Zinc Powder. *Adv. Mater.* **2005**, *17*, 2753-2756.

94. Yang, R.; Fan, Y.; Ye, R.; Tang, Y.; Cao, X.; Yin, Z.; Zeng, Z., $MnO_2$ -Based Materials for Environmental Applications. *Adv. Mater.* **2021**, *33*, 2004862.

95. Pan, H.; Ellis, J. F.; Li, X.; Nie, Z.; Chang, H. J.; Reed, D., Electrolyte Effect on the Electrochemical Performance of Mild Aqueous Zinc-Electrolytic Manganese Dioxide Batteries. *ACS Appl. Mater. Interfaces* **2019**, *11*, 37524-37530.

96. Liu, Y.; Zhi, J.; Sedighi, M.; Han, M.; Shi, Q.; Wu, Y.; Chen, P., $Mn^{2+}$ Ions Confined by Electrode Microskin for Aqueous Battery Beyond Intercalation Capacity. *Adv. Energy Mater.* **2020**, *10*, 2002578.

97. Wu, B.; Zhang, G.; Yan, M.; Xiong, T.; He, P.; He, L.; Xu, X.; Mai, L., Graphene Scroll-Coated α-$MnO_2$ Nanowires as High-Performance Cathode Materials for Aqueous Zn-Ion Battery. *Small* **2018**, *14*, 1703850.

98. Moon, H.; Ha, K. H.; Park, Y.; Lee, J.; Kwon, M. S.; Lim, J.; Lee, M. H.; Kim, D. H.; Choi, J. H.; Choi, J. H.; Lee, K. T., Direct Proof of the Reversible Dissolution/Deposition of $Mn^{2+}/Mn^{4+}$ for Mild-Acid Zn-$MnO_2$ Batteries with Porous Carbon Interlayers. *Adv. Sci.* **2021**, *8*, 2003714.

99. Jiao, Y.; Kang, L.; Berry-Gair, J.; McColl, K.; Li, J.; Dong, H.; Jiang, H.; Wang, R.; Corà, F.; Brett, D. J. L.; He, G.; Parkin, I. P., Enabling Stable $MnO_2$ Matrix for Aqueous Zinc-Ion Battery Cathodes. *J. Mater. Chem. A* **2020**, *8*, 22075-22082.

100. Fu, Y.; Wei, Q.; Zhang, G.; Wang, X.; Zhang, J.; Hu, Y.; Wang, D.; Zuin, L.; Zhou, T.; Wu, Y.; Sun, S., High-Performance Reversible Aqueous Zn-Ion Battery Based on Porous Mnox Nanorods Coated by MOF-Derived N-Doped Carbon. *Adv. Energy Mater.* **2018**, *8*, 1801445.

101. Zhao, S.; Zuo, Y.; Liu, T.; Zhai, S.; Dai, Y.; Guo, Z.; Wang, Y.; He, Q.; Xia, L.; Zhi, C.; Bae, J.; Wang, K.; Ni, M., Multi-Functional Hydrogels for Flexible Zinc-Based Batteries Working under Extreme Conditions. *Adv. Energy Mater.* **2021**, *11*, 2101749.

102. Chen, J.; Zhou, Y.; Islam, M. S.; Cheng, X.; Brown, S. A.; Han, Z.; Rider, A. N.; Wang, C. H., Carbon Fiber Reinforced Zn-$MnO_2$ Structural Composite Batteries. *Compos. Sci. Technol.* **2021**, *209*, 108787.

103. Xie, C.; Li, T.; Deng, C.; Song, Y.; Zhang, H.; Li, X., A Highly Reversible Neutral Zinc/Manganese Battery for Stationary Energy Storage. *Energy Environ. Sci.* **2020**, *13*, 135-143.

104. Qiu, W.; Li, Y.; You, A.; Zhang, Z.; Li, G.; Lu, X.; Tong, Y., High-Performance Flexible Quasi-Solid-State Zn-$MnO_2$ Battery Based on $MnO_2$ Nanorod Arrays Coated 3D Porous Nitrogen-Doped Carbon Cloth. *J. Mater. Chem. A* **2017**, *5*, 14838-14846.

105. Liu, T.; Zhou, Z.; Guo, Y.; Guo, D.; Liu, G., Block Copolymer Derived Uniform Mesopores Enable Ultrafast Electron and Ion Transport at High Mass Loadings. *Nat. Commun.* **2019**, *10*, 675.

106. Alfaruqi, M. H.; Islam, S.; Gim, J.; Song, J.; Kim, S.; Pham, D. T.; Jo, J.; Xiu, Z.; Mathew, V.; Kim, J., A High Surface Area Tunnel-Type α-$MnO_2$ Nanorod Cathode by a Simple Solvent-Free Synthesis for Rechargeable Aqueous Zinc-Ion Batteries. *Chem. Phys. Lett.* **2016**, *650*, 64-68.

107. Alfaruqi, M. H.; Gim, J.; Kim, S.; Song, J.; Pham, D. T.; Jo, J.; Xiu, Z.; Mathew, V.; Kim, J., A Layered δ-$MnO_2$ Nanoflake Cathode with High Zinc-Storage Capacities for Eco-Friendly Battery Applications. *Electrochem. Commun.* **2015**, *60*, 121-125.

108. Zhu, S.; Li, L.; Liu, J.; Wang, H.; Wang, T.; Zhang, Y.; Zhang, L.; Ruoff, R. S.; Dong, F., Structural Directed Growth of Ultrathin Parallel Birnessite on β-$MnO_2$ for High-Performance Asymmetric Supercapacitors. *ACS Nano* **2018**, *12*, 1033-1042.

109. Zhu, H. T.; Luo, J.; Yang, H. X.; Liang, J. K.; Rao, G. H.; Li, J. B.; Du, Z. M., Birnessite-Type $MnO_2$ Nanowalls and Their Magnetic Properties. *J. Phys. Chem. C* **2008**, *112*, 17089-17094.

110. Putro, D. Y.; Alfaruqi, M. H.; Islam, S.; Kim, S.; Park, S.; Lee, S.; Hwang, J.-Y.; Sun, Y.-K.; Kim, J., Quasi-Solid-State Zinc-Ion Battery Based on α-$MnO_2$ Cathode with Husk-Like Morphology. *Electrochim. Acta* **2020**, *345*, 136189.

111. Moazzen, E.; Timofeeva, E. V.; Segre, C. U., Controlled Synthesis of $MnO_2$ Nanoparticles for Aqueous Battery Cathodes: Polymorphism-Capacity Correlation. *J. Mater. Sci.* **2017**, *52*, 8107-8118.

112. Xia, H.; Wang, Y.; Lin, J.; Lu, L., Hydrothermal Synthesis of $MnO_2$/CNT Nanocomposite with a CNT Core/Porous $MnO_2$ Sheath Hierarchy Architecture for Supercapacitors. *Nanoscale Res. Lett.* **2012**, *7*, 33-43.

113. Zhang, M.; Wu, W.; Luo, J.; Zhang, H.; Liu, J.; Liu, X.; Yang, Y.; Lu, X., A High-Energy-Density Aqueous Zinc-Manganese Battery with a La-Ca Co-Doped ε-$MnO_2$ Cathode. *J. Mater. Chem. A* **2020**, *8*, 11642-11648.

114. Liu, J.; Zhang, Y.; Li, Y.; Li, J.; Chen, Z.; Feng, H.; Li, J.; Jiang, J.; Qian, D., In situ Chemical Synthesis of Sandwich-Structured $MnO_2$/Graphene Nanoflowers and Their Supercapacitive Behavior. *Electrochim. Acta* **2015**, *173*, 148-155.

115. Jin, Y.; Zou, L.; Liu, L.; Engelhard, M. H.; Patel, R. L.; Nie, Z.; Han, K. S.; Shao, Y.; Wang, C.; Zhu, J.; Pan, H.; Liu, J., Joint Charge Storage for High-Rate Aqueous Zinc-Manganese Dioxide Batteries. *Adv. Mater.* **2019**, *31*, 1900567.

116. Chen, Y. H.; Wang, C. W.; Liu, G.; Song, X. Y.; Battaglia, V. S.; Sastry, A. M., Selection of Conductive Additives in Li-Ion Battery Cathodes. *J. Electrochem. Soc.* **2007**, *154*, A978-A986.

# Chapter 2. Sub-10 nm Domains in High-Performance Polyetherimides

This chapter is reproduced from a published manuscript by Dong Guo, Assad U. Khan, Tianyu Liu, Zhengping Zhou and Guoliang Liu from the following reference: *Polym. Chem.* **2019**, 10, 379. Reproduced with permission from the Royal Society of Chemistry. Copyright 2019 Royal Society of Chemistry.

## 2.1 Abstract

Dielectric polyetherimide (PEI) thin films require ultra-small air voids to reduce the dielectric constant and maintain the structural integrity. Conventional synthesis of dielectric PEI uses thermally labile high-molecular-weight polymers to create air voids. The air voids, however, range from hundreds of nanometers to several micrometers, which limits the use of PEI in ultrathin films. Herein we present the synthesis of polystyrene-*b*-polyetherimide-*b*-polystyrene (PS-*b*-PEI-*b*-PS) triblock copolymers with ultra-low molecular weights. The molecular weights of the thermally labile polystyrene (PS) blocks are controlled to be as low as 1.5 kDa. By tuning the molecular weight of the PEI block to be 8, 10, and 12 kDa, the volume fractions of PS are 30.4%, 26.4%, and 23.4%, respectively. The triblock copolymers exhibit PS nanostructures of < 8 nm in size. Such small domains will potentially enable the preparation of ultra-small air voids in PEIs.

## 2.2 Introduction

Polyetherimide (PEI) is a class of polyimides that have low dielectric constant, high mechanical strength, flame retardancy, chemical resistance, and good processibility.[1-5] Owing to these outstanding properties, PEIs are promising low-κ dielectric polymers in microelectronics.[6] To further reduce the dielectric constant of PEIs, there are generally two strategies. One is to incorporate alicyclic structures[6, 7] or fluorine groups[8, 9] to increase the free volume in the PEIs. The other is to synthesize PEI-based block copolymers which consist of low dielectric or thermally labile peripheral blocks. The latter is attractive due to the simplicity of preparing the monomers. After forming the block copolymer nanostructures, the labile blocks are often removed via thermolysis to produce air voids or pores (κ~1) in the polyimide matrix and reduce the overall dielectric constant.[10-22] The synthesis of dielectric polymers with ultra-small thermally labile blocks, however, has been the key challenge.

To maintain the structural integrity of porous PEI thin films, the pore size must be significantly smaller than the thickness of the films. The inclusion of porous structures in polyimides has been successful, notably when the pore size is in the 100 nm region.[13, 14, 17, 21, 22] Many researchers have produced porous polyimides with the pore size even up to several micrometers.[10-12, 15, 16, 18-20] The large pore sizes are due to the large molecular weights of the thermally labile blocks. In terms of the polymer composition, various thermally labile polymers were employed to react with polyimides, for example, polystyrene (PS),[14] poly(methyl methacrylate),[10, 17] poly(propylene oxide),[12, 13, 20] poly(ε-caprolactone),[15, 16, 21] poly(ethylene glycol),[18] and poly(α-methyl styrene).[11, 19, 22] Among the thermally labile polymers, PS is the most attractive because it has a slow decomposition rate and minimizes the generation of "blowing agents".[14] Other polymers such as poly(α-

methyl styrene) generate "blowing agents" that plasticize the matrix polymer and detrimentally increase the pore sizes.[11, 19, 22] The large pores, however, limit the preparation of extremely thin dielectric polymer films. Therefore, it is highly desirable to synthesize PS and PEI-based block copolymers, in which the thermally labile PS blocks have ultra-low molecular weights but maintain the capability of forming nanoscale domains in the PEI matrix.

Herein we establish a synthetic route for polystyrene-*b*-polyetherimide-*b*-polystyrene triblock copolymers (PS-*b*-PEI-*b*-PS, abbreviated as SIS). We also demonstrate the formation of ultra-small thermally labile domains by utilizing the disordered nanostructures of block copolymers. The SIS triblock copolymers were prepared by reacting anhydride-terminated telechelic PEI (PEI-DA) with amine-terminated PS oligomers. The volume fractions of the PS blocks were controlled to be 23.4%, 26.4%, and 30.4% by changing the molecular weight of PEI-DA but keeping PS at a constant molecular weight of 1.5 kDa. Due to the low molecular weight of PS, the SIS triblock copolymers exhibited disordered nanostructures after thermal annealing at temperatures above the glass transition temperatures of both blocks, leading to ultra-small PS domains embedded in the PEI matrix. The average dimension of the PS domains was less than 8 nm and the nanostructures exhibited semi-periodic spacings of 14.1-15.2 nm, showing great promise of preparing PEI thin films with ultra-small porous structures.

## 2.3 Experimental Section

### *2.3.1 Materials*

2,2-bis[4-(3,4-dicarboxyphenoxy)phenyl]propane dianhydride (BPADA) was dried by one heating-cooling cycle between room temperature (RT) and 200 °C prior to use. *m*-Phenylenediamine (mPD, Sigma-Aldrich) was purified by sublimation. Styrene, *N,N,N′,N″,N‴*-pentamethyldiethylenetriamine (PMDETA), *o*-dichlorobenzene (oDCB), copper(I) chloride (CuCl), phthalic anhydride, 3-phenylpropylamine, *N*-bromosuccinimide (NBS), benzoyl peroxide (BPO), sodium sulphate, carbon tetrachloride ($CCl_4$), dioxane, dichloromethane (DCM), toluene, tri-*n*-butyltin hydride, azobisisobutyronitrile (AIBN), hydrazine solution (1 M) in tetrahydrofuran (THF), and ninhydrin reagent N7285 were used as received from Sigma-Aldrich.

### *2.3.2 Synthesis of 2-(3-bromo-3-phenylpropyl)isoindoline-1,3-dione (BPI)*

BPI was synthesized according to a report by Pourjavadi *et al*.[23] and used as the initiator for the polymerization of PS. Briefly, 3-phenylpropylamine (4.1 g, 30 mmol) and phthalic anhydride (4.4 g, 30 mmol) were mixed in a 250-mL round-bottom flask. The mixture was heated at 120 °C for 1 h under constant agitation by a magnetic stirring bar. The viscous mixture was cooled to RT and dissolved in 15 mL of DCM. The DCM solution was then transferred to a separatory funnel. After addition of 15 mL of deionized water and vigorous agitation, the bottom portion, *i.e.*, the DCM phase, was extracted. The extraction was repeated three times. The resulting DCM solution was dried using anhydrous sodium sulphate. After the evaporation of DCM using a rotary evaporator, a yellowish powder was collected and dried *in vacuo*. A portion of the yellow powder (1.0 g, 3.8 mmol), NBS (0.71 g, 4.0 mmol), and BPO (0.020 g, 0.083 mmol) were dissolved in 20 mL of $CCl_4$ and

refluxed at 85 °C overnight in a 100-mL round-bottom flask. After cooling down to RT and subsequent filtration, the filtrate was collected and $CCl_4$ was removed using a rotary evaporator, resulting in another yellow powder. After drying at RT overnight *in vacuo*, the powder was further purified by column chromatography using silica gel (200-425 mesh) and an eluent composed of hexane and DCM with a volumetric mixing ratio of 1:1. The retention factor (Rf) was ~0.5. Finally, white crystals of BPI were obtained after evaporating the eluent and drying at RT overnight *in vacuo*. The yield of BPI was ~85%.

### *2.3.3 Synthesis of phthalimido-polystyrene-Br (PTA-PS-Br)*

Following the synthesis in a previous report,[24] 5 mL of styrene (with inhibitor removed by aluminum oxide chromatography) and PMDETA (0.43 g, 2.4 mmol) were dissolved in 10 mL of dioxane in a Schlenk tube. After three freeze-pump-thaw cycles, the solution was frozen again. Afterwards, CuCl (0.24 g) and BPI (0.83 g) were added while the tube was purged with a stream of ultrapure nitrogen. The tube was then pumped for 45 min, thawed, and immersed in an oil bath at 110 °C. After reacting for 10 h under constant stirring, the solution was precipitated in methanol. The white precipitate of PTA-PS-Br was filtered and dried at 70 °C overnight *in vacuo*.

### *2.3.4 Synthesis of phthalimido-PS-H (PTA-PS)*

PTA-PS-Br was reduced to PTA-PS following a previous report.[25] PTA-PS-Br (1.0 g, 0.67 mmol), tri-*n*-butyltin hydride (0.58 g, 2.0 mmol), and AIBN (0.055 g, 0.33 mmol) were dissolved in 20 mL of toluene and heated in an oil bath at 70 °C for 10 h. After the reaction, PTA-PS was precipitated in methanol and dried at 70 °C *in vacuo*.

### *2.3.5 Synthesis of amine-terminated PS (PS-$NH_2$)*

In a round-bottom flask, 1 g of PTA-PS was dissolved in 20 mL of 1 M hydrazine in THF. The solution was refluxed at ~65 °C for 10 h, and the polymer was precipitated in methanol. The white precipitate (PS-$NH_2$) was filtered and dried at 70 °C *in vacuo*.

### *2.3.6 Synthesis of polyetherimide (PEI-DA)*

PEI-DA oligomers with number average molecular weight ($M_n$) of 8, 10, and 12 kDa were synthesized using a method in previous reports.[2, 26] Taking 8k-PEI-DA as an example, BPADA (21.861 g, 42.001 mmol) and mPD (4.216 g, 38.99 mmol) were mixed in 80 mL of oDCB in a 500-mL three-neck round-bottom flask equipped with a mechanical stirrer, a nitrogen inlet, and a Dean Stark receiver. The mixture was constantly purged with ultrapure nitrogen and heated at 180 °C overnight. Afterwards, the resulting amber-colored viscous solution was heated at 380 °C for 30 min to evaporate the solvent, which was collected by a cold flask immersed in an ice bath. The viscous fluid was cooled down to 60 °C and solidified. The solid was dissolved in 80 mL of chloroform and precipitated in 1 L of anhydrous acetone. The precipitate was filtered and washed with acetone three times. The resulting white solid was ground into powder and dried at 220 °C overnight *in vacuo*.

### *2.3.7 Synthesis of PS-PEI-PS (SIS)*

SIS block copolymers were synthesized by reacting PS-$NH_2$ with PEI-DA. For example, PS-PEI-PS with a molecular weight of 1.5-8-1.5 kDa (denoted as SIS-8) was synthesized as follows. In a two-neck round-bottom flask with a magnetic stir bar, PS-$NH_2$ (1.5 kDa, 250 mg, 0.167 mmol) and PEI-DA (8 kDa, 750 mg, 0.0912 mmol) were dissolved in 20 mL of oDCB. The solution was refluxed at 180 °C overnight under a constant stream of

nitrogen. Afterwards, the solvent was evaporated by heating at 220 °C for 30 min. The resulting amber-colored solid was dissolved in 20 mL of DCM and precipitated in 200 mL of acetone. The pale brown precipitate was filtered, washed with acetone, and dried overnight at 180 °C *in vacuo*.

### *2.3.8 Characterization*

Proton nuclear magnetic resonance ($^1$H NMR) spectroscopy was performed on a Varian Unity at 400 MHz in deuterated chloroform. Size exclusion chromatography (SEC) tests were performed on a Tosoh EcoSEC HLC-8320 using a refractive index detector and THF as the eluent at a flow rate of 0.5 mL/min. Thermogravimetric analysis (TGA) was performed on a TA 5500 with a typical sample loading of 4-6 mg and a constant nitrogen purge. Differential scanning calorimetry (DSC) was performed on TA 2500 with a heat rate of 10 °C min$^{-1}$. The DSC instrument was calibrated using a Trios-Temperature/Cell Constant Calibration program and an Indium standard before use. Dynamic mechanical analysis (DMA) was performed on TA Q800 in a tension mode at a frequency of 1 Hz, a strain of 0.03%, and a heat rate of 3 °C min$^{-1}$ under air purge. Scanning electron microscopy (SEM) was performed on a LEO Zeiss 1550 at an accelerating voltage of 2 kV and a working distance of ~4 mm. The SEM images were processed using ImageJ 1.51. Oxygen plasma was performed on a South Bay Technology PC-2000 with ultra-pure oxygen. The etching rates of PS and PEI were determined by measuring the film thicknesses before and after oxygen plasma. The film thicknesses were measured on a Veeco DekTak 150 Stylus Profilometer with a 2.5 μm tip radius stylus and an application of 1 mg force. Small angle X-ray scattering (SAXS) was performed on a Bruker N8 Horizon (Cu $K_\alpha$ radiation, 1.54 Å in wavelength) at a generator voltage of 50 kV and a current of 1 mA.

DMA samples were prepared by casting chloroform solutions of SIS into dry films and then baked at 220 °C overnight *in vacuo*. SEM samples were prepared by drop-casting aliquots of SIS solutions in DCM (10 mg $mL^{-1}$) on silicon substrates and subsequent annealing at 220 °C overnight. To improve the contrast, the SEM samples were treated with oxygen plasma for 1 min and then sputtered with iridium of ~2 nm in thickness. Ninhydrin test was performed by adding 0.2 mL of ninhydrin reagent to 1.0 mL of a sample solution (polymer in DCM at 1 mM). The mixture was incubated in warm water (~40 °C) for 20 min.

## 2.4 Results and discussion

The synthesis of SIS was divided into three parts (Scheme 1): the synthesis of amine-terminated PS oligomers (PS-$NH_2$, panel a),[23-25] the synthesis of dianhydride-terminated PEI (PEI-DA, panel b),[2, 26] and the condensation of PS-$NH_2$ and PEI-DA into SIS (panel c) *via* imidization between the amine and anhydride groups. $^1$H NMR confirmed the successful synthesis of 2-(3-bromo-3-phenylpropyl)isoindoline-1,3-dione (BPI, Figure S2.1), PS-$NH_2$ (Figure S2.2) and SIS-8 (Figure S2.3). The molecular weights of PTA-PS-Br and PEI-DA were determined by end-group analyses of the $^1$H NMR spectra.[27] In the synthesis of BPI (Figure S2.1), after bromination of 2-(3-phenylpropyl)isoindoline-1,3-dione, protons e' and f' shifted downfield. By normalizing the spectra using the protons in the phthalimido group, the integration of the peak f'' reduced from two to one, suggesting the successful addition of bromide into BPI. After the reduction of PTA-PS-Br to PTA-PS (Figure S2.2), the peaks c shifted upfield from ~4.35 ppm and merged with the peaks at ~1.15-2.40 ppm (labelled as c'), similar to that in a previous report.[25] After removal of the phthalimido group and reduction of PTA-PS to PS-$NH_2$, peak a' corresponding to the four protons in the phthalimido group disappeared. In addition, peak d' at

~3.38 ppm shifted to ~2.33 ppm (peak d") due to the formation of primary amine.[28] After the reaction of PS-$NH_2$ and PEI-DA into SIS (Figure S2.3), the broad peaks corresponding to PS and the sharp peaks corresponding to PEI were distinguishable in the $^1H$ NMR spectrum of SIS.

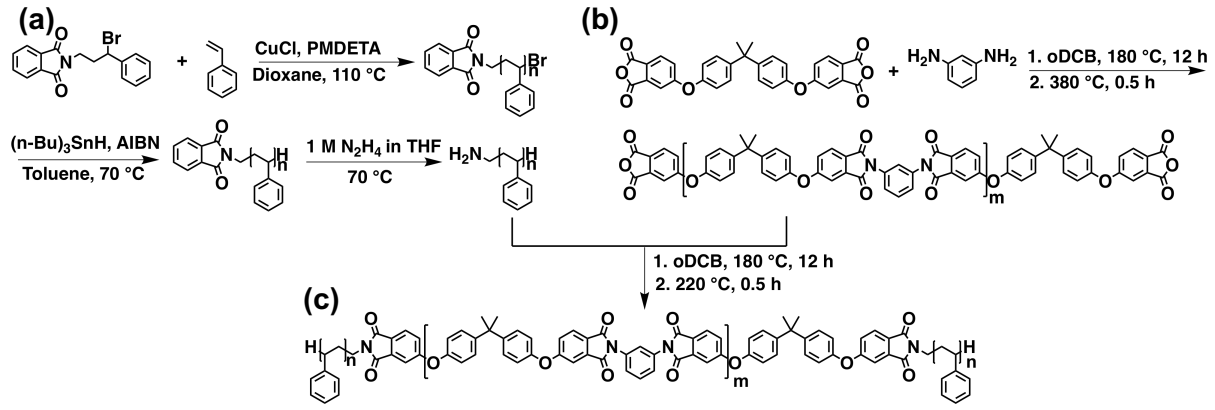


**Scheme 2.1.** The synthesis of PS-PEI-PS (SIS) triblock copolymer. The constituent (a) PS-$NH_2$ and (b) PEI-DA are first prepared and then reacted to generate (c) SIS triblock copolymer. PMDETA: *N,N,N′,N″,N″*-pentamethyldiethylenetriamine; AIBN: azobisisobutyronitrile; oDCB: 1,2-dichlorobenzene; THF: tetrahydrofuran.

To further confirm the condensation of PS-$NH_2$ and PEI-DA into SIS, we performed size exclusion chromatography (SEC) and ninhydrin tests. Figure 2.1 shows the SEC traces of PTA-PS-Br and PEI-DA (dashed lines), as well as those of SIS (solid lines). PTA-PS-Br was chosen because PS-$NH_2$ potentially has an affinity to the stationary phase in the SEC columns.[26] All SIS exhibited single elution peaks. The retention times of all SIS were shorter than those of PS and PEI-DA, confirming the formation of SIS triblock copolymers. In addition, the ninhydrin test further confirmed the conversion of PS-$NH_2$ to SIS. Ninhydrin reacts with primary amine and yields products of a dark purple color.[29] As shown in Figure 2.2a-d, among (a) blank solvent, (b) 8k-PEI-DA, (c) PS-$NH_2$, and (d) SIS-8, only PS-$NH_2$ showed the dark purple color. The absence

of the dark purple color in SIS-8 confirms that all PS-$NH_2$ reacted with 8k-PEI-DA to generate SIS-8. SIS triblock copolymers of other molecular weights (*i.e.*, SIS-10 and SIS-12) exhibited similar results to SIS-8 (Figure 2.2e-l).

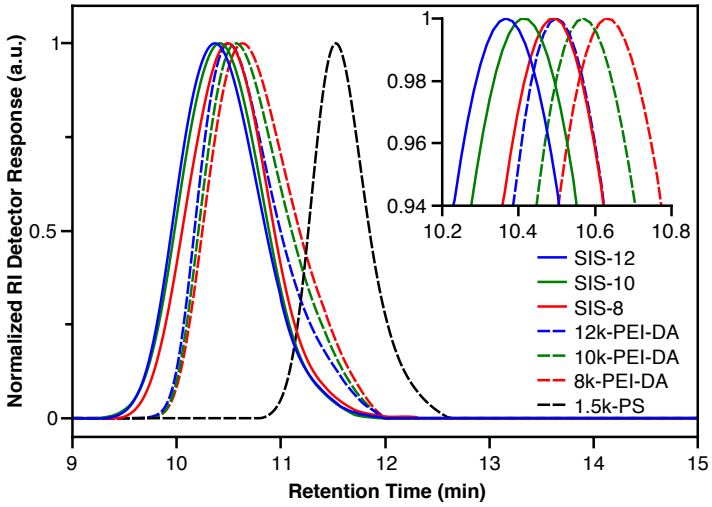


**Figure 2.1.** SEC traces of PS, PEI-DA, and SIS triblock copolymers of various molecular weights using a refractive index (RI) detector. (Inset) Magnified views of the SEC peaks of PEI-DA and SIS. To avoid the potential interactions with the SEC columns, PTA-PS-Br was used for molecular weight characterization.

The formation of SIS triblock copolymers is also evident from the thermal properties. Thermogravimetric analysis (TGA, Figure 2.3a) showed that the decomposition of PS and PEI-DA started at ~230 and ~500 °C, respectively. The SIS triblock copolymers exhibited two weight-loss stages at ~370 and ~500 °C, corresponding to the decomposition of the PS and PEI blocks, respectively. The increased thermal decomposition temperature of the PS block suggested that the thermal stability of PS was improved after condensation with PEI due to the augment effect of the PS and PEI interphase.[30] The existence of the PS and PEI interphase was also verified by differential scanning calorimetry (DSC, Figure 2.3b). The glass transition temperature ($T_g$) of the PS oligomer was ~80 °C. After condensation, the $T_g$ of the PS block became almost

indistinguishable due to the small volume fractions in the block copolymers, while the $T_g$ of the PEI block decreased slightly. For example, the $T_g$ of 12k-PEI-DA was 211 °C and that of the PEI block in SIS-12 became less pronounced and decreased to 208 °C. The shifts in $T_g$ of the two blocks confirmed that the products were block copolymers. It is noteworthy that the decomposition temperature of PS increased from ~230 to ~370 °C after incorporating into SIS. Because the decomposition temperatures of PS blocks were higher than the $T_g$ of PEI matrices, the thermolysis of PS at high temperatures would cause the softening or collapse of PEI. If thermolysis is to be used for creating air voids, either the decomposition temperature of the thermally labile block must be lower or the glass transition temperature of the matrix block must be higher.

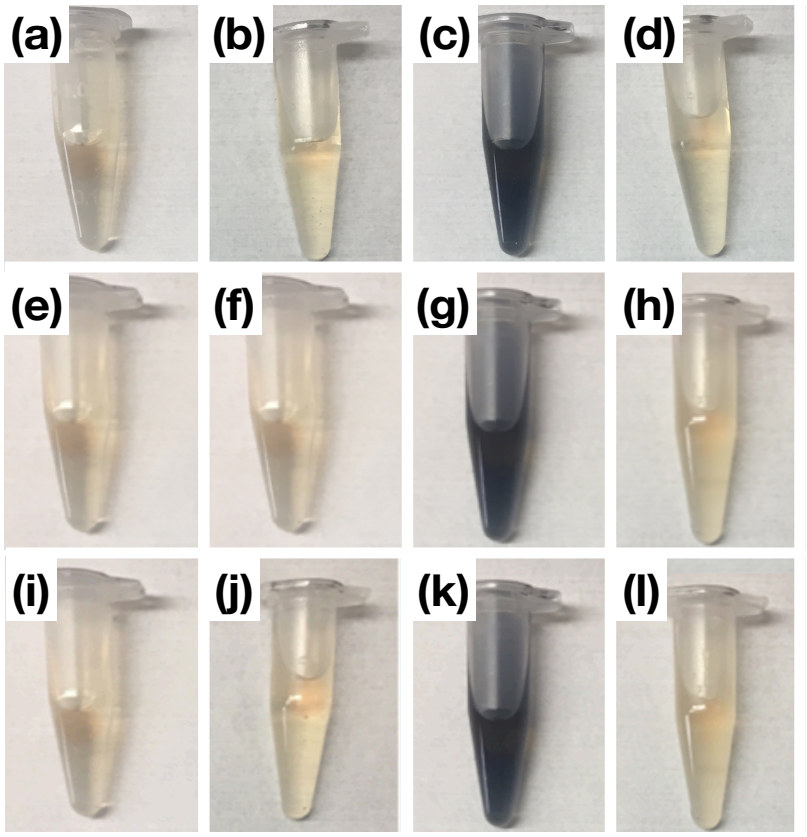


**Figure 2.2.** Ninhydrin test: (a, e, i) blank ninhydrin reagent in DCM; ninhydrin reagent mixed with a DCM solution of (b) 8k-PEI-DA, (f) 10k-PEI-DA, (j) 12k-PEI-DA, (c, g, k) PS-NH2, and (d)

SIS-8, (h) SIS-10, (l) SIS-12. The disappearance of the dark purple color in (d, h, l) confirmed that PS-$NH_2$ was fully reacted with PEI-DA to generate SIS.

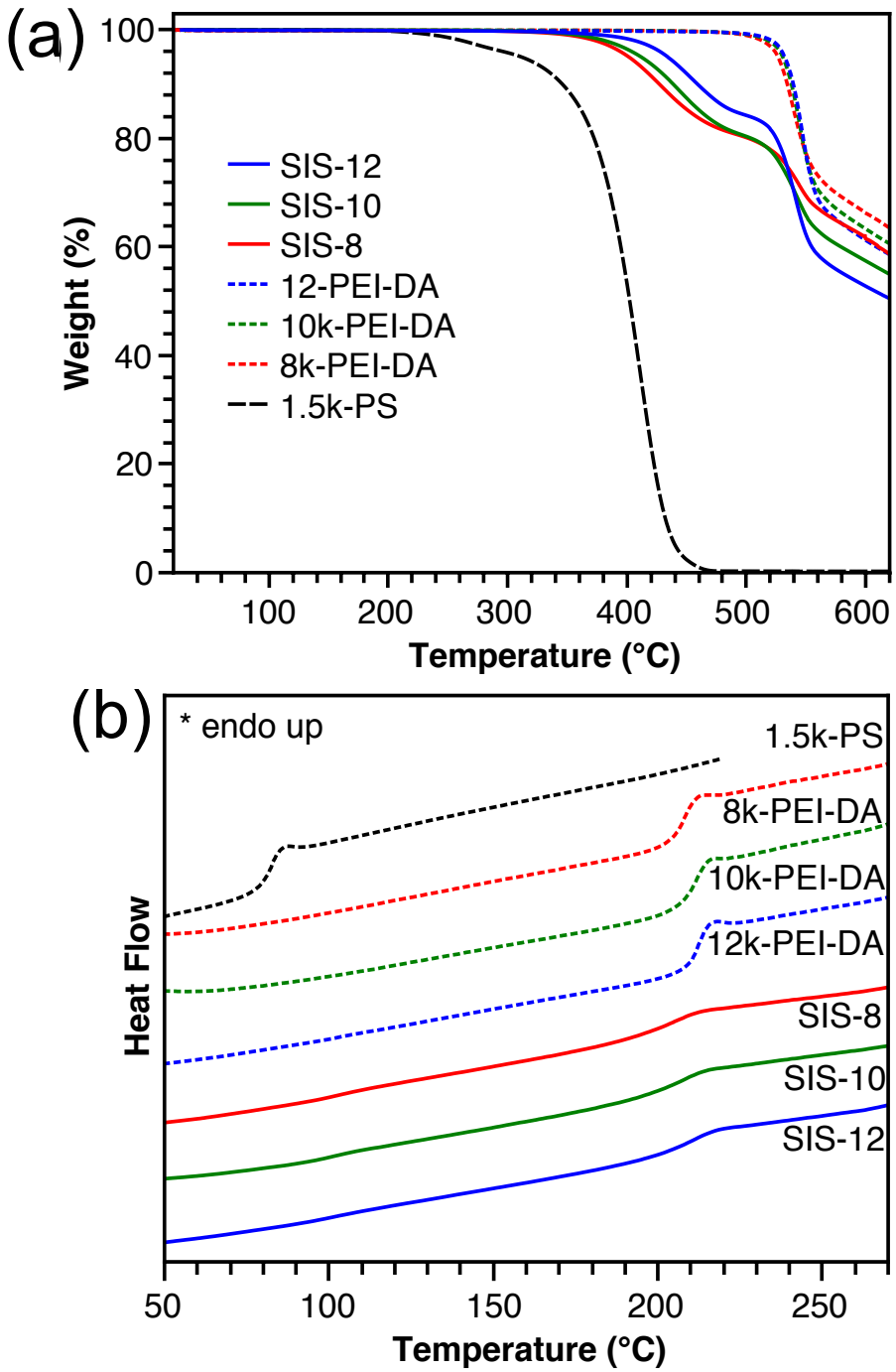


**Figure 2.3.** Thermal analyses of SIS**.** (a) TGA and (b) DSC of PS-$NH_2$, PEI-DA, and SIS.

We further investigated the mechanical properties of the SIS triblock copolymers using dynamic mechanical analysis (DMA). Figure 2.4a shows the storage and loss moduli of SIS at different temperatures. The storage moduli of all SIS were above 3 GPa at 30 °C, which was comparable to that of pure PEI.[26] When the temperature was increased to 200 °C, the storage moduli decreased to 468, 213, and 117 MPa for SIS-12, SIS-10, and SIS-8, respectively. The trend that the storage modulus decreases with an increasing volume fraction of PS is in accordance with the fact that the PS block weakens the mechanical strength of SIS. The loss moduli showed two peaks at ~100 and ~200 °C, which were assigned to the softening of the PS-rich and PEI-rich domains. The $T_g$ values of the PS and PEI blocks were determined according to tanδ (Figure 2.4b). The $T_g$ values of the PS-blocks in SIS-8, SIS-10 and SIS-12 were 112, 107 and 106 °C, respectively. The $T_g$ values of the PS blocks were higher than that of the PS oligomer (~80 °C, Figure 2.3b), which is mainly ascribed to the augment effect of the PS and PEI interphase as discussed earlier. Similarly, the $T_g$ values of the PEI-blocks in SIS-8, SIS-10, and SIS-12 were determined to be 206, 207, and 209 °C, respectively.

We continued to investigate the nanostructures of the SIS triblock copolymers. All SIS triblock copolymers were annealed at 220 °C for 24 h and then examined using scanning electron microscopy (SEM). To improve the contrast under SEM, the samples were exposed to an oxygen plasma to selectively remove part of the PS domains. Despite the low molecular weights of SIS, the PS and PEI domains were clearly observed in all films (Figure 2.5). The PS domains appeared dark and were embedded in a bright PEI matrix. The average spacings of the nanostructures were characterized with small angle x-ray scattering (SAXS). In the SAXS spectra (Figure 2.6), the characteristic peaks ($q^*$) of SIS-8, SIS-10, and SIS-12 were at0.446, 0.426, to 0.412 $nm^{-1}$, respectively, which are associated with the average periodic spacings ($L_0$) according to $L_0=2\pi/q^*$

(Table 1). $L_0$ increased as the molecular weight of the PEI-block was increased because the PS domains were further separated by the PEI blocks. Regardless of the molecular weights of the triblock copolymers, the average width of the PS domains maintained to be less than 8 nm.

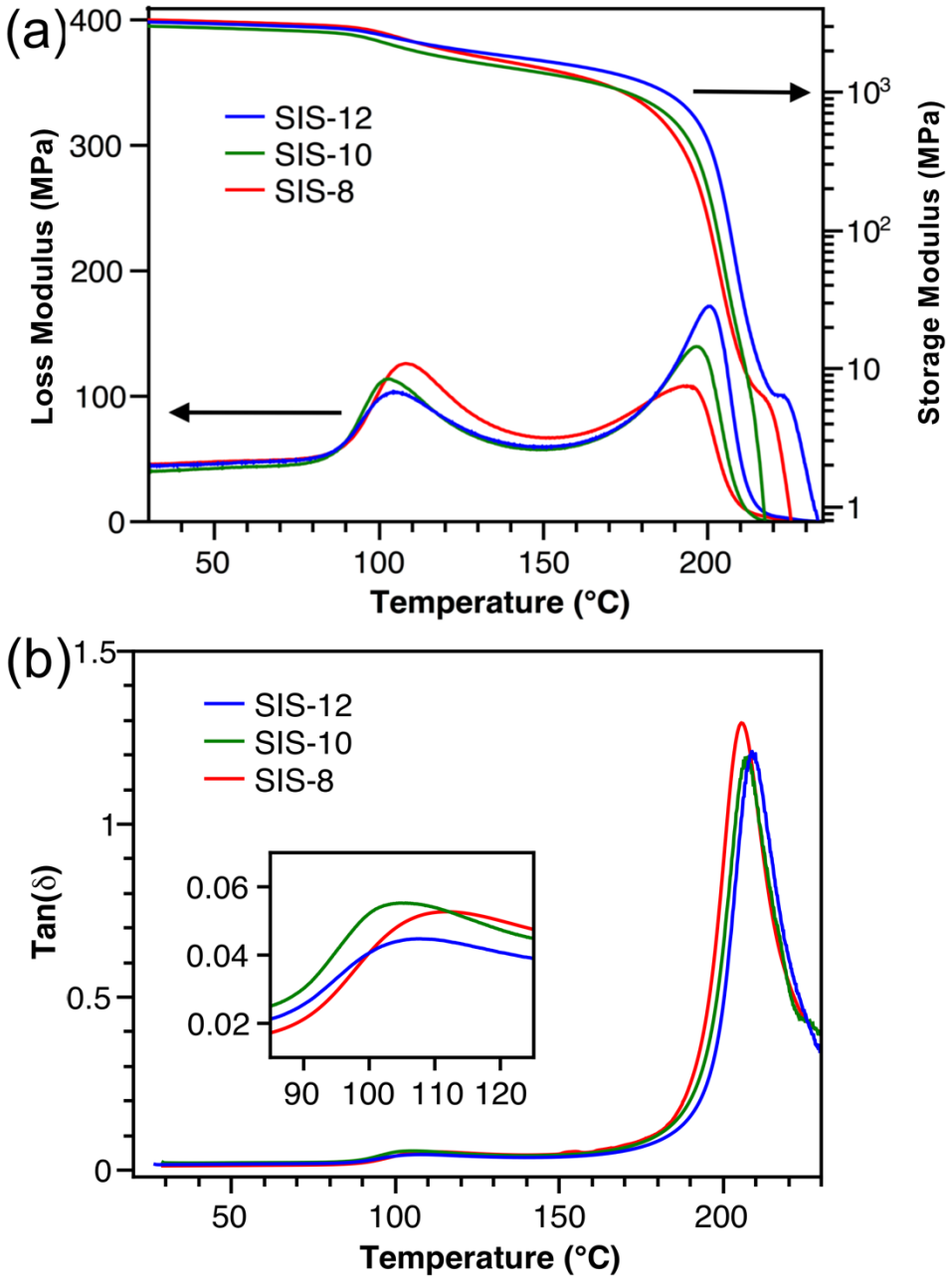


**Figure 2.4.** Thermomechanical analyses of SIS. (a) Loss and storage moduli and (b) tanδ of SIS. The inset of (b) magnifies the glass transitions of the PS blocks.

Interestingly, despite the low molecular weights, the SIS triblock copolymers exhibit semi-periodic nanostructures, as shown by the SEM images and the SAXS spectra. In the SAXS spectra, the relatively broad first-order peaks and the absence of the higher-order peaks indicate that the phase-separation of PS and PEI in the nanostructures is weak. The SIS most likely formed disordered structures. In addition, different from the strongly phase-separated nanostructures such as lamellae, cylinders and spheres,[31, 32] the nanostructures by our SIS triblock copolymers show much less regularity. The nanostructures are PS domains embedded in a PEI matrix.

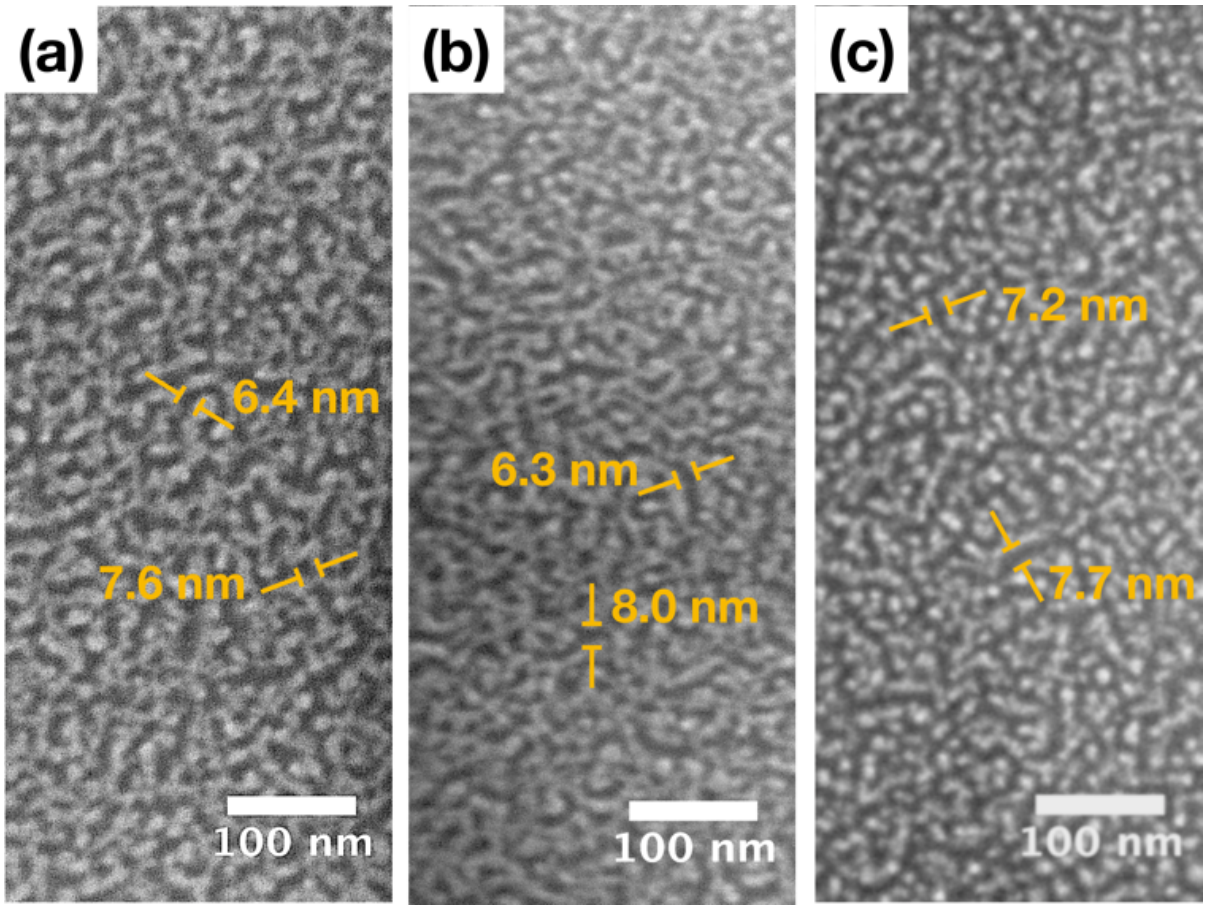


**Figure 2.5.** SEM images of (a) SIS-8, (b) SIS-10 and (c) SIS-12. The bright and dark regions are PEI and PS, respectively.

**Table 2.1** Compositions and nanostructure parameters of SIS triblock copolymers.

| | $M_{n,PEI}$ (kDa) | $M_{n,PS}$ (kDa) | PS (wt%) | PS (vol%) | $q^*$ (nm$^{-1}$) | $L_0$ (nm) |
|---|---|---|---|---|---|---|
| SIS-8 | 8 | 1.5 | 26.3 | 30.4 | 0.446 | 14.1 |
| SIS-10 | 10 | 1.5 | 22.7 | 26.4 | 0.426 | 14.7 |
| SIS-12 | 12 | 1.5 | 20.0 | 23.4 | 0.412 | 15.2 |

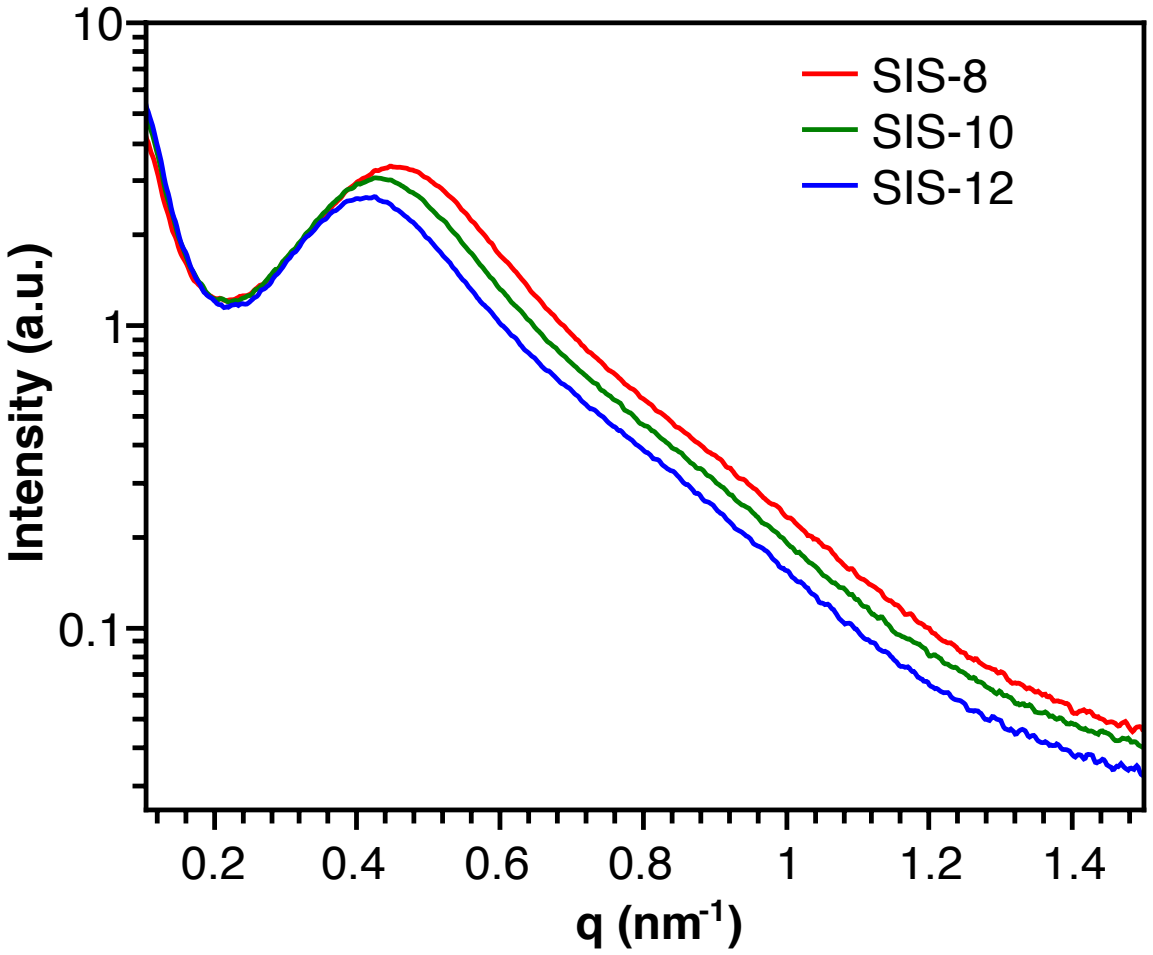


**Figure 2.6.** SAXS spectra of SIS. The pronounced characteristic peaks ($q^*$) of SIS-8, SIS-10, and SIS-12 are at 0.446, 0.426, and 0.412 nm$^{-1}$, respectively.

We attribute the observed nanostructures to the following reasons. First, both the low molecular weights of SIS and the high annealing temperature contribute to a low $\chi N$ (the product

of Flory-Huggins interaction parameter and the degree of polymerization) under the self-assembly conditions.[33] Second, due to the condensation polymerization that is used for synthesizing PEIs, the PEI blocks of the SIS block copolymers have high dispersity. The high dispersity of the major block (*i.e.*, PEI) in SIS contributes to an increase in the segregation limit at the order-disorder transition (ODT), $(\chi N)_{ODT}$.[34] Third, PEI and PS have different Kuhn lengths, and this conformational asymmetry further contributes to a high $(\chi N)_{ODT}$ at PEI volume fractions of 69.6-76.6%.[35, 36] As a result, in the triblock copolymer phase diagram,[31, 32] the SIS block copolymers are most likely disordered or at most at the boundary of order-disorder transition. Therefore, they form not-highly-ordered and semi-periodic nanostructures after the self-assembly.

## 2.5 Conclusions

In summary, we synthesized SIS triblock copolymers by the condensation reaction between amine-terminated PS and anhydride-terminated PEI. The triblock copolymers consisted of a middle PEI block and two peripheral PS blocks with an ultra-small molecular weight of 1.5 kDa. The formation of the triblock copolymers was confirmed by SEC and ninhydrin tests. Due to the augment effect of the PS/PEI interphase, the $T_g$ of PS was increased, and the thermal stability of PS was improved. Despite the low molecular weights, SIS formed nanostructures. Compared to the previous reports,[13, 14, 16] the nanostructures of SIS were clearly observed, and the domain sizes were relatively uniform. By tuning the molecular weight of PEI and the volume fraction of PS, the spacings of the nanostructures were controlled to be ~14-15 nm and the average PS domains size was less than 8 nm. Our future work will focus on removing the small-molecular-weight labile blocks to produce porous polyimides with air voids. The work represents a route for synthesizing polyimide-based

ABA triblock copolymers with small domain sizes. The study is expected to inspire future synthesis of polyimide-based block copolymers with complex nanoscopic structures and advanced functionalities, which can be used as ultrathin low-$\kappa$ dielectric films,[37-39] separation[40, 41] and filtration[42] membranes, nanolithographic templates,[43, 44] and compatibilizers.[45]

## 2.6 Supporting Information

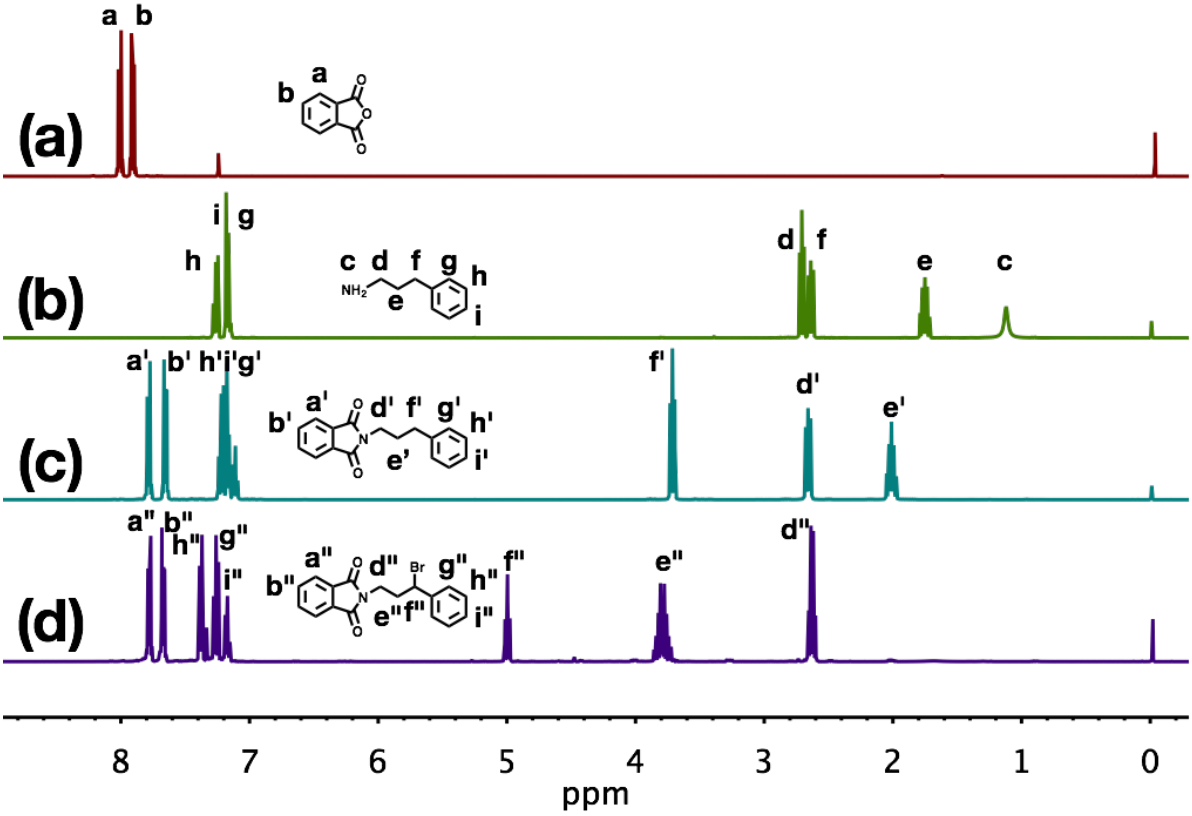


**Figure S2.1.** $^{1}$H NMR spectra of (a) phthalic anhydride, (b) 3-phenylpropylamine, (c) 2-(3-phenylpropyl)isoindoline-1,3-dione, (d) 2-(3-bromo-3-phenylpropyl)isoindoline-1,3-dione (BPI). The two peaks at 0.00 ppm and 7.26 ppm are from tetramethylsilane and chloroform,

respectively. In comparison to peaks f' and e' in (c), f'' and e'' in (d) shifts downfield, and the integration of f'' reduces to 1, which indicates the successful bromination.

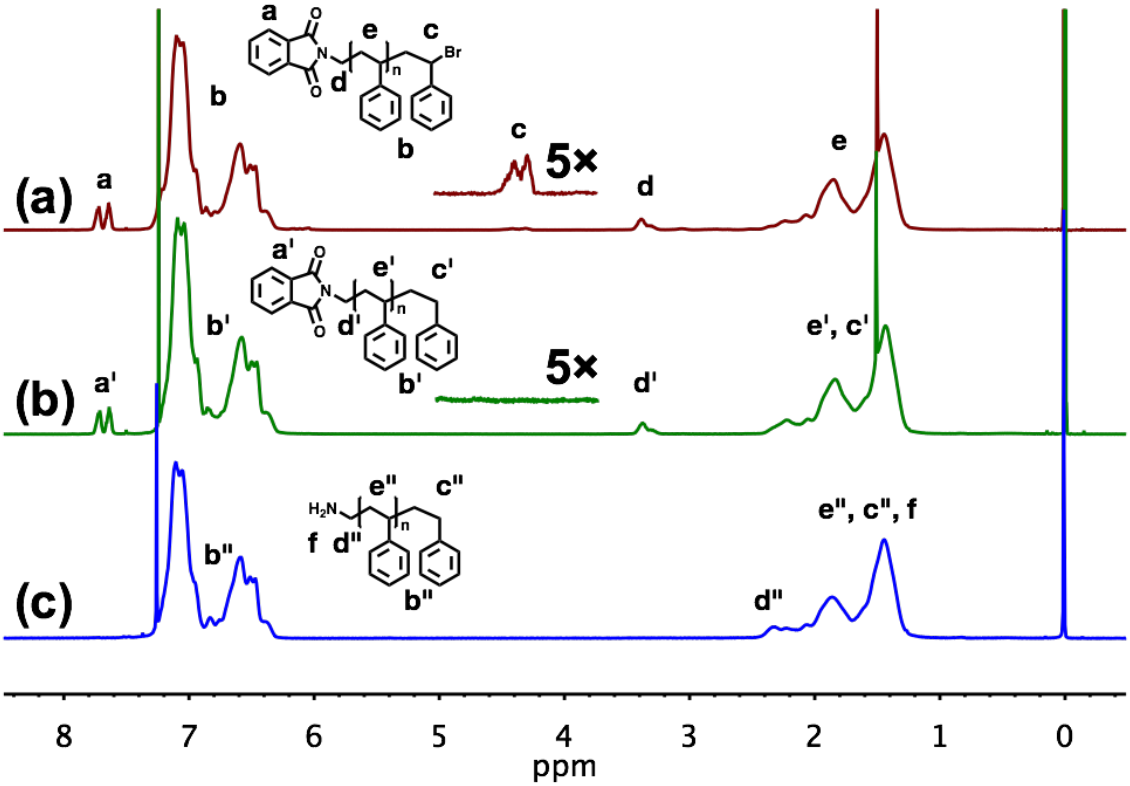


**Figure S2.2.** $^{1}$H NMR spectra of (a) PTA-PS-Br, (b) PTA-PS, and (c) PS-$NH_2$. In spectrum (a), the peaks between 1.15 and 2.40 ppm (group e) are assigned to the aliphatic protons in the PS backbone, the peaks between 6.25 and 7.30 ppm (group b) are assigned to the aromatic protons in the phenyl rings. After reducing (a) PTA-PS-Br to (b) PTA-PS, the peaks c at ~4.35 ppm disappear and the resonance of the resulting terminal protons c' merges with that of the proton group e' in PTA-PS. After reducing (b) PTA-PS to (c) PS-$NH_2$, peaks a' in phthalimido group disappear. Peak d' shifts upfield to peak d'' due to the formation of primary amine. The signal corresponding to the primary amine (peak f) merges in group e''. Three sharp spikes at 0.00 ppm, 1.56 ppm and 7.26 ppm are assigned to tetramethylsilane, water, and chloroform, respectively.

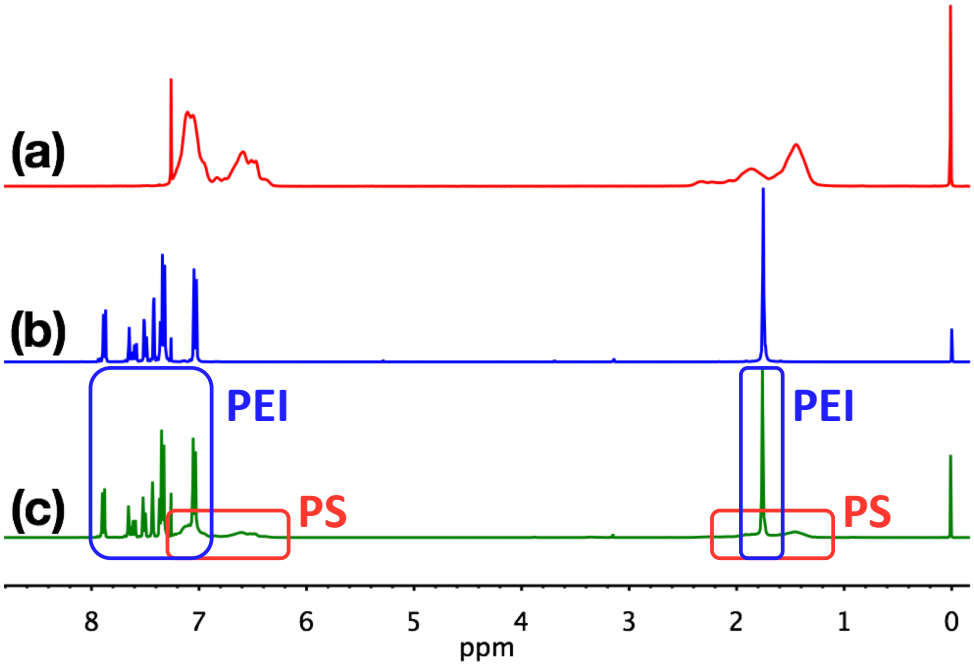


**Figure S2.3.** $^{1}$H NMR spectra of (a) PS-$NH_2$, (b) 8k-PEI-DA, and (c) PS-PEI-PS (SIS-8). The red and blue boxes highlight the peaks from PS and PEI, respectively.

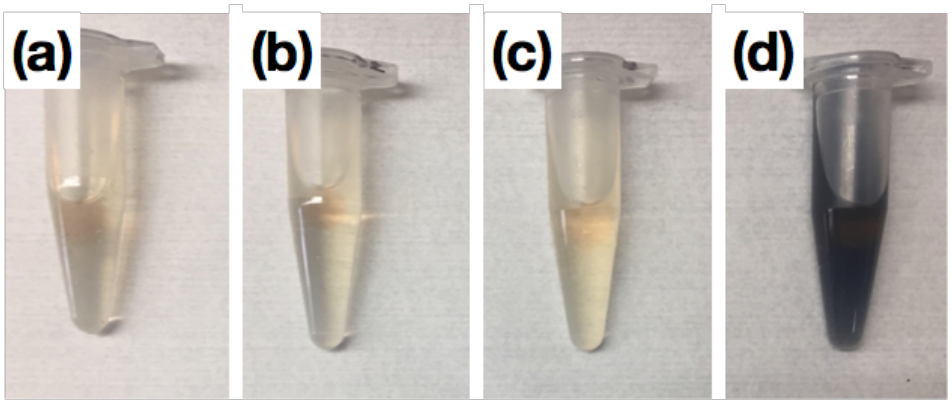


**Figure S2.4.** Ninhydrin test: (a) blank ninhydrin reagent in DCM; (b-d) ninhydrin reagent mixed with a DCM solution of (b) PTA-PS-Br, (c) PTA-PS, and (d) PS-$NH_2$. The appearance of a dark purple color in (d) confirms the formation of primary amine after the deprotection of phthalimido in PTA-PS.

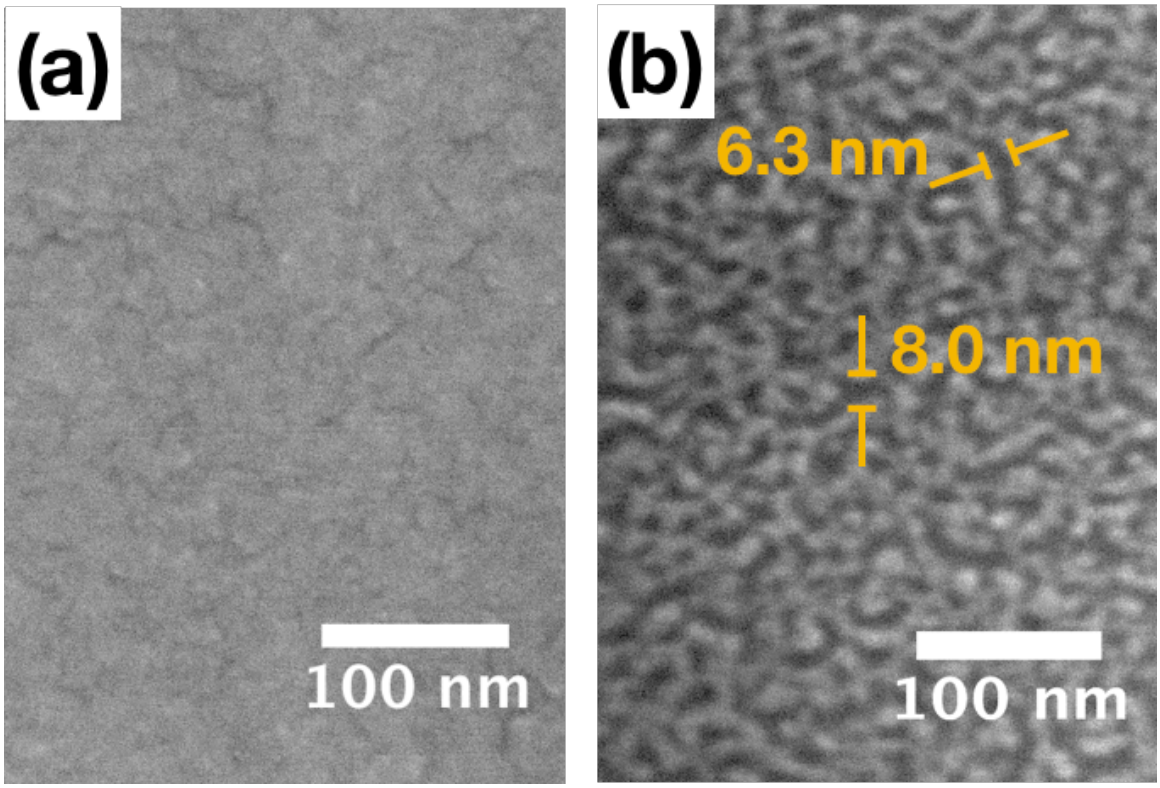


**Figure S2.5.** SEM images of SIS-10 (a) before oxygen plasma etching and (b) after oxygen plasma etching for 1 min.

**Table S2.1.** Etching rates of PS and PEI by oxygen plasma.

| Sample | Before Etching | | After Etching for 1 min | | Etching Rate |
|---|---|---|---|---|---|
| | Thickness (nm) | Roughness (nm) | Thickness (nm) | Roughness (nm) | (nm/min) |
| 1.5k-PTA-PS-Br | 144.0 ± 2.6 | 12.7 ± 4.6 | 127.5 ± 4.9 | 12.9 ± 5.2 | 16.5 ± 5.5 |
| 8k-PEI-DA | 49.2 ± 2.4 | 6.3 ± 1.1 | 40.7 ± 1.1 | 4.5 ± 1.7 | 8.5 ± 2.6 |
| 10k-PEI-DA | 48.5 ± 2.6 | 3.1 ± 1.1 | 43.3 ± 1.8 | 4.2 ± 0.6 | 5.2 ± 3.2 |
| 12-kPEI-DA | 47.8 ± 1.1 | 4.6 ± 0.9 | 42.7 ± 0.8 | 4.1 ± 0.5 | 5.1 ± 1.4 |

## 2.7 Acknowledgements

This material is based upon work supported by the Air Force Office of Scientific Research under award number FA9550-17-1-0112 through the Young Investigator Program (YIP). D. G. acknowledges the support of Virginia Tech Sustainable Nanotechnology (VTSuN). The authors acknowledge the use of facilities in Institute for Critical Technology and Applied Science (ICTAS), Virginia Tech. The authors appreciate Dr. Stephen M. Martin for providing access to the SAXS characterization.

## 2.8 References

1. Huang, F.; Wang, X.; Li, S., The Thermal Stability of Polyetherimide. *Polym. Degrad. Stab.* **1987**, *18*, 247-259.

2. Takekoshi, T., Polyimides. In *New Polymer Materials*, 1 ed.; Springer: Berlin Heidelberg, 1990; Vol. 94, pp 1-25.

3. Liu, X.-Y.; Zhan, M.-S.; Wang, K., Preparation and Characterization of Electromagnetic Interference Shielding Polyimide Foam. *J. Appl. Polym. Sci.* **2013**, *127*, 4129-4137.

4. Xiao, X.; Kong, D.; Qiu, X.; Zhang, W.; Zhang, F.; Liu, L.; Liu, Y.; Zhang, S.; Hu, Y.; Leng, J., Shape-Memory Polymers with Adjustable High Glass Transition Temperatures. *Macromolecules* **2015**, *48*, 3582-3589.

5. Qian, G.; Wang, L.; Shang, Y.; He, X.; Tang, S.; Liu, M.; Li, T.; Zhang, G.; Wang, J., Polyimide Binder: A Facile Way to Improve Safety of Lithium Ion Batteries. *Electrochim. Acta* **2016**, *187*, 113-118.

6. Fay, C. C.; CLAIR, A. K. S., Dimensionally Stable Polyimide Copolymers for Microelectronics Applications. *J. Appl. Polym. Sci.* **1998**, *69*, 2383–2393.

7. Yoo, D. K.; Lim, S. K.; Yoon, T. H.; Kim, D., Physical Properties and Stress Analysis of Low Dielectric Polyimide Films Containing Adamantane Pendant Group. *Polym. J.* **2003**, *35*, 697-703.

8. Kang, D. W.; Kim, Y. M., Preparation and Surface Characteristics of Poly[(Diphenylmethyltrifluoropropylsiloxane)-*b*-Polyimide] Copolymer as an Interlayer Dielectric Material. *J. Inorg. Organomet. Polym.* **2002**, *12*, 79-97.

9. Stoakley, D. M.; Clair, A. K. S.; Croall, C. I., Low Dielectric, Fluorinated Polyimide Copolymers. *J. Appl. Polym. Sci.* **1994**, *51*, 1479-1483.

10. Carter, K. R.; DiPietro, R. A.; Sanchez, M. I.; Swanson, S. A., Nanoporous Polyimides Derived from Highly Fluorinated Polyimide/Poly(propylene oxide) Copolymers. *Chem. Mater.* **2001**, *13*, 213-221.

11. Charlier, Y.; Hedrick, J. L.; Russell, T. P.; Swanson, S.; Sanchez, M.; Jérôme, R., Crosslinked Polyimide Foams Derived from Pyromellitic Dianhydride and 1,1-Bis(4-aminophenyl)-1-phenyl-2,2,3-trifluoroethane with Poly(α-methylstyrene). *Polymer* **1995**, *36*, 1315-1320.

12. Chung, C.-M.; Lee, J.-H.; Cho, S.-Y.; Kim, J.-G.; Moon, S.-Y., Preparation of Porous Thin Films of a Partially Aliphatic Polyimide. *J. Appl. Polym. Sci.* **2006**, *101*, 532-538.

13. Hedrick, J. L.; Carter, K.; Sanchez, M.; Pietro, R. D.; Swanson, S., Crosslinked Polyimide Foams Derived from Poly(imide-propylene oxide) Copolymers. *Macromol. Chem. Phys.* **1997**, *198*, 549-559.

14. Hedrick, J. L.; Hawker, C. J.; DiPietro, R.; Jérôme, R.; Charlier, Y., The Use of Styrenic Copolymers to Generate Polyimide Nanofoams. *Polymer* **1995**, *36*, 4855-4866.

15. Ju, J.; Wang, Q.; Wang, T.; Wang, C., Low Dielectric, Nanoporous Fluorinated Polyimide Films Prepared from PCL-PI-PCL Triblock Copolymer Using Retro-Diels-Alder Reaction. *J. Colloid Interface Sci.* **2013**, *404*, 36-41.

16. Meleshko, T. K.; Kashina, A. V.; Saprykina, N. N.; Kostyuk, S. V.; Vasilenko, I. V.; Nikishev, P. A.; Yakimanskii, A. V., Synthesis and Morphology of Polycaprolactone-*b*-Polyimide-*b*-Polycaprolactone Triblock Copolymers for Film Separation Membranes. *Russ. J. Appl. Chem.* **2017**, *90*, 602-612.

17. Miyata, S.; Yoshida, K.; Shirokura, H.; Kashio, M.; Nagai, K., Solid and Thermal Properties of ABA-Type Triblock Copolymers Designed Using Difunctional Fluorine-Containing Polyimide Macroinitiators with Methyl Methacrylate. *Polym. Int.* **2009**, *58*, 1148-1159.

18. Wang, L.; Lu, J.; Liu, M.; Lin, L.; Li, J., Preparation of Porous Polyimide Microspheres by Thermal Degradation of Block Copolymers. *Particuology* **2014**, *14*, 63-70.

19. Hedrick, J. L.; DiPietro, R.; Plummer, C. J. G.; Hilborn, J.; Jérôme, R., Polyimide Foams Derived from a High $T_g$ Polyimide with Grafted Poly(α-methylstyrene). *Polymer* **1996**, *37*, 5229-5236.

20. Hedrick, J. L.; Russell, T. P.; Labadie, J.; Lucas, M.; Swanson, S., High Temperature Nanofoams Derived from Rigid and Semi-Rigid Polyimides. *Polymer* **1995**, *36*, 2685-2697.

21. Hedrick, J. L.; Russell, T. P.; Sanchez, M.; DiPietro, R.; Swanson, S., Polyimide Nanofoams from Caprolactone-Based Copolymers. *Macromolecules* **1996**, *29*, 3642-3646.

22. Charlier, Y.; Hedrick, J.; Russell, T. P., Polyimides Foams Prepared from Homepolymer/Copoymer Mixtures. *Polymer* **1995**, *36*, 4529-4534.

23. Pourjavadi, A.; Seidi, F.; Jahromi, P. E.; Salimi, H.; Roshan, S.; Najafi, A.; Bruns, N., Use of a Novel Initiator for Synthesis of Amino-End Functionalized Polystyrene ($NH_2$-PS) by Atom Transfer Radical Polymerization. *J. Polym. Res.* **2011**, *19*, 9752-9760.

24. Postma, A.; Davis, T. P.; Moad, G.; O'Shea, M. S., Approaches to Phthalimido and Amino End-Functional Polystyrene by Atom Transfer Radical Polymerisation (ATRP). *React. Funct. Polym.* **2006**, *66*, 137-147.

25. Coessens, V.; Matyjaszewski, K., Dehalogenation of Polymers Prepared by Atom Transfer Radical Polymerization. *Macromol. Rapid Commun.* **1999**, *20*, 66-70.

26. Cao, K.; Liu, G., Low-Molecular-Weight, High-Mechanical-Strength, and Solution-Processable Telechelic Poly(ether imide) End-Capped with Ureidopyrimidinone. *Macromolecules* **2017**, *50*, 2016-2023.

27. Page, T. F. J.; Bresler, W. E., End-Group Analysis and Number-Average Molecular Weight Determination of Some Polyalkylene Glycols and Glycol Polyesters Using Nuclear Magnetic Resonance Spectroscopy. *Anal. Chem.* **1964**, *36*, 1981-1985.

28. Ju, M.; Gong, F.; Cheng, S.; Gao, Y., Fast and Convenient Synthesis of Amine-Terminated Polylactide as a Macroinitiator For ω-Benzyloxycarbonyl-L-Lysine-N-Carboxyanhydrides. *Int. J. Polym. Sci.* **2011**, *6*, 1-7.

29. Isidro-Llobet, A.; Alvarez, M.; Albericio, F., Amino Acid-Protecting Groups. *Chem Rev* **2009**, *109*, 2455-504.

30. Daimon, H.; Okitsu, H.; Kumanotani, J., Glass Transition Behaviors of Random and Block Copolymers and Polymer Blends of Styrene and Cycldodecyl Acrylate. *Polym. J.* **1975**, *7*, 460-466.

31. Matsen, M. W.; Thompson, R. B., Equilibrium Behavior of Symmetric ABA Triblock Copolymer Melts. *J. Chem. Phys.* **1999**, *111*, 7139-7146.

32. Yang, S.; Vishnyakov, A.; Neimark, A. V., Self-Assembly in Block Polyelectrolytes. *J. Chem. Phys.* **2011**, *134*, 054104.

33. Hickey, R. J.; Gillard, T. M.; Irwin, M. T.; Morse, D. C.; Lodge, T. P.; Bates, F. S., Phase Behavior of Diblock Copolymer-Homopolymer Ternary Blends: Congruent First-Order Lamellar-Disorder Transition. *Macromolecules* **2016**, *49*, 7928-7944.

34. Lynd, N. A.; Hillmyer, M. A., Effects of Polydispersity on the Order-Disorder Transition in Block Copolymer Melts. *Macromolecules* **2007**, *40*, 8050-8055.

35. Inoue, T.; Osaki, K., Role of Polymer Chain Flexibility on the Viscoelasticity of Amorphous Polymers around the Glass Transition Zone. *Macromolecules* **1996**, *29*, 1595-1599.

36. Matsen, M. W.; Schick, M., Microphases of a Diblock Copolymer with Conformational Asymmetry. *Macromolecules* **1994**, *27*, 4014-4015.

37. Lv, P.; Dong, Z.; Dai, X.; Zhao, Y.; Qiu, X., Low-Dielectric Polyimide Nanofoams Derived from 4,4′ -(Hexafluoroisopropylidene) diphthalic Anhydride and 2,2′ -Bis(trifluoromethyl) benzidine. *RSC Adv.* **2017**, *7*, 4848-4854.

38. Jin, Y.; Tang, J.; Hu, J.; Han, X.; Shang, Y.; Liu, H., One-Step Fabrication of Ultralow Dielectric Polyimide Films Consisting of Size-Controlled Mesoporous Nanoparticles. *Colloids Surf. A* **2011**, *392*, 178-186.

39. Meador, M. A. B.; Wright, S.; Sandberg, A.; Nguyen, B. N.; Van Keuls, F. W.; Mueller, C. H.; Rodríguez-Solís, R.; Miranda, F. A., Low Dielectric Polyimide Aerogels as Substrates for Lightweight Patch Antennas. *ACS Appl. Mater. Interfaces* **2012**, *4*, 6346-6353.

40. Kim, K.; Schulze, M. W.; Arora, A.; Lewis, R. M.; Hillmyer, M. A.; Dorfman, K. D.; Bates, F. S., Thermal Processing of Diblock Copolymer Melts Mimics Metallurgy. *Science* **2017**, *356*, 520-523.

41. Kanehashi, S.; Sato, S.; Nagai, K., Synthesis and Gas Permeability of Hyperbranched and Cross-Linked Polyimide Membranes. In *Membrane Gas Separation*, 1 ed.; Yampolskii, Y.; Freeman, B., Eds. John Wiley and Sons: 2010; pp 1-27.

42. Vanherck, K.; Koeckelberghs, G.; Vankelecom, I. F. J., Crosslinking Polyimides for Membrane Applications: A Review. *Prog. Polym. Sci.* **2013**, *38*, 874-896.

43. Liu, G.; Thomas, C. S.; Craig, G. S. W.; Nealey, P. F., Integration of Density Multiplication in the Formation of Device-Oriented Structures by Directed Assembly of Block Copolymer-Homopolymer Blends. *Adv. Funct. Mater.* **2010**, *20*, 1251-1257.

44. Lin, E.; Soles, C. L.; Goldfarb, D. L.; Trinque, B. C.; Burns, S. D.; Jones, R. L.; Lenhart, J. L.; Angelopoulos, M.; Willson, C. G.; Satija, S. K.; Wu, W.-l., Direct Measurement of the Reaction Front in Chemically Amplified Photoresists. *Science* **2002**, *19*, 372-375.

45. Gao, C.; Zhang, S.; Li, X.; Zhu, S.; Jiang, Z., Synthesis of Poly(ether ether ketone)-*block*-Polyimide Copolymer and Its Compatibilization for Poly(ether ether ketone)/Thermoplastic Polyimide Blends. *Polymer* **2014**, *55*, 119-125.

# Chapter 3. Mesoporous Polyetherimide Thin Films *via* Hydrolysis of Polylactide-*b*-Polyetherimide-*b*-Polylactide

This chapter is reproduced from a published manuscript by Dong Guo, Jocelyn Riet, Assad Khan, Yichen Guo, Zhen Xu, Tianyu Liu and Guoliang Liu from the following reference: *Polym. Chem.* **2021**, 12, 3939. Reproduced with permission from the Royal Society of Chemistry. Copyright 2021 Royal Society of Chemistry.

## 3.1 Abstract

Mesoporous polyetherimides are important high-performance polymers. Conventional strategies to prepare porous polyetherimides, and polyimide in general, are based on covalent organic framework or thermolysis of sacrificial polymers. The former produces micropores due to intrinsically crosslinked microstructures, and the latter results in macropores because of a blowing effect by the sacrificial polymers. The preparation of mesopores remains a challenge. Here we have prepared mesoporous polyetherimide films by hydrolyzing polylactide-*b*-polyetherimide-*b*-polylactide (AIA). Controlled by molecular weight and volume fraction of polylactide in AIA, the porous films exhibit an average pore width of 24 nm. The mesoporous polyetherimide films exhibit a storage modulus of ~1 GPa at ambient temperatures. This work advances the chemistry of high-performance polymers and provides an alternative strategy to prepare mesoporous polymers, enabling potential use as high-performance membranes for separation, purification, and electrochemistry.

## 3.2 Introduction

Porous polyimides (PIs) are high-performance engineering materials with broad applications in gas separation,[1-6] $CO_2$ capture,[7-14] water purification,[15, 16] oil retention,[17-19] catalysis,[20] microelectronics,[21-26] and electrochemical energy storage.[27-32] Porous polyimides not only inherit mechanical strength, thermal stability and chemical resistance from polyimides,[33] but also gain delicately designed porosity and functionality. Among various PIs, polyetherimide (PEI) attracts extensive interests because of the excellent combination of high thermomechanical performance and good processability, in both solution and melt processings.[33] Conventionally, porous PEI and PI in general are prepared by synthesis of covalent organic frameworks,[1, 7-11, 34] introduction of porogens,[23, 27, 31, 35-48] utilization of phase inversion,[2, 5, 23, 36, 49, 50] electrospinning,[28-30, 51, 52] and thermolysis of block or graft copolymers.[22, 53-65] These methods often yield microporous (pore width < 2 nm) or macroporous structures (pore width > 50 nm). However, the preparation of PEI and PI in general with mesoporous structures (2 - 50 nm) via environmentally benign methods remains a challenge.

Among the various methods for preparing porous structures, covalent organic frameworks stand out for preparing micropores. For instance, trigonal/tetrahedral centers and rigid linkers can crosslink and construct polyimide frameworks with intrinsic micropores.[7-11, 34] The topology of frameworks and length of linkers, however, limit the pore size to be smaller than 3 nm.[7-9, 34] Alternatively, porogens with pre-defined sizes are well-suited for templating pores. The porogens are initially embedded in a polymer matrix and then eliminated to create pores. Various porogens and eliminating methods have been developed, including $SiO_2$ nanospheres via HF etching,[27, 31, 35-37] salts or dibutyl phthalate via solvent extraction,[38-41] solvents via freeze-drying (or lyophilization),[44, 45] polymer blends via thermolysis,[42, 43] and isocyanates generating $CO_2$ to induce

foaming.[23, 46, 47] In these systems, the porogens often aggregate into macro-scale domains, therefore resulting in macropores. Similarly, in wet phase inversion-induced pore generation, the non-solvents occupy volumes within wet polymer films as macro-scale domains and thus create macropores.[23, 36, 49, 50] Lastly, electrospinning produces inter-fiber voids in fiber mats during processing, and hence the pore sizes are also in macro-scales.[28-30, 51]

Different from the above methods that cannot reliably produce mesopores, block or graft copolymers are capable of microphase-separation to form mesoscale domains, holding great promise for preparing mesoporous structures.[62, 63] Various thermally labile polymers have been employed to synthesize block or graft copolymers of PEI and PI in general, including polystyrene,[54, 66] poly(α-methyl styrene),[55, 56] poly(ethylene oxide),[57] poly(propylene oxide),[53, 58-61] poly(methyl methacrylate),[62, 63] polycaprolactone,[22, 64, 65, 67] etc. After microphase separation, the thermally labile polymers are thermalized to create pores. However, gaseous species, which are produced by decomposition of the labile phase, often detrimentally plasticize the polymer matrix, even for PI with high glass transition temperatures ($T_g$). The gaseous species blow across the softened polymer matrix to create porous structures.[54, 68] The pore sizes, albeit smaller than those created by porogens, phase inversion, and electrospinning, remain in the range of hundreds of nanometers.[22, 53-65] Therefore in the fabrication of mesoporous polymers, it is critical to avoid the blowing effect from thermolysis while removing the labile phase.

Herein, we report the use of hydrolysis to prepare mesoporous PEI from triblock copolymers of polylactide-*b*-polyetherimide-*b*-polylactide (AIA). Polylactide (PLA) was chosen as the labile phase because of its susceptibility to hydrolysis. Under mild conditions of pH ~7.4 at 70 °C, PLA decomposed to water-soluble species, *i.e.*, potassium lactate, without producing any gaseous species to plasticize PEI, resulting in mesoporous PEI films with an average pore size of 24 nm.

We found that the mesoporous PEI films prepared by hydrolysis exhibited storage moduli (E') of about 1 GPa at room temperature, and glass transition temperatures ($T_g$) higher than 230 ℃ in thermodynamic tests.

## 3.3 Experimental Section

### *3.3.1 Materials*

4,4′-(4,4′-Isopropylidenediphenoxy)bis(phthalic anhydride) (*a.k.a.* 4,4'-bisphenol A dianhydride, BPADA) and *m*-phenylenediamine (mPD) were purchased from Sigma-Aldrich and purified as follows. In a nitrogen stream, the BPADA was melted at 200 ℃ and then cooled down to room temperature to eliminate moisture. The mPD was sublimated into white crystals at 70 ℃ under reduced pressure. Stannous 2-ethylhexanoate ($Sn(Oct)_2$), $_{D,L}$-lactide, *o*-dichlorobenzene (oDCB), and phosphate buffer solution (1.0 M, pH ~7.4 at 25 ℃) were purchased from Sigma-Aldrich and used as received. Deuterated chloroform ($CDCl_3$) was purchased from Cambridge Isotope Laboratories, Inc., and used as received. Dimethylformamide (DMF, HPLC grade) and lithium bromide (LiBr) were purchased from Fisher Scientific.

### *3.3.2 Instrumentation*

Proton nuclear magnetic resonance ($^1$H NMR) spectra were collected on a Varian Unity at 400 MHz in $CDCl_3$. Size exclusion chromatography (SEC) was performed on a Tosoh EcoSEC HLC-8320 equipped with a refractive index detector, using DMF containing 0.05 M of LiBr as the eluent at a flow rate of 0.5 mL/min. Thermogravimetric analysis (TGA) was performed on a TA 5500 (TA Instruments) under air atmosphere. Scanning electron microscopy (SEM) was performed on a LEO Zeiss 1550 at an acceleration voltage of 2 kV and a working distance of ~4 mm. Oxygen

plasma was conducted on a South Bay Technology PC-2000 with ultra-pure oxygen. Nitrogen adsorption isotherm was performed on a Micromeritics 3Flex Adsorption Analyzer. All the porous films were degassed at 120 ℃ for 1000 min to remove moisture. The specific surface area was calculated based on Brunauer-Emmett-Teller (BET) theory, and the pore size distribution was determined using nonlocal density functional theory (NLDFT). Dynamic mechanical analysis (DMA) was performed on a TA Q800 with a ramp rate of 3 ℃/min, a strain of 0.1% and a frequency of 1 Hz.

### *3.3.3 Synthesis of PEI-$NH_2$*

Amine-terminated PEI (PEI-$NH_2$) was synthesized via condensation polymerization (Scheme 1). In a typical synthesis of PEI-$NH_2$ with a number average molecular weight ($M_n$) of 45 kDa (denoted as PEI-45), BPADA (10000.0 mg) and mPD (2105.3 mg) were added to a three-necked round bottom flask (500 mL) equipped with a mechanical stirrer, a Dean-Stark trap, and a nitrogen inlet with a constant flow of nitrogen. Subsequently, oDCB (100 mL) was added, then the resulting slurry mixture was immersed in an oil bath at 180 ℃ and reacted for 12 h with nitrogen purging. Afterward, the amber-colored solution was heated to 230 ℃ with constant nitrogen purging for one hour to remove the solvent. The viscous product was cooled down to room temperature and then dissolved in chloroform (100 mL). The resulting solution was added dropwise into methanol (1 L). A yellowish precipitate was collected via vacuum filtration and dried at 220 ℃ overnight *in vacuo*.

### *3.3.4 Synthesis of PLA-b-PEI-b-PLA (AIA)*

AIA was synthesized via ring-opening polymerization of lactide using PEI-$NH_2$ as a macro-initiator (Scheme 1).[69] To synthesize AIA with a PLA weight fraction of 40% from PEI-45 (denoted as AIA-45), PEI-$NH_2$ (PEI-45, 500 mg) and lactide (1000 mg) were dissolved in anhydrous chloroform (20 mL) and added to a 100-mL Schlenk tube equipped with a magnetic stir bar. After degassing the solution *via* three freeze-pump-thaw cycles, $Sn(Oct)_2$ (10 mg) was added to the Schlenk tube in an argon-filled glovebox. The solution was set at 65 ℃ and reacted for 36 h. The viscous solution was cooled down to room temperature and precipitated in methanol. The resulting fine white powders were obtained *via* centrifugation and dried at 150 ℃ overnight *in vacuo*.

### *3.3.5 Preparation of AIA thin films*

AIA (500 mg) was dissolved in chloroform (10 mL). The resulting solution was poured onto a glass slide (7 cm by 7 cm), and slowly dried in a desiccator for 2 days. The resulting thin film was baked at 150 ℃ overnight *in vacuo*.

### *3.3.6 Hydrolysis of AIA thin films*

Both sides of AIA thin films were etched by oxygen plasma (2 min on each side) to remove the skin layers. The resulting films were then hydrolyzed in a phosphate solution (60 mL, 1.0 M) at 70 ℃, following a previous report.[70] After hydrolysing for 1, 3, 5, 7 and 9 days, a small portion of AIA films (~20 mg) were sampled for compositional and morphological characterizations using $^1$H NMR and SEM, respectively, to investigate the hydrolysis efficiency. After 9-day hydrolysis,

the resulting mesoporous PEI films were soaked in DI water to remove the absorbed buffer solution, and then dry at 80 ℃ overnight *in vacuo.*

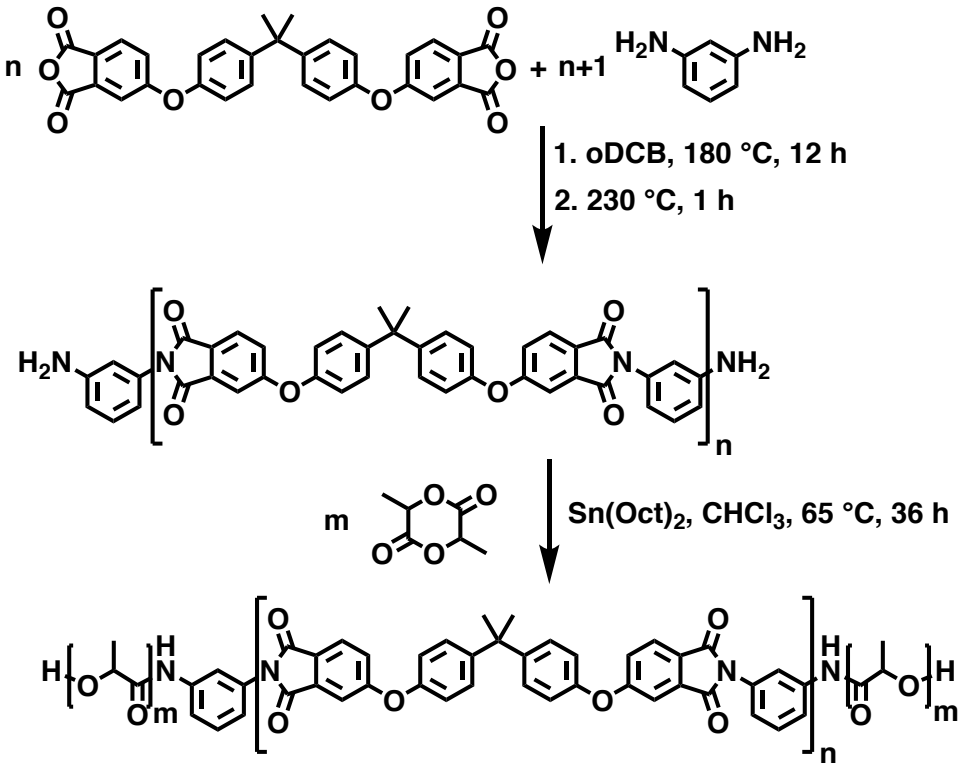


**Scheme 3.1.** Synthesis of AIA. PEI-$NH_2$ was synthesized via condensation polymerization of BPADA and mPD. The amine end groups in PEI initiated ring-opening polymerization of PLA to produce AIA triblock copolymers.

## 3.4 Results and Discussion

Polymer molecular weight dictates the mechanical performance and thus the integrity of porous thin films. To investigate the effect of molecular weight on the mechanical strength of mesoporous PEIs, we synthesized three PEI-$NH_2$ macro-initiators (Scheme 1, Table S1) with molecular weights of 45, 60 and 75 kDa (designated PEI-45, -60 and -75, respectively; Figure 3.1). The molecular structure was confirmed by $^1$H NMR (Figure 3.2a). From the three macro-initiators, we

further synthesized three AIA block copolymers with a PLA weight fraction of ~40% (designated AIA-45, -60 and -75, respectively). SEC confirmed the conversion of PEI macro-initiators to AIA triblock copolymers (Figure 3.1). The decreasing retention times from PEI-45 to PEI-75 indicated good control over the PEI molecular weights. After the polymerization of PLA, the retention time was shorter than that of the corresponding PEI, suggesting the successful incorporation of PLA onto the PEI chain ends. Noteworthy, the AIA SEC traces had smaller full widths at half maximum (FWHM) than the corresponding PEI macro-initiators. The smaller FWHM was a signature of the intrinsically better-controlled dispersity by ring-opening polymerization than condensation polymerization.

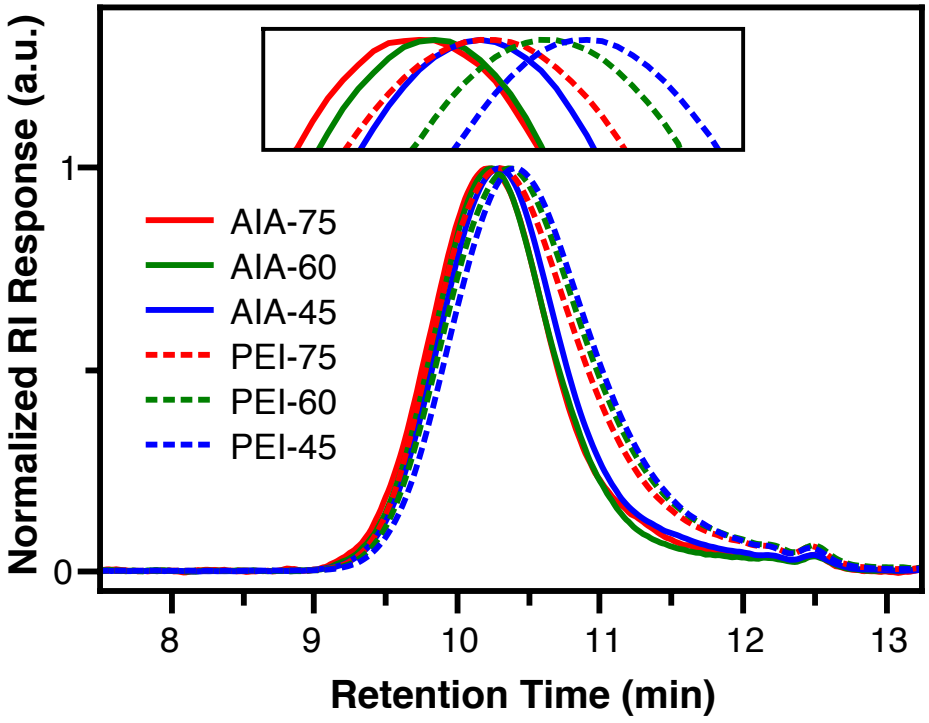


**Figure 3.1.** SEC traces of AIA and the corresponding PEI macro-initiators. The shorter retention times of AIA than those of the corresponding PEI macro-initiator confirm the successful synthesis of AIA.

The weight fraction of PLA in AIA was calculated according to $^1$H NMR spectrum (*i.e.*, AIA-45, Figure 3.2b). Peak o at ~5.17 ppm was assigned to the methines in PLA repeating units, and peak e' at ~7.14 ppm was assigned to the aromatic protons near the ether moieties in PEI repeating units. All other peaks were assigned, confirming the structure of block copolymer (Figure 3.2a). The weight fraction of PLA in AIA was calculated according to Equation 3.1.

$$\varphi_{PLA} = \frac{I_o \times M_{PLA}}{I_o \times M_{PLA} + I_{e'}/4 \times M_{PEI}} \qquad (3.1)$$

where $\varphi_{PLA}$ is the weight fraction of PLA in AIA; $I_o$ and $I_{e'}$ are the integral values of peak o and e', respectively; $M_{PLA}$ (72.1 Da) and $M_{PEI}$ (592.6 Da) are the molecular weights of PLA and PEI repeating units. The integral ratio of peak o and peak e' was measured to be 130:100, corresponding to a $\varphi_{PLA}$ of 38.8%. Similarly, $\varphi_{PLA}$ is 38.4% for AIA-60, and 38.2% for AIA-75.

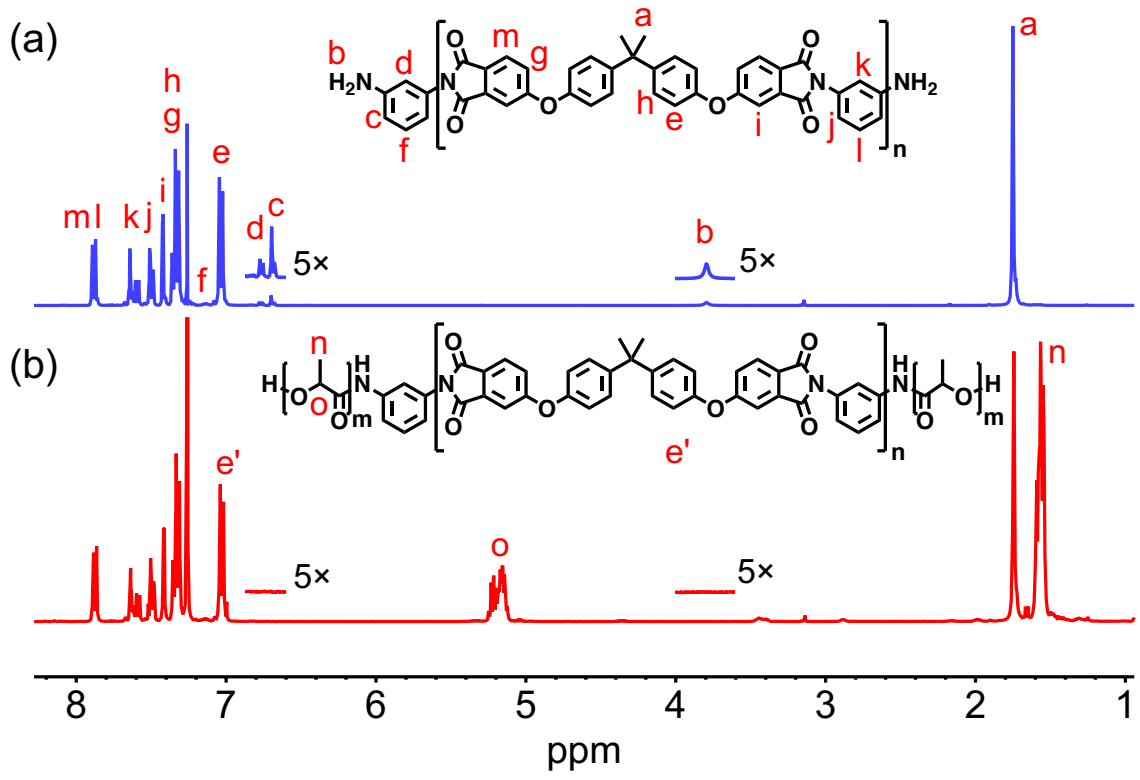


**Figure 3.2.** Representative $^1$H NMR spectra of (a) PEI-45 and (b) AIA-45. According to the integrated areas of peak o and e', the weight fraction of PLA in AIA was 38.8%.

The weight fraction of PLA in AIA was also confirmed by TGA (Figure 3.3). The TGA traces of AIA exhibited two distinct weight loss regimes: the first regime (180 - 300 °C) was attributed to the thermal degradation of PLA,[71] while the second one (above 450 °C) was the decomposition of PEI.[72] The weight losses at 400 °C after PLA degradation were measured to be 39.8%, 38.1% and 38.0% for AIA-45, -60 and -75, respectively, in agreement with the $\varphi_{PLA}$ determined from $^1$H NMR. Noteworthy, the thermal decomposition of PLA overlapped the glass transition of PEI (typically ~217 °C[66]), which ruled out the use of thermolysis to create uniform porous structures. For example, AIA-45 had a 5% weight loss decomposition temperature ($T_{d,5\%}$) of 224 °C. If this temperature was used to thermalize PLA to create pores, the decomposition gaseous species would blow the softened PEI matrix to create nonuniform macropores, similar to the thermolysis process in previous reports.[54, 68]

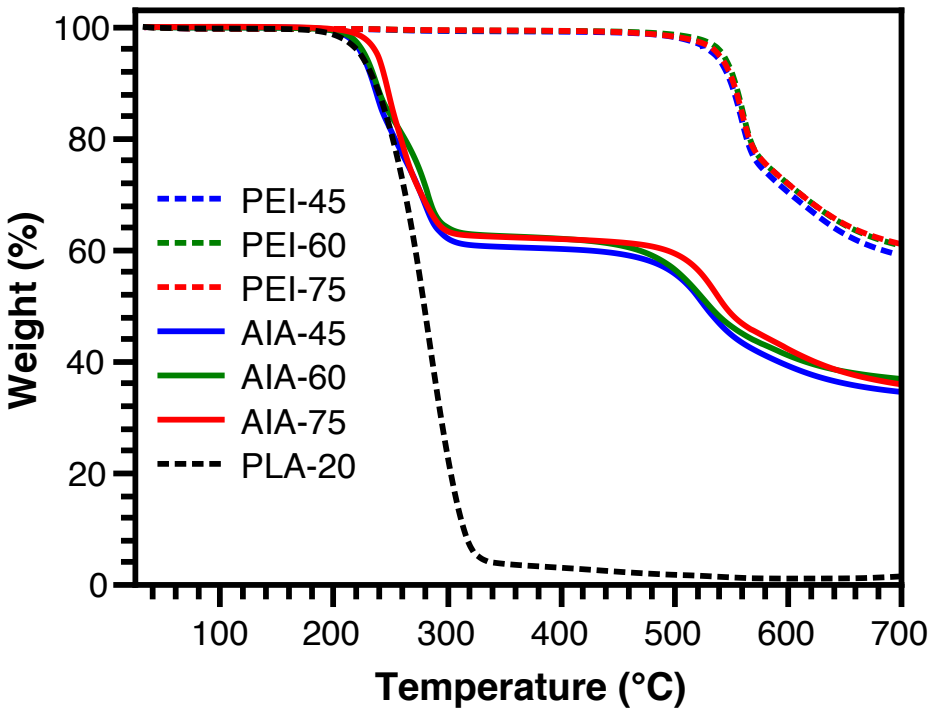


**Figure 3.3.** TGA of AIA, PEI and PLA. The first and second weight loss of AIA at 180 – 300 °C and above 450 °C corresponded to the thermal decomposition of PLA and PEI, respectively.

According to the weight loss, the weight fractions of PLA in AIA-45, -60 and -75 were 39.8%, 38.1% and 38.0%, respectively.

Instead of thermolysis, we have used hydrolysis to prepare mesoporous PEI thin films. AIA triblock copolymers formed thin films after solution casting on a glass slide. Subjected to oxygen plasma and subsequent hydrolysis in a phosphate solution, the microstructures of AIA films changed as the hydrolysis time was increased. The oxygen plasma treatment removed the skin layers of the films and facilitated the subsequent hydrolysis. After oxygen plasma etching, for instance, the AIA-45 thin film exhibited a rough surface due to the different etching rates of PLA and PEI. The PLA phase had a faster etching rate by oxygen plasma thus appeared dark (Figure 3.4). After hydrolysis for 1 and 5 days, the PLA phase was further etched and developed into mesopores. After 9 days, the hydrolysis completed, generating well developed mesoporous structures (Figure 3.4 and Figure S3.6).

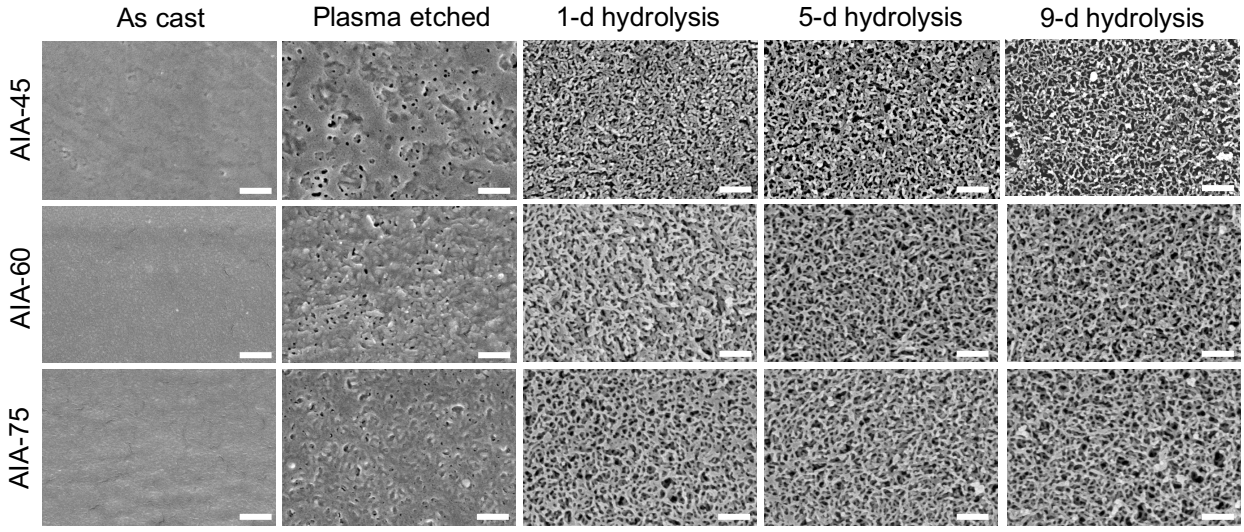


**Figure 3.4.** Morphological evolution of AIA films. All scale bars, 300 nm.

The pore sizes of mesoporous PEI (MP) films were further characterized using nitrogen sorption. Based on the isotherms, the BET surface areas of MP-45, -60 and -75 were 36, 42 and 61 $m^2$ $g^{-1}$, respectively (Figure 3.5a). All MP films exhibited an average pore width of 24 nm (Figure 3.5b). This mesoscale pore size is prominently smaller than the pore sizes of conventional porous polyimides,[22, 53-65] validating our hypothesis that the hydrolysis process avoids the blowing effect and creates uniform mesopores.

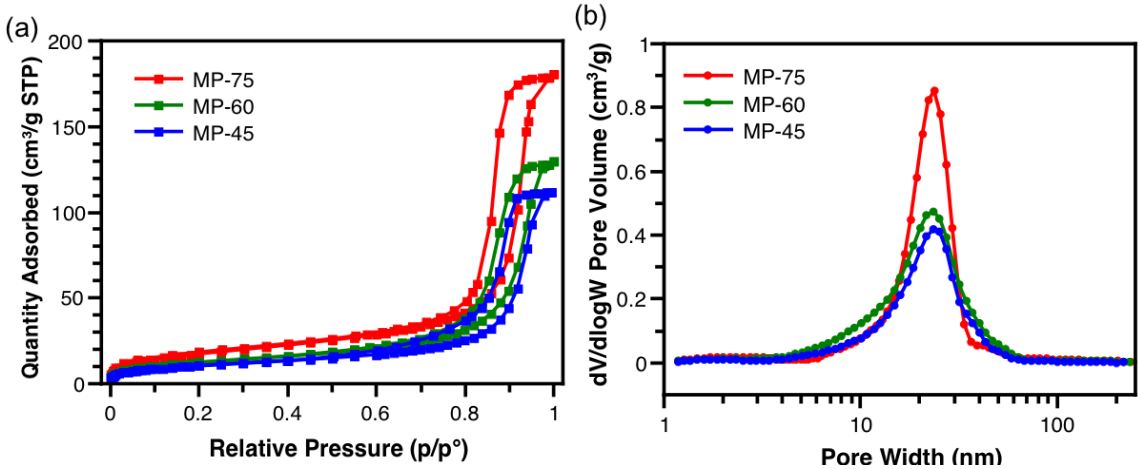


**Figure 3.5.** Nitrogen sorption isotherms and pore size distributions of mesoporous PEI films. (a) The isotherms show specific surface areas of 36, 42 and 61 $m^2/g$ for MP-45, -60 and -75, respectively. (b) The pore size distributions display an average pore width of 24 nm for all MP films.

The hydrolysis rate of PLA in AIA was investigated by measuring the amount of PLA residue using $^1$H NMR after various lengths of hydrolysis time in phosphate buffer solutions (Figure 3.6a). PLA showed a fast hydrolysis rate in the first 3 days. For instance, the PLA weight fraction in AIA-45 decreased from 38.8% to 13.0% (Figure 3.6b). After hydrolysing for 9 days, the mesopores were well developed, and the weight fractions of residual PLA stabilized at 8.8%, 7.4% and 7.0% for AIA-45, -60 and -75, respectively.

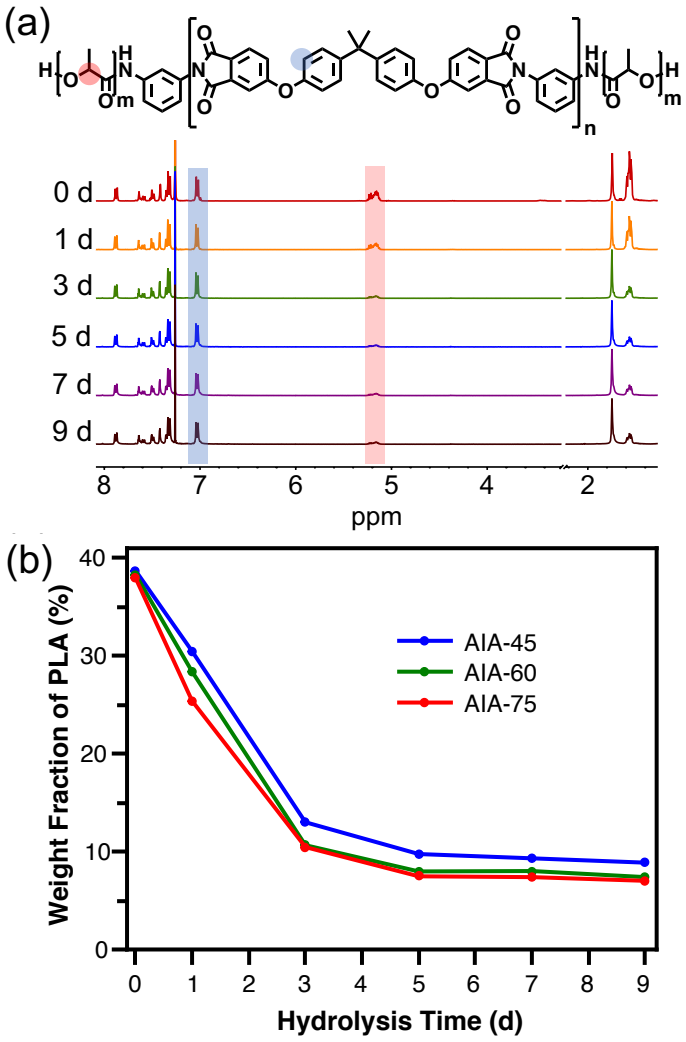


**Figure 3.6.** Hydrolysis rate of AIA films in phosphate buffer solution. (a) $^{1}$H NMR spectra display a decreasing signal of PLA repeating units in AIA-45. (b) The PLA weight fractions in all AIA films were below 9% after hydrolysis for 9 days.

After hydrolysis, the thermomechanical properties of mesoporous PEI (MP) films were evaluated using DMA. All MP films exhibited high storage moduli (E') and glass transition temperatures ($T_g$). At 30 °C, MP-45, -60 and -75 from AIA-45, -60, and -75 precursor films showed E' of 978, 1127 and 1216 MPa, respectively (Figure 3.7a). The peaks of loss moduli (E'') at 217,

223 and 227 ℃ indicated the softening of PEI (Figure 3.7b). Based on *Tan(δ)*, the glass transition temperatures were 233, 234 and 236 ℃ for MP-45, -60 and -75, respectively (Figure 3.7c).

To prepare mesoporous PEI films via hydrolysis, three factors are essential. First, appropriate sacrificial domain sizes are an important starting point to create mesopores. In the case of using polymer blends or polymer/salt mixtures to prepare porous structures, the thermodynamically driven macrophase separation inevitably produces macro-scale domains that eventually lead to macropores after removing the sacrificial phase.[38-43] In contrast, block copolymer-based microphase separation ensures the formation of mesoscale domains, which ultimately create mesoporous structures.[66] Nevertheless, it is critical to remove the sacrificial phase without damaging the polymer matrix. Thus, the second important factor is well-controlled removal of the sacrificial phase. In previous reports,[22, 53-66, 68] thermolysis of polyimide-based block copolymers decomposes the sacrificial phase and produces gaseous species, which plasticize the softened polyimide matrix, and worse, blow the resulting structures into macropores. Conversely, in this work, hydrolysis of PLA via mild chain-scission removes the sacrificial phase without producing gas or softening the PEI matrix, avoiding the blowing effect that distorts and enlarges the mesopores. Third, the polymer matrix must be mechanically strong to support the mesoporous structure. After removing the sacrificial phase, the increasing pore volume reduces the overall mechanical strength of the films. A systematic investigation of the $M_n$ of PEI and the resultant porous structures reveals that the PEI with $M_n$ of 45 kDa and higher formed mesoporous PEI with good thermomechanical performance. Porous films made from AIA with a $M_n$ of the PEI block lower than 30 kDa appeared fairly brittle and the porous structures collapsed after complete hydrolysis (Table S3.1, Figure S3.1-S3.5).

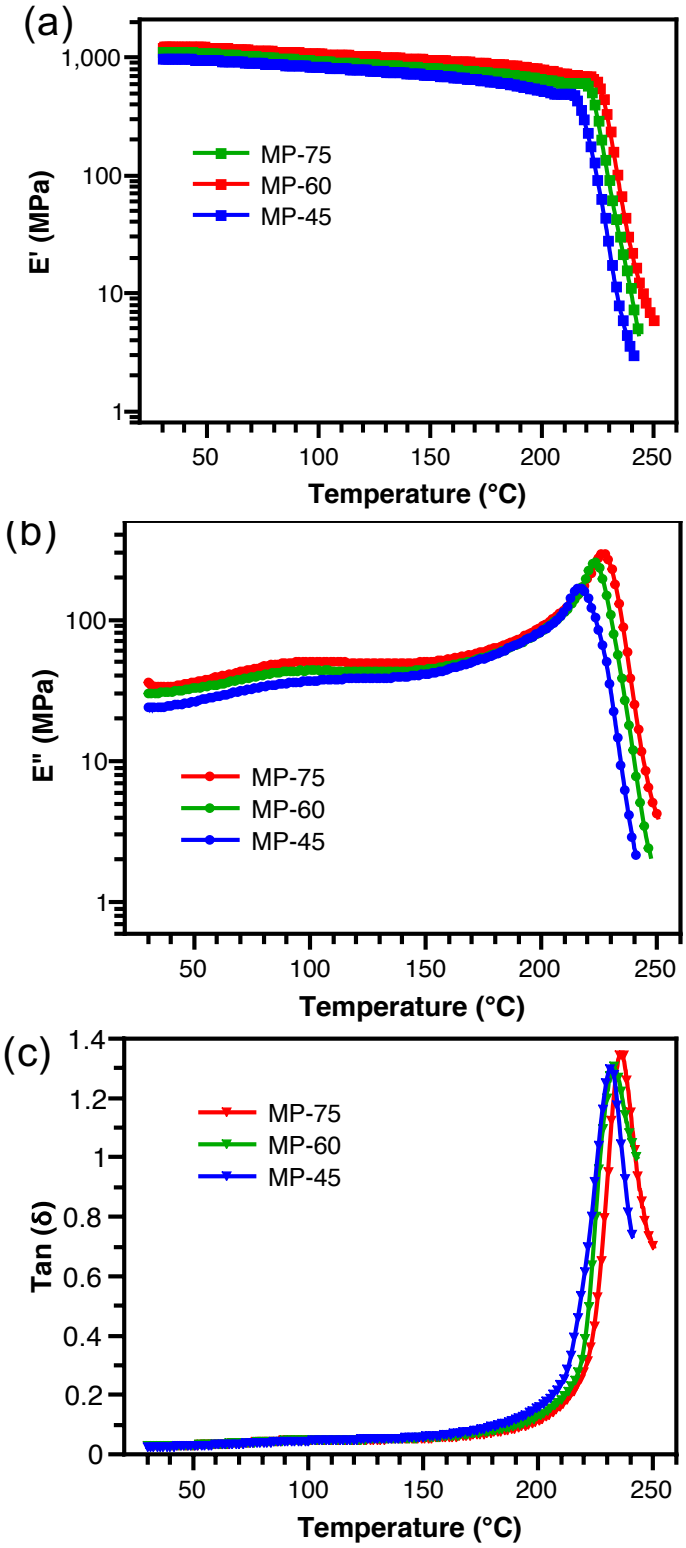


**Figure 3.7.** Dynamic mechanical analysis of mesoporous PEI films after hydrolysis: (a) storage moduli, (b) loss moduli and (c) tan (δ) of MP-45, -60 and -75.

## 3.5 Conclusions

In this work, we produced mesoporous polyetherimide thin films with pore sizes of 24 nm via hydrolysis of AIA triblock copolymers, which were synthesized by growing PLA peripheral blocks from PEI-$NH_2$ macro-initiators. The SEC retention time decreased after converting PEI-$NH_2$ macro-initiators to AIA. The weight fraction of PLA in AIA was confirmed to be ~40% by both $^1$H NMR and TGA. AIA was solution-cast into films. After oxygen plasma and hydrolysis to remove the PLA phase, AIA thin films became porous. The mesoporous PEI films exhibit outstanding thermomechanical performance with E' of ~1 GPa at RT and $T_g$ above 230 °C. This work presents an effective strategy to prepare mesoporous PEI thin films. The hydrolysis method is adaptable to other high-performance polymers. The mesoporous thin films are expected to find applications in various fields such as battery separators to suppress dendrites in lithium batteries.

## 3.6 Supporting Information

**Table S3.1** Compositions of PLA-*b*-PEI-*b*-PLA (AIA) block copolymers.

| Entry | $M_n$ of PEI (kDa) | $\varphi_{PLA}$ by $^1$H NMR (%) | $\varphi_{PLA}$ by TGA (%) |
|---|---|---|---|
| AIA-12 | 11.5 | 38.8 | 38.5 |
| AIA-16 | 16.1 | 37.5 | 37.3 |
| AIA-20 | 20.4 | 37.6 | 37.3 |
| AIA-25 | 25.4 | 37.8 | 37.3 |
| AIA-30 | 30.3 | 37.2 | 36.6 |
| AIA-45 | 44.6 | 38.8 | 39.8 |
| AIA-60 | 60.0 | 38.4 | 38.1 |
| AIA-75 | 74.8 | 38.2 | 38.0 |

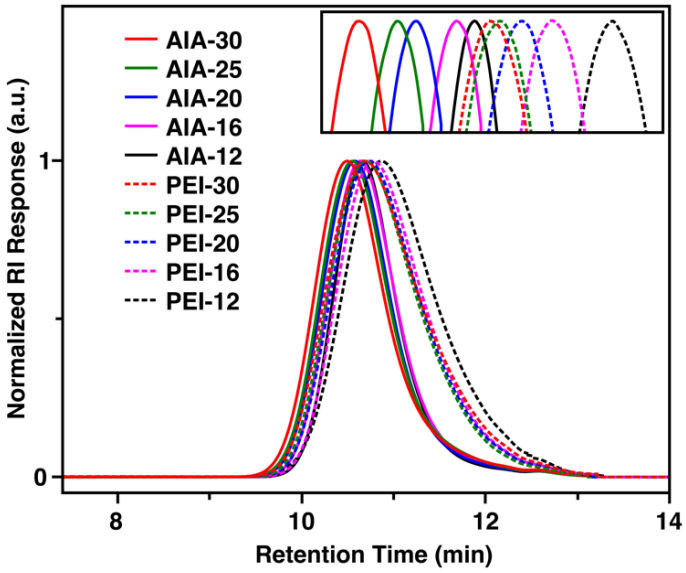


**Figure S3.1.** SEC traces of a series of low-molecular-weight AIA and the corresponding PEI macro-initiators. The shorter retention times of AIA than those of the corresponding PEI macro-initiator confirm the successful synthesis of AIA.

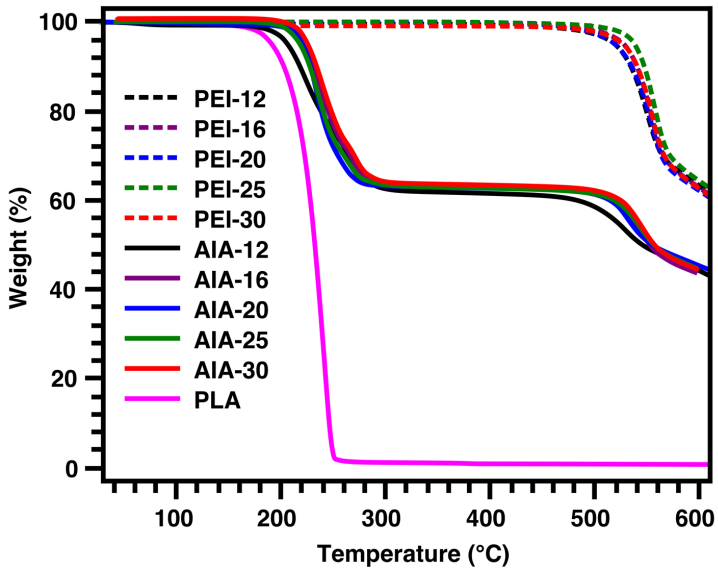


**Figure S3.2.** TGA of a series of low-molecular-weight AIA, PEI and PLA. The first and second weight loss of AIA at 180 – 300 ℃ and above 450 ℃ were assigned to the thermal decomposition of PLA and PEI, respectively. According to the weight loss, the weight fractions of PLA in AIA was approximately 40%.

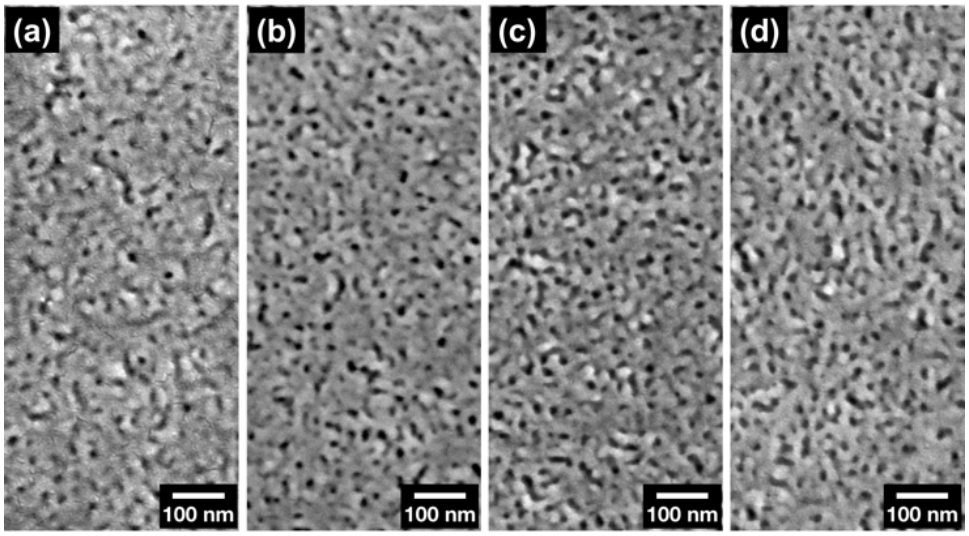


**Figure S3.3.** SEM images of oxygen-plasma-etched AIA-30 hydrolyzed for (a) 0, (b) 1, (c) 3 and (d) 10 days.

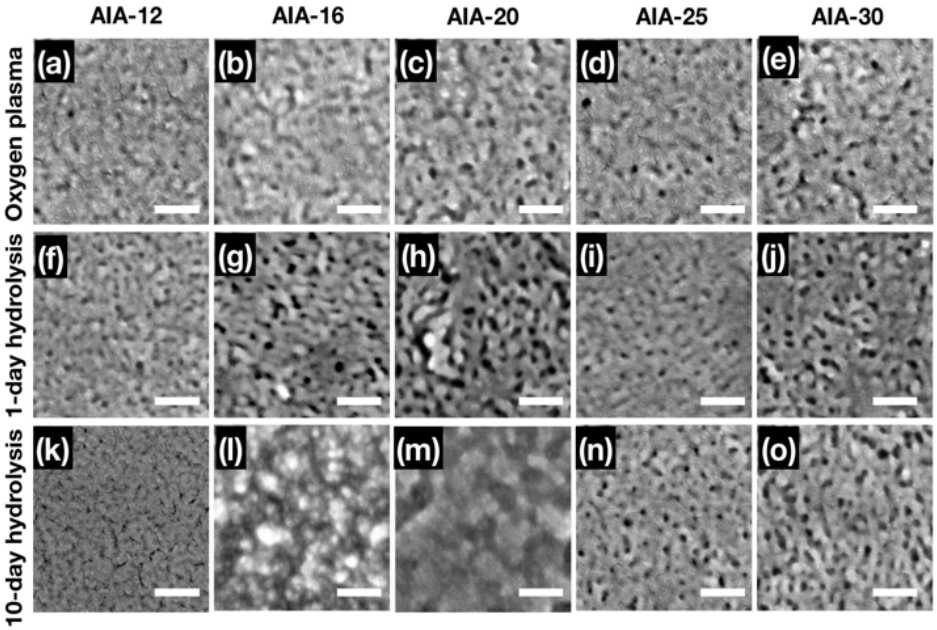


**Figure S3.4.** SEM images of hydrolyzed AIA. (a, f, k) AIA-12, (b, g, l) AIA-16, (c, h, m) AIA-20, (d, i, n) AIA-25, and (e, j, o) AIA-30 triblock copolymers (a-e) after oxygen plasma etching, (f-j) after hydrolysis for 1 d, and (k-o) after hydrolysis for 10 d. After 10-d hydrolysis, AIA-12,

AIA-16, and AIA-20 displayed collapsed structures, but AIA-25 and AIA-30 partially retained the mesoporous structures. The scale bars represent 100 nm.

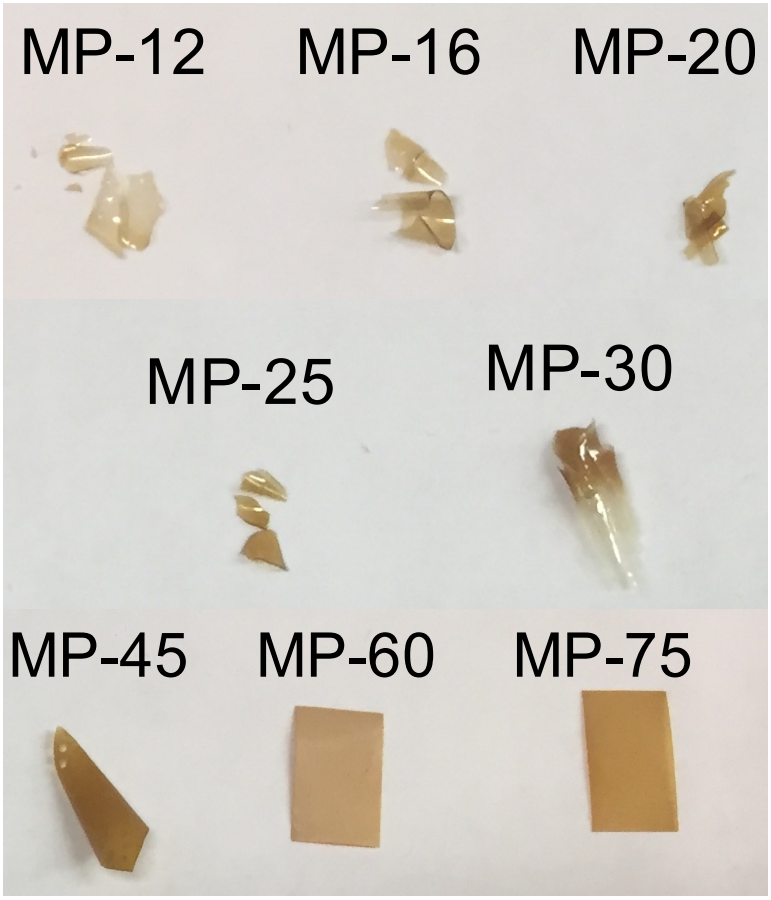


**Figure S3.5.** Photographs of mesoporous polyetherimide (MP) films after 9-day hydrolysis. If the molecular weight of constituent polyetherimide was lower than 45 kDa, the film appeared fairly brittle, i.e., MP-12, -16, -20, -25 and 30. In contrast, MP-45, -60 and -75 exhibited good structural integrity and mechanical performance.

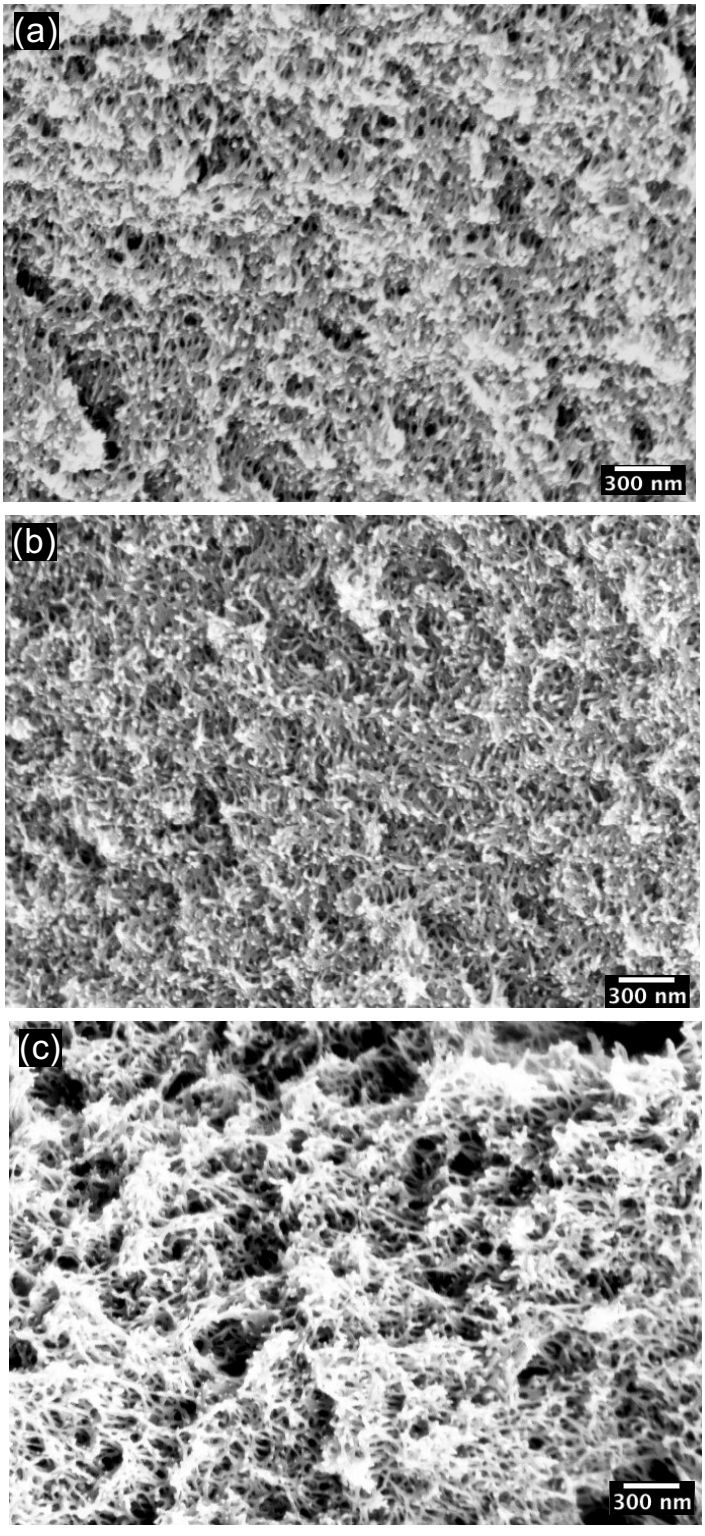


**Figure S3.6.** Cross sections of mesoporous PEI films after 9-day hydrolysis. The morphologies of (a)MP-45, (b) MP-60 and (c) MP-75 are displayed.

## 3.7 Acknowledgements

This material is based upon work supported by the National Science Foundation under Grant No. DMR-1752611 and CMMI-1914565, and the American Chemical Society Petroleum Research Foundation Doctoral New Investigator Award. The authors acknowledge the use of facilities in Nanoscale Characterization and Fabrication Laboratory (NCFL) at the Institute for Critical Technology and Applied Science (ICTAS), Virginia Tech.

## 3.8 References

1. Li, G.; Wang, Z., Microporous Polyimides with Uniform Pores for Adsorption and Separation of $CO_2$ Gas and Organic Vapors. *Macromolecules* **2013**, *46*, 3058-3066.

2. Niwa, M.; Kawakami, H.; Kanamori, T.; Shinbo, T.; Kaito, A.; Nagaoka, S., Gas Separator of Asymmetric 6FDA Polyimide Membrane with Oriented Surface Skin Layer. *Macromolecules* **2001**, *34*, 9039-9044.

3. Swaidan, R.; Al-Saeedi, M.; Ghanem, B.; Litwiller, E.; Pinnau, I., Rational Design of Intrinsically Ultramicroporous Polyimides Containing Bridgehead-Substituted Triptycene for Highly Selective and Permeable Gas Separation Membranes. *Macromolecules* **2014**, *47*, 5104-5114.

4. Swaidan, R.; Ghanem, B.; Al-Saeedi, M.; Litwiller, E.; Pinnau, I., Role of Intrachain Rigidity in the Plasticization of Intrinsically Microporous Triptycene-Based Polyimide Membranes in Mixed-Gas $CO_2/CH_4$ Separations. *Macromolecules* **2014**, *47*, 7453-7462.

5. Iwase, M.; Sannomiya, A.; Nagaoka, S.; Suzuki, Y.; Iwaki, M.; Kawakami, H., Gas Permeation Properties of Asymmetric Polyimide Membranes with Partially Carbonized Skin Layer. *Macromolecules* **2004**, *37*, 6892-6897.

6. Zhuang, Y.; Seong, J. G.; Do, Y. S.; Jo, H. J.; Cui, Z.; Lee, J.; Lee, Y. M.; Guiver, M. D., Intrinsically Microporous Soluble Polyimides Incorporating Tröger's Base for Membrane Gas Separation. *Macromolecules* **2014**, *47*, 3254-3262.

7. Rao, K. V.; Haldar, R.; Maji, T. K.; George, S. J., Porous Polyimides from Polycyclic Aromatic Linkers: Selective $CO_2$ Capture and Hydrogen Storage. *Polymer* **2014**, *55*, 1452-1458.

8. Liebl, M. R.; Senker, J., Microporous Functionalized Triazine-Based Polyimides with High $CO_2$ capture Capacity. *Chem. Mater.* **2013**, *25*, 970-980.

9. Farha, O. K.; Bae, Y. S.; Hauser, B. G.; Spokoyny, A. M.; Snurr, R. Q.; Mirkin, C. A.; Hupp, J. T., Chemical Reduction of a Diimide Based Porous Polymer for Selective Uptake of Carbon Dioxide Versus Methane. *Chem. Commun. (Camb)* **2010**, *46*, 1056-8.

10. Yao, H.; Zhang, N.; Song, N.; Shen, K.; Huo, P.; Zhu, S.; Zhang, Y.; Guan, S., Microporous Polyimide Networks Constructed through a Two-Step Polymerization Approach, and Their Carbon Dioxide Adsorption Performance. *Polym. Chem.* **2017**, *8*, 1298-1305.

11. Yan, J.; Zhang, B.; Wang, Z., Monodispersed Ultramicroporous Semi-Cycloaliphatic Polyimides for the Highly Efficient Adsorption of $CO_2$, $H_2$ and Organic Vapors. *Polym. Chem.* **2016**, *7*, 7295-7303.

12. Song, N.; Wang, T.; Yao, H.; Ma, T.; Shi, K.; Tian, Y.; Zou, Y.; Zhu, S.; Zhang, Y.; Guan, S., Construction and Carbon Dioxide Capture of Microporous Polymer Networks with High Surface Area Based on Cross-Linkable Linear Polyimides. *Polym. Chem.* **2019**, *10*, 4611-4620.

13. Shaplov, A. S.; Morozova, S. M.; Lozinskaya, E. I.; Vlasov, P. S.; Gouveia, A. S. L.; Tomé, L. C.; Marrucho, I. M.; Vygodskii, Y. S., Turning into Poly(ionic liquid)s as a Tool for Polyimide Modification: Synthesis, Characterization and $CO_2$ Separation Properties. *Polym. Chem.* **2016**, *7*, 580-591.

14. Zhang, J.; Han, X.; Yue, C.; Liu, D.; Lin, Z.; Sun, Y.; Chen, L.; Pang, J.; Jiang, Z., Synthesis of Novel Co(II) Complexed Bipyrimidine Polyimide and Preparation of Thin Film Composite Membranes. *Polym. Chem.* **2020**, *11*, 5057-5066.

15. Pan, Z.; Zhang, X.; Wang, X., Adsorption of Acid Orange 10 on Cross-Linked Porous Polyimide. *SN Appl. Sci.* **2019**, *1*, 239-248.

16. Zhao, G.; Huang, X.; Tang, Z.; Huang, Q.; Niu, F.; Wang, X., Polymer-Based Nanocomposites for Heavy Metal Ions Removal from Aqueous Solution: A Review. *Polym. Chem.* **2018**, *9*, 3562-3582.

17. Zhang, D.; Wang, T.; Wang, Q.; Wang, C., Selectively Enhanced Oil Retention of Porous Polyimide Bearing Materials by Direct Chemical Modification. *J. Appl. Polym. Sci.* **2017**, *134*, 45106-45113.

18. Tian, L.; Zhang, C.; He, X.; Guo, Y.; Qiao, M.; Gu, J.; Zhang, Q., Novel Reusable Porous Polyimide Fibers for Hot-Oil Adsorption. *J. Hazard. Mater.* **2017**, *340*, 67-76.

19. Topuz, F.; Abdulhamid, M. A.; Nunes, S. P.; Szekely, G., Hierarchically Porous Electrospun Nanofibrous Mats Produced from Intrinsically Microporous Fluorinated Polyimide for the Removal of Oils and Non-Polar Solvents. *Environ. Sci. Nano* **2020**, *7*, 1365-1372.

20. Zhu, W.; Wang, X.; Li, T.; Shen, R.; Hao, S.-J.; Li, Y.; Wang, Q.; Li, Z.; Gu, Z.-G., Porphyrin-Based Porous Polyimide Polymer/Pd Nanoparticle Composites as Efficient Catalysts for Suzuki-Miyaura Coupling Reactions. *Polym. Chem.* **2018**, *9*, 1430-1438.

21. Jin, Y.; Tang, J.; Hu, J.; Han, X.; Shang, Y.; Liu, H., One-Step Fabrication of Ultralow Dielectric Polyimide Films Consisting of Size-Controlled Mesoporous Nanoparticles. *Colloids Surf. A* **2011**, *392*, 178-186.

22. Ju, J.; Wang, Q.; Wang, T.; Wang, C., Low Dielectric, Nanoporous Fluorinated Polyimide Films Prepared from Pcl-Pi-Pcl Triblock Copolymer Using Retro-Diels-Alder Reaction. *J. Colloid Interface Sci.* **2013**, *404*, 36-41.

23. Meador, M. A.; Aleman, C. R.; Hanson, K.; Ramirez, N.; Vivod, S. L.; Wilmoth, N.; McCorkle, L., Polyimide Aerogels with Amide Cross-Links: A Low Cost Alternative for Mechanically Strong Polymer Aerogels. *ACS Appl. Mater. Interfaces* **2015**, *7*, 1240-1249.

24. Meador, M. A. B.; Wright, S.; Sandberg, A.; Nguyen, B. N.; Van Keuls, F. W.; Mueller, C. H.; Rodríguez-Solís, R.; Miranda, F. A., Low Dielectric Polyimide Aerogels as Substrates for Lightweight Patch Antennas. *ACS Appl. Mater. Interfaces* **2012**, *4*, 6346-6353.

25. Carter, K. R.; Cha, H. J.; Dipietro, R. A.; Hawker, C. J.; Hedrick, J. L.; Labadie, J. W.; McGrath, J. E.; Russell, T. P.; Sanchez, M. I.; Swanson, S. A.; Volksen, W.; Yoon, D. Y., Polyimide Nanofoams for Low Dielectric Applications. *MRS Proceedings* **2011**, *381*, 79-91.

26. Chen, D.; Liu, C.; Tang, J.; Luo, L.; Yu, G., Fluorescent Porous Organic Polymers. *Polym. Chem.* **2019**, *10*, 1168-1181.

27. Shimizu, Y.; Kanamura, K., Effect of Pore Size in Three Dimensionally Ordered Macroporous Polyimide Separator on Lithium Deposition/Dissolution Behavior. *J. Electrochem. Soc.* **2019**, *166*, A754-A761.

28. Jiang, W.; Liu, Z.; Kong, Q.; Yao, J.; Zhang, C.; Han, P.; Cui, G., A High Temperature Operating Nanofibrous Polyimide Separator in Li-Ion Battery. *Solid State Ion.* **2013**, *232*, 44-48.

29. Lee, J.; Lee, C.-L.; Park, K.; Kim, I.-D., Synthesis of an $Al_2O_3$-Coated Polyimide Nanofiber Mat and Its Electrochemical Characteristics as a Separator for Lithium Ion Batteries. *J. Power Sources* **2014**, *248*, 1211-1217.

30. Zhou, Z.; Zhao, T.; Lu, X.; Cao, H.; Zha, X.; Zhou, Z., Functionalized Polyimide Separators Enable High Performance Lithium Sulfur Batteries at Elevated Temperature. *J. Power Sources* **2018**, *396*, 542-550.

31. Maeyoshi, Y.; Ding, D.; Kubota, M.; Ueda, H.; Abe, K.; Kanamura, K.; Abe, H., Long-Term Stable Lithium Metal Anode in Highly Concentrated Sulfolane-Based Electrolytes with Ultrafine Porous Polyimide Separator. *ACS Appl. Mater. Interfaces* **2019**, *11*, 25833-25843.

32. Nagasaki, M.; Kanamura, K., High-Performance Lithium Metal Rechargeable Battery Using an Ultrafine Porous Polyimide Separator with Three-Dimensionally Ordered Macroporous Structure. *ACS Appl. Energy Mater.* **2019**, *2*, 3896-3903.

33. Takekoshi, T., Polyimides. In *New Polymer Materials*, 1 ed.; Springer: Berlin Heidelberg, 1990; Vol. 94, pp 1-25.

34. Luo, Y.; Li, B.; Liang, L.; Tan, B., Synthesis of Cost-Effective Porous Polyimides and Their Gas Storage Properties. *Chem. Commun. (Camb)* **2011**, *47*, 7704-6.

35. Wang, Q.; Wang, C.; Wang, T., Controllable Low Dielectric Porous Polyimide Films Templated by Silica Microspheres: Microstructure, Formation Mechanism, and Properties. *J. Colloid Interface Sci.* **2013**, *389*, 99-105.

36. Wang, H.; Wang, T.; Yang, S.; Fan, L., Preparation of Thermal Stable Porous Polyimide Membranes by Phase Inversion Process for Lithium-Ion Battery. *Polymer* **2013**, *54*, 6339-6348.

37. Munakata, H.; Yamamoto, D.; Kanamura, K., Three-Dimensionally Ordered Macroporous Polyimide Composite Membrane with Controlled Pore Size for Direct Methanol Fuel Cells. *J. Power Sources* **2008**, *178*, 596-602.

38. Li, Z.; Zou, H.; Liu, P., Morphology and Properties of Porous Polyimide Films Prepared through Thermally Induced Phase Separation. *RSC Adv.* **2015**, *5*, 37837-37842.

39. Xiao, J.-m.; Shang, X.-c.; Qin, L.-p., A New Route of Fabricating Porous Polyimide Membranes. *Int. J. Miner. Metall. Mater.* **2010**, *17*, 782-785.

40. Chisca, S.; Sava, I.; Bruma, M., Porous Polyimide Films Obtained by Using Lithium Chloride as Pore-Forming Agent. *Polym. Int.* **2013**, *62*, 1634-1643.

41. Taki, K.; Hosokawa, K.; Takagi, S.; Mabuchi, H.; Ohshima, M., Rapid Production of Ultralow Dielectric Constant Porous Polyimide Films via $CO_2$-Tert-Amine Zwitterion-Induced Phase Separation and Subsequent Photopolymerization. *Macromolecules* **2013**, *46*, 2275-2281.

42. Chen, Z.; Zhu, D.; Tong, F.; Lu, X.; Lu, Q., Low Dielectric Constant Polyimide Hybrid Films Prepared by in situ Blow-Balloon Method. *ACS Appl. Polym. Mater.* **2019**, *1*, 2189-2196.

43. Zhou, H.-Z.; Zhan, M.-S.; Wang, K.; Liu, X.-Y., Preparation of Porous Polyimide Films by Selective Decomposition of Poly(methyl methacrylate) from PI/PMMA-Blended Films. *High Perform. Polym.* **2012**, *25*, 33-41.

44. Choi, J.; Yang, K.; Bae, H. S.; Phiri, I.; Ahn, H. J.; Won, J. C.; Lee, Y. M.; Kim, Y. H.; Ryou, M. H., Highly Stable Porous Polyimide Sponge as a Separator for Lithium-Metal Secondary Batteries. *Nanomaterials (Basel)* **2020**, *10*, 1976.

45. Liu, M.; Wang, Y.; Ji, J.; Chang, X.; Xu, Q.; Liu, X.; Qin, J., A Facile Method to Fabricate the Polyimide Aerogels with Controllable Microstructure by Freeze-Drying. *Mater. Lett.* **2020**, *267*, 127558.

46. Kanehashi, S.; Sato, S.; Nagai, K., Synthesis and Gas Permeability of Hyperbranched and Cross-Linked Polyimide Membranes. In *Membrane Gas Separation*, 1 ed.; Yampolskii, Y.; Freeman, B., Eds. John Wiley and Sons: 2010; pp 1-27.

47. Liu, X.-Y.; Zhan, M.-S.; Wang, K., Preparation and Characterization of Electromagnetic Interference Shielding Polyimide Foam. *J. Appl. Polym. Sci.* **2013**, *127*, 4129-4137.

48. Hernández-Guerrero, M.; Stenzel, M. H., Honeycomb Structured Polymer Films Via Breath Figures. *Polym. Chem.* **2012**, *3*, 563-577.

49. Ren, Y.; Lam, D. C. C., Properties and Microstructures of Low-Temperature-Processable Ultralow-Dielectric Porous Polyimide Films. *J. Electron. Mater.* **2008**, *37*, 955-961.

50. Taketani, Y.; Nagaoka, S.; Kawakami, H., Fabrication of Three-Dimensionally Ordered Microporous Membrane by Wet Phase Separation. *J. Appl. Polym. Sci.* **2004**, *92*, 3016-3021.

51. Wang, L.; Deng, N.; Fan, L.; Wang, L.; Wang, G.; Kang, W.; Cheng, B., A Novel Hot-Pressed Electrospun Polyimide Separator for Lithium-Sulfur Batteries. *Mater. Lett.* **2018**, *233*, 224-227.

52. Jiang, S.; Chen, Y.; Duan, G.; Mei, C.; Greiner, A.; Agarwal, S., Electrospun Nanofiber Reinforced Composites: A Review. *Polym. Chem.* **2018**, *9*, 2685-2720.

53. Hedrick, J. L.; Carter, K.; Sanchez, M.; Pietro, R. D.; Swanson, S., Crosslinked Polyimide Foams Derived from Poly(imide-propylene oxide) Copolymers. *Macromol. Chem. Phys.* **1997**, *198*, 549-559.

54. Hedrick, J. L.; Hawker, C. J.; DiPietro, R.; Jérôme, R.; Charlier, Y., The Use of Styrenic Copolymers to Generate Polyimide Nanofoams. *Polymer* **1995**, *36*, 4855-4866.

55. Hedrick, J. L.; DiPietro, R.; Plummer, C. J. G.; Hilborn, J.; Jérôme, R., Polyimide Foams Derived from a High $T_g$ Polyimide with Grafted Poly(α-methylstyrene). *Polymer* **1996**, *37*, 5229-5236.

56. Charlier, Y.; Hedrick, J. L.; Russell, T. P.; Swanson, S.; Sanchez, M.; Jérôme, R., Crosslinked Polyimide Foams Derived from Pyromellitic Dianhydride and 1,1-Bis(4-aminophenyl)-1-phenyl-2,2,3-trifluoroethane with Poly(α-methylstyrene). *Polymer* **1995**, *36*, 1315-1320.

57. Wang, L.; Lu, J.; Liu, M.; Lin, L.; Li, J., Preparation of Porous Polyimide Microspheres by Thermal Degradation of Block Copolymers. *Particuology* **2014**, *14*, 63-70.

58. Hedrick, J. L.; Russell, T. P.; Labadie, J.; Lucas, M.; Swanson, S., High Temperature Nanofoams Derived from Rigid and Semi-Rigid Polyimides. *Polymer* **1995**, *36*, 2685-2697.

59. Chung, C.-M.; Lee, J.-H.; Cho, S.-Y.; Kim, J.-G.; Moon, S.-Y., Preparation of Porous Thin Films of a Partially Aliphatic Polyimide. *J. Appl. Polym. Sci.* **2006**, *101*, 532-538.

60. Charlier, Y.; Hedrick, J.; Volksen, W., High Temperature Polymer Nanofoams Based on Amorphous, High $T_g$ Polyimides. *Polymer* **1995**, *36*, 987-1002.

61. Carter, K. R.; DiPietro, R. A.; Sanchez, M. I.; Swanson, S. A., Nanoporous Polyimides Derived from Highly Fluorinated Polyimide/Poly(propylene oxide) Copolymers. *Chem. Mater.* **2001**, *13*, 213-221.

62. Miyata, S.; Yoshida, K.; Shirokura, H.; Kashio, M.; Nagai, K., Solid and Thermal Properties of Aba-Type Triblock Copolymers Designed Using Difunctional Fluorine-Containing Polyimide Macroinitiators with Methyl Methacrylate. *Polym. Int.* **2009**, *58*, 1148-1159.

63. Fu, G. D.; Zong, B. Y.; Kang, E. T.; Neoh, K. G.; Lin, C. C.; Liaw, D. J., Nanoporous Low-Dielectric Constant Polyimide Films Via Poly(amic acid)s with RAFT-Graft Copolymerized Methyl Methacrylate Side Chains. *Ind. Eng. Chem. Res.* **2004**, *43*, 6723-6730.

64. Hedrick, J. L.; Russell, T. P.; Sanchez, M.; DiPietro, R.; Swanson, S., Polyimide Nanofoams from Caprolactone-Based Copolymers. *Macromolecules* **1996**, *29*, 3642-3646.

65. Meleshko, T. K.; Kashina, A. V.; Saprykina, N. N.; Kostyuk, S. V.; Vasilenko, I. V.; Nikishev, P. A.; Yakimanskii, A. V., Synthesis and Morphology of Polycaprolactone-*block*-Polyimide-*block*-Polycaprolactone Triblock Copolymers for Film Separation Membranes. *Russ. J. Appl. Chem.* **2017**, *90*, 602-612.

66. Guo, D.; Khan, A. U.; Liu, T.; Zhou, Z.; Liu, G., Sub-10 Nm Domains in High-Performance Polyetherimides. *Polym. Chem.* **2019**, *10*, 379-385.

67. Liu, C.; Liu, B.; Chan-Park, M. B., Synthesis of Polycaprolactone-Polyimide-Polycaprolactone Triblock Copolymers via a 2-Step Sequential Copolymerization and Their Application as Carbon Nanotube Dispersants. *Polym. Chem.* **2017**, *8*, 674-681.

68. Ando, S.; Yoshida, A.; Nagai, K., Preparation of Porous Membranes by Selective Decomposition of Adamantane Unit in ABA-Type Triblock Copolymer. *Polym. Eng. Sci.* **2016**, *56*, 1191-1200.

69. Ju, M.; Gong, F.; Cheng, S.; Gao, Y., Fast and Convenient Synthesis of Amine-Terminated Polylactide as a Macroinitiator For ω-Benzyloxycarbonyl-L-Lysine-N-Carboxyanhydrides. *Int. J. Polym. Sci.* **2011**, *6*, 1-7.

70. Li, S.; McCarthy, S., Further Investigations on the Hydrolytic Degradation of Poly($_{DL}$-lactide). *Biomaterials* **1999**, *20*, 35-44.

71. Ohkita, T.; Lee, S.-H., Thermal Degradation and Biodegradability of Poly (lactic acid)/Corn Starch Biocomposites. *J. Appl. Polym. Sci.* **2006**, *100*, 3009-3017.

72. Huang, F.; Wang, X.; Li, S., The Thermal Stability of Polyetherimide. *Polym. Degrad. Stab.* **1987**, *18*, 247-259.

# Chapter 4. Mesoporous Polyimide Thin Films as Dendrite-Suppressing Separators for Lithium-Metal Batteries

## 4.1 Abstract

Lithium-metal batteries require the effective suppression of lithium dendrites to guarantee both high performance and safety. Today's separators have macropores allowing lithium dendrites to traverse, leading to internal short circuits and other catastrophic results. Herein, we report a mesoporous polyimide separator for dendrite suppression. The polyimide separator exhibits mesopores of 21 nm in width, and a high storage modulus of 1.80 GPa. This mesoporous polyimide separator assists in the electrodeposition to form flat-top protrusions instead of sharp dendrites, therefore allowing the safe cycling of lithium-metal batteries. This work is expected to advance the development of dendrite-suppressing strategies, and contribute to the revival of lithium-metal batteries.

## 4.2 Introduction

Lithium-metal batteries represent a high-performance energy storage technology because metallic lithium provides a high theoretical capacity of 3860 mAh/g, a low density of 0.534 g/cm$^3$, and a low electrochemical potential of -3.040 V vs. SHE (the standard hydrogen electrode).[1-6] Since the debut in the 1970s, the commercialization of lithium-metal batteries, however, has been plagued due to severe safety concerns.[3, 5] Lithium dendrites arise from the nonuniform nucleation of lithium on the anode surface.[7-9] The amplified electrical field near the lithium crystals further promotes dendritic growth.[8, 10] The resulting lithium dendrites expose large reactive surfaces and consume

the electrolyte to form a solid-electrolyte interphase (SEI).[2, 8, 11, 12] The uneven stripping/plating of lithium causes accumulative stress and brittle fractures in the SEI, further drying the electrolyte to grow more SEI.[2, 11, 13, 14] This uncontrollable process deteriorates the performance of lithium-metal batteries, including increasing the internal impedance, forming isolated lithium, and lowering the coulombic efficiency (CE).[2, 8, 11, 12] And worse, the growing dendrites traverse the separator, causing short-circuits and even fire hazards once.[6, 7, 10] Therefore, suppressing lithium dendrites is imperative to guarantee the safe operation of high-performance lithium-metal batteries.

In the past decades, various strategies have been evaluated to suppress lithium dendrites, including (1) employing high-modulus solid-state electrolytes or ceramic-coated separators to block the dendritic growth,[15-19] (2) applying concentrated liquid electrolytes or pulse charging currents to mitigate the depletion of $Li^+$ near the anode surface,[2, 20-22] (3) increasing operation temperatures to facilitate $Li^+$ diffusion,[4, 23] (4) employing three-dimensional lithium-metal electrodes or hosts to enlarge the surface area,[9, 24, 25] (5) engineering the composition, density and elasticity of SEI to ensure interphase stability.[2, 25-28] Although the high-modulus solid-state electrolytes are promising to suppress the dendritic growth, lithium dendrites can still penetrate the grain boundaries of the electrolytes.[16, 29-31] Moreover, at room temperature, the solid-state electrolytes usually have limited conductivity and high electrolyte/electrode contact resistance.[16, 29-31] Contrarily, liquid electrolytes provide high ionic conductivity and good contact with electrodes, but the dendritic growth is uncontrolled. Especially, the deposition-diffusion competition causes $Li^+$ depletion near the metallic lithium surface, promoting the fast tip-growth of dendrites. High-concentration liquid electrolytes, pulse charging, elevated temperatures, and high-surface-area electrodes mitigate the depletion of $Li^+$ near the metallic lithium surface, but still cannot cease the invasion of lithium dendrites. Although the stable SEI tailors the lithium

deposition, the limited mechanical strength is still vulnerable to the dendritic penetration.[12, 32] At the frontline of dendritic invasion, high-modulus separators are promising for suppressing unhealthy dendrite growth in liquid electrolytes.

The state-of-the-art separators are made of macroporous polyolefins, such as polyethylene (PE) and polypropylene (PP). The large macropores are susceptible to lithium dendrite penetration, causing safety concerns.[33] We hypothesize that mesopores smaller than the width of lithium dendrites can provide a strong physical barrier and stop lithium dendrite from penetrating the separator. But the mesoporous separators must possess a high modulus to withstand the cumulative axial stress.[1] Compared with PE and PP, polyimides have superior mechanical performance, but controlling the pore size in polyimides at the mesoscale remains challenging. We adopt the strategy to prepare porous polyimides using ABA triblock copolymers comprising polyimide and thermally labile blocks. To synthesize polyimide-based triblock copolymers, various thermally labile blocks have been deployed, such as poly(methyl methacrylate),[34, 35] polystyrene,[36, 37] poly(*α*-methyl styrene),[38, 39] polycaprolactone,[40-43] poly(ethylene oxide),[44] and poly(propylene oxide).[45-49] The triblock copolymers microphase-separate to form domains in tens of nanometers. Via thermolysis, the labile blocks decompose to create mesopores. But high-temperature thermolysis inevitably results in too-fast decomposition of the labile block, producing a large amount of gaseous species, *e.g.*, poly(*α*-methyl styrene) fully decomposes within 4.5 h at 325 °C.[38] The gaseous species expands in the softened polyimide matrices, resulting in pore sizes of hundreds of nanometers or even micrometers.[36] Thus, judicious selection of the labile block to achieve a low thermolysis temperature is crucial to preparing mesoporous polyimides without perturbing the porous network.

In this work, we report the preparation of a mesoporous polyimide thin film *via* the thermolysis of polylactide-*b*-polyimide-*b*-polylactide triblock copolymers at a low temperature of 280 °C. The

thermolysis slowly removes polylactide blocks to create mesoporous polyimide thin films with a median pore width of 21 nm and a storage modulus of 1.80 GPa. The mesoporous polyimide thin films, serving as separators in lithium-metal batteries, not only show good rate capabilities comparable with PP/PE/PP trilayer separators, but also assist in lithium deposition as flat-top protrusions, enabling long-term safe cycling.

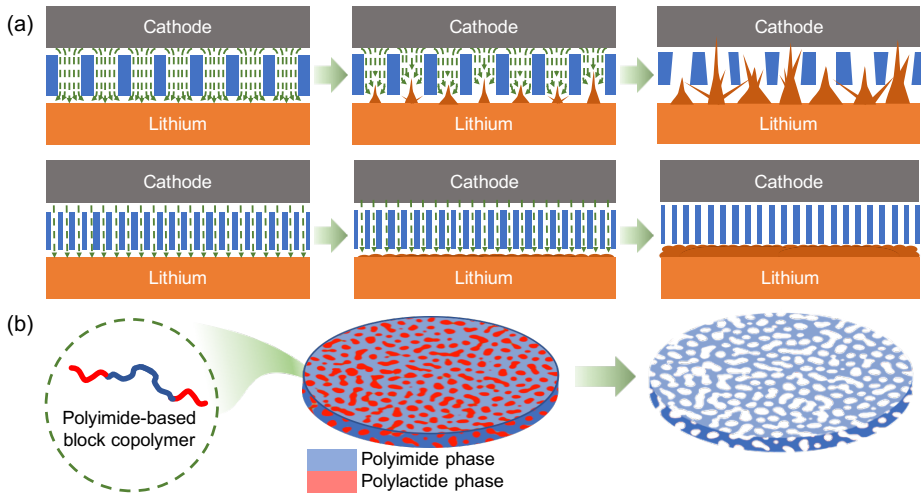


**Figure 4.2.** Effects of pore size and modulus of separators on dendrite suppression. (a) Upper: conventional macroporous PP/PE/PP separator induces non-uniform $Li^+$ flux and promotes uneven lithium deposition and dendritic growth. The macropores (40 – 400 nm wide) and low modulus of PP/PE/PP separators (~0.5 GPa in transverse direction) cannot suppress lithium dendrites, resulting in short circuits.[33, 50, 51] Lower: the mesoporous polyimide separator provides uniform $Li^+$ flux and ensures more even lithium deposition. The mesopores and high modulus (1.80 GPa) suppress the invasion of dendrites for safe cycling. The tortuous macro/mesopores are simplified as straight pores, in which the green dashed lines represent the $Li^+$ flux. (b) Our strategy to prepare mesoporous, high-modulus polyimide separators from a polyimide-based block copolymer. The solution casting and chemical imidization of PLA-b-PAA-b-PLA forms a polyimide-based thin

film. The subsequent thermolysis produces a mesoporous polyimide separator for the lithium-metal battery.

## 4.3 Experimental

### *4.3.1 Chemicals.*

$_{D,L}$-Lactide was recrystallized in ethyl acetate before use as follows. $_{D,L}$-Lactide (10.0 g, Sigma-Aldrich) was dissolved in ethyl acetate (15.0 mL, Fisher Scientific) at 75 °C and stored at -4 °C for 1 h. Afterward, pure white lactide crystals was collected *via* vacuum filtration and dried at reduced pressure overnight. 3-(Boc-amino)-1-propanol (Sigma-Aldrich) was heated at 120 °C under a reduced pressure for 2 h to remove moisture and then stored over 4 Å molecular sieves. Chloroform (Fisher Scientific) was stirred with $CaH_2$ (Sigma-Aldrich) overnight and distilled before use. 1,8-Diazabicyclo[5.4.0]undec-7-ene (DBU), dichloromethane (DCM), trifluoroacetic acid (TFA), sodium bicarbonate, anhydrous dimethyl sulfoxide (DMSO), pyromellitic dianhydride (PMDA), 4,4'-oxydianiline (oDA), benzoyl chloride, acetic anhydride, pyridine, and ninhydrin were purchased from Sigma-Aldrich and used as received. Deuterated chloroform ($CDCl_3$) and DMSO (DMSO-$d_6$) were purchased from Cambridge Isotope Laboratories. $LiPF_6$ in EC/DEC (1 M, Sigma-Aldrich) was utilized as the liquid electrolyte. In battery tests, $LiFePO_4$ coated on aluminum foil (120 g/m$^2$, 68 μm coating thickness, MTI corporation) was employed as the cathode and lithium foil (0.20 mm thickness, Signa-Aldrich) as the anode. Battery cases, spacers, and springs (MTI corporation) were cleaned *via* sonication in a mixture of acetone/isopropanol (v:v = 1:1) for 1 h and dried at 80 °C overnight. The polypropylene/polyethylene/polypropylene trilayer separators (PP/PE/PP, Celgard 2325) were purchased from Celgard, LLC.

### *4.3.2 Instrumentation.*

Proton nuclear magnetic resonance ($^1$H NMR) spectra were collected in $CDCl_3$ or DMSO-$d_6$ on a 400 MHz Varian Unity. Thermal gravimetric analysis (TGA) was conducted on a TGA 5500 (TA instrument) in the air. Fourier transform infrared spectroscopy (FT-IR) was performed on a Thermo Scientific Nicolet iS5 spectrometer with an iD7 ATR accessory. Nitrogen adsorption was performed on a Micromeritics 3Flex Adsorption Analyzer. Scanning electron microscopy (SEM) was conducted on a LEO Zeiss 1550. Dynamic mechanical analysis (DMA) was performed on a TA Q800. Oxygen plasma etching was conducted in a South Bay Technology PC-2000 using a forward power of 60 W. The coin cells were crimped on an MTI MSK-160 E. Electrochemical Impedance Spectroscopy (EIS) was performed on a PARSTAT 4000, Princeton Applied Research-AMETEK. The lithium-metal batteries and lithium/lithium batteries were tested on a Neware BTS4000.

### *4.3.3 Polymerization of Boc-terminated polylactide (Boc-PLA).*

To a 100-mL Schlenk tube, $_{D,L}$-lactide (8.50 g) and 3-(Boc-amino)-1-propanol (18.3 mg) were dissolved in anhydrous chloroform (60.0 mL). The resulting solution was degassed with three freeze-pump-thaw cycles. Afterward, DBU (15.9 mg) was added to the solution in an argon-filled glovebox. The resulting solution was stirred at room temperature for 1 h. The polymerization was terminated by adding benzoyl chloride (30.0 mg) and stirring for another 1.5 h. Subsequently, the solution was poured into chilled methanol (300.0 mL). The white precipitates were collected as the product *via* vacuum filtration and then dried at 80 °C overnight *in vacuo*.

### *4.3.4 Synthesis of amine-terminated PLA (PLA-$NH_2$).*

Boc-PLA (4.00 g) was dissolved in a mixture of DCM and TFA (v:v = 1:1, 40.0 mL in total) and reacted overnight. Afterwards, the solvents were removed on a rotary evaporator. The resulting viscous residue was dissolved in DCM (50.0 mL) and then neutralized using a saturated $NaHCO_3$ aqueous solution. The organic phase was collected and poured into chilled methanol (300 mL). The PLA-$NH_2$ product as white precipitates was collected using vacuum filtration and then dried at 70 °C overnight *in vacuo*.

### *4.3.5 Synthesis of polylactide-b-poly(amic acid)-b-polylactide (PLA-b-PAA-b-PLA) triblock copolymer.*

To a 500-mL round bottom flask, PLA-$NH_2$ (3.022 g), PMDA (2.588 g), and oDA (2.370 g) were dissolved in anhydrous DMSO (150.0 mL). The mixture was stirred at room temperature for 12 h and then heated at 100 °C for another 12 h.

### 4.3.6 Preparation of mesoporous polyimide film.

An aliquot of PLA-*b*-PAA-*b*-PLA in DMSO solution (5.0 mL) was mixed with acetic anhydride (220 μL) and pyridine (70 μL) and then poured onto a glass slide (7.0 cm by 7.0 cm). The solution layer was baked at 60 °C under reduced pressure to produce a thin film. The film was further baked stepwise at 100 °C for 1 h, 150 °C for 1 h, 220 °C for 1 h, 280 °C for 24 h and 350 °C for 1 h. The resulting thin film was peeled off from the supporting glass slide, and then both sides were etched using oxygen plasma for 30 min to enhance the wettability of the liquid electrolytes. The final porous polyimide thin film of ~20 μm in thickness was cut into discs of 19 mm in diameter and used as battery separators.

#### *4.3.7 Battery assembly and tests.*

The mesoporous polyimide separators were tested using electrochemical impedance spectroscopy (EIS), lithium-metal batteries, and lithium/lithium symmetric batteries. For EIS batteries, the separators were interposed between two stainless steel spaces, filled with 30 μL of electrolyte. For lithium-metal batteries, $LiFePO_4$ on aluminum foil (12 mm in diameter, 12 mg/cm$^2$) and lithium foil (15 mm in diameter) were employed as the cathodes and anodes, respectively. The volume of electrolyte was 60 μL. For lithium/lithium symmetric batteries, separators were inserted between two lithium-metal electrodes, filled with 60 μL of electrolyte.

## 4.4 Results and discussion

The mesoporous polyimide separators suppress Li dendrites following three mechanisms: i) the mesopores uniformly redistribute $Li^+$ flux to the lithium-metal electrode, facilitating the even plating of lithium;[52, 53] ii) the mesopores are smaller than the typical width of lithium dendrites, therefore efficiently blocking the dendrites; iii) the high modulus ceases the invasion of lithium dendrites (Figure 4.1a).[1, 54-57] To fulfill those characteristics, on the one hand, we select polyimide as the matrix because it has a high mechanical strength and high degradation temperature. On the other hand, we select PLA as the sacrificial block owing to its reasonable thermolysis temperature that does not significantly soften the polyimide matrix. (Figure 4.1b). To synthesize the block copolymer, PLA with a number-average molecular weight ($M_n$) of 50 kDa was first synthesized *via* a ring-opening polymerization using 3-(Boc-amino)-1-propanol as the initiator and DBU as the catalyst (Figure 4.2a and S4.1). The deprotection of tert-butoxycarbonyl (Boc) end group generated amine-terminated PLA (PLA-$NH_2$) (Figure S4.2). Then, PLA-$NH_2$ was reacted with PMDA and oDA to produce a polylactide-*b*-poly(amic acid)-*b*-polylactide (PLA-*b*-PAA-*b*-PLA)

triblock copolymer. We targeted a PLA volume fraction ($\phi_{PLA}$) of 40% to access the bicontinuous phase of the triblock copolymer so that the final polyimide film would contain interconnected mesopores.[58] The actual $\phi_{PLA}$ was determined based on $^1$H NMR (Figure 4.2a). Peak *b* corresponded to the methine protons in PLA repeating units and Peak *c* to all aromatic protons in poly(amic acid) repeating units (Figure 4.2a). The integral ratio of Peak *c* and Peak *b*, $I_b$: $I_c$= 39.0:100, indicated an actual $\phi_{PLA}$ of 40.2% using Equation 1.

$$\phi_{PLA} = \frac{I_b \times M_{PLA}}{I_b \times M_{PLA} + I_c/10 \times M_{PAA}} \qquad \text{(Equation 1)}$$

where $I_b$, $I_c$ are the integrals of Peak *b* and *c*, respectively. $M_{PLA}$ = 72.1 g/mol and $M_{PAA}$ = 418 g/mol are the molar masses of PLA and poly(amic acid) repeating units, respectively.

PLA-*b*-PAA-*b*-PLA triblock copolymers, mixed with acetic anhydride and pyridine, were cast into a thin film using DMSO as the solvent. Acetic anhydride and pyridine chemically imidized poly(amic acid) into polyimide, ensuring the film with high thermal and structural stabilities and to survive the subsequent thermolysis.[59] Removing PLA without perturbing the polyimide matrix necessitated a low thermolysis temperature. Thermogravimetric analysis of polylactide-*b*-polyimide-*b*-polylactide (LIL) thin films showed three weight loss regimes (Figure 4.2b). The initial weight loss below 260 °C arose from the evaporation of volatile species such as the solvent and chemical imidization reagents. The weight loss between 260 and 440 °C was assigned to the thermal decomposition of PLA.[60] The remaining weight evolving from 89.4% to 54.5% indicated a $\phi_{PLA}$ of 39.0% in the dry LIL film, concurring with the $\phi_{PLA}$ calculated using $^1$H NMR (Figure 4.2a). The weight loss above 440 °C was due to the decomposition of polyimide matrices.[61] To remove the PLA phase without plasticizing the polyimide matrix, 280 °C was selected as the thermolysis temperature to prepare mesoporous polyimide thin films. To confirm that thermolysis at 280 °C could slowly removes the PLA phase, we used an isothermal gravimetric analysis to

monitor the weight loss of LIL for 24 h (Figure 4.2c). The PLA decomposition in the first hour resulted in a weight loss of 8.3%. In the subsequent hours, the incremental weight loss per hour decreased gradually. The cumulative weight loss approached 37.5% after 24 h, implying the removal of most of the PLA phase.

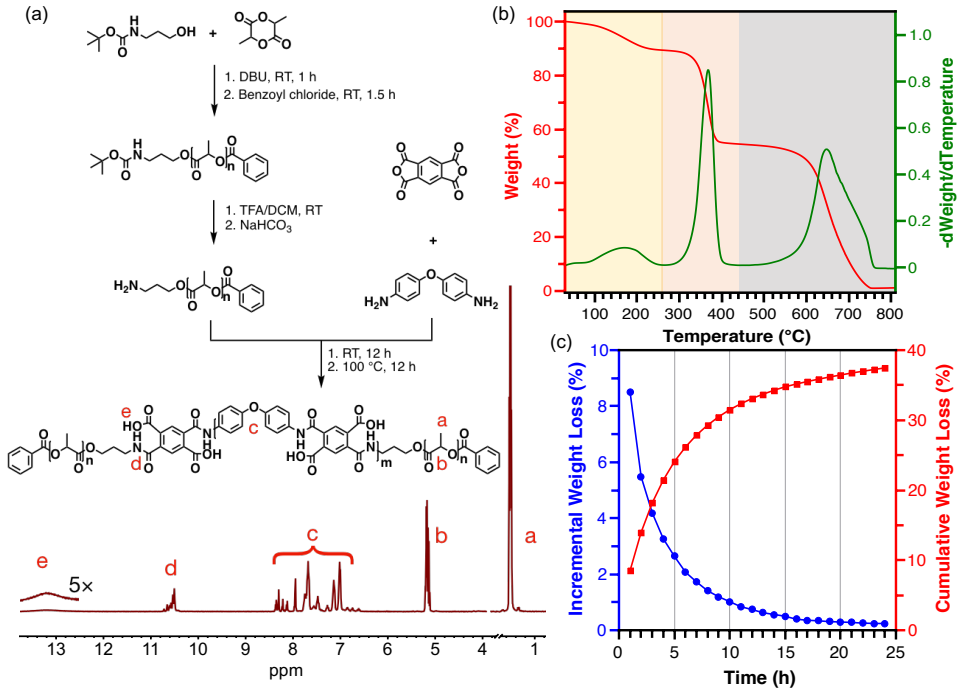


**Figure 4.2.** Synthesis and thermogravimetric analysis of LIL. (a) Synthesis of PLA-*b*-PAA-*b*-PLA, and its $^{1}$H NMR spectrum indicates a $\phi_{PLA}$ of 40.2%. (b) Thermogravimetric analysis of LIL films indicates a $\phi_{PLA}$ of 39.0%, and suggests a thermolysis temperature of PLA at 280 °C. (c) Isothermal weight loss at 280 °C for 24 h indicates the removal of most PLA.

The evolution of the PLA content and the degree of imidization was recorded using ATR FT-IR employing the PLA-$NH_2$ and commercial PMDA-oDA polyimides as references (Figure 4.3a). The efficient chemical imidization of LIL was confirmed by the profound peaks at 1777, 1717 and 1370 $cm^{-1}$, corresponding to the asymmetric stretching of C=O, symmetric stretching of C=O, and stretching of C-N in polyimides, respectively.[62-64] The peak at 1752 $cm^{-1}$ was assigned to the C=O

stretching of PLA.[65-67] The LIL thin film heating at 220 °C for 24 h retained a strong PLA C=O stretching. After the thermolysis at 280 °C for 24 h, the absence of C=O stretching at 1752 $cm^{-1}$ indicated the removal of PLA. PMDA-oDA polyimide usually requires a high temperature for complete imidization. After heating at 350 °C for 1 h, the appearance of LIL resembled that of commercial polyimide, confirming a high degree of imidization. The morphologies of LIL before and after thermolysis were imaged using SEM, confirming the mesopore development (Figure 4.3b, c and S4.3). The as-cast LIL thin film showed a non-porous flat surface. After thermolysis, interconnected mesopores formed in the polyimide matrices. The color of LIL films changed from amber to brownish due to the formation of charge-transfer complexes in polyimides.[68] Nitrogen sorption analysis suggested the mesopores had a median size of 21 nm (Figure 4.3c inset and S4.4).

The mesoporous polyimide separators must have high thermal stability and mechanical strength to ensure electrode segregation both under working conditions and during the thermal runaway.[69] Thermogravimetric analysis confirmed the good thermal stability of mesoporous polyimide films, showing a $T_{d,5\%}$ of 540 °C (Figure 4.3d). PLA was completely removed, as evidenced by no additional weight loss related to PLA. The thermomechanical properties of mesoporous polyimide were further tested using dynamic mechanical analysis (DMA). The mesoporous polyimide film exhibited a storage modulus ($E'$) of ~1.80 GPa at room temperature, and retained an $E'$ of 0.94 GPa at 300 °C (Figure. 4.3e). $E'$ was greater than $E''$ in the tested temperature range, affording a maximum of $Tan(\delta)$ at 393 °C and confirming the high thermomechanical stability. The high modulus of mesopores polyimide separators would cease the dendritic growth and enable safe cycling of lithium-metal batteries.[1, 54]

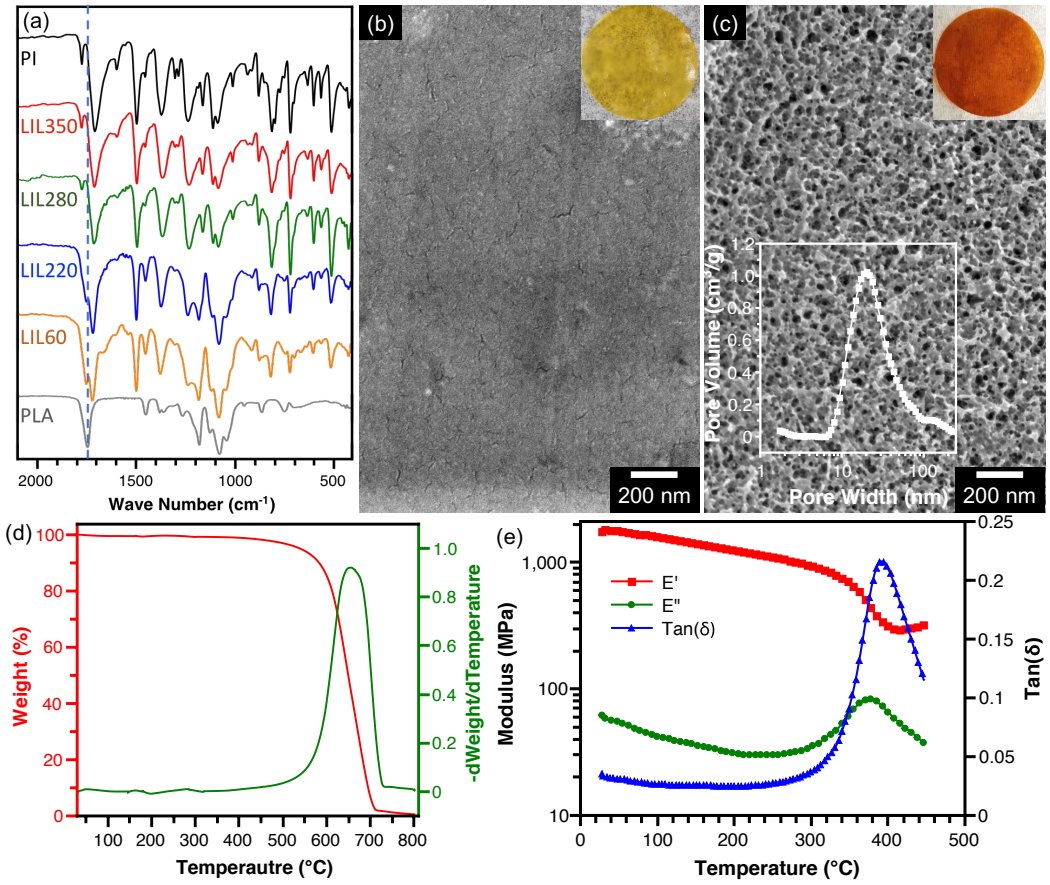


**Figure 4.3.** Thermolysis and microstructures of mesoporous polyimide films. (a) FT-IR spectra of PLA, PI, and LIL thermalized at 60, 220, 280 and 350 °C. The dashed line at 1752 $cm^{-1}$ corresponds to the carbonyl stretching of PLA. (b) Before and (c) after thermolysis at 280 °C for 24 hours, LIL thin films show a non-porous and mesoporous morphology, respectively. The insets show the optical images of 19-mm-wide LIL discs. The pore size distribution of the mesoporous polyimide film indicates a median pore width of 21 nm. (d) Thermogravimetric analysis of mesoporous polyimide thin film shows a $T_{d,5\%}$ of 540 °C. (e) Dynamic mechanical analysis shows a high storage modulus $E'$ of 1.80 GPa at RT. The $E'$ is greater than $E''$ at all testing temperatures between 25 and 450 °C.

As a benchmark, the electrochemical performance of mesoporous polyimide was evaluated along with commercial PP/PE/PP separators. Electrochemical impedance of both separators was measured between two stainless steel spacers (Figure 4.4a). The impedance was 2.6 Ω for PP/PE/PP and 13 Ω for the mesoporous polyimide. The higher impedance of mesoporous polyimide separators was caused by the smaller pore size and thus hindered ion transport, which could be tuned by the block copolymer molecular weight and volume fraction. Both separators were tested in $LiFePO_4$/lithium coin cells at increasing current densities from 0.2 to 1.0 mA/cm$^2$. The mesoporous polyimide separator showed rate capabilities comparable to the PP/PE/PP separator (Figure 4.4b). Despite a higher ionic impedance than the PP/PE/PP separator, the mesoporous polyimide separator exhibited a slightly higher initial overpotential, *e.g.,* 3.76 V vs. 3.70 V at a current density of 0.8 mA/cm$^2$ (Figure 4.4c and d).

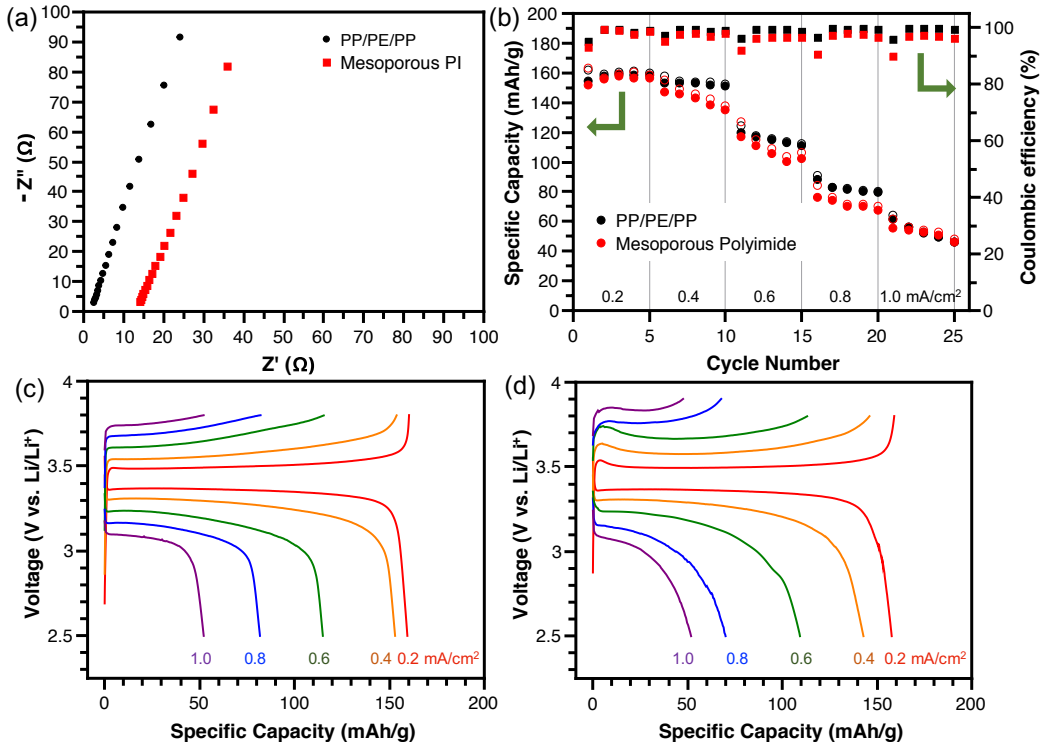


**Figure 4.4.** Electrochemical performance of mesoporous polyimide separators. (a) The ionic impedances, (b) rate capabilities, and (c, d) Voltage profiles of (c) PP/PE/PP and (d) mesoporous

polyimide separators are compared. Current densities ranging from 0.2 to 1.0 mA/cm$^2$ were employed in (b), (c) and (d). Mesoporous polyimide separators show comparable good performance with PP/PE/PP separators. Cathode: $LiFePO_4$ on aluminum foil (12 mg/cm$^2$, 12 mm in diameter).

The dendrite-suppressing capability of mesoporous polyimide separators was tested in symmetric Li/Li batteries at a current density of 4 mA/cm$^2$ and a capacity of 4 mAh/cm$^2$ (Figure 4.5a). The symmetric Li/Li battery employing the PP/PE/PP separator showed a growing overpotential after 30 h, corresponding to the increasing internal impedance due to the dendritic growth, electrolyte consumption, and thick SEI formation. After 57 h, the lithium dendrites penetrated the PP/PE/PP separator and caused internal short circuit, resulting in an abrupt decrease of potential to 0.01 V. In contrast, the mesoporous polyimide separator effectively suppressed the lithium dendrites and retained a stable potential for > 500 h.

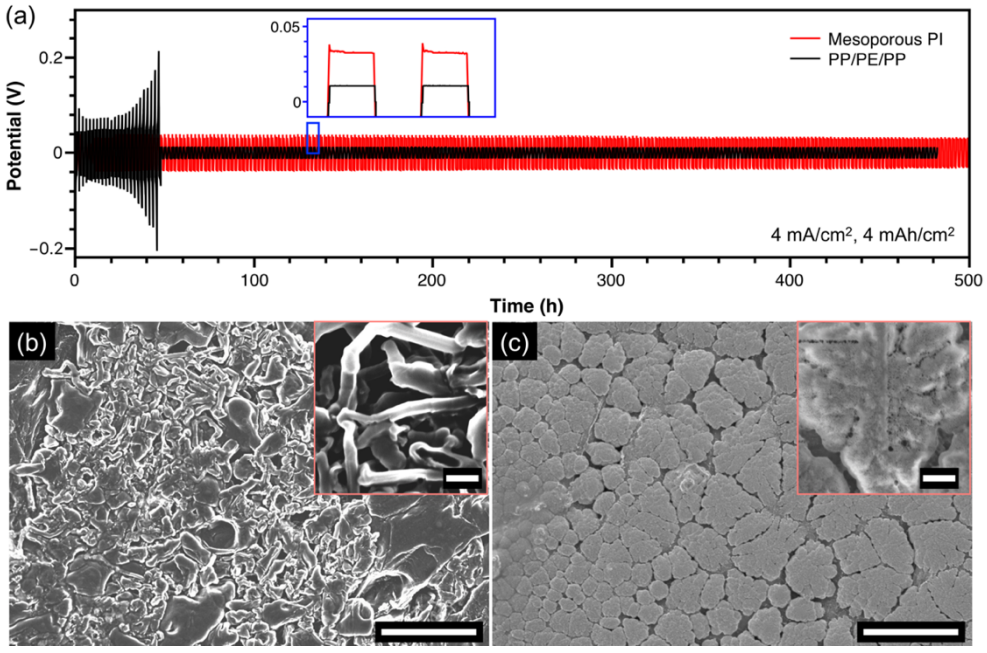


**Figure 4.5.** Li/Li symmetric battery test. (a) The potential profile indicates the battery employing a PP/PE/PP separator encounters the short circuit after 50-hour cycling. Whereas the mesoporous

polyimide separator enables safe charging/discharging without short circuits for 500 hours. The inset shows the detailed potential profiles after cycling for 130 hours. (b) After charging/discharging for 130 hours, the lithium-metal electrode contacting a PP/PE/PP separator shows a dendritic morphology. The zoomed-in view shows kinked dendrites with a width of 200 nm. (c) Whereas the lithium-metal electrode contacting a mesoporous polyimide separator shows flat-top protrusions. The zoomed-in view shows the detailed morphology of a lithium protrusion. Scale bars in both (b) and (c), 5 μm. In zoomed-in views, 500 nm.

The morphologies of lithium-metal electrodes in both batteries were imaged using SEM after charging/discharging for 130 h (Figure 4.5b and c). With PP/PE/PP separator in the battery, sharp lithium dendrites grew on the lithium-metal electrode and an average dendrite width was 200 nm (Figure 4.5b). Since the pore sizes in the PP/PE/PP separator were 40 - 400 nm,[33] the lithium dendrites traversed the large pores and caused short circuits. In contrast, in the battery with mesoporous polyimide separator, flat-top lithium protrusions formed on the electrode, absent of any sharp lithium dendrites (Figure 4.5c).

The mesoporous polyimide separators show outstanding dendrite-suppressing capability because of three characteristics: i) the mesopores allow uniform $Li^+$ flux across the separator, minimizing the dendritic growth;[52, 53] ii) the mesopore width is smaller than the width of lithium dendrites, preventing dendrites from penetrating the separator; iii) the high modulus withstand the high axial stress, ceasing the invasion of lithium dendrites.[1, 54-57] The smaller pore size, however, slows down ion transport, resulting in a slightly higher overpotential. Reducing the ionic impedance will be an important aspect of future optimizations. Decreasing the thickness of mesoporous polyimide separators and shortening the ion diffusion length will be an attractive means to reduce the apparent ionic impedance.

## 4.5 Conclusions

In this contribution, a mesoporous polyimide thin film was produced *via* slow thermolysis of a polylactide-*b*-polyimide-*b*-polylactide triblock copolymer. The slow thermolysis at 280 °C gradually removed polylactide to create mesopores of 21 nm, without perturbing the polyimide matrix. The resulting mesoporous polyimide thin films exhibited a storage modulus of 1.80 GPa. The mesoporous structures and high modulus together contributed to excellent dendrite-suppressing capability. Separated by mesoporous polyimide, lithium only formed flat-top protrusions, enabling safe cycling for > 500 h. This work highlights the potential of uniform mesoporous engineering polymers for dendrite suppression. We anticipate the mesoporous polyimide separators applicable to suppressing dendrites in "beyond Li-ion" energy storage technologies.

## 4.6 Supporting Information

The DBU catalyst was extraordinarily efficient in ring-opening polymerization of polylactide. The polymerization was accomplished within 1 h at room temperature, as monitored using $^{1}$H NMR (Figure S4.1a). The peak *b* and *a* at 5.02 and 1.63 ppm corresponded to the methine and methyl protons in lactide monomers, whereas the peak *d* and *c* at 5.14 and 1.53 ppm correlated to the methine and methyl protons in polylactide.[70] The growing peak *d* and reducing peak *b* suggested the ring-opening polymerization progress. After 1 h, the conversion of lactide to polylactide was > 99%. The polymerization kinetics was investigated by plotting $\ln([M_0]/[M])$ vs. time. This good linearity indicated that polymerization was "controlled", including fast initiation and no termination (Figure S4.1b). [71, 72] The slope of $\ln([M_0]/[M])$ vs. time suggested an apparent rate constant of 0.074 $min^{-1}$.

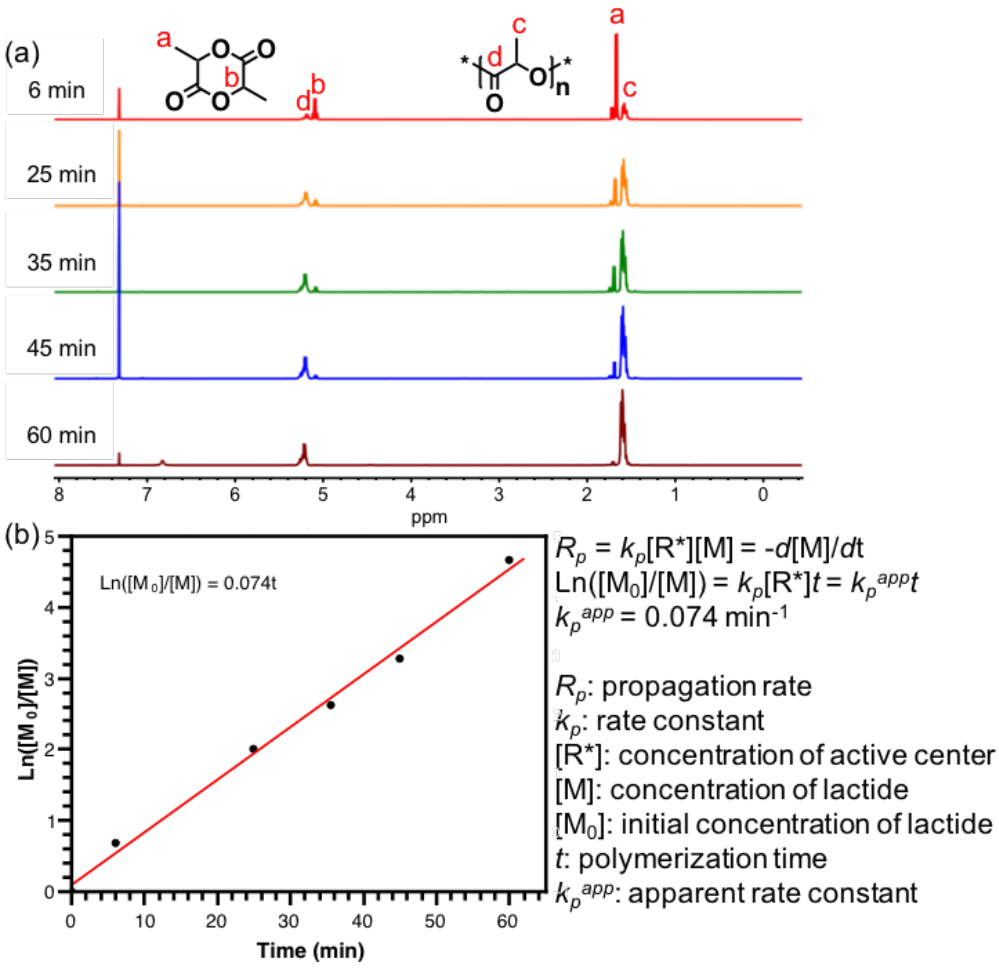


**Figure S4.1.** Kinetics of the ring-opening polymerization of lactide using a DBU catalyst. (a) $^{1}$H NMR monitored the conversion of lactide to polylactide. (b) The kinetic plot indicates a "controlled" polymerization with a fast initiation and no termination.

The deprotection of Boc-terminated PLA produces amine-terminate PLA (PLA-$NH_2$). The amine end group is vital to incorporate PLA onto poly(amic acid) (PAA) chain ends to synthesize PLA-*b*-PAA-*b*-PLA. However, due to the high molecular weight of PLA, *i.e.,* 50 kDa, confirming the existence of amine end groups is challenging using conventional spectroscopic methods, *e.g.,* $^{1}$H NMR or FT-IR. Therefore, ninhydrin tests are performed to attest to the formation of amine end groups (Figure S4.2).[73] In the ninhydrin tests, PLA-$NH_2$ (100 mg) was dissolved in chloroform (1.0 ml). Ninhydrin reagent (100 µL) was added to the resulting solution. The mixture was

incubated at 60 °C for 2 hours. The characteristic purple color qualitatively confirmed the formation of amine end groups (Figure S4.2a).[73] Whereas the Boc-PLA and blank chloroform showed no purple color because of the absence of amine end groups (Figure S4.2b and c).

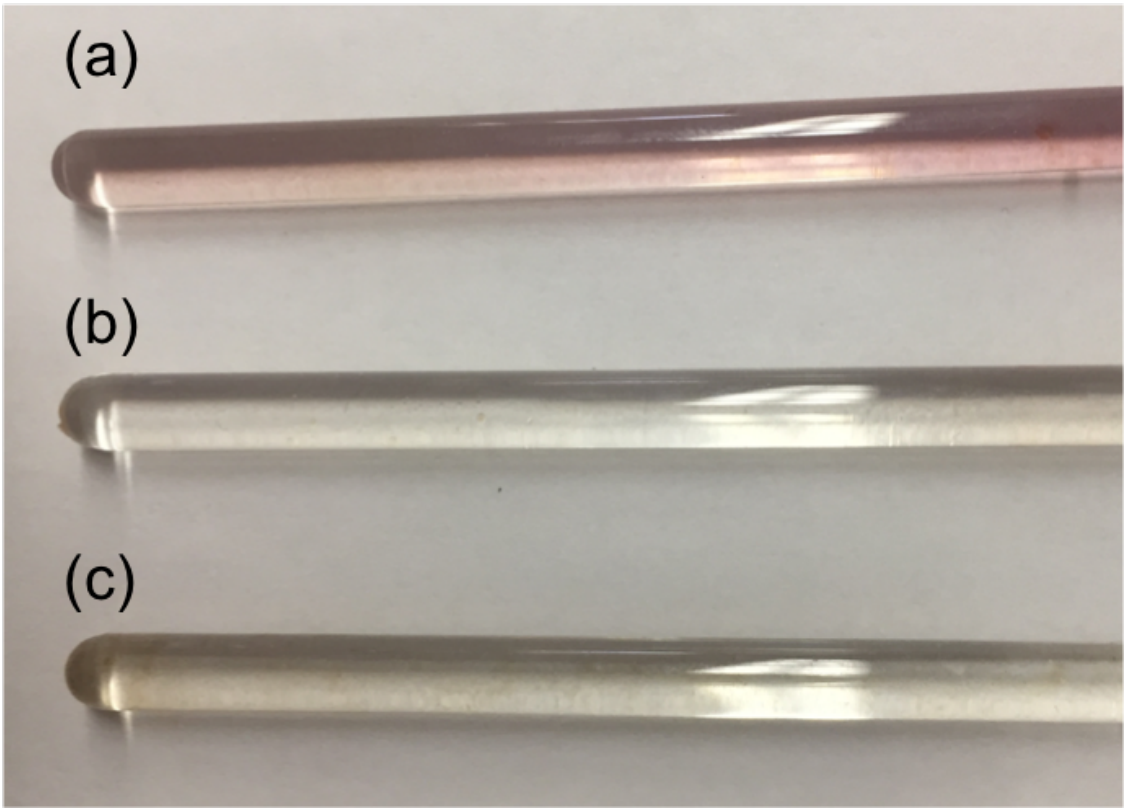


**Figure S4.2.** Ninhydrin tests of amine-terminated PLA. Ninhydrin reagent incubated with (a) amine-terminate PLA in chloroform, (b) Boc-terminated PLA in chloroform and (c) pure chloroform at 60 °C for 2 hours. The appearance of the characteristic purple color in amine-terminated PLA confirms the formation of amine end groups.

The thermolysis of LIL developed mesopores in polyimide thin films. Before the thermolysis, a non-porous flat morphology is observed on the top, cross-sectional and bottom surfaces of LIL thin films (Figure S4.3a-c). The top surface is the LIL-air interface, whereas the bottom surface refers to the LIL-substrate interface. After the thermolysis, the mesopores develop on all the top, cross-sectional and bottom surfaces of polyimide thin films (Figure S4.3d-f).

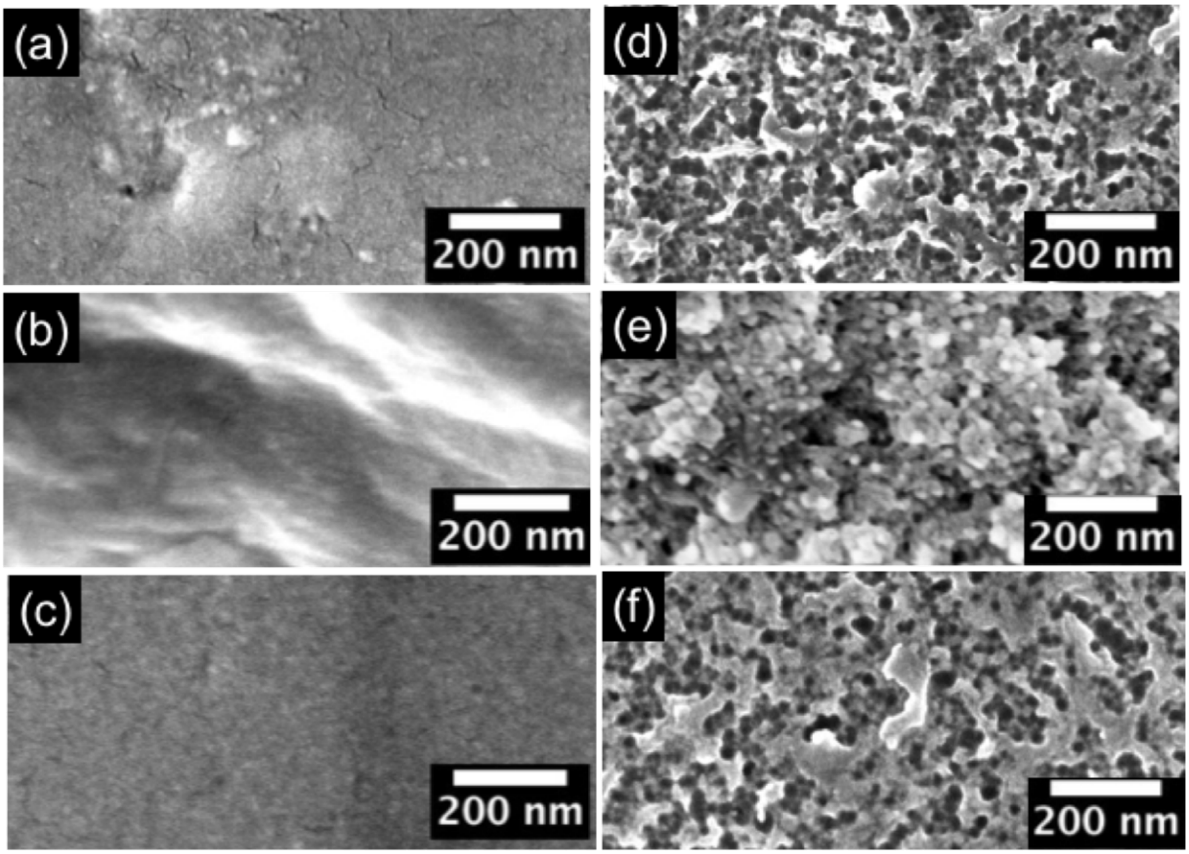


**Figure S4.3.** Morphologies of LIL films on the (a)(d) top surface, (b)(e) cross-section and (c)(f) bottom surface (a)(b)(c) before and (d)(e)(f) after the thermolysis. The thermolysis created mesopores in polyimide thin films on the (d) top surface, (e) cross-section and (f) bottom surface.

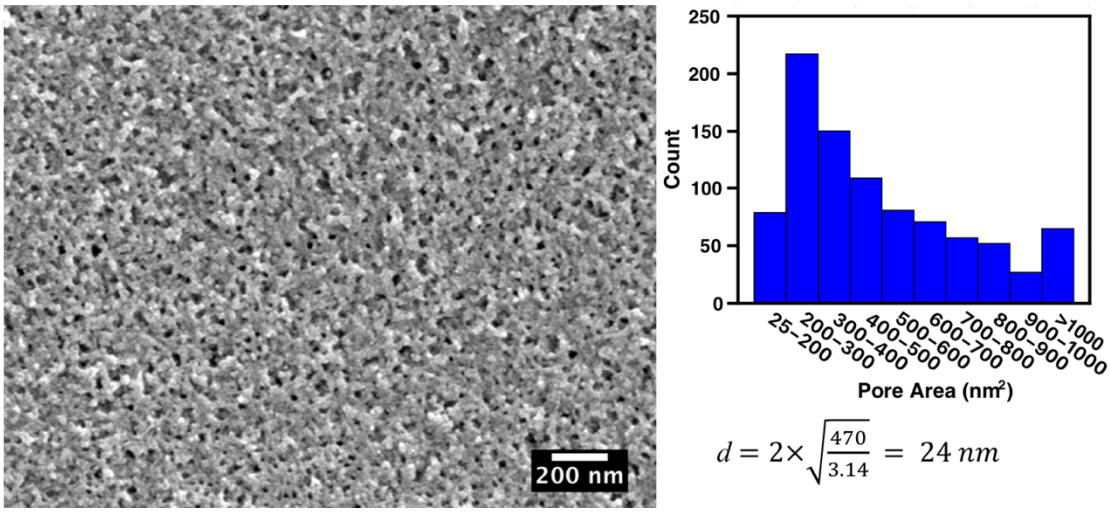


**Figure S4.4.** Pore size analysis of mesoporous polyimide thin films. The statistical analysis of pore area distribution unveils a median mesopore area of 470 $nm^2$, indicating a median pore width of 24 nm.

Besides utilizing nitrogen sorption, the pore size distribution of mesopore polyimide thin films is also analyzed using *ImageJ*, Version 1.53 (Figure S4.4). The mesopores appear as dark domains in the SEM image, thus the boundaries of dark domains define the cross-sectional areas of mesopores. Deploying an approximation of circular cross-section of those mesopores, the median domain size of 470 $nm^2$ derives a median pore width of 24 nm, close to the median pore width of 21 nm determined by nitrogen sorption.

## 4.7 Acknowledgement

This work was performed in part at the Nanoscale Characterization and Fabrication Laboratory (NCFL), supported by the National Center for Earth and Environmental Nanotechnology Infrastructure (NanoEarth, Virginia Tech). NanoEarth is a member of the National Nanotechnology Coordinated Infrastructure (NNCI), supported by NSF (ECCS 1542100 and ECCS 2025151). This work was made possible by the use of facilities in the Materials

Characterization Laboratory (MCL), Virginia Tech. MCL is supported by the Institute for Critical Technology and Applied Science (ICTAS), the Macromolecules Innovation Institute (MII), and the Office of the Vice President for Research and Innovation at Virginia Tech.

## 4.8 References

1. He, Y.; Ren, X.; Xu, Y.; Engelhard, M. H.; Li, X.; Xiao, J.; Liu, J.; Zhang, J. G.; Xu, W.; Wang, C., Origin of Lithium Whisker Formation and Growth under Stress. *Nat. Nanotechnol.* **2019**, *14*, 1042-1047.

2. Cao, X.; Ren, X.; Zou, L.; Engelhard, M. H.; Huang, W.; Wang, H.; Matthews, B. E.; Lee, H.; Niu, C.; Arey, B. W.; Cui, Y.; Wang, C.; Xiao, J.; Liu, J.; Xu, W.; Zhang, J.-G., Monolithic Solid–Electrolyte Interphases Formed in Fluorinated Orthoformate-based Electrolytes Minimize Li Depletion and Pulverization. *Nat. Energy* **2019**, *4*, 796-805.

3. Tarascon, J. M.; Armand, M., Issues and Challenges Facing Rechargeable Lithium Batteries. *Nature* **2001**, *414*, 359-367.

4. Li, L.; Base, S.; Wang, Y.; Chen, Z.; Hundekar, P.; Wang, B.; Shi, J.; Shi, Y.; Narayanan, S.; Koratkar, N., Self-Heating-Induced Healing of Lihtium Dendrites. *Science* **2018**, *359*, 1513-1516.

5. Mukhopadhyay, A.; Jangid, M. K., Li Metal Battery, Heal Thyself. *Science* **2018**, *359*, 1463.

6. Lin, D.; Liu, Y.; Cui, Y., Reviving the Lithium Metal Anode for High-Energy Batteries. *Nat. Nanotechnol.* **2017**, *12*, 194-206.

7. Frenck, L.; Sethi, G. K.; Maslyn, J. A.; Balsara, N. P., Factors That Control the Formation of Dendrites and Other Morphologies on Lithium Metal Anodes. *Front. Energy Res.* **2019**, *7*, 115.

8. Bieker, G.; Winter, M.; Bieker, P., Electrochemical in Situ Investigations of SEI and Dendrite Formation on the Lithium Metal Anode. *Phys. Chem. Chem. Phys.* **2015**, *17*, 8670.

9. Niu, C.; Pan, H.; Xu, W.; Xiao, J.; Zhang, J. G.; Luo, L.; Wang, C.; Mei, D.; Meng, J.; Wang, X.; Liu, Z.; Mai, L.; Liu, J., Self-Smoothing Anode for Achieving High-Energy Lithium Metal Batteries under Realistic Conditions. *Nat. Nanotechnol.* **2019**, *14*, 594-601.

10. Bai, P.; Li, J.; Brushett, F. R.; Bazant, M. Z., Transition of Lithium Growth Mechanisms in Liquid Electrolytes. *Energy Environ. Sci.* **2016**, *9*, 3221-3229.

11. Deng, Q.; Hu, R.; Xu, C.; Chen, B.; Zhou, J., Modeling Fracture of Solid Electrolyte Interphase in Lithium-Ion Batteries During Cycling. *J. Solid State Electrochem.* **2019**, *23*, 2999-3008.

12. Peled, E.; Menkin, S., Review—SEI: Past, Present and Future. *J. Electrochem. Soc.* **2017**, *164*, A1703-A1719.

13. Shi, F.; Pei, A.; Boyle, D. T.; Xie, J.; Yu, X.; Zhang, X.; Cui, Y., Lithium Metal Stripping beneath the Solid Electrolyte Interphase. *Proc. Natl. Acad. Sci. USA* **2018**, *115*, 8529-8534.

14. Gireaud, L.; Grugeon, S.; Laruelle, S.; Yrieix, B.; Tarascon, J. M., Lithium Metal Stripping/Plating Mechanisms Studies: A Metallurgical Approach. *Electrochem. Commun.* **2006**, *8*, 1639-1649.

15. Liu, Z.; Zinkevich, T.; Indris, S.; He, X.; Liu, J.; Xu, W.; Bai, J.; Xiong, S.; Mo, Y.; Chen, H., $Li_{15}P_4S_{16}Cl_3$, a Lithium Chlorothiophosphate as a Solid-State Ionic Conductor. *Inorg. Chem.* **2019**, *59*, 226-234.

16. Chen, R.; Li, Q.; Yu, X.; Chen, L.; Li, H., Approaching Practically Accessible Solid-State Batteries: Stability Issues Related to Solid Electrolytes and Interfaces. *Chem Rev* **2020**, *120*, 6820–6877.

17. Ji, X.; Hou, S.; Wang, P.; He, X.; Piao, N.; Chen, J.; Fan, X.; Wang, C., Solid-State Electrolyte Design for Lithium Dendrite Suppression. *Adv. Mater.* **2020**, *32*, 2002741.

18. Ansari, Y.; Guo, B.; Cho, J. H.; Park, K.; Song, J.; Ellison, C. J.; Goodenough, J. B., Low-Cost, Dendrite-Blocking Polymer-$Sb_2O_3$ Separators for Lithium and Sodium Batteries. *J. Electrochem. Soc.* **2014**, *161*, A1655-A1661.

19. Liang, J.; Chen, Q.; Liao, X.; Yao, P.; Zhu, B.; Lv, G.; Wang, X.; Chen, X.; Zhu, J., A Nano-Shield Design for Separators to Resist Dendrite Formation in Lithium-Metal Batteries. *Angew. Chem. Int. Ed.* **2020**, *59*, 6561-6566.

20. Chen, S.; Zheng, J.; Mei, D.; Han, K. S.; Engelhard, M. H.; Zhao, W.; Xu, W.; Liu, J.; Zhang, J. G., High-Voltage Lithium-Metal Batteries Enabled by Localized High-Concentration Electrolytes. *Adv. Mater.* **2018**, *30*, 1706102.

21. Li, Q.; Tan, S.; Li, L.; Lu, Y.; He, Y., Understanding the Molecular Mechanism of Pulse Current Charging for Stable Lithium-Metal Batteries. *Sci. Adv.* **2017**, *3*, 1701246.

22. Maeyoshi, Y.; Ding, D.; Kubota, M.; Ueda, H.; Abe, K.; Kanamura, K.; Abe, H., Long-Term Stable Lithium Metal Anode in Highly Concentrated Sulfolane-Based Electrolytes with Ultrafine Porous Polyimide Separator. *ACS Appl. Mater. Interfaces* **2019**, *11*, 25833-25843.

23. Wang, J.; Huang, W.; Pei, A.; Li, Y.; Shi, F.; Yu, X.; Cui, Y., Improving Cyclability of Li Metal Batteries at Elevated Temperatures and Its Origin Revealed by Cryo-Electron Microscopy. *Nat. Energy* **2019**, *4*, 664-670.

24. Cao, D.; Xing, Y.; Tantratian, K.; Wang, X.; Ma, Y.; Mukhopadhyay, A.; Cheng, Z.; Zhang, Q.; Jiao, Y.; Chen, L.; Zhu, H., 3D Printed High-Performance Lithium Metal Microbatteries Enabled by Nanocellulose. *Adv. Mater.* **2019**, *31*, 1807313.

25. Xie, J.; Wang, J.; Lee, H. R.; Yan, K.; Li, Y.; Shi, F.; Huang, W.; Pei, A.; Chen, G.; Subbaraman, R.; Christensen, J.; Cui, Y., Engineering Stable Interfaces for Three-Dimensional Lithium Metal Anodes. *Sci. Adv.* **2018**, *4*, eaat5168.

26. Zhao, C.-Z.; Chen, P.-Y.; Zhang, R.; Chen, X.; Li, B.-Q.; Zhang, X.-Q.; Cheng, X.-B.; Zhang, Q., An Ion Redistributor for Dendrite-Free Lithium Metal Anodes. *Sci. Adv.* **2018**, *4*, eaat3446.

27. Fang, C.; Lu, B.; Pawar, G.; Zhang, M.; Cheng, D.; Chen, S.; Ceja, M.; Doux, J.-M.; Musrock, H.; Cai, M.; Liaw, B.; Meng, Y. S., Pressure-Tailored Lithium Deposition and Dissolution in Lithium Metal Batteries. *Nat. Energy* **2021**, *6*, 987-994.

28. Guo, J.; Wen, Z.; Wu, M.; Jin, J.; Liu, Y., Vinylene Carbonate–$LiNO_3$: A Hybrid Additive in Carbonic Ester Electrolytes for Sei Modification on Li Metal Anode. *Electrochem. Commun.* **2015**, *51*, 59-63.

29. Varzi, A.; Raccichini, R.; Passerini, S.; Scrosati, B., Challenges and Prospects of the Role of Solid Electrolytes in the Revitalization of Lithium Metal Batteries. *J. Mater. Chem. A* **2016**, *4*, 17251-17259.

30. Zhao, Q.; Liu, X.; Stalin, S.; Khan, K.; Archer, L. A., Solid-State Polymer Electrolytes with in-Built Fast Interfacial Transport for Secondary Lithium Batteries. *Nat. Energy* **2019**, *4*, 365-373.

31. Zhao, W.; Yi, J.; He, P.; Zhou, H., Solid-State Electrolytes for Lithium-Ion Batteries: Fundamentals, Challenges and Perspectives. *EER* **2019**, *2*, 574-605.

32. Horstmann, B.; Shi, J.; Amine, R.; Werres, M.; He, X.; Jia, H.; Hausen, F.; Cekic-Laskovic, I.; Wiemers-Meyer, S.; Lopez, J.; Galvez-Aranda, D.; Baakes, F.; Bresser, D.; Su, C.-C.; Xu, Y.; Xu, W.; Jakes, P.; Eichel, R.-A.; Figgemeier, E.; Krewer, U.; Seminario, J. M.; Balbuena, P. B.; Wang, C.; Passerini, S.; Shao-Horn, Y.; Winter, M.; Amine, K.; Kostecki, R.; Latz, A., Strategies Towards Enabling Lithium Metal in Batteries: Interphases and Electrodes. *Energy Environ. Sci.* **2021**, *14*, 5289-5314.

33. Peter, C.; Nikolowski, K.; Reuber, S.; Wolter, M.; Michaelis, A., Chronoamperometry as an Electrochemical in Situ Approach to Investigate the Electrolyte Wetting Process of Lithium-Ion Cells. *J. Appl. Electrochem.* **2020**, *50*, 295-309.

34. Miyata, S.; Yoshida, K.; Shirokura, H.; Kashio, M.; Nagai, K., Solid and Thermal Properties of ABA-Type Triblock Copolymers Designed Using Difunctional Fluorine-Containing Polyimide Macroinitiators with Methyl Methacrylate. *Polym. Int.* **2009**, *58*, 1148-1159.

35. Fu, G. D.; Zong, B. Y.; Kang, E. T.; Neoh, K. G.; Lin, C. C.; Liaw, D. J., Nanoporous Low-Dielectric Constant Polyimide Films via Poly(amic acid)s with RAFT-Graft Copolymerized Methyl Methacrylate Side Chains. *Ind. Eng. Chem. Res.* **2004**, *43*, 6723-6730.

36. Hedrick, J. L.; Hawker, C. J.; DiPietro, R.; Jérôme, R.; Charlier, Y., The Use of Styrenic Copolymers to Generate Polyimide Nanofoams. *Polymer* **1995**, *36*, 4855-4866.

37. Guo, D.; Khan, A. U.; Liu, T.; Zhou, Z.; Liu, G., Sub-10 nm Domains in High-Performance Polyetherimides. *Polym. Chem.* **2019**, *10*, 379-385.

38. Hedrick, J. L.; DiPietro, R.; Plummer, C. J. G.; Hilborn, J.; Jérôme, R., Polyimide Foams Derived from a High $T_g$ Polyimide with Grafted Poly(α-Methylstyrene). *Polymer* **1996**, *37*, 5229-5236.

39. Charlier, Y.; Hedrick, J. L.; Russell, T. P.; Swanson, S.; Sanchez, M.; Jérôme, R., Crosslinked Polyimide Foams Derived from Pyromellitic Dianhydride and 1,1-Bis(4-aminophenyl)-1-phenyl-2,2,3-trifluoroethane with Poly(α-Methylstyrene). *Polymer* **1995**, *36*, 1315-1320.

40. Hedrick, J. L.; Russell, T. P.; Sanchez, M.; DiPietro, R.; Swanson, S., Polyimide Nanofoams from Caprolactone-Based Copolymers. *Macromolecules* **1996**, *29*, 3642-3646.

41. Ju, J.; Wang, Q.; Wang, T.; Wang, C., Low Dielectric, Nanoporous Fluorinated Polyimide Films Prepared from PCL-PI-PCL Triblock Copolymer Using Retro-Diels-Alder Reaction. *J. Colloid Interface Sci.* **2013**, *404*, 36-41.

42. Meleshko, T. K.; Kashina, A. V.; Saprykina, N. N.; Kostyuk, S. V.; Vasilenko, I. V.; Nikishev, P. A.; Yakimanskii, A. V., Synthesis and Morphology of Polycaprolactone-*block*-Polyimide-*block*-Polycaprolactone Triblock Copolymers for Film Separation Membranes. *Russ. J. Appl. Chem.* **2017**, *90*, 602-612.

43. Liu, C.; Liu, B.; Chan-Park, M. B., Synthesis of Polycaprolactone-Polyimide-Polycaprolactone Triblock Copolymers via a 2-Step Sequential Copolymerization and Their Application as Carbon Nanotube Dispersants. *Polym. Chem.* **2017**, *8*, 674-681.

44. Wang, L.; Lu, J.; Liu, M.; Lin, L.; Li, J., Preparation of Porous Polyimide Microspheres by Thermal Degradation of Block Copolymers. *Particuology* **2014**, *14*, 63-70.

45. Hedrick, J. L.; Carter, K.; Sanchez, M.; Pietro, R. D.; Swanson, S., Crosslinked Polyimide Foams Derived from Poly(imide-propylene Oxide) Copolymers. *Macromol. Chem. Phys.* **1997**, *198*, 549-559.

46. Hedrick, J. L.; Russell, T. P.; Labadie, J.; Lucas, M.; Swanson, S., High Temperature Nanofoams Derived from Rigid and Semi-Rigid Polyimides. *Polymer* **1995**, *36*, 2685-2697.

47. Chung, C.-M.; Lee, J.-H.; Cho, S.-Y.; Kim, J.-G.; Moon, S.-Y., Preparation of Porous Thin Films of a Partially Aliphatic Polyimide. *J. Appl. Polym. Sci.* **2006**, *101*, 532-538.

48. Charlier, Y.; Hedrick, J.; Volksen, W., High Temperature Polymer Nanofoams Based on Amorphous, High $T_g$ Polyimides. *Polymer* **1995**, *36*, 987-1002.

49. Carter, K. R.; DiPietro, R. A.; Sanchez, M. I.; Swanson, S. A., Nanoporous Polyimides Derived from Highly Fluorinated Polyimide/Poly(propylene oxide) Copolymers. *Chem. Mater.* **2001**, *13*, 213-221.

50. Cannarella, J.; Liu, X.; Leng, C. Z.; Sinko, P. D.; Gor, G. Y.; Arnold, C. B., Mechanical Properties of a Battery Separator under Compression and Tension. *J. Electrochem. Soc.* **2014**, *161*, F3117-F3122.

51. Kalnaus, S.; Wang, Y.; Turner, J. A., Mechanical Behavior and Failure Mechanisms of Li-Ion Battery Separators. *J. Power Sources* **2017**, *348*, 255-263.

52. Chen, X. R.; Yao, Y. X.; Yan, C.; Zhang, R.; Cheng, X. B.; Zhang, Q., A Diffusion-Reaction Competition Mechanism to Tailor Lithium Deposition for Lithium-Metal Batteries. *Angew. Chem. Int. Ed.* **2020**, *59*, 7743-7747.

53. Nagasaki, M.; Kanamura, K., High-Performance Lithium Metal Rechargeable Battery Using an Ultrafine Porous Polyimide Separator with Three-Dimensionally Ordered Macroporous Structure. *ACS Appl. Energy Mater.* **2019**, *2*, 3896-3903.

54. Ferrese, A.; Newman, J., Mechanical Deformation of a Lithium-Metal Anode Due to a Very Stiff Separator. *J. Electrochem. Soc.* **2014**, *161*, A1350-A1359.

55. Monroe, C.; Newman, J., The Impact of Elastic Deformation on Deposition Kinetics at Lithium/Polymer Interfaces. *J. Electrochem. Soc.* **2005**, *152*, A396-A404.

56. Na, W.; Lee, A. S.; Lee, J. H.; Hwang, S. S.; Kim, E.; Hong, S. M.; Koo, C. M., Lithium Dendrite Suppression with UV-Curable Polysilsesquioxane Separator Binders. *ACS Appl. Mater. Interfaces* **2016**, *8*, 12852-12858.

57. Wan, J.; Xie, J.; Kong, X.; Liu, Z.; Liu, K.; Shi, F.; Pei, A.; Chen, H.; Chen, W.; Chen, J.; Zhang, X.; Zong, L.; Wang, J.; Chen, L. Q.; Qin, J.; Cui, Y., Ultrathin, Flexible, Solid Polymer

Composite Electrolyte Enabled with Aligned Nanoporous Host for Lithium Batteries. *Nat. Nanotechnol.* **2019**, *14*, 705-711.

58. Guo, D.; Riet, J.; Khan, A.; Guo, Y.; Xu, Z.; Liu, T.; Liu, G., Mesoporous Polyetherimide Thin Films Via Hydrolysis of Polylactide-*b*-Polyetherimide-*b*-Polylactide. *Polym. Chem.* **2021**, *12*, 3939-3946.

59. Yu, H.-C.; Jung, J.-W.; Choi, J.-Y.; Chung, C.-M., Kinetic Study of Low-Temperature Imidization of Poly(amic acid)s and Preparation of Colorless, Transparent Polyimide Films. *J. Polym. Sci., Part A: Polym. Chem.* **2016**, *54*, 1593-1602.

60. Ohkita, T.; Lee, S.-H., Thermal Degradation and Biodegradability of Poly (lactic acid)/Corn Starch Biocomposites. *J. Appl. Polym. Sci.* **2006**, *100*, 3009-3017.

61. Zaragoza, S.; Álvarez, A.; Álvarez, B.; López-Beceiro, J.; Naya, S.; Forcén, P.; Artiaga, R., Thermogravimetric Study of Thermal Degradation of Polyetherimide. *J. Appl. Polym. Sci.* **2015**, *132*, 42329.

62. Lee, S.-C.; Tai, F.-C.; Wei, C.-H.; Yu, J.-I., Atr-Ftir and Nanoindentation Measurements of Pmda-Oda Polyimide Film under Different Curing Temperature. *Mater. Trans.* **2007**, *48*, 1554-1557.

63. Wang, C.; Cao, S.; Chen, W.; Xu, C.; Zhao, X.; Li, J.; Ren, Q., Synthesis and Properties of Fluorinated Polyimides with Multi-Bulky Pendant Groups. *RSC Adv.* **2017**, *7*, 26420-26427.

64. Grabiec, E.; Schab-Balcerzak, E.; Wolińska-Grabczyk, A.; Jankowski, A.; Jarząbek, B.; Kożuch-Krawczyk, J.; Kurcok, M., Physical, Optical and Gas Transport Properties of New Processable Polyimides and Poly(Amideimide)S Obtained from 4,4′-[Oxybis(4,1-Phenylenethio)]Dianiline and Aromatic Dianhydrides. *Polym. J.* **2011**, *43*, 621-629.

65. Savaris, M.; Braga, G. L.; dos Santos, V.; Carvalho, G. A.; Falavigna, A.; Machado, D. C.; Viezzer, C.; Brandalise, R. N., Biocompatibility Assessment of Poly(lactic acid) Films after Sterilization with Ethylene Oxide in Histological Study in vivo with Wistar Rats and Cellular Adhesion of Fibroblasts in vitro. *Int. J. Polym. Sci.* **2017**, *2017*, 1-9.

66. Cuiffo, M. A.; Snyder, J.; Elliott, A. M.; Romero, N.; Kannan, S.; Halada, G. P., Impact of the Fused Deposition (Fdm) Printing Process on Polylactic Acid (PLA) Chemistry and Structure. *Appl. Sci.* **2017**, *7*, 579.

67. Tang, G.; Huang, X.; Ding, H.; Wang, X.; Jiang, S.; Zhou, K.; Wang, B.; Yang, W.; Hu, Y., Combustion Properties and Thermal Degradation Behaviors of Biobased Polylactide Composites Filled with Calcium Hypophosphite. *RSC Adv.* **2014**, *4*, 8985-8993.

68. Lee, T.-H.; Kim, J. H.; Bae, B.-S., Synthesis of Colorless Imide Hybrid Nanocomposites Using Amine Functionalized Oligosiloxane Nano-Building Clusters. *J. Mater. Chem.* **2006**, *16*, 1657-1664.

69. Zhu, Y.; Xie, J.; Pei, A.; Liu, B.; Wu, Y.; Lin, D.; Li, J.; Wang, H.; Chen, H.; Xu, J.; Yang, A.; Wu, C.-L.; Wang, H.; Chen, W.; Cui, Y., Fast Lithium Growth and Short Circuit Induced by Localized-Temperature Hotspots in Lithium Batteries. *Nat. Commun.* **2019**, *10*, 1-7.

70. Sherck, N. J.; Kim, H. C.; Won, Y. Y., Elucidating a Unified Mechanistic Scheme for the DBU-Catalyzed Ring-Opening Polymerization of Lactide to Poly(lactic acid). *Macromolecules* **2016**, *49*, 4699-4713.

71. Grubbs, R. B.; Grubbs, R. H., 50th Anniversary Perspective: Living Polymerization-Emphasizing the Molecule in Macromolecules. *Macromolecules* **2017**, *50*, 6979-6997.

72. Qiu, J.; Charleux, B.; Matyjaszewski, K., Controlled/Living Radical Polymerization in Aqueous Media: Homogeneous and Heterogeneous Systems. *Prog. Polym. Sci.* **2001**, *26*, 2083-2134.

73. Friedman, M., Applications of the Ninhydrin Reaction for Analysis of Amino Acids, Peptides, and Proteins to Agricultural and Biomedical Sciences. *J. Agric. Food Chem.* **2004**, *52*, 386-406.

# Chapter 5. Block Copolymer-Derived Porous Carbon Fibers Enable High $MnO_2$ Loading and Fast Charging in Aqueous Zinc-Ion Battery

This chapter is reproduced from a published manuscript by Dong Guo, Wenqi Zhao, Fuping Pan and Guoliang Liu from the following reference: *Batteries & Supercaps* **2022**, e202100380, doi.org/10.1002/batt.202100380. Reproduced with permission from Wiley. Copyright 2022 The Authors. Batteries & Supercaps published by Wiley-VCH GmbH.

## 5.1 Abstract

Rechargeable aqueous Zn-$MnO_2$ batteries are promising for stationary energy storage because of their high energy density, safety, environmental benignity, and low cost. Conventional gravel $MnO_2$ cathodes have low electrical conductivity, slow ion (de-)insertion, and poor cycle stability, resulting in poor recharging performance and severe capacity fading. To improve the rechargeability of $MnO_2$, strategies have been devised such as depositing micrometer-thick $MnO_2$ on carbon cloth and blending nanostructured $MnO_2$ with additives and binders. The low electrical conductivity of binders and sluggish ion (de-)insertion in micrometer-thick $MnO_2$, however, still limit the fast-charging performance. Herein, we have prepared porous carbon fiber (PCF) supported $MnO_2$ cathodes (PCF@$MnO_2$), comprised of nanometer-thick $MnO_2$ uniformly deposited on electrospun block copolymer-derived PCF that have abundant uniform mesopores. The high electrical conductivity of PCF, fast electrochemical reactions in nanometer-thick $MnO_2$,

and fast ion transport through porous nonwoven fibers contribute to a high rate capability at high loadings. PCF@$MnO_2$, at a $MnO_2$ loading of 59.1wt%, achieves a $MnO_2$-based specific capacity of 326 and 184 mAh $g^{-1}$ at a current density of 0.1 and 1.0 A $g^{-1}$, respectively. Our approach of block copolymer-based PCF as a support for zinc-ion cathode inspires future designs of fast-charging electrodes with other active materials.

## 5.2 Introduction

Reliable energy supports the prosperity of human society since time immemorial.[1, 2] Lithium-ion batteries dominate the secondary energy storage nowadays, but the scarcity and uneven distribution of lithium in Earth's crust, as well as the potential fire hazard, still draw concerns.[3-5] Rechargeable aqueous zinc-ion battery (ZIB) is promising for highly demanding stationary energy storage owing to the abundant zinc reserve, non-flammable aqueous electrolyte, high energy density, environmental friendliness, and low cost.[1, 3-15] The development of fast-charging cathodes for ZIBs, however, remains a challenge.[3, 4, 8, 9, 14, 16] Pioneered by Georges Leclanché in his design of Zn-$MnO_2$ cell since the 1860s,[17] $MnO_2$ has been the primary cathode material in ZIBs due to its high voltage vs. $Zn/Zn^{2+}$ and the aforementioned traits.[12, 18-23] However, the low electrical conductivity and slow ion (de-)insertion of micrometer-sized $MnO_2$ gravels result in poor recharging performance.[19, 24] Furthermore, the bulky $MnO_2$ gravels are susceptible to capacity fading due to low tolerance to cycling-induced volume expansion and $Mn^{2+}$ dissolution,[25-30] limiting the rechargeability.

To overcome the limitations of monolithic $MnO_2$ gravels, $MnO_2$ has been structurally engineered as nanorods[8, 22, 26, 29, 31], nanosheets[20, 32-34] and nanospheres[35-40] *via* hydrothermal reactions. The nanostructured $MnO_2$ to some extent improves the kinetics of ion (de-)insertion.[8,

[20, 26, 29, 31-39] However, the discrete $MnO_2$ nanoparticles rely on conductive additives (such as acetylene black, 15-25wt%) and binders (*i.e.*, PVDF, 10-15wt%) to construct electrically conductive cathodes,[20, 26, 32, 35] yet the inadequate overall conductivity hinders fast charging especially at high current densities.[26, 32, 41] Disparately, electrodepositing $MnO_2$ on carbon cloth yields highly conductive cathodes thanks to the continuous graphitic carbon matrix.[9, 42-45] Due to the limited surface area, however, high mass loading and low thickness of $MnO_2$ on carbon cloth are mutually exclusive.[9, 42-45] Therefore, it is imperative to develop electrically conductive electrodes with high $MnO_2$ loadings while simultaneously maintaining the $MnO_2$ nanostructures to ensure fast charging.

Herein, we report a judiciously designed fast-charging electrode of porous carbon fiber (PCF) supported $MnO_2$ (PCF@$MnO_2$). Nanometer-thick $MnO_2$ is deposited on block copolymer-derived PCF. The graphitic PCF provides high electrical conductivity. Additionally, the internal uniform mesopores, defined by block copolymer microphase separation, offer a high surface area and enable a high loading of $MnO_2$. Systematic investigations into the kinetics of $MnO_2$ deposition suggest that room temperature (RT) incubation of PCF in $KMnO_4$ solutions favors uniform in-mesopore deposition of thin $MnO_2$. Benefiting from the synergistically combined advantages of good electrical conductivity, fast ion transport, and fast electrochemical reactions in thin $MnO_2$, the resulting PCF@$MnO_2$ containing 59.1wt% of $MnO_2$ exhibits a high $MnO_2$-based capacity of 326 and 184 mAh $g^{-1}$ at a current density of 0.1 and 1.0 A $g^{-1}$, respectively, as well as outstanding specific power/energy densities.

## 5.3 Experimental Section

### *5.3.1 Chemicals.*

Methyl methacrylate (MMA), acrylonitrile (AN), and aluminum oxide (alumina, activated, neutral) were purchased from Sigma-Aldrich. MMA and AN were passed through an alumina-packed column chromatography to remove inhibitors before polymerizations. Cumyl dithiobenzoate (CDB), 2,2′-azobis(2-methylpropionitrile) (AIBN), benzene, dimethyl sulfoxide (DMSO), N,N-dimethylformamide (DMF), methanol, and lithium bromide (LiBr) were purchased form Sigma-Aldrich and used as received. Potassium permanganate ($KMnO_4$), water (HPLC grade), isopropanol, acetone, anhydrous ethanol, zinc sulfate heptahydrate ($ZnSO_4 \cdot 7H_2O$), manganese sulfate monohydrate ($MnSO_4 \cdot H_2O$), zinc foil (0.25 mm in thickness), CR2032 coin cell cases, spacers, and springs were purchased from Fisher Scientific. The CR2032 coin cell cases, spacers and springs were cleaned before use by sonicating in an isopropanol and acetone (w/w = 1:1) solution for 1 h, subsequently drying at 80 ℃ overnight *in vacuo*. The zinc foil was cut into discs of 11 mm in diameter, then sonicated in anhydrous ethanol for 1 h. The resulting zinc discs were dried at 80 ℃ overnight *in vacuo* before serving as anodes. The Whatman 1823-090 glass microfiber filters (GE Healthcare Life Sciences) were cut into 19-mm-diameter discs and then used as separators. Deuterated dimethyl sulfoxide (DMSO-$d_6$) was purchased from Cambridge Isotope Laboratories, Inc.

### *5.3.2 Instruments.*

Size exclusion chromatography (SEC) was conducted on a Tosoh EcoSEC HLC-8320 equipped with a Wyatt DynaPro Nanostar light scattering detector, using DMF containing 0.05 M of LiBr as the eluent at a flow rate of 0.5 mL $min^{-1}$. Proton nuclear magnetic resonance ($^1H$ NMR) spectra

were collected on a 400 MHz Varian Unity in DMSO-$d_6$. The electrospinning was performed at a voltage of 18 kV (Acopian high voltage power supply P030HP1) and a flow rate of 0.015 μL $min^{-1}$ (Braintree Scientific BS-300). The distance between the syringe needle and rotating drum collector was 18 cm, and the rotational rate was 200 rpm. The oxidation and carbonization were performed in a Lindberg Blue M STF55433C tube furnace. Nitrogen sorption was performed on a Micromeritics 3Flex Adsorption Analyzer. Scanning electron microscopy (SEM) was conducted on a LEO Zeiss 1550. The coin cells were pressed on an MTI MSK-160 E. Cyclic voltammetry was performed on a PARSTAT 4000 (Princeton Applied Research-AMETEK). The rate capabilities of zinc-ion coin cells were tested on a Neware BTS4000. X-ray diffraction (XRD) was performed on a Rigaku Miniflex 600.

### *5.3.3 Synthesis of polymer precursors for carbon fibers.*

PMMA-*b*-PAN with a number-average molecular weight ($M_n$) of 56-*b*-76 kDa was synthesized according to our previous report.[45] To a 500 mL Schlenk flask equipped with a magnetic stir bar, MMA (63.8 mL), CDB (163.2 mg), AIBN (19.7 mg) and benzene (88.0 mL) were added. The solution was degassed with three freeze-pump-thaw cycles, and reacted at 65 ℃ for 45 h. Afterwards, the resulting pink solution was dropwise added to methanol (~1 L). The product as a pink precipitate, denoted as PMMA-CTA, was collected *via* vacuum filtration and dried overnight *in vacuo*. To synthesize PMMA-*b*-PAN, in a 500 mL Schlenk flask, PMMA-CTA (30444.0 mg), AN (125.6 mL), AIBN (18.5 mg) were dissolved in DMSO (340.0 mL). The resulting solution was degassed with three freeze-pump-thaw cycles, and reacted at 65 ℃ for 48 h. Afterwards, the viscous yellowish solution was poured into methanol (~2 L). The block copolymer product was collected *via* vacuum filtration, followed by drying at 70 ℃ overnight *in vacuo*. Besides PMMA-

*b*-PAN as the precursor of porous carbon fibers (PCF), PAN homopolymer ($M_n$ = 140 kDa) was synthesized to produce non-porous carbon fibers (CF). In a 500 mL Schlenk flask, AN (50.00 mL), CDB (61.2 mg), AIBN (7.4 mg), DMSO (135.00 mL) were mixed and degassed with three freeze-pump-thaw cycles, and then reacted at 65 ℃ for 48 h. Subsequently, the solution was added dropwise to methanol (~1 L). The PAN product was collected *via* vacuum filtration, followed by drying at 70 ℃ overnight *in vacuo*.

### *5.3.4 Preparation of porous carbon fibers.*

The PMMA-*b*-PAN (2.0 g) was dissolved in DMF (13 mL), and the solution was electro-spun into a polymer mat (42 cm by 18 cm). The resulting polymer mats were oxidized in an air-purged tube furnace that was ramped from room temperature (RT) to 280 ℃ at a rate of 1 ℃ $min^{-1}$ and then kept isothermal at 280 ℃ for 8 h. Subsequently, the polymer mats were carbonized by ramping the temperature to 800 ℃ at 10 ℃ $min^{-1}$ in a nitrogen stream of 100 standard cubic centimeters per minute (sccm), and then keeping isothermal at 800 ℃ for 1 h. After cooling down to RT, the porous carbon fibers were collected as black mats. As a control experiment, carbon fiber (CF) mats containing no mesopores were prepared from the PAN homopolymer with the same electrospinning and pyrolysis procedures.

### *5.3.5 Preparation of PCF@$MnO_2$ cathodes.*

To elucidate the impact of incubation on the cathode morphology and fast-charging performance, PCF@$MnO_2$ cathodes were prepared in two different $KMnO_4$ aqueous solutions: (i) 10 mM at 80 ℃ and (ii) 63 mM (1wt%) at RT. To incubate PCF@$MnO_2$ at 80 ℃, $KMnO_4$ solutions (10 mM, 100 mL per vial, 4 vials in total) were freshly prepared in water (HPLC grade) and then set in an

oil bath at 80 °C. After ~30 min for the solutions to reach an equilibrium temperature, a piece of PCF mat (100 mg) was immersed in each vial of $KMnO_4$ solution. The four solutions were sealed and incubated for 15, 30, 60 and 120 min, respectively. To incubate PCF@$MnO_2$ at RT, fresh $KMnO_4$ solutions (63 mM, 100 mL per vial, 5 vials in total) were equilibrated at room temperature. Then, 100 mg of PCF mat was immersed in each vial of $KMnO_4$ solution. The solutions were covered and incubated for 3, 6, 12, 24 and 48 h, respectively. After incubation, all PCF@$MnO_2$ mats were collected from the $KMnO_4$ solutions and rinsed with deionized water three times to remove any residual $KMnO_4$. Afterwards, the PCF@$MnO_2$ mats were dried at 80 °C overnight *in vacuo*.

### *5.3.6 Aqueous zinc-ion battery tests.*

The fast-charging performance was evaluated in CR2032 coin cells consisting of PCF@$MnO_2$ cathodes, zinc metal anodes, glass fiber separators, and aqueous electrolytes. The aqueous electrolyte contained 1 M of $ZnSO_4$ and 0.1 M of $MnSO_4$. An aliquot of 100 μL of aqueous electrolyte was added in each cell. The mass of $MnO_2$ in each PCF@$MnO_2$ cathode was ~1.4 mg. The assembled zinc-ion coin cells were tested at $MnO_2$-based current densities of 0.1, 0.2, 0.4, 0.6, 0.8, 1.0, 2.0, 3.0 and 6.0 A $g^{-1}$ between 1.80 and 1.00 volt to determine the rate capability.

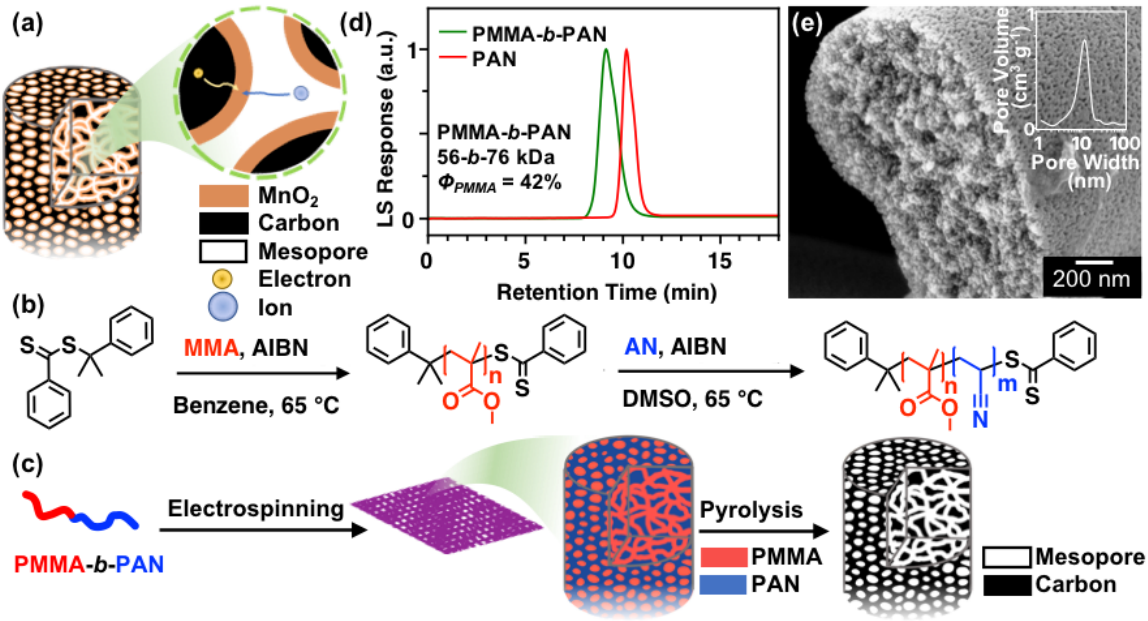


**Figure 5.1.** Preparation of PCF and PCF@$MnO_2$ cathodes. (a) Design of high-loading fast-charging PCF@$MnO_2$ cathode using PCF with uniform mesopores. The high surface area of internal mesopores in PCF affords a high loading of nanometer-thick $MnO_2$, which minimizes the ion (de-)insertion length to achieve fast charging. The continuous fiber provides highly conductive pathways for electrons to ensure fast charging. (b) Synthesis of PMMA-b-PAN as a PCF precursor. (c) Preparation of PCF. PMMA-b-PAN was electro-spun into a mat of block copolymer fibers. The zoomed-in view shows that block copolymer fibers undergo microphase separation to form uniform nanoscale domains and pyrolysis to form mesoporous carbon structures. (d) Size exclusion chromatography (SEC) traces of PMMA-b-PAN and PMMA using a light scattering (LS) detector. (e) Representative cross-sectional SEM image of PCF shows mesopores uniformly distributed in the fiber. The inset shows the pore size distribution with a median pore width of 12 nm, as determined by gas sorption.

## 5.4 Results

Fast charging requires high electrical conductivity, swift ion transport, and prompt electrochemical reactions in the electrode. PCF@$MnO_2$ meets these criteria because i) PCF has high electrical conductivity, ii) the porous fibrous network allows for fast ion transport, and iii) the uniform thin $MnO_2$ affords fast electrochemical reactions (Figure 5.1a). Importantly, PCF has highly uniform mesopores to enable high loadings of $MnO_2$ in the cathode. In this work, PCF mats were prepared by electrospinning, microphase separation, and pyrolysis of block copolymer poly(methyl methacrylate)-*block*-polyacrylonitrile (PMMA-*b*-PAN) fibers. Synthesized *via* reversible addition-fragmentation chain-transfer (RAFT) polymerization,[45-47] PMMA-*b*-PAN had a number-average molecular weight ($M_n$) of 56-*b*-76 kDa, giving a PMMA weight fraction ($\phi_{PMMA}$) of 42% (Figure 5.1b, d and S5.1). After electrospinning and pyrolysis, PAN was converted to carbon, and PMMA was decomposed to create mesopores (Figure 5.1c). The PCF exhibited a median mesopore width of ~12 nm (Figure 5.1e) with a high specific surface area of 537 $m^2$ $g^{-1}$ (Figure S5.2).

The high surface area facilitated the subsequent $MnO_2$ deposition *via* incubation in $KMnO_4$ solutions involving the following chemical reaction.[45]

$$4\,KMnO_4 + 3\,C + H_2O \rightarrow 4\,MnO_2 + K_2CO_3 + 2\,KHCO_3$$

$MnO_2$ was produced from the redox reaction between $KMnO_4$ and carbon on the interface of the aqueous $KMnO_4$ solution and PCF. $KMnO_4$ served as the source of Mn. In this redox reaction, the oxidation state of Mn in $KMnO_4$ reduced to produce $MnO_2$. Meanwhile, a small amount of carbon on the interface was oxidized. The resulting $MnO_2$ was not soluble in the aqueous medium, thus being deposited on PCF. The $MnO_2$ was primarily in the form of $\delta$-$MnO_2$ (Figure S5.3). To examine the effects of incubation on $MnO_2$ deposition, we prepared PCF@$MnO_2$ under two

conditions: 1) in a 10 mM $KMnO_4$ solution at 80 °C for up to 120 min and 2) in a 63 mM $KMnO_4$ solution at room temperature (RT) for up to 48 hours. The resulting PCF@$MnO_2$ were characterized using scanning electron microscopy (SEM) (Figure 5.2). PCF@$MnO_2$ incubated at 80 °C displayed petal-like $MnO_2$ nanosheets on the fiber surface, because in an oxidation-intercalation-exfoliation process,[48] carbon sheets exfoliated from PCF and $MnO_2$ was deposited on the exposed carbon sheets. As incubation time was increased, the size and areal density of $MnO_2$ petals increased. As incubation time was further increased, the redox reaction consumed the exfoliated carbon sheets, resulting in discontinuous carbon detached from PCF and a large amount of $MnO_2$ deposited outside the mesopores (Figure 5.2a to e). Conversely, the incubation at RT maintained intact PCF and thin $MnO_2$ layers uniformly deposited on both internal and external surfaces of PCF (Figure 5.2f to j). As a result, the mesopore widths decreased, confirming that $MnO_2$ filled in mesopores. To highlight the importance of mesopores, carbon fibers (CF) containing no mesopores were also incubated under similar conditions. CF incubated at 80 °C underwent a surface exfoliation and thus displayed similar petal-like $MnO_2$ sheets (Figure 5.3a-e). Whereas the incubation of CF at RT yielded uniform thin $MnO_2$ layers on CF surface (Figure 5.3f-j).

**Table 5.1.** Mass loadings of $MnO_2$ in PCF@$MnO_2$ and CF@$MnO_2$.

| Incubation Condition | 10 mM $KMnO_4$ at 80 °C | | | | 63 mM $KMnO_4$ at RT | | | | |
|---|---|---|---|---|---|---|---|---|---|
| Time | 15 min | 30 min | 60 min | 120 min | 3 h | 6 h | 12 h | 24 h | 48 h |
| $\phi_{MnO2}$ of PCF@$MnO_2$ (%) | 34.6 | 42.7 | 55.9 | 71.2 | 23.7 | 31.0 | 40.9 | 50.2 | 59.1 |
| $S_{MnO2}$ (mg $cm^{-2}$)[a)] | 1.66 | 2.29 | 3.71 | 6.53 | 1.00 | 1.42 | 2.14 | 3.02 | 4.16 |
| $\phi_{MnO2}$ of CF@$MnO_2$ (%) | 9.69 | 18.5 | 32.3 | 53.4 | 4.05 | 6.57 | 11.6 | 18.1 | 25.7 |
| $\phi_{mesopore}$ of PCF@$MnO_2$ (%) | 79.7 | 69.6 | 62.2 | 53.6 | 86.5 | 84.4 | 81.0 | 78.0 | 76.0 |

[a)] Areal $MnO_2$ loading of PCF@$MnO_2$.

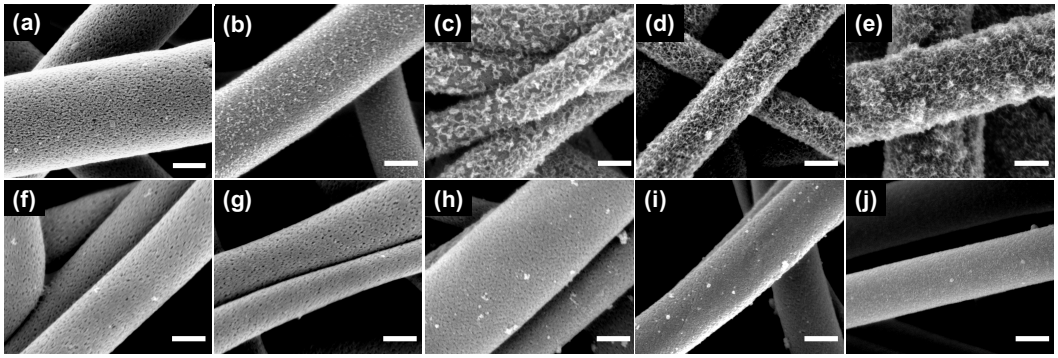


**Figure 5.2.** Morphologies of PCF@$MnO_2$ cathodes. PCF@$MnO_2$ cathodes were prepared by incubating (a) pristine PCF in an aqueous solution of 10 mM $KMnO_4$ at 80 ℃ for (b) 15 min, (c) 30 min, (d) 60 min, and (e) 120 min or incubating PCF in an aqueous solution of 63 mM $KMnO_4$ at RT for (f) 3 h, (g) 6 h, (h) 12 h, (i) 24 h, and (j) 48 h, respectively. Scale bars, 300 nm.

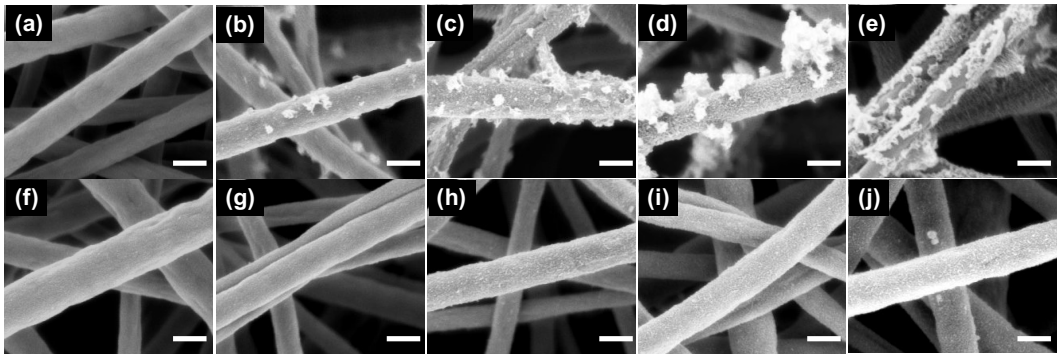


**Figure 5.3.** Morphologies of CF@$MnO_2$. CF@$MnO_2$ were prepared by incubating (a) CF in a 10 mM $KMnO_4$ aqueous solution at 80 ℃ for (b) 15 min, (c) 30 min, (d) 60 min, and (e) 120 min or incubating CF in a 63 mM $KMnO_4$ solution at RT for (f) 3 h, (g) 6 h, (h) 12 h, (i) 24 h, and (j) 48 hours, respectively. Scale bars, 300 nm.

The mass loadings of $MnO_2$, $\phi_{MnO2}$, after varying incubation time was calculated using Equation 5.1.[45]

$$\phi_{MnO2} = \frac{(m_{PCF@MnO2} - m_{PCF}) \times 4M_{MnO2}}{m_{PCF@MnO2} \times (4M_{MnO2} - 3M_C)} \quad (5.1)$$

where $m_{PCF@MnO2}$ and $m_{PCF}$ are the masses of PCF@$MnO_2$ and PCF mats, respectively. $M_{MnO2}$ and $M_C$ are the molar mass of $MnO_2$ and carbon, 86.9 and 12.0 g $mol^{-1}$, respectively. As summarized in **Table 5.1**, **Figure 5.4**a and b, $\phi_{MnO2}$ increased with incubation time under both conditions. As expected, a higher incubation temperature at 80 ℃ enabled faster $MnO_2$ deposition than RT. After incubating at 80 ℃ for 120 min, $\phi_{MnO2}$ attained 71.2%, almost comparable to $MnO_2$ loadings in cathodes prepared using $MnO_2$ powders, conductive additives, and binders.[20, 26, 32, 35] The incubation at RT exhibited slow kinetics, but the PCF@$MnO_2$ still reached a high $\phi_{MnO2}$ of 59.1% after 48 h, approaching the $MnO_2$ loading in powder-additive-binder based cathodes.

The in-mesopore nanometer-thick $MnO_2$ is imperative for fast charging because it has a large electrolyte/electrode interface and a short ion diffusion path.[9] To estimate the fraction of in-mesopore $MnO_2$, PCF@$MnO_2$ was compared against the corresponding CF@$MnO_2$ (Table 5.1, Figure 5.4a and b). The CF@$MnO_2$ had a smaller $\phi_{MnO2}$ than the corresponding PCF@$MnO_2$ because CF had no mesopores. The disparity of $\phi_{MnO2}$ between CF@$MnO_2$ and PCF@$MnO_2$ provides a means to estimate the in-mesopore fraction of $MnO_2$, $\phi_{mesopore}$, using Equation 5.2.

$$\phi_{mesopore} = \frac{(m_{PCF@MnO2} - m_{PCF}) - (m_{CF@MnO2} - m_{CF})}{m_{PCF@MnO2} - m_{PCF}} \qquad (5.2)$$

where $m_{PCF@MnO2}$, $m_{PCF}$, $m_{CF@MnO2}$ and $m_{CF}$ are the masses of PCF@$MnO_2$, PCF, CF@$MnO_2$ and CF mats, respectively. PCF@$MnO_2$ incubated at RT displayed a higher $\phi_{mesopore}$ than the counterpart incubated at 80 ℃ at the same overall loading of $MnO_2$ (Figure 5.4c), owing to two reasons. First, the slow incubation reaction at RT and high $KMnO_4$ concentration avoided the depletion of $KMnO_4$ in the mesopores. Second, the RT-incubation minimized the surface exfoliation of PCF occurring at high temperatures, thus almost no petal-like $MnO_2$ appeared on PCF surfaces (Figure 5.2). The in-mesopore deposition of $MnO_2$ was further confirmed by the pore size reduction of PCF@$MnO_2$, as characterized using nitrogen sorption (Figure 5.4d, S5.2).

The median mesopore size of pristine PCF was 11.7 nm. As $\phi_{MnO2}$ increased from 23.7% to 40.9% and to 59.1% (denoted as PCF@$MnO_2$ RT-23.7%, -40.9% and -59.1%), the pore width decreased from 9.3 to 3.4 and to 2.9 nm, indicating increasing in-mesopore $MnO_2$ deposition of 1.2, 4.2, and 4.4-nm-thick, respectively, and concurring the observation under SEM (Figure 5.2f-j). Importantly, PCF@$MnO_2$ incubated at 80 ℃ with a $\phi_{MnO2}$ of 55.9% (denoted as PCF@$MnO_2$ 80 ℃-55.9%) displayed a larger pore width of 5.4 nm than the 2.9 nm for the counterpart at RT with a $\phi_{MnO2}$ of 59.1% (PCF@$MnO_2$ RT-59.1%), further consolidating that the incubation at RT allowed more in-mesopore deposition of $MnO_2$ and held greater promise for producing fast-charging electrodes.

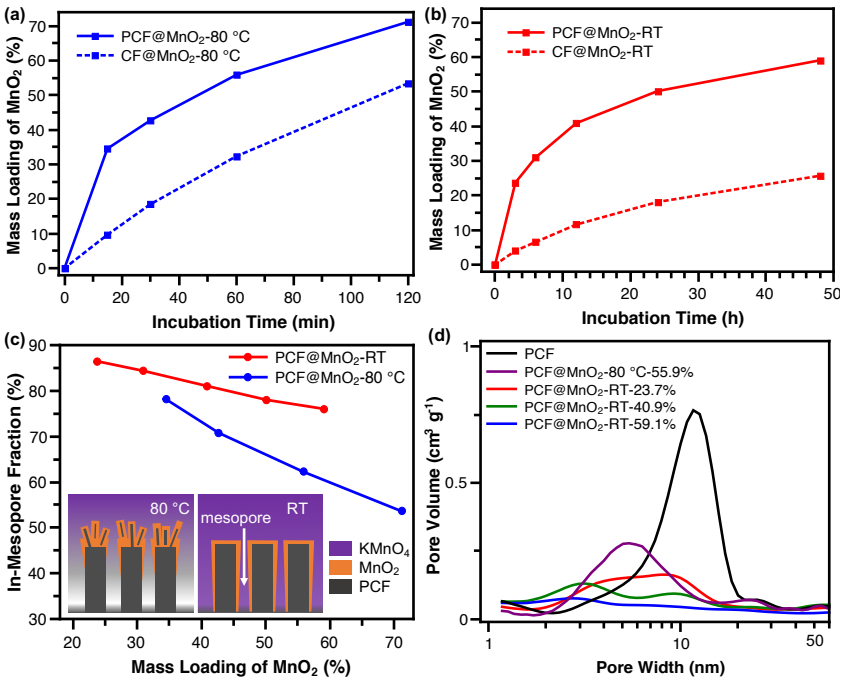


**Figure 5.4.** Mass loadings of $MnO_2$ ($\phi_{MnO2}$) in PCF@$MnO_2$ and CF@$MnO_2$ incubated at (a) 80 ℃ and (b) RT. (c) The in-mesopore fraction of $MnO_2$ ($\phi_{mesopore}$) decreased at higher $\phi_{MnO2}$. Incubation at RT favors higher $\phi_{mesopore}$. The insets show the carbon exfoliation and $KMnO_4$ depletion at 80 ℃ resulted in less in-mesopore $MnO_2$, whereas RT-incubation uniformly deposited

$MnO_2$ both inside and outside mesopores. (d) Pore size distribution confirms that pore widths decreased at higher $\phi_{MnO2}$ due to $MnO_2$ filling in mesopores. Incubation at RT yields more $MnO_2$ deposition in the mesopores than at 80 ℃.

The electrochemical kinetics of PCF@$MnO_2$ was investigated using cyclic voltammetry (Figure 5.5a, b and S5.4). PCF@$MnO_2$ 80 ℃-55.9% and RT-59.1% exemplified the current-voltage profiles at different scan rates, exhibiting two oxidative peaks (Peak 1 near 1.56V, Peak 2 near1.61 V) and two reductive peaks (Peak 3 near 1.37, Peak 4 near 1.23 V) due to the debatable two-regime electrochemical reactions reported in the literature.[8, 9, 49, 50] Usually the peak currents, $i$, scales with scan rates, $v$, following the relationship $i = av^b$, where $a$ is a constant and the exponent $b$ is indicative of the electrochemical kinetics to be battery-like or capacitor-like.[51] An ideal battery has a $b$ value of 0.5 and an ideal capacitor displays $b$ = 1.[51, 52] Peak 1 showed $b$ values of 0.56 and 0.55 for PCF@$MnO_2$ 80 ℃-55.9% and RT-59.1%, respectively, suggesting dominantly battery-like energy storage (Figure 5.5c and d). Peak 2 exhibited $b$ values of 0.70 and 0.69 for PCF@$MnO_2$ 80 ℃-55.9% and RT-59.1%, respectively, implying combined behaviors of battery and capacitor. Peak 3 and 4, as the reversed reactions of Peak 2 and 1, respectively, presented similar kinetics during discharging.

To further decouple the capacitive and diffusion-controlled contributions, the currents at varying scan rates from 0.1 to 0.5 mV $s^{-1}$ were analyzed using Equation 5.3.[53]

$$i = k_1 v + k_2 v^{0.5} \quad (5.3)$$

where $k_1$, $k_2$ are constants, $k_1 v$ represents the capacitive contribution and $k_2 v^{0.5}$ is the diffusion-controlled contribution.[53] The decoupled currents displayed total capacitive contributions in the range of 53% - 75% for PCF@$MnO_2$ 80 ℃-55.9%, and 49% - 69% for PCF@$MnO_2$ RT-59.1% (Figure 5.5e and f). The capacitive contributions for PCF@$MnO_2$ 80

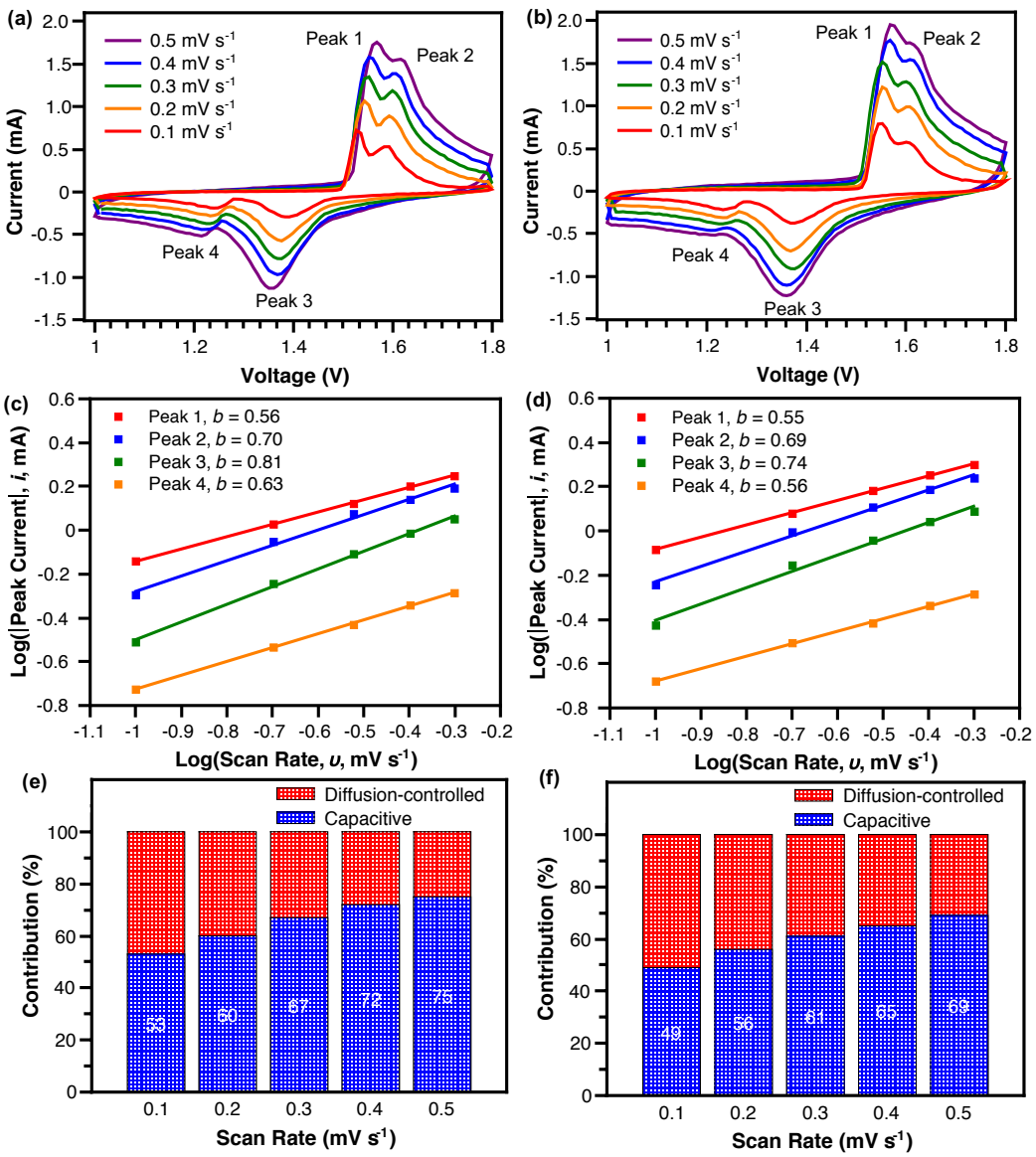


**Figure 5.5.** Kinetic analysis of PCF@$MnO_2$. (a, b) Cyclic voltammograms, (c, d) metric b of peak currents, and (e, f) capacitive contributions of (a, c, e) PCF@$MnO_2$ 80 °C-55.9% and (b, d, f) PCF@$MnO_2$ RT-59.1%.

°C-55.9% were in general slightly higher than PCF@$MnO_2$ RT-59.1%, presumably due to two reasons: i) PCF@$MnO_2$ 80 °C-55.9% has a higher specific surface area than PCF@$MnO_2$ RT-59.1%, resulting from less in-mesopore $MnO_2$ deposition (Figure S5.2). The higher surface area of PCF@$MnO_2$ 80 °C-55.9% resulted in more ion storage on surfaces. ii) The uniform $MnO_2$ thin

layer and good electrical conductivity of PCF in PCF@$MnO_2$ RT-59.1% better facilitated the diffusion-controlled ion (de-)insertion.

The fast charging of PCF@$MnO_2$ cathodes was evaluated using rate capability at increasing current densities. PCF@$MnO_2$ 80 ℃-55.9%, RT-59.1% (Figure 5.6a, b) and all other cathodes (Figure S5.5) exhibited a two-stage discharging voltage profile because of the two-regime mechanism.[8, 9, 49] As the current density increased from 0.1 to 6.0 A $g^{-1}$, all PCF@$MnO_2$ cathodes showed decreasing $MnO_2$-based specific capacities because fast charging rates retarded the cathodic reactions. PCF@$MnO_2$ cathodes with higher $\phi_{MnO2}$ displayed lower rate capabilities, because thicker $MnO_2$ layers hindered electron conduction and slowed down ion (de-)insertion (Figure 5.6c and d). After charging at 6.0 A $g^{-1}$, all PCF@$MnO_2$ cathodes were cycled at 0.1 A $g^{-1}$ again. The recovered capacities indicated good structural stability of PCF@$MnO_2$ at various current densities.

The RT-incubated PCF@$MnO_2$ cathodes showed better rate capability than the 80 ℃-incubated analogues at similar $\phi_{MnO2}$, confirming that the uniform thin-layer $MnO_2$ on PCF benefited better fast charging than the petal-like $MnO_2$ sheet on exfoliated PCF (Figure 5.6e). The long-term cycle stability of PCF@$MnO_2$ is also expected to improve because the PCF supported thin-layer $MnO_2$ can better tolerate volume expansion. Furthermore, the mesopores confine the potentially dissolved $Mn^{2+}$ and enable better $MnO_2$ recovery during cycling.[25-30] After initial charging at 0.1 A $g^{-1}$ for 5 cycles, PCF@$MnO_2$ 80 ℃-55.9% and RT-59.1% were repeatedly charged at a current density of 1.0 A $g^{-1}$. PCF@$MnO_2$ 80 ℃-55.9% and RT-59.1% both displayed stable specific capacities for 500 cycles (Figure 5.6f). The slight increase in specific capacity after 50 cycles is presumably resulted from the electric activation and recovered $Mn^{2+}$ additives.[9, 25, 29, 50, 54] The areal loading of $MnO_2$ significantly altered the energy density and power density. The

RT-incubated PCF@$MnO_2$ with areal $MnO_2$ loadings of 1.00 and 1.42 mg $cm^{-2}$ showed leading $MnO_2$-based energy and power densities (Figure 5.6g). A $MnO_2$ areal loading of ~2 mg $cm^{-2}$ is widely employed in cathodes consisting of nanostructured $MnO_2$, conductive additives and binders.[6, 20] PCF@$MnO_2$ with a $MnO_2$ loading of 2.14 mg $cm^{-2}$ exhibited comparable energy and power densities with graphene scroll-coated $\alpha$-$MnO_2$ nanowires,[26] implying the good electrical conductivity of graphitic PCF and graphene is crucial for fast charging. Even at high loadings of 3.06 and 4.16 mg $cm^{-2}$, PCF@$MnO_2$ retained high energy and power densities comparable to $\alpha$-$MnO_2$ and $\beta$-$MnO_2$ cathodes that were at a much lower $MnO_2$ loading of ~2 mg $cm^{-2}$.

Our RT-incubated PCF@$MnO_2$ cathodes exhibit outstanding fast-charging performance at high mass loadings in aqueous zinc-ion batteries. The PCF@$MnO_2$ cathodes embrace following attributes: 1) good electrical conductivity of PCF, 2) fast ion (de-)insertion in nanometer-thick $MnO_2$, and 3) fast ion transport in the porous nonwoven cathodic structure. Based on the findings herein, we propose that future designs of superior fast-charging $MnO_2$-based cathodes must fulfill the following characteristics. First, $MnO_2$ should be in the form of low-dimension nanostructures, preferably nanometer-thick layers. The low-dimension $MnO_2$ promotes fast ion (de-)insertion by increasing the electrode/electrolyte interface and shortening the ion diffusion path.[9, 20, 32-34] Additionally, the low-dimension $MnO_2$ within confined spaces enables long-term cycle stability because of the tolerance to volume expansion and the ability to recover dissolved $Mn^{2+}$.[25-30] Second, fast-charging cathodes demand good electrical conductivity. Intimate $MnO_2$/matrices contact and highly electroconductive matrices (*e.g.*, graphitic carbon fibers and graphene) are essential to ensure good electrical conductivity.[26] Third, a porous network benefits fast charging because of easy electrolyte infiltration and fast ion transport. With internal mesopores molecularly

defined by block copolymers, the porous nonwoven fibrous structure from electrospinning is highly effective in high loading and fast charging.

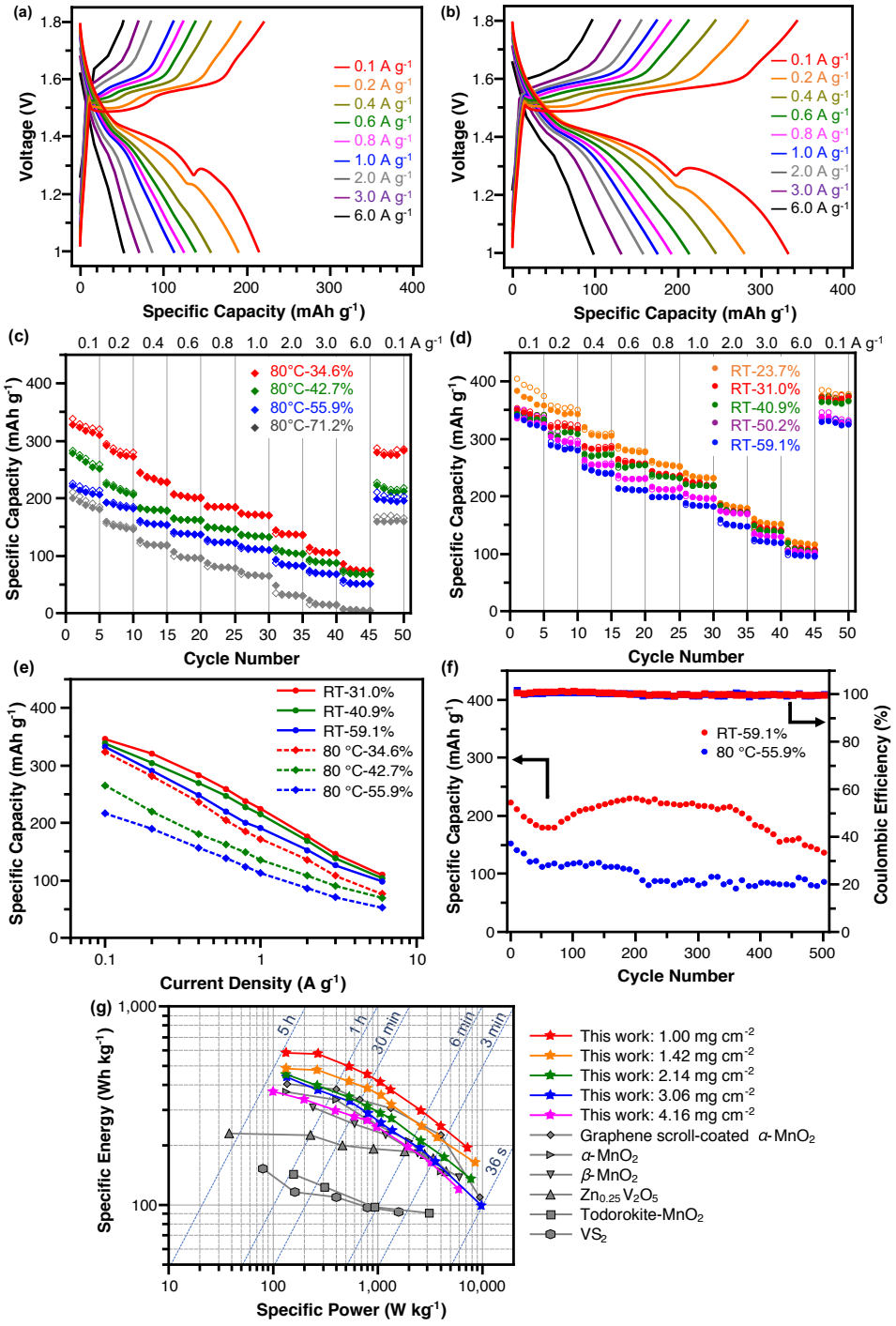


**Figure 5.6.** (a, b) Charge-discharge profiles and (c, d) rate capability of PCF@$MnO_2$ (a, c) 80 °C-55.9% and (b, d) RT-59.1% in aqueous ZIBs. (e) Comparison of the specific capacity of cathodes

prepared at varying temperatures with varying $MnO_2$ loadings. PCF@$MnO_2$ cathodes incubated at RT exhibited higher rate capabilities than the counterparts incubated at 80 °C at similar $MnO_2$ loadings. (f) Cycle stability tests of both PCF@$MnO_2$ 80 °C-55.9% and RT-59.1%. (g) Ragone plot of PCF@$MnO_2$ in comparison with other cathodes: graphene scroll-coated α-$MnO_2$,[26] α-$MnO_2$,[8] β-$MnO_2$,[6] $Zn_{0.25}V_2O_5$,[55] Todorokite-$MnO_2$[56] and $VS_2$[57]. The areal $MnO_2$ loadings of our materials are shown.

## 5.5 Conclusions

In summary, we have prepared PCF@$MnO_2$ consisting of nanometer-thick $MnO_2$ deposited on block copolymer-derived PCF that had a large amount of uniform mesopores. RT incubation of PCF in $KMnO_4$ solutions promoted more uniform in-mesopore deposition of $MnO_2$ than high-temperature incubation. As cathodes in aqueous ZIB, PCF@$MnO_2$ exhibited fast-charging capabilities, owing to the high electrical conductivity of PCF, fast ion (de-)insertion in nanometer-thick $MnO_2$, and fast ion transport through the fibrous cathode. PCF@$MnO_2$ reached a high loading of 59.1% of $MnO_2$ and showed a high capacity of 326 and 184 mAh $g^{-1}$ at a current density of 0.1 and 1.0 A $g^{-1}$, respectively. This work is expected to inspire the design of fast-charging Mn-based cathodes and advance the development of high energy/power-density batteries.

## 5.6 Supporting Information

The $^1$H NMR spectra elucidated the molecular structures of PMMA-CTA and PMMA-*b*-PAN as labeled in Figure S5.1. Particularly, in the spectrum of PMMA-*b*-PAN, peak a' at 3.55 corresponded to the methacrylate protons in PMMA repeating units, and peak e at 3.14 corresponded to the methine proton in PAN repeating units. The ratio of peak a' and e, 100:88, indicated the weight fraction of PMMA ($\phi_{PMMA}$) to be 42% using Equation S1, concurring the $\phi_{PMMA}$ determined using light scattering in SEC traces.

$$\phi_{PMMA} = \frac{I_{a'}/3 \times 100.1}{I_{a'}/3 \times 100.1 + I_e \times 53.06} \quad \text{(S1)}$$

where $I_{a'}$ and $I_e$ are the integrals of peak a' and e. 100.1 and 53.06 g mol$^{-1}$ are the molar masses of PMMA and PAN repeating units, respectively.

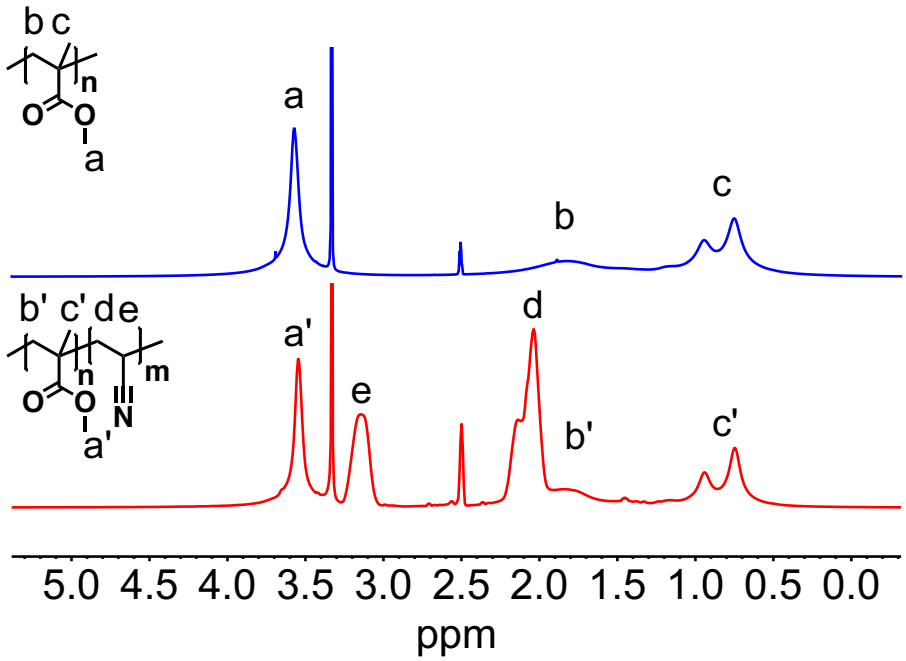


**Figure S5.1.** $^1$H NMR spectra of PMMA-CTA (upper) and PMMA-b-PAN (lower).

The pore size distributions of PCF@$MnO_2$ at varying $MnO_2$ loadings were characterized using nitrogen sorption isotherms. The pristine PCF had a large amount of uniform mesopores, therefore exhibited a high specific surface area of 537 $m^2$ $g^{-1}$. Whereas CF containing no mesopores showed a low specific surface area of only 52 $m^2$ $g^{-1}$. For RT-incubated PCF@$MnO_2$, as the $MnO_2$ loadings increased from 23.7% to 40.9%, and to 59.1% (denoted as PCF@$MnO_2$ RT-23.7%, -40.9% and -59.1%, respectively), the surface area decreased from 194 to 190, and to 184 $m^2$ $g^{-1}$, indicating the increasing in-mesopore $MnO_2$ deposition. Importantly, PCF@$MnO_2$ incubated at 80 °C with a $MnO_2$ loading of 55.9% (denoted as PCF@$MnO_2$ 80 °C-55.9%) showed a larger surface area of 224 $m^2$ $g^{-1}$ than the 184 $m^2$ $g^{-1}$ for the counterpart at RT with a $MnO_2$ loading of 59.1% (denoted as PCF@$MnO_2$ RT-59.1%), consolidating that the RT-incubation allowed more in-mesopore $MnO_2$ deposition than high temperatures.

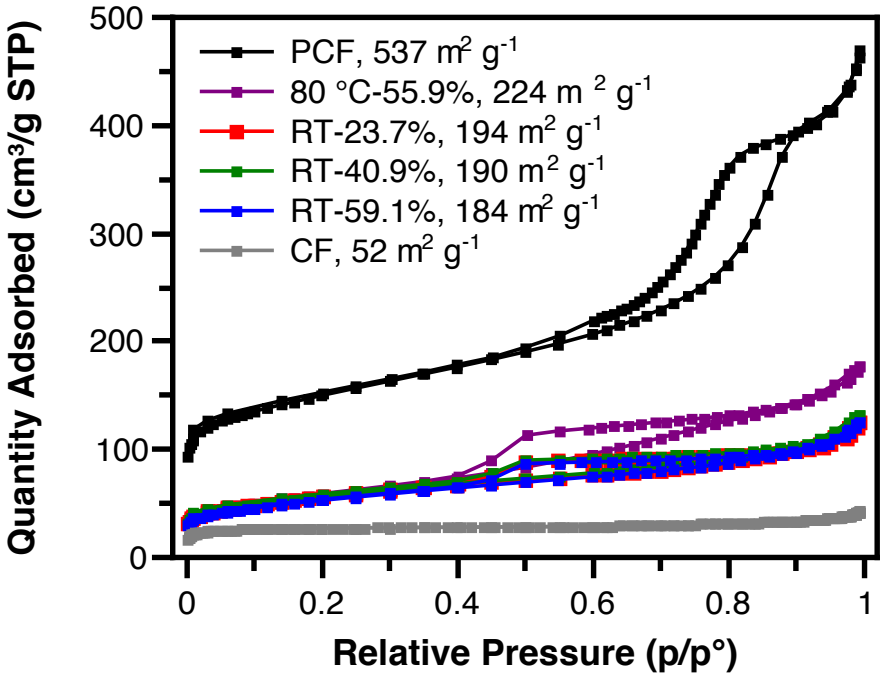


**Figure S5.2.** Nitrogen sorption isotherms of PCF, PCF@$MnO_2$, and CF.

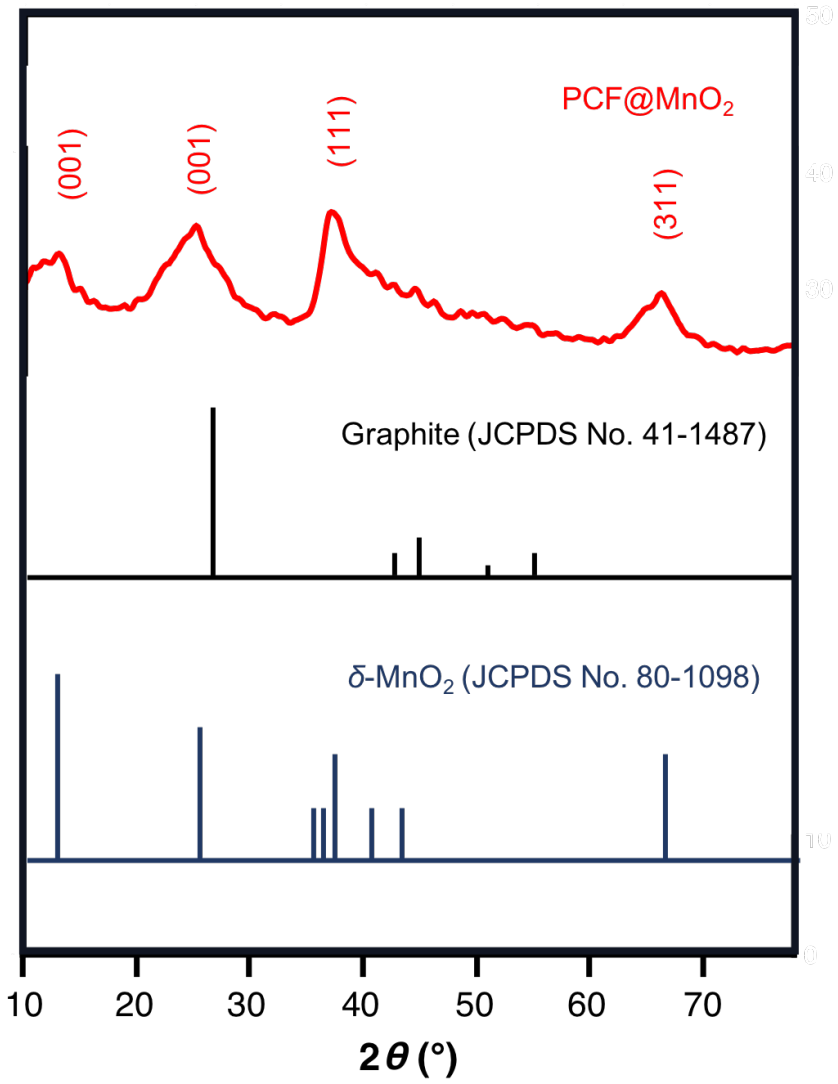


**Figure S5.3.** X-ray diffraction spectrum of PCF@$MnO_2$, JCPDS references of graphite and δ-$MnO_2$.

The PCF@$MnO_2$ was characterized using X-ray diffraction. The crystal peaks of the PCF@$MnO_2$ appear as a combination of JCPDS references of graphite and $\delta$-$MnO_2$, indicating that PCF@$MnO_2$ consists of graphitic carbon and primarily $\delta$-$MnO_2$. The broad full width at half maximum (FWHM) implies a limited crystallinity of $\delta$-$MnO_2$.[58]

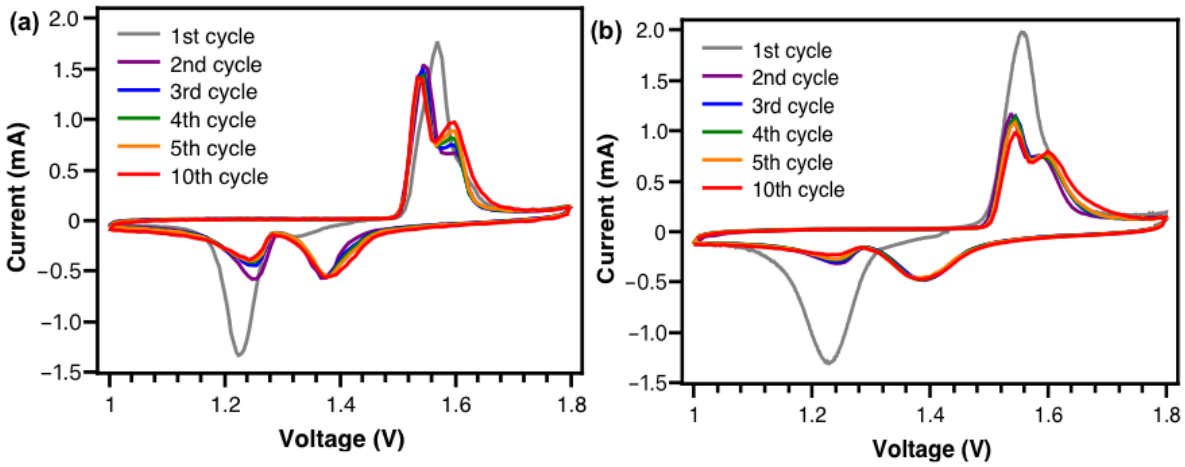


**Figure S5.4.** Initial cycles of (a) PCF@$MnO_2$ 80 ℃-55.9% and (b) PCF@$MnO_2$ RT-59.1% at 0.1 mV $s^{-1}$.

In the cyclic voltammetry of PCF@$MnO_2$, only one reductive peak at 1.22 V and one oxidative peak at 1.57 V appeared in the first discharging-charging cycle, corresponding to the phase transition from $MnO_2$ to a layered hydrated structure (Zn-buserite).[50] The following cycles showed two distinct reductive peaks (1.23 V, 1.37 V) and two oxidative peaks (1.56 V, 1.61 V), corresponding to the debatable two-regime electrochemical mechanism.[8, 9, 49, 50]

PCF@$MnO_2$ cathodes incubated at different temperatures with varying $MnO_2$ loadings were tested in coin cells at increasing current densities. As expected, all cells exhibited a two-stage voltage profile.[8, 9, 49, 50] The detailed rate capabilities of PCF@$MnO_2$ cathodes were compared in Figure 6c, d and e.

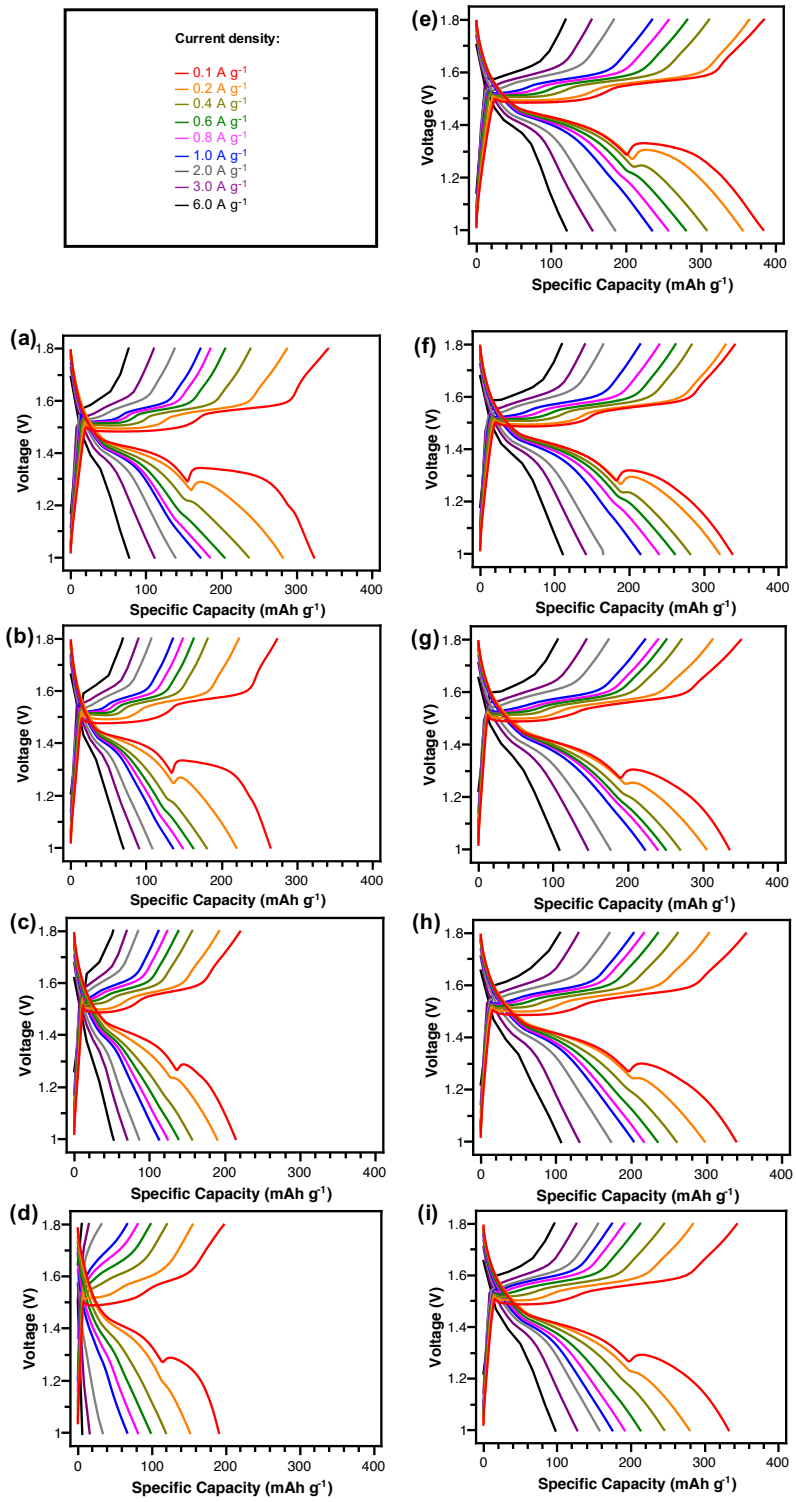


**Figure S5.5.** Voltage profiles of aqueous ZIBs containing PCF@$MnO_2$ cathodes incubated at 80 °C with a $MnO_2$ loading of (a) 34.6%, (b) 42.7%, (c) 55.9% and (d) 71.2%, or PCF@$MnO_2$ incubated at RT with a $MnO_2$ loading of (e) 23.7%, (f) 31.0%, (g) 40.9%, (h) 50.2% and (i) 59.1%.

## 5.7 Acknowledgements

This material is based upon work supported by the National Science Foundation under Grant No. DMR-1752611 and the American Chemical Society Petroleum Research Foundation Doctoral New Investigator Award. The authors acknowledge the use of facilities in Nanoscale Characterization and Fabrication Laboratory (NCFL) at the Institute for Critical Technology and Applied Science (ICTAS), Virginia Tech.

## 5.8 References

1. Dunn, B.; Kamath, H.; Tarascon, J. M., Electrical Energy Storage for the Grid: A Battery of Choices. *Science* **2011**, *334*, 928-935.

2. Larcher, D.; Tarascon, J. M., Towards Greener and More Sustainable Batteries for Electrical Energy Storage. *Nat. Chem.* **2015**, *7*, 19-29.

3. Xia, C.; Guo, J.; Lei, Y.; Liang, H.; Zhao, C.; Alshareef, H. N., Rechargeable Aqueous Zinc-Ion Battery Based on Porous Framework Zinc Pyrovanadate Intercalation Cathode. *Adv. Mater.* **2018**, *30*, 1705580.

4. Li, S.; Liu, Y.; Zhao, X.; Shen, Q.; Zhao, W.; Tan, Q.; Zhang, N.; Li, P.; Jiao, L.; Qu, X., Sandwich-Like Heterostructures of $MoS_2$/Graphene with Enlarged Interlayer Spacing and Enhanced Hydrophilicity as High-Performance Cathodes for Aqueous Zinc-Ion Batteries. *Adv. Mater.* **2021**, *33*, 2007480.

5. Chao, D.; Zhu, C. R.; Song, M.; Liang, P.; Zhang, X.; Tiep, N. H.; Zhao, H.; Wang, J.; Wang, R.; Zhang, H.; Fan, H. J., A High-Rate and Stable Quasi-Solid-State Zinc-Ion Battery with Novel 2D Layered Zinc Orthovanadate Array. *Adv. Mater.* **2018**, *30*, 1803181.

6. Zhang, N.; Cheng, F.; Liu, J.; Wang, L.; Long, X.; Liu, X.; Li, F.; Chen, J., Rechargeable Aqueous Zinc-Manganese Dioxide Batteries with High Energy and Power Densities. *Nat. Commun.* **2017**, *8*, 405.

7. Sun, W.; Wang, F.; Zhang, B.; Zhang, M.; Küpers, V.; Ji, X.; Theile, C.; Bieker, P.; Xu, K.; Wang, C.; Wenter, M., A Rechargeable Zinc-Air Battery Based on Zinc Peroxide Chemistry. *Science* **2021**, *371*, 46-51.

8. Pan, H.; Shao, Y.; Yan, P.; Cheng, Y.; Han, K. S.; Nie, Z.; Wang, C.; Yang, J.; Li, X.; Bhattacharya, P.; Mueller, K. T.; Liu, J., Reversible Aqueous Zinc/Manganese Oxide Energy Storage from Conversion Reactions. *Nat. Energy* **2016**, *1*, 16039.

9. Sun, W.; Wang, F.; Hou, S.; Yang, C.; Fan, X.; Ma, Z.; Gao, T.; Han, F.; Hu, R.; Zhu, M.; Wang, C., $Zn/MnO_2$ Battery Chemistry with $H^+$ and $Zn^{2+}$ Coinsertion. *J. Am. Chem. Soc.* **2017**, *139*, 9775-9778.

10. Yuan, D.; Zhao, J.; Ren, H.; Chen, Y.; Chua, R.; Jie, E. T. J.; Cai, Y.; Edison, E.; Manalastas, W., Jr.; Wong, M. W.; Srinivasan, M., Anion Texturing Towards Dendrite-Free Zn Anode for Aqueous Rechargeable Batteries. *Angew. Chem. Int. Ed.* **2021**, *60*, 7213-7219.

11. Wang, F.; Hu, E.; Sun, W.; Gao, T.; Ji, X.; Fan, X.; Han, F.; Yang, X.-Q.; Xu, K.; Wang, C., A Rechargeable Aqueous $Zn^{2+}$-Battery with High Power Density and a Long Cycle-Life. *Energy Environ. Sci.* **2018**, *11*, 3168-3175.

12. Chen, M.; Chen, J.; Zhou, W.; Han, X.; Yao, Y.; Wong, C. P., Realizing an All-Round Hydrogel Electrolyte toward Environmentally Adaptive Dendrite-Free Aqueous Zn-$MnO_2$ Batteries. *Adv. Mater.* **2021**, *33*, 2007559.

13. Ding, J.; Du, Z.; Li, B.; Wang, L.; Wang, S.; Gong, Y.; Yang, S., Unlocking the Potential of Disordered Rocksalts for Aqueous Zinc-Ion Batteries. *Adv. Mater.* **2019**, *31*, 1904369.

14. Wang, W.; Kale, V. S.; Cao, Z.; Lei, Y.; Kandambeth, S.; Zou, G.; Zhu, Y.; Abouhamad, E.; Shekhah, O.; Cavallo, L.; Eddaoudi, M.; Alshareef, H. N., Molecular Engineering of Covalent Organic Framework Cathodes for Enhanced Zinc-Ion Batteries. *Adv. Mater.* **2021**, *33*, 2103617.

15. Tan, Q.; Li, X.; Zhang, B.; Chen, X.; Tian, Y.; Wan, H.; Zhang, L.; Miao, L.; Wang, C.; Gan, Y.; Jiang, J.; Wang, Y.; Wang, H., Valence Engineering via in situ Carbon Reduction on Octahedron Sites $Mn_3O_4$ for Ultra-Long Cycle Life Aqueous Zn-Ion Battery. *Adv. Energy Mater.* **2020**, *10*, 2001050.

16. Liu, S.; Zhu, H.; Zhang, B.; Li, G.; Zhu, H.; Ren, Y.; Geng, H.; Yang, Y.; Liu, Q.; Li, C. C., Tuning the Kinetics of Zinc-Ion Insertion/Extraction in $V_2O_5$ by in situ Polyaniline Intercalation Enables Improved Aqueous Zinc-Ion Storage Performance. *Adv. Mater.* **2020**, *32*, 2001113.

17. George Blomgren, J. H., Batteries, Primary Cells. In *Kirk-Othmer Encyclopedia of Chemical Technology.*, John Wiley & Sons, Inc.: 2000; Vol. 3, pp 434-477.

18. Li, Y.; Fu, J.; Zhong, C.; Wu, T.; Chen, Z.; Hu, W.; Amine, K.; Lu, J., Recent Advances in Flexible Zinc-Based Rechargeable Batteries. *Adv. Energy Mater.* **2018**, *9*, 1802605.

19. Shin, J.; Seo, J. K.; Yaylian, R.; Huang, A.; Meng, Y. S., A Review on Mechanistic Understanding of $MnO_2$ in Aqueous Electrolyte for Electrical Energy Storage Systems. *Int. Mater. Rev.* **2019**, *65*, 356-387.

20. Liu, L.; Wu, Y. C.; Huang, L.; Liu, K.; Duployer, B.; Rozier, P.; Taberna, P. L.; Simon, P., Alkali Ions Pre-Intercalated Layered $MnO_2$ Nanosheet for Zinc-Ions Storage. *Adv. Energy Mater.* **2021**, *11*, 2101287.

21. Chao, D.; Ye, C.; Xie, F.; Zhou, W.; Zhang, Q.; Gu, Q.; Davey, K.; Gu, L.; Qiao, S. Z., Atomic Engineering Catalyzed $MnO_2$ Electrolysis Kinetics for a Hybrid Aqueous Battery with High Power and Energy Density. *Adv. Mater.* **2020**, *32*, 2001894.

22. Cheng, F. Y.; Chen, J.; Gou, X. L.; Shen, P. W., High-Power Alkaline Zn-$MnO_2$ Batteries Using $\gamma$-$MnO_2$ Nanowires/Nanotubes and Electrolytic Zinc Powder. *Adv. Mater.* **2005**, *17*, 2753-2756.

23. Yang, R.; Fan, Y.; Ye, R.; Tang, Y.; Cao, X.; Yin, Z.; Zeng, Z., $MnO_2$ -Based Materials for Environmental Applications. *Adv. Mater.* **2021**, *33*, 2004862.

24. Pan, H.; Ellis, J. F.; Li, X.; Nie, Z.; Chang, H. J.; Reed, D., Electrolyte Effect on the Electrochemical Performance of Mild Aqueous Zinc-Electrolytic Manganese Dioxide Batteries. *ACS Appl. Mater. Interfaces* **2019**, *11*, 37524-37530.

25. Liu, Y.; Zhi, J.; Sedighi, M.; Han, M.; Shi, Q.; Wu, Y.; Chen, P., $Mn^{2+}$ Ions Confined by Electrode Microskin for Aqueous Battery Beyond Intercalation Capacity. *Adv. Energy Mater.* **2020**, *10*, 2002578.

26. Wu, B.; Zhang, G.; Yan, M.; Xiong, T.; He, P.; He, L.; Xu, X.; Mai, L., Graphene Scroll-Coated α-$MnO_2$ Nanowires as High-Performance Cathode Materials for Aqueous Zn-Ion Battery. *Small* **2018**, *14*, 1703850.

27. Moon, H.; Ha, K. H.; Park, Y.; Lee, J.; Kwon, M. S.; Lim, J.; Lee, M. H.; Kim, D. H.; Choi, J. H.; Choi, J. H.; Lee, K. T., Direct Proof of the Reversible Dissolution/Deposition of $Mn^{2+}$/$Mn^{4+}$ for Mild-Acid Zn-$MnO_2$ Batteries with Porous Carbon Interlayers. *Adv. Sci.* **2021**, *8*, 2003714.

28. Jiao, Y.; Kang, L.; Berry-Gair, J.; McColl, K.; Li, J.; Dong, H.; Jiang, H.; Wang, R.; Corà, F.; Brett, D. J. L.; He, G.; Parkin, I. P., Enabling Stable $MnO_2$ Matrix for Aqueous Zinc-Ion Battery Cathodes. *J. Mater. Chem. A* **2020**, *8*, 22075-22082.

29. Fu, Y.; Wei, Q.; Zhang, G.; Wang, X.; Zhang, J.; Hu, Y.; Wang, D.; Zuin, L.; Zhou, T.; Wu, Y.; Sun, S., High-Performance Reversible Aqueous Zn-Ion Battery Based on Porous Mnox Nanorods Coated by MOF-Derived N-Doped Carbon. *Adv. Energy Mater.* **2018**, *8*, 1801445.

30. Zhao, S.; Zuo, Y.; Liu, T.; Zhai, S.; Dai, Y.; Guo, Z.; Wang, Y.; He, Q.; Xia, L.; Zhi, C.; Bae, J.; Wang, K.; Ni, M., Multi-Functional Hydrogels for Flexible Zinc-Based Batteries Working under Extreme Conditions. *Adv. Energy Mater.* **2021**, *11*, 2101749.

31. Alfaruqi, M. H.; Islam, S.; Gim, J.; Song, J.; Kim, S.; Pham, D. T.; Jo, J.; Xiu, Z.; Mathew, V.; Kim, J., A High Surface Area Tunnel-Type α-$MnO_2$ Nanorod Cathode by a Simple Solvent-Free Synthesis for Rechargeable Aqueous Zinc-Ion Batteries. *Chem. Phys. Lett.* **2016**, *650*, 64-68.

32. Alfaruqi, M. H.; Gim, J.; Kim, S.; Song, J.; Pham, D. T.; Jo, J.; Xiu, Z.; Mathew, V.; Kim, J., A Layered δ-$MnO_2$ Nanoflake Cathode with High Zinc-Storage Capacities for Eco-Friendly Battery Applications. *Electrochem. Commun.* **2015**, *60*, 121-125.

33. Zhu, S.; Li, L.; Liu, J.; Wang, H.; Wang, T.; Zhang, Y.; Zhang, L.; Ruoff, R. S.; Dong, F., Structural Directed Growth of Ultrathin Parallel Birnessite on β-$MnO_2$ for High-Performance Asymmetric Supercapacitors. *ACS Nano* **2018**, *12*, 1033-1042.

34. Zhu, H. T.; Luo, J.; Yang, H. X.; Liang, J. K.; Rao, G. H.; Li, J. B.; Du, Z. M., Birnessite-Type $MnO_2$ Nanowalls and Their Magnetic Properties. *J. Phys. Chem. C* **2008**, *112*, 17089-17094.

35. Putro, D. Y.; Alfaruqi, M. H.; Islam, S.; Kim, S.; Park, S.; Lee, S.; Hwang, J.-Y.; Sun, Y.-K.; Kim, J., Quasi-Solid-State Zinc-Ion Battery Based on α-$MnO_2$ Cathode with Husk-Like Morphology. *Electrochim. Acta* **2020**, *345*, 136189.

36. Moazzen, E.; Timofeeva, E. V.; Segre, C. U., Controlled Synthesis of Mno2 Nanoparticles for Aqueous Battery Cathodes: Polymorphism-Capacity Correlation. *J. Mater. Sci.* **2017**, *52*, 8107-8118.

37. Xia, H.; Wang, Y.; Lin, J.; Lu, L., Hydrothermal Synthesis of $MnO_2$/CNT Nanocomposite with a CNT Core/Porous $MnO_2$ Sheath Hierarchy Architecture for Supercapacitors. *Nanoscale Res. Lett.* **2012**, *7*, 33-43.

38. Zhang, M.; Wu, W.; Luo, J.; Zhang, H.; Liu, J.; Liu, X.; Yang, Y.; Lu, X., A High-Energy-Density Aqueous Zinc-Manganese Battery with a La-Ca Co-Doped ε-$MnO_2$ Cathode. *J. Mater. Chem. A* **2020**, *8*, 11642-11648.

39. Liu, J.; Zhang, Y.; Li, Y.; Li, J.; Chen, Z.; Feng, H.; Li, J.; Jiang, J.; Qian, D., In Situ Chemical Synthesis of Sandwich-Structured $MnO_2$ /Graphene Nanoflowers and Their Supercapacitive Behavior. *Electrochim. Acta* **2015**, *173*, 148-155.

40. Jin, Y.; Zou, L.; Liu, L.; Engelhard, M. H.; Patel, R. L.; Nie, Z.; Han, K. S.; Shao, Y.; Wang, C.; Zhu, J.; Pan, H.; Liu, J., Joint Charge Storage for High-Rate Aqueous Zinc-Manganese Dioxide Batteries. *Adv. Mater.* **2019**, *31*, 1900567.

41. Chen, Y. H.; Wang, C. W.; Liu, G.; Song, X. Y.; Battaglia, V. S.; Sastry, A. M., Selection of Conductive Additives in Li-Ion Battery Cathodes. *J. Electrochem. Soc.* **2007**, *154*, A978-A986.

42. Chen, J.; Zhou, Y.; Islam, M. S.; Cheng, X.; Brown, S. A.; Han, Z.; Rider, A. N.; Wang, C. H., Carbon Fiber Reinforced Zn-$MnO_2$ Structural Composite Batteries. *Compos. Sci. Technol.* **2021**, *209*, 108787.

43. Xie, C.; Li, T.; Deng, C.; Song, Y.; Zhang, H.; Li, X., A Highly Reversible Neutral Zinc/Manganese Battery for Stationary Energy Storage. *Energy Environ. Sci.* **2020**, *13*, 135-143.

44. Qiu, W.; Li, Y.; You, A.; Zhang, Z.; Li, G.; Lu, X.; Tong, Y., High-Performance Flexible Quasi-Solid-State Zn-$MnO_2$ Battery Based on $MnO_2$ Nanorod Arrays Coated 3D Porous Nitrogen-Doped Carbon Cloth. *J. Mater. Chem. A* **2017**, *5*, 14838-14846.

45. Liu, T.; Zhou, Z.; Guo, Y.; Guo, D.; Liu, G., Block Copolymer Derived Uniform Mesopores Enable Ultrafast Electron and Ion Transport at High Mass Loadings. *Nat. Commun.* **2019**, *10*, 675.

46. Serrano, J. M.; Liu, T.; Khan, A. U.; Botset, B.; Stovall, B. J.; Xu, Z.; Guo, D.; Cao, K.; Hao, X.; Cheng, S.; Liu, G., Composition Design of Block Copolymers for Porous Carbon Fibers. *Chem. Mater.* **2019**, *31*, 8898-8907.

47. Zhou, Z.; Liu, T.; Khan, A. U.; Liu, G., Block Copolymer-Based Porous Carbon Fibers. *Sci. Adv.* **2019**, *9*, eaau6852.

48. Chen, Y.; Zhang, Y.; Geng, D.; Li, R.; Hong, H.; Chen, J.; Sun, X., One-Pot Synthesis of $MnO_2$/Graphene/Carbon Nanotube Hybrid by Chemical Method. *Carbon* **2011**, *49*, 4434-4442.

49. Li, Y.; Wang, S.; Salvador, J. R.; Wu, J.; Liu, B.; Yang, W.; Yang, J.; Zhang, W.; Liu, J.; Yang, J., Reaction Mechanisms for Long-Life Rechargeable Zn/$MnO_2$ Batteries. *Chem. Mater.* **2019**, *31*, 2036-2047.

50. Chamoun, M.; Brant, W. R.; Tai, C.-W.; Karlsson, G.; Noréus, D., Rechargeability of Aqueous Sulfate Zn/$MnO_2$ Batteries Enhanced by Accessible $Mn^{2+}$ Ions. *Energy Storage Mater.* **2018**, *15*, 351-360.

51. Augustyn, V.; Come, J.; Lowe, M. A.; Kim, J. W.; Taberna, P. L.; Tolbert, S. H.; Abruna, H. D.; Simon, P.; Dunn, B., High-Rate Electrochemical Energy Storage through $Li^+$ Intercalation Pseudocapacitance. *Nat. Mater.* **2013**, *12*, 518-522.

52. Simon, P.; Gogotsi, Y.; Dunn, B., Where Do Batteries End and Supercapacitors Begin? *Science* **2014**, *343*, 1210.

53. Augustyn, V.; Simon, P.; Dunn, B., Pseudocapacitive Oxide Materials for High-Rate Electrochemical Energy Storage. *Energy Environ. Sci.* **2014**, *7*, 1597-1614.

54. Zeng, Y.; Zhang, X.; Meng, Y.; Yu, M.; Yi, J.; Wu, Y.; Lu, X.; Tong, Y., Achieving Ultrahigh Energy Density and Long Durability in a Flexible Rechargeable Quasi-Solid-State Zn-$MnO_2$ Battery. *Adv. Mater.* **2017**, *29*, 1700274.

55. Kundu, D.; Adams, B. D.; Duffort, V.; Vajargah, S. H.; Nazar, L. F., A High-Capacity and Long-Life Aqueous Rechargeable Zinc Battery Using a Metal Oxide Intercalation Cathode. *Nat. Energy* **2016**, *1*, 16119.

56. Lee, J.; Ju, J. B.; Cho, W. I.; Cho, B. W.; Oh, S. H., Todorokite-Type $MnO_2$ as a Zinc-Ion Intercalating Material. *Electrochim. Acta* **2013**, *112*, 138-143.

57. He, P.; Yan, M.; Zhang, G.; Sun, R.; Chen, L.; An, Q.; Mai, L., Layered $VS_2$ Nanosheet-Based Aqueous Zn Ion Battery Cathode. *Adv. Energy Mater.* **2017**, *7*, 1601920.

58. Ahmad, K.; Mobin, S. M., Design and Fabrication of Cost-Effective and Sensitive Non-Enzymatic Hydrogen Peroxide Sensor Using Co-Doped δ-$MnO_2$ Flowers as Electrode Modifier. *Anal. Bioanal. Chem.* **2021**, *413*, 789-798.

# Chapter 6. Conclusions and Future Perspectives

## 6.1 Overall conclusions.

This dissertation reports the method of utilizing block copolymers to derive mesoporous polyimide thin films and porous carbon fibers for high-performance energy storage. Block copolymers consisting of stable blocks and labile blocks undergo phase separation to form bicontinuous microstructures. Subsequently, the selective removal of the labile phase creates mesopores, whereas the remaining stable phase produces mesoporous polymeric materials. Noteworthy, removing the labile phase without plasticizing the remaining stable phase is crucial to fabricating mesopores. Two examples adopting this method are investigated systematically. i) Mesoporous polyimide thin films, functionating as dendrite-suppressing separators, enable the safe cycling of lithium-metal batteries. ii) Porous carbon fibers, supporting nanometer-thin-layer $MnO_2$, produce fast-charging cathodes for aqueous zinc-ion batteries.

First, **Chapter 2** investigates the microphase separation of polyimide-based ABA-type triblock copolymers. Those triblock copolymers comprise a polyimide middle block and oligomeric polystyrene end blocks. Due to the intrinsic broad dispersity of polyimide middle block synthesized *via* polycondensation, those triblock copolymers form a unique irregular bicontinuous structure, even at ultra-low molecular weights of 11, 13 and 15 kDa. Notably, the microphase separation of those low-molecular-weight copolymers forms domains smaller than 10 nm.

Second, **Chapter 3** reports mesoporous polyimide thin films produced by hydrolyzing polylactide-*b*-polyimide-*b*-polylactide copolymers. The hydrolysis removes polylactide without perturbing the polyimide matrices, therefore affording high-modulus mesoporous polyimide thin

films with 24 nm wide mesopores. This hydrolysis takes place at low temperatures, thus this methode is felicitous to prepare mesoporous polyimides having low glass transition temperatures.

Third, **Chapter 4** explores mesoporous polyimide thin films as dendrite-suppressing separators in lithium-metal batteries. The mesoporous polyimide thin films are prepared *via* thermolysis of polylactide-*b*-polyimide-*b*-polylactide at gradually elevated temperatures, possessing a median pore width of 21 nm and a modulus of 1.80 GPa. Serving as a battery separator, the mesoporous polyimide thin film suppresses the dendritic growth of lithium and enables safe cycling for 500 hours at a current density of 4 $mA/cm^2$.

Fourth, **Chapter 5** investigates porous carbon fiber-supported $MnO_2$ cathode for fast-charging zinc-ion batteries. The porous carbon fibers are derived by thermalizing electrospun poly(methyl methacrylate)-*b*-polyacrylonitrile fibers. The thermolysis converts polyacrylonitrile into graphitic carbon, meanwhile, poly(methyl methacrylate) decomposes to create mesopores. The porous carbon fibers not only provide good electrical conductivity, but also offer a high specific area to deposit a high loading of $MnO_2$ as a nanometer-thin-layer. The high electrical conductivity of PCF, fast electrochemical reactions in nanometer-thick $MnO_2$, and fast ion transport through porous nonwoven fibers contribute to a high rate capability. PCF@$MnO_2$, at a $MnO_2$ loading of 59.1 wt%, achieves a $MnO_2$-based specific capacity of 326 and 184 mAh/g at a current density of 0.1 and 1.0 A/g, respectively.

## 6.2 Perspectives

### *6.2.1 Sub-10 nm Domains in High-Performance Polyetherimides*

In Chapter 2, the polystyrene-*b*-polyimide-*b*-polystyrene copolymers are featured with the broad dispersity of polyimide middle blocks but narrow dispersity of polystyrene end blocks. Unlike the

regular microstructures formed by narrow-dispersity AB-type diblock or ABA-type triblock copolymers, the broad dispersity of those polystyrene-*b*-polyimide-*b*-polystyrene copolymers incurs an irregular bicontinuous microstructure. However, the effects of the dispersity of polystyrene end blocks on the microphase-separated structures remain to be explored (Figure 6.1, Case (4)). The broad-dispersity polystyrene end blocks not only break the symmetry of polystyrene-*b*-polyimide-*b*-polystyrene, but also change the segregation driving force. Therefore, a design of experiment to produce both narrow-dispersity and broad-dispersity polystyrene end blocks is proposed for future investigations.

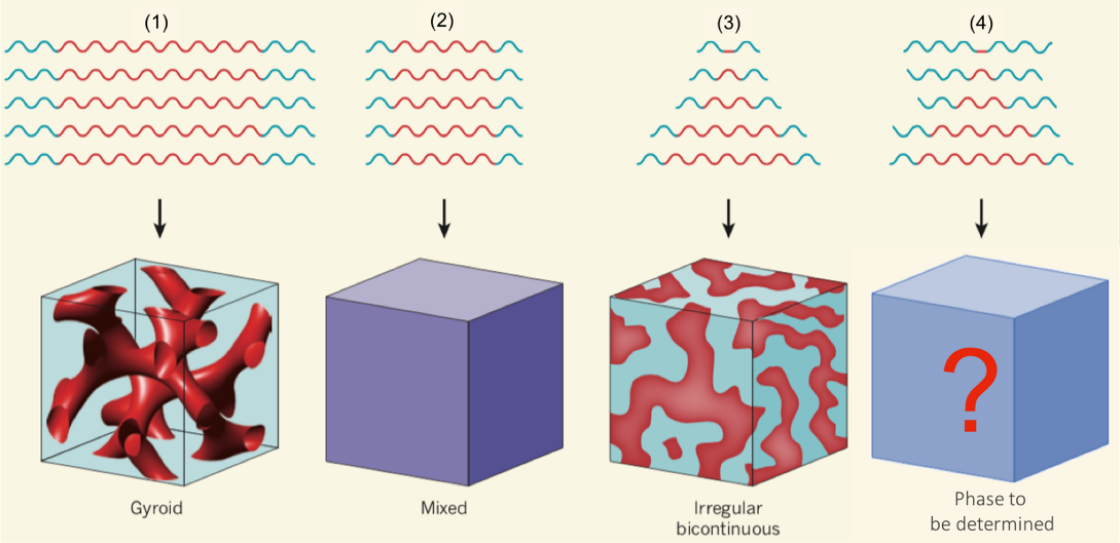


**Figure 6.1.** Effects of dispersity on microphase separations. Case (1), (2) and (3) are elaborated in Figure 1.4, Chapter 1.1. Case (1): narrow-dispersity and high-molecular-weight ABA-type triblock copolymers form a gyroid microstructure at a certain volume fraction. Case (2): narrow-dispersity and low-molecular-weight ABA-type triblock copolymers cannot form domains. Case (3): low-molecular-weight ABA-type triblock copolymers, consisting of narrow-dispersity A blocks and broad-dispersity B blocks, form a robust bicontinuous microstructure, though A blocks have the same lengths as in Case (2) and broad-dispersity B blocks have a shorter average length than that in Case (2). Reprint with permission from *Nature* **2012**, 483, 167-168.[1] Copyright 2012 Springer

Nature. Case (4): low-molecular-weight ABA-type triblock copolymers comprise broad-dispersity A blocks and broad-dispersity B blocks. The microphase-separated morphology remains to be explored.

The narrow-dispersity amine-terminated polystyrene (PS-$NH_2$) was synthesized using atomic transfer radical polymerization (ATRP) (Scheme 2.1).[2] Contrarily, to produce the broad-dispersity PS-$NH_2$, an "uncontrolled" free-radical polymerization is suggested (Scheme 6.1). The polymerization is initiated by azobisisobutyronitrile (AIBN) to grow polystyrene exhibiting the dispersity of 2.[2] The AIBN moieties are converted to terminal amine groups by the reduction using $LiAlH_4$ and the protonation using a small amount of $H_2O$.[3] This broad-dispersity PS-$NH_2$ is then incorporated onto the chain ends of anhydride-terminated polyimide to produce polystyrene-*b*-polyimide-*b*-polystyrene having broad dispersity of 2 for all constituent blocks. Subsequently, the microphase separations of those broad-broad-broad dispersity triblock copolymers are compared against the narrow-broad-narrow dispersity triblock copolymers in Chapter 2 to elucidate the effects of end block dispersity.

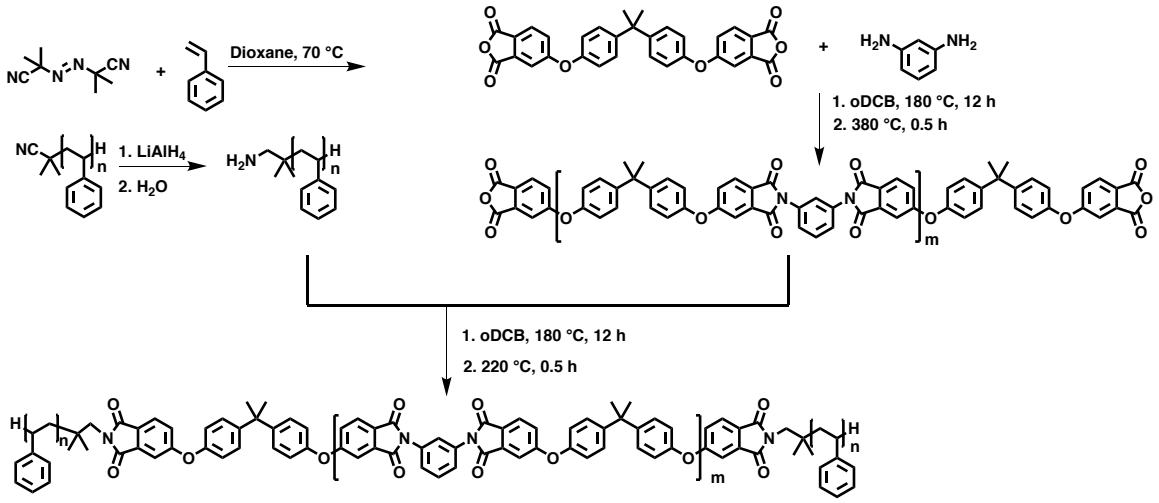


**Scheme 6.1.** Synthesis of broad-dispersity amine-terminated polystyrene and all-broad-dispersity polystyrene-*b*-polyimide-*b*-polystyrene.

Presumably, the broad dispersity of polystyrene end blocks will further increase the irregularity of the microphase-separated structures. Especially, three aspects are worthy of extra attention: i) is the ability to undergo microphase separations at low molecular weights retained. ii) Do those broad-broad-broad dispersity copolymers form small domain sizes, *e.g.*, sub-10 nm domains, or form swelled larger domains. iii) Is the phase diagram, $\chi N$ vs. volume fraction of polyimide, still asymmetric, or becoming symmetric as observed for narrow-dispersity AB or ABA-type block copolymers.

In addition, this dissertation explores the microphase separations of polyimide-based ABA-type triblock copolymers having different polyimide volume fractions $f_B$, including PS-*b*-PI-*b*-PS with an $f_B$ between 70 to 77% in Chapter 2, PLA-*b*-PI-*b*-PLA with an $f_B$ of 60% in Chapter 3 and 4. All the polyimide-based triblock copolymers show irregular bicontinuous microstructures, though the phase diagram based on poly(styrene-*b*-1,4-butadiene-*b*-styrene) copolymers (SBS) indicates a lamellar structure for the $f_B$ between 56 and 80% (Figure 1.3). Two reasons may account for this discrepancy: i) the significantly different persistent lengths of polyimide and polystyrene/polylactide shift the boundary of microphase-separated structures.[4-6] ii) The polyimide-based triblock copolymers form a metastable bicontinuous microstructure instead of the stable lamellar structure.[7] To elucidate if those bicontinuous microstructures are metastable or stable, both self-consistent mean field simulations and microphase separations under different annealing conditions are necessary for further investigations.

### *6.2.2 Mesoporous Polyetherimide Thin Films via Hydrolysis of Polylactide-b-Polyetherimide-b-Polylactide*

Mesoporous polyetherimide thin films are produced *via* the hydrolysis of polylactide-*b*-polyetherimide-*b*-polylactide (AIA) in Chapter 3. The hydrolysis in a phosphate buffer solution removed the polylactide phase in the microphase-separated AIA to produce mesopores polyimide thin films. The polylactide was hydrolyzed into soluble species, *e.g.*, potassium lactate, to expose the underlying polylactide domains, thereby further hydrolysis continues to remove more polylactide. The polylactide weight fraction in hydrolyzed AIA decreased from 40% to about 9% after 5-day hydrolysis. Noteworthy, further extending hydrolysis time to 9 days did not remove more polylactide (Figure 3.6a and b). The residual polylactide immune to hydrolysis presumably resulted from the isolated polylactide domains. Although the polylactide volume fraction of 40% in AIA favors a bicontinuous microstructure consisting of polylactide and polyetherimide,[8] the irregular microstructure retains a small number of polylactide domains discontinued from the major polylactide phase (Figure 6.2). Therefore, those isolated polylactide domains were not exposed to the phosphate buffer solution owing to the surrounding polyetherimide, resulting in polylactide residue of about 9% regardless of prolonged hydrolysis time.

To investigate the effects of polylactide volume fraction in AIA on the continuity of polylactide phase after the microphase separation, AIA copolymers comprise different polylactide volume fractions should be systematically explored. Potentially, a higher polylactide fraction incurs better polylactide phase continuity. Tuning the polymerization time of polylactide tailors the molecular weight of polylactide constituent blocks, thus varying the volume fraction of polylactide in AIA. Comparing the polylactide residue of AIA comprising different fractions of polylactide, using $^{1}$H NMR as in Figure 3.6a and b, will disclose the correlation between the

polylactide volume fraction and phase continuity. The AIA exhibiting the best polylactide phase continuity affords the least polylactide residue after the hydrolysis.

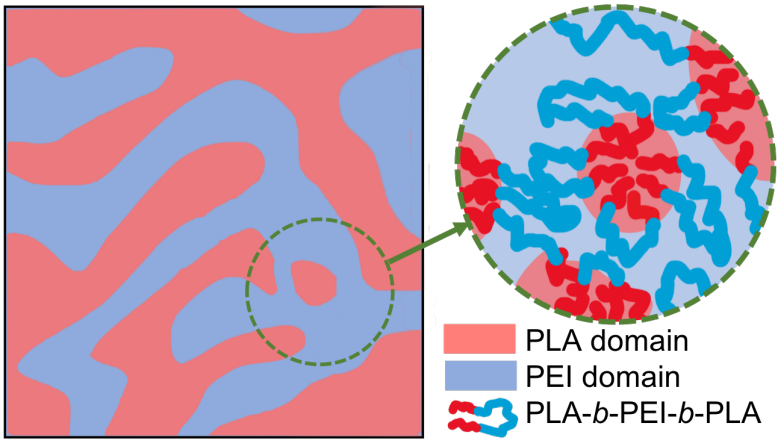


**Figure 6.2.** Illustration of isolated polylactide (PLA) domains. The green area highlights an isolated PLA domain in the microphase-separated structures. The isolated PLA domain is surrounded by polyetherimide (PEI) so that it is not exposed to the hydrolytic solution. Therefore, those isolated PLA cannot be removed even after extending hydrolysis time.

Moreover, Chapter 3 reports the hydrolysis of PLA taking place under mild conditions, *i.e.*, a pH of 7.4 at 70 °C. The weight fraction of PLA decreased gradually in the first 5 days to reach an ultimate residue of about 9%. To prepare mesoporous polyimide thin films within a shorter time, future investigations of hydrolysis conditions to remove PLA more efficiently are necessary. Two parameters are momentous for the hydrolysis efficiency: i) increasing the pH value expedites the hydrolysis of polylactide,[9, 10] ii) increasing the temperature accelerates the removal of polylactide.[9, 10] However, on one hand, a strongly basic solution also possibly hydrolyzes polyetherimide to promote imide ring-opening or chain scission, jeopardizing the mechanical performance of resulting mesoporous polyimide films. On the other hand, although a higher hydrolysis temperature is advantageous for faster hydrolysis, the temperatures should be limited

to be lower than the boiling point of the aqueous buffer solution. A combination of the appropriate pH, temperature and AIA composition is able to fully remove the polylactide phase to produce mesoporous polyimide thin films efficiently.

### *6.2.3 Mesoporous Polyimide Thin Films as Dendrite-Suppressing Separators for Lithium-Metal Batteries*

The mesoporous polyimide separators show a good dendrite-suppressing capability to enable the safe cycling of lithium-metal batteries. The ionic impedance of mesoporous polyimide separators, however, is higher than the commercial polyolefin separators because of the smaller pore size. The higher ionic impedance of mesoporous polyimide separators incurs slightly lower specific capacity at increasing charging rates due to the retarded ion transport. Therefore, reducing the ionic impedance of the mesoporous polyimide separators is imperative to improve the capability at high charging rates. Decreasing the thickness of mesoporous polyimide separators, *e.g.*, from 20 μm to hundreds of nanometers, significantly lowers the ionic impedance. The good solubility of the polylactide-*b*-poly(amic acid)-*b*-polylactide allows utilizing spin-coating technique to prepare mesoporous polyimide thin films with hundreds of nanometers in thickness. The outstanding mechanical performance enables the dendrite-suppression of mesoporous polyimide films even as ultra-thin separators. To produce a lithium-metal battery containing the ultra-thin mesoporous polyimide separator, polylactide-*b*-poly(amic acid)-*b*-polylactide, as well as acetic anhydride and pyridine as the chemical imidization reagents, is spin-coated on the cathode surface. The thermolysis creates the ultra-thin polyimide separator with a thickness of hundreds of nanometers using the same procedure as detailed in Chapter 4. Routinely, the spin coating technique robustly prepares uniform thin films with hundreds of nanometers to micrometers in thickness.[11, 12] The

thickness of the ultra-thin mesoporous polyimide separator is tailored by the spin coating conditions, such as the spinning rates, concentrations, and temperatures. Reducing the thickness of mesoporous polyimide separators lowers the ionic impedance, benefiting the high rate capability and high energy density at high charging currents.

### *6.2.4 Block Copolymer-Derived Porous Carbon Fibers Enable High $MnO_2$ Loading and Fast Charging in Aqueous Zinc-Ion Battery*

The porous carbon fiber-supported $MnO_2$ (PCF@$MnO_2$) cathodes incubated at room temperature (RT) showed higher rate capabilities than the analogues incubated at 80 °C. However, the incubations at RT took a longer time to reach high $MnO_2$ loadings, *e.g.*, 48 h to reach 59.1 wt% at RT vs. 2 h to reach 71.0 wt% at 80 °C. Therefore, increasing the incubation rate while retaining good rate capabilities is desirable for the future investigations.

The high rate capabilities demand thin-layered $MnO_2$ uniformly deposited on the carbon surface, especially the internal mesoporous surface. The $MnO_2$ thin layer was generated utilizing the redox reaction between $KMnO_4$ and carbon. The good uniformity of $MnO_2$ requires minimizing the $KMnO_4$ depletion when the $KMnO_4$ diffuses into mesopores and reacts with carbon simultaneously (Figure 6.3). Increasing the concentration of $KMnO_4$ and decreasing temperatures are able to mitigate the $KMnO_4$ depletion. However, decreasing the incubation temperatures significantly slows down the redox reaction. Consequently, the improved incubation conditions require a high $KMnO_4$ concentration and an appropriate temperature to balance a fast redox reaction and timely $KMnO_4$ diffusion. To elucidate the optimal incubation conditions, PCF@$MnO_2$ cathodes prepared using increasing $KMnO_4$ concentrations from 1 wt% (63 mM in Chapter 5) to 43 wt% (maximum solubility at RT) and temperatures between RT and 80 °C should

be investigated. Moreover, three concerns should be taken into consideration for the condition screening: i) high temperatures lead to carbon surface exfoliation, resulting in low electrical conductivity and extra nonuniformly out-of-pore $MnO_2$ deposition. ii) High temperatures and the high $KMnO_4$ concentration promote the self-redox of $KMnO_4$ in the following reaction.

$$2\,KMnO_4 \rightarrow K_2MnO_4 + MnO_2 + O_2$$

This reaction not only consumes $KMnO_4$, but also produces $MnO_2$ not depositing on the carbon surface, instead, precipitating from the incubation solution. iii) The solubility of $KMnO_4$ in aqueous solutions varies profoundly with temperatures. Therefore, crystallization of $KMnO_4$ needs to be avoided when adopting high $KMnO_4$ concentrations at varying temperatures. An optimal incubation condition, including a $KMnO_4$ concentration higher than 63 mM and a temperature between RT and 80 °C, will afford PCF@$MnO_2$ exhibiting uniform $MnO_2$ thin layers within a short incubation time.

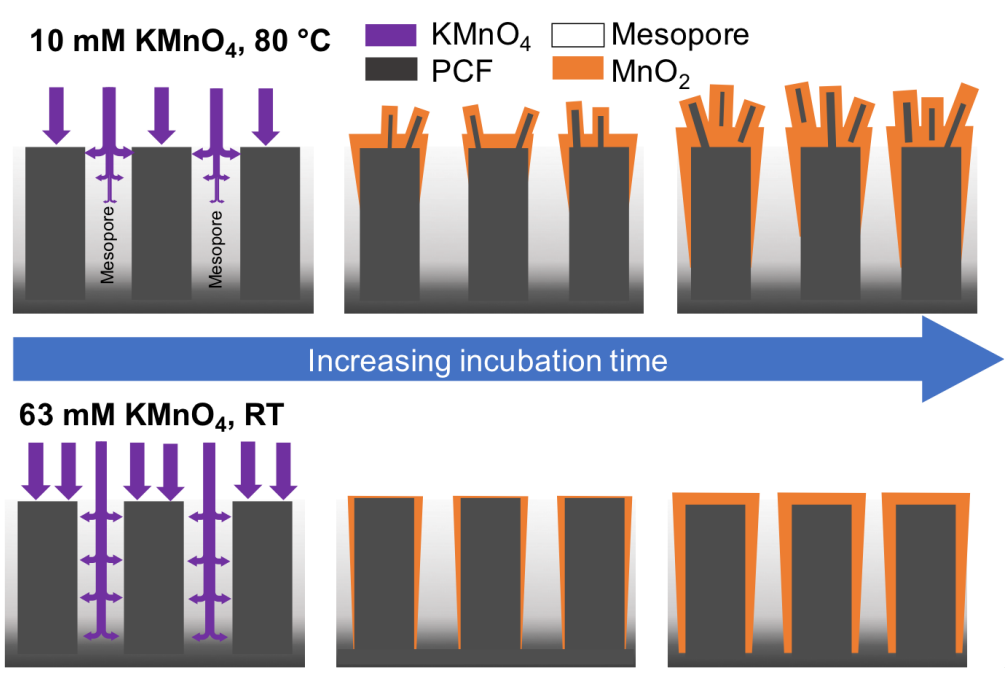


**Figure 6.3.** Effect of $KMnO_4$ concentration and temperature on the morphology of PCF@$MnO_2$. The high-temperature incubations incur the depletion of $KMnO_4$ in mesopores and exfoliation of

carbon. Whereas the RT-incubation mitigates the $KMnO_4$ depletion and carbon exfoliation, allowing for uniform $MnO_2$ deposition and intact carbon.

### *6.2.5 References*


1. Register, R. A., Continuity through Dispersity. *Nature* **2012**, *483*, 167-168.

2. Odian, G., Principles of Polymerization In *Principles of Polymerizaiton*, 4th ed.; John Wiley & Sons, Inc.: Hoboken, New Jersey, 2004; pp 289-292.

3. Amundsen, L. H.; Nelson, L. S., Reduction of Nitrile to Primary Amine with Lithium Aluminum Hydride. *J. Am. Chem. Soc.* **1951**, *73*, 242–244.

4. Matsen, M. W.; Thompson, R. B., Equilibrium Behavior of Symmetric ABA Triblock Copolymer Melts. *J. Chem. Phys.* **1999**, *111*, 7139-7146.

5. Inoue, T.; Osaki, K., Role of Polymer Chain Flexibility on the Viscoelasticity of Amorphous Polymers around the Glass Transition Zone. *Macromolecules* **1996**, *29*, 1595-1599.

6. Matsen, M. W.; Schick, M., Microphases of a Diblock Copolymer with Conformational Asymmetry. *Macromolecules* **1994**, *27*, 4014-4015.

7. Aoyagi, T., Deep Learning Model for Predicting Phase Diagrams of Block Copolymers. *Comput. Mater. Sci.* **2021**, *188*, 110224.

8. Widin, J. M.; Schmitt, A. K.; Schmitt, A. L.; Im, K.; Mahanthappa, M. K., Unexpected Consequences of Block Polydispersity on the Self-Assembly of ABA Triblock Copolymers. *J. Am. Chem. Soc.* **2012**, *134*, 3834-3844.

9. Xu, L.; Crawford, K.; Gorman, C. B., Effects of Temperature and Ph on the Degradation of Poly(lactic acid) Brushes. *Macromolecules* **2011**, *44*, 4777-4782.

10. Li, S.; McCarthy, S., Further Investigations on the Hydrolytic Degradation of Poly($_{DL}$-lactide). *Biomaterials* **1999**, *20*, 35-44.

11. Croft, Z. L.; Xu, Z.; Cao, K.; Guo, D.; Sreeharikesan, S.; Thompson, C.; Zeltzer, G.; Liu, G., Can the Voigt Model Be Directly Used for Determining the Modulus of Graphene in Laminate Thin Films? *ACS Appl. Polym. Mater.* **2021**, *4*, 394-402.

12. Khan, A. U.; Zeltzer, G.; Speyer, G.; Croft, Z. L.; Guo, Y.; Nagar, Y.; Artel, V.; Levi, A.; Stern, C.; Naveh, D.; Liu, G., Mutually Reinforced Polymer-Graphene Bilayer Membranes for Energy-Efficient Acoustic Transduction. *Adv. Mater.* **2021**, *33*, 2004053.